

**Design and Optimal Control of a Magnet Assisted Scanning Stage for
Precise and Energy Efficient Positioning**

by

Deokkyun Yoon

A dissertation submitted in partial fulfillment
of the requirements for the degree of
Doctor of Philosophy
(Mechanical Engineering)
in the University of Michigan
2019

Doctoral Committee:

Associate Professor Chinedum E. Okwudire, Chair
Associate Professor Shorya Awtar
Dr. Xinyi Ge, Delphi Technologies
Professor Albert J. Shih
Professor Emeritus A. Galip Ulsoy

Deokkyun Yoon

yydkyoon@umich.edu

ORCID iD: 0000-0001-8220-5496

© Deokkyun Yoon 2019

DEDICATION

This dissertation is dedicated to my family, Hanna and Jino.

ACKNOWLEDGEMENTS

When I first arrived in Ann Arbor in August of 2005, I did not know that I would be studying three degrees – B.S., M.S., and Ph.D. – at one school. After finishing the M.S. degree, I worked in Daejeon at Korea Institute of Machinery and Materials. Experience there had led me to pursue the Ph.D. degree and I can tell that I made the right decision at that time to study more. The more I dig deeper into the subjects, the more I realized that there are so many works researchers have done in the past, and I am benefitting vastly from their accomplishments. Thus, it is my obligation to society to give back and make rightful contributions to advance the knowledge. Fast-forwarding to the year 2018 and now I am finishing the highest degree the school offers. It has been long, but I have truly enjoyed life in Ann Arbor.

First, I want to thank my advisor, Professor Chinedum Okwudire, who has guided me throughout my entire Ph.D. study since my arrival at the lab in January 2014. He has provided constructive feedback on my research works, valuable wisdom that go beyond the academic setting, and scientific knowledge and resources. Without his thorough and thoughtful guidance, I would not have been able to accomplish what I have so far. I also want to give thanks to the other committee members, Professors Shorya Awtar, Albert Shih, Galip Ulsoy, and Dr. Xinyi Ge. Their inputs on my doctoral research have greatly improved the quality and direction of my dissertation. I want to thank Professor Galip Ulsoy, as his previous work on assist devices has provided an elegant design-based pathway to solve the thermal and vibration-induced error problems in the scanning stages, which is presented in Chapter 3. I also want to thank Dr. Xinyi Ge as we worked out the optimal ILC approach presented in Chapter 5 together, often until late nights with heated discussions. Professors Shorya Awtar and Albert Shih's inputs on improving the analysis works presented in Chapter 3 are also gratefully acknowledged.

I want to thank my current and former lab mates, especially Dr. Molong Duan and Mr. Keval Ramani for their suggestions of using B-splines as a tool for simplifying signals. If I were not closely discussing with them about the state of research, I would not be able to figure out how to further simplify the problem and solve with limited computational resources as discussed in

Chapters 4 and 5. I also want to thank other members of Smart and Sustainable Automation Research Lab. Their feedback has helped me a lot in refining the modeling and mathematical derivation approaches presented in the dissertation.

Additionally, I want to thank Dr. Steve Ludwick of Aerotech for bringing up the thermal and vibration issues in scanning stages used in the industry to my attention. Constructive discussions we had during the initial phase of research helped me correctly formulate the problem and set the overall research direction.

I also want to thank my funding sources, the University of Michigan and the National Science Foundation, for providing me financial means to continue my Ph.D. study and construct/test the design and control-based approaches presented in the dissertation.

I want to thank my wife, Hanna, for her remarkable support all throughout the Ph.D. study. We got married just before I started my Ph.D. study and she graciously agreed to move to a foreign city without knowing what would happen next. Lastly, I want to thank my brothers and sisters of Campus Town Church of Ann Arbor, who have also supported me throughout the years with their warm fellowship.

TABLE OF CONTENTS

DEDICATION	ii
ACKNOWLEDGEMENTS	iii
LIST OF APPENDICES	vii
LIST OF TABLES	ix
LIST OF FIGURES	x
ABSTRACT	xix
Chapter 1 Introduction	1
1.1 Use of scanning stages in semiconductor manufacturing	1
1.2 Thermal and residual vibration problems in scanning stages	7
1.3 Outline of dissertation	9
Chapter 2 Literature Review	11
2.1 Design approaches for reducing temperature and vibration-induced errors	11
2.2 Complementary control approaches and tracking control of dynamic systems..	14
2.3 Contribution of dissertation.....	17
Chapter 3 Design of an Over Actuated Scanning Stage with Permanent Magnet-based Assist Devices.....	19
3.1 Assist device for scanning stages	19
3.2 Design and sizing of permanent magnets.....	23
3.3 Transmission design for automatic positioning of permanent magnets	29
3.4 Design and construction of magnet-assisted scanning stage prototype	33
3.5 Chapter summary	40
Chapter 4 B-Spline based Optimal Trajectory Planning for Magnet-assisted Scanning Stage	42
4.1 Control strategy overview of magnet assisted scanning stage	42
4.2 System modeling and identification.....	43

4.3	Optimal control allocation via PM trajectory optimization	48
4.4	Overview of B-splines representation of motion trajectory	50
4.5	Optimization of B-spline-based trajectory for PMs	54
4.6	Numerical example	56
4.7	Experimental examples	58
4.7.1	Case study I: Scanning for photo-lithography	59
4.7.2	Case study II: Scanning for wafer inspection.....	62
4.7.3	Analysis of stage heat.....	65
4.8	Chapter summary	68
Chapter 5 Optimal Inversion-based Iterative Learning Control of Magnet Assisted Scanning Stage		69
5.1	Overview of optimal inversion-based ILC for over-actuated systems.....	70
5.1.1	Derivation of optimal inversion-based ILC update law	70
5.1.2	Tunable monotonic error convergence rate of optimal inversion-based ILC ..	73
5.2	Incorporation of system model uncertainty.....	75
5.3	Validation of optimal inversion-based ILC using a coarse-fine stage testbed....	79
5.4	Application of optimal inversion-based ILC to magnet assisted scanning stage	79
5.5	Experimental example.....	88
5.6	Chapter summary	93
Chapter 6 Conclusion and Future Work		95
APPENDICES		99
BIBLIOGRAPHY.....		164

LIST OF APPENDICES

Appendix A	Bill of Materials of Magnet Assisted Scanning Stage Prototype	100
Appendix B	CAD Drawings of Magnet Assisted Scanning Stage Prototype.....	103
B.1	CAD drawings for Base Frame	103
B.1.2	Scale Block.....	106
B.1.3	Bumper Block.....	107
B.1.4	Base Frame Connecting Plate #1	108
B.1.5	Base Frame Connecting Plate #2.....	109
B.1.6	Base Frame Connecting Plate #3.....	110
B.1.7	Air Spring Mount #1	111
B.1.8	Air Spring Mount #2	112
B.1.9	Cable Carrier Plate	113
B.1.10	Encoder Readhead Mount	114
B.1.11	Spacer	115
B.1.12	Shaft Support (modification).....	116
B.2	CAD drawings for Machine Frame	117
B.2.1	Connecting Plate.....	118
B.2.2	Nut Mounting Block.....	121
B.2.3	Nut Mounting Plate	122
B.2.4	Fixed Side Plate.....	124
B.2.5	Support Side Plate	125
B.2.6	Step Motor Holder.....	126
B.2.7	Machine Frame Base	127
B.2.8	Force Frame.....	128
B.2.9	Force Frame #2.....	129
B.2.10	Limit sensor L	130
B.2.11	Scale Mount.....	131
B.3	CAD drawings for Wafer Table	132
B.3.1	Table.....	133
B.3.2	Table (modification).....	136

B.3.3	PM Force Frame	137
B.3.4	Readhead Holder	138
B.3.5	Readhead Holder #2	139
B.3.6	Cable Carrier Plate	140
B.3.7	Spacer	141
B.3.8	Air Bushing Mounting Block (modification)	142
B.4	CAD drawing for Halbach Array	143
B.4.1	Halbach 2D	144
Appendix C Validation of Optimal Inversion-based ILC		145
C.1	Coarse-fine stage and reference trajectory	145
C.1.1	Overview of coarse-fine stage	145
C.1.2	Modeling of coarse-fine stage	146
C.1.3	Reference trajectory	147
C.2	Numerical examples	149
C.2.1	Optimal control effort allocation	149
C.2.2	Tunable error convergence rate and effect of output measurement noise	152
C.3	Experimental example	153
C.3.1	Coarse-fine stage with feedback controller	153
C.3.2	System identification and optimal inversion-based ILC update law of coarse-fine stage with feedback controller	154
C.3.3	Conservative selection of model to ensure robustness	156
C.3.4	Optimal selection of model to ensure robustness and maximize tracking performance	159
C.3.5	Case study: Sinusoidal sweep	161
C.4	Summary	163

LIST OF TABLES

Table 3.1 Parameters used in optimal lead selection for PM positioning servo presented in Section 3.4.....	33
Table 4.1 Identified system parameters of stage. (The subscripts associated with each parameter listed in the first column is provided in parentheses in the first row).....	48
Table 4.2.Comparison of computation times and objective function values (based on $T_s = 0.1$ ms) for the three optimization approaches (direct, B-splines without windowing, and B-splines with windowing).	58
Table 4.3 Experimental results of scanning stage with photo-lithography process motion trajectory	61
Table 4.4 Experimental results of scanning stage with wafer topology inspection process motion trajectory.	65
Table 4.5 Thermal equilibrium simulation of scanning table with the scanning motion for photo-lithography process with a range of convective heat transfer coefficients.	67
Table A.1 Bill of materials of magnet assisted scanning stage prototype.	100
Table C.1 Model parameters for simulation case studies.	147
Table C.2 Control efforts comparison between the inversion-based squared ILC and the optimal inversion-based ILC approaches.	151
Table C.3 Steady-state performance of experiments without ILC and using optimal inversion-based ILC (with optimal and conservative models) based on the last 15 iterations.	162

LIST OF FIGURES

Figure 1.1 Flow of semiconductor manufacturing process (<i>Schmidt et al., 2014</i>).	2
Figure 1.2 Schematic of photo-lithography wafer scanning principle (<i>Schmidt et al., 2014</i>).	3
Figure 1.3 Scan and step motions of lithography process (<i>Butler, 2011</i>).	4
Figure 1.4 Typical velocity and acceleration profiles of lithography scanner (<i>Butler, 2011</i>).	4
Figure 1.5 Magnetic levitation stages used in some photo-lithography equipment (<i>Schmidt et al., 2014</i>).	5
Figure 1.6 Stacked scanning stage for silicon wafer processing (<i>Aerotech Inc., (a)</i>).....	6
Figure 1.7 Split-axis motion stage. Either axis can be configured for scanning (<i>Aerotech Inc., (b)</i>).	6
Figure 1.8 Historical trends of semiconductor manufacturing development on (a) reducing feature size, and (b) increasing number of transistors embedded in each chip (<i>Mack, 2011</i>).	7
Figure 1.9 Technical roadmap for deep ultraviolet (DUV) lithography equipment of ASML, the world’s leading lithography equipment manufacturer (<i>McLaren, 2014</i>).	8
Figure 1.10 Schematic of scanning stage mounted on vibration isolated base.....	8
Figure 3.1 Typical scanning profile comprising step and scan motions. Each scan stroke can be divided into constant velocity (CV) and motion reversal (MR) regions.	20
Figure 3.2 Schematic of scanning stage with assist device	21

Figure 3.3 (a) Realization of magnet-based assist device shown for only one side of the table. (b) Characteristic force-distance relationship of a pair of repelling magnets.....	22
Figure 3.4 Schematic of scanning stage with movable magnet-based assist devices.....	23
Figure 3.5 (a) Magnet array design candidates. (b) Force-distance relationship of a pair of repelling magnets with different magnet array designs (<i>Moser et al., 2002</i>).	23
Figure 3.6 (a) Schematic of simplified Coulombian magnetic force model for determining force between two magnetized surfaces. (b) Magnetic pole arrangement for 2D Halbach array. Arrows indicate N pole direction. Gray spaces contain no magnets.	25
Figure 3.7 Finite element analysis (FEA) model for repelling 2D Halbach arrays. Half model of repelling magnet arrays is created and meshed using COMSOL Multiphysics®.	25
Figure 3.8 Comparison between magnetic force prediction.	26
Figure 3.9 Sizing of 2D Halbach array for feasibility study using an existing motion stage.	27
Figure 3.10 (a) Constructed 2D Halbach array for feasibility study. (b) A pair of 2D Halbach arrays installed on existing motion stage for feasibility study.	28
Figure 3.11 Measured magnetic force of a pair of prototype 2D Halbach arrays with different speeds of approach.....	28
Figure 3.12 Comparison between predicted and measured magnetic force of a pair of 2D Halbach arrays.....	29
Figure 3.13 (a) Scan trajectory with varying scan strokes/positions, (b) Velocity profiles of scan table and PM during two successive scan strokes.	31
Figure 3.14 Versatility objective function (J_{vers}) vs. ball screw lead (l_s) for PM-assisted stage presented in Section 3.4.	33
Figure 3.15 CAD model of prototype magnet assisted scanning stage.	35
Figure 3.16 CAD model of MR-side PM mounted on bridge (connected to ground).....	35

Figure 3.17 Vibration mode shapes of the ground bridge: (a) 1 st mode at 66 Hz. (b) 2 nd mode at 184 Hz.....	36
Figure 3.18 Vibration mode shapes of table: (a) 1 st mode at 222 Hz. (b) 2 nd mode at 844 Hz.....	37
Figure 3.19 Constructed magnet assisted scanning stage.	38
Figure 3.20 MR-side PM assist device.	39
Figure 3.21 Bottom view of scanning table (without table-side PMs).	40
Figure 3.22 Scanning table installed on isolated base frame (with table-side PMs)	40
Figure 4.1 Control strategy of magnet assisted scanning stage. C denotes the controller transfer function and FF and FB denote feedforward and feedback, respectively.	43
Figure 4.2 Representation of isolation system using a mass-spring-damper model.....	44
Figure 4.3 Measured and fitted PM repulsion force (f_{PMi}) vs. distance (d) relationship; (a) PM1. (b) PM2.....	47
Figure 4.4 Measured and fitted frequency response functions from (a) f_{LM} to x_T , (b) f_{RM1} to x_{PM1} , (c) f_{RM2} to x_{PM2} , and (d) f_{LM} to x_B	47
Figure 4.5 (a) Columns of basis function matrix showing the local property of B-splines. (b) Local property of B-splines; effect of changing a control point is only on nearby curve segments.....	53
Figure 4.6 Optimal x_{PM1} and x_{PM2} , along with their time derivative profiles solved by three optimization approaches (direct, B-splines without windowing, and B-splines with windowing) in the original sampling resolution with $T_s = 0.1$ ms.	57
Figure 4.7 Step and scan profile for photo-lithography process of 200 mm silicon wafer.....	60
Figure 4.8 Scan trajectory of table and optimal PM trajectories for photo-lithography process of 200 mm silicon wafer.....	60

Figure 4.9 Measured signals for two configurations (Without and with AD) processing photo-lithography process motion trajectory.	62
Figure 4.10 Step and scan profile for inspection of 200 mm silicon wafer.	63
Figure 4.11 Scan trajectory of table and optimal PM trajectories for inspection of 200 mm silicon wafer.	63
Figure 4.12 Measured signals for two configurations (Without and with AD) processing wafer topology inspection process motion trajectory.	64
Figure 4.13 Surface temperature distribution of scan table and stage after 40 cycles of processing the photo-lithography scanning trajectory	66
Figure 5.1 (a) Bode plot for illustrating system model uncertainty, (b) mesh grid for system model candidates on Nyquist plot at frequency highlighted in (a). In this illustration, P_C consists of 100 elements (i.e., grid points).....	77
Figure 5.2 Dynamics model of the magnet assisted scanning stage; yellow blocks indicate nonlinear transfer functions (i.e., nonlinear magnetic force and distance relationships).	80
Figure 5.3 Schematic of the magnet assisted scanning stage for the purpose of ILC model analysis.	81
Figure 5.4 Simulated frequency response functions when (a) x_T is output, (b) x_B is output, (c) $x_T - x_B$ is output. (d) Magnitude and phase differences between $P_{M,LM}$ and $P_{M,PM}$. The magnitude unit is [m/N].....	83
Figure 5.5 Simplified dynamics model of the magnet assisted scanning stage; yellow blocks indicate nonlinear transfer functions (i.e., nonlinear magnetic force and distance relationship).	84
Figure 5.6 Frequency response function used to construct the ILC update law and optimal robustness filter. Shaded regions represent the experimentally obtained system uncertainties that include the modeling error.	89

Figure 5.7 PM repulsion force uncertainty regions and fitted force curve presented in Section 4.2; (a) PM1. (b) PM2.....	90
Figure 5.8 (a) Input force uncertainty based on the PM repulsion force uncertainty and previous iteration's input signals. (b) Input force uncertainty is converted into the frequency domain via DFT.....	90
Figure 5.9 Optimized robustness filter, Q , selected based on the model and input force uncertainties for the 15 th iteration of the Start w/o assist case.	91
Figure 5.10 RMS MA tracking error during the CV regions.....	91
Figure 5.11 RMS linear motor force.....	92
Figure 5.12 Reference motion trajectories of PM-based ADs for the 20 th iteration; (a) PM1, (b) PM2.....	93
Figure 5.13 Force applied to table used for control input allocation.	93
Figure B.1 Isometric view of Base Frame sub-assembly.	103
Figure B.2 Manufacturing drawing of Base Frame Block (pg. 1 of 2).....	104
Figure B.3 Manufacturing drawing of Base Frame Block (pg. 2 of 2).....	105
Figure B.4 Isometric view of Scale Block.....	106
Figure B.5 Manufacturing drawing of Scale Block.....	106
Figure B.6 Isometric view of Bumper Block.....	107
Figure B.7 Manufacturing drawing of Bumper Block.....	107
Figure B.8 Isometric view of Base Frame Connecting Plate #1.....	108
Figure B.9 Manufacturing drawing of Base Frame Connecting Plate #1.....	108
Figure B.10 Isometric view of Base Frame Connecting Plate #2.....	109

Figure B.11 Manufacturing drawing of Base Frame Connecting Plate #2.....	109
Figure B.12 Isometric view of Base Frame Connecting Plate #3.....	110
Figure B.13 Manufacturing drawing of Base Frame Connecting Plate #3.....	110
Figure B.14 Isometric view of Air Spring Mount #1.....	111
Figure B.15 Manufacturing drawing of Air Spring Mount #1.....	111
Figure B.16 Isometric view of Air Spring Mount #2.....	112
Figure B.17 Manufacturing drawing of Air Spring Mount #2.....	112
Figure B.18 Isometric view of Cable Carrier Plate.....	113
Figure B.19 Manufacturing drawing of Cable Carrier Plate.....	113
Figure B.20 Manufacturing drawing of Encoder Readhead Mount.	114
Figure B.21 Isometric view of Spacer.	115
Figure B.22 Manufacturing drawing of Spacer.	115
Figure B.23 Isometric view of modified Shaft Support.....	116
Figure B.24 Manufacturing drawing of modified Shaft Support.....	116
Figure B.25 Isometric view of Machine Frame sub-assembly.	117
Figure B.26 Manufacturing drawing of Connecting Plate (pg. 1 of 3).....	118
Figure B.27 Manufacturing drawing of Connecting Plate (pg. 2 of 3).....	119
Figure B.28 Manufacturing drawing of Connecting Plate (pg. 3 of 3).....	120
Figure B.29 Isometric view of Nut Mounting Block.....	121
Figure B.30 Manufacturing drawing of Nut Mounting Block.....	121

Figure B.31 Isometric views of Nut Mounting Plate.....	122
Figure B.32 Manufacturing drawing of Nut Mounting Plate.	123
Figure B.33 Manufacturing drawing of Fixed Side Plate.....	124
Figure B.34 Manufacturing drawing of Support Side Plate.	125
Figure B.35 Isometric view of Step Motor Holder.....	126
Figure B.36 Manufacturing drawing of Step Motor Holder.	126
Figure B.37 Isometric view of Machine Frame Base.	127
Figure B.38 Manufacturing drawing of Machine Frame Base.	127
Figure B.39 Isometric view of Force Frame.....	128
Figure B.40 Manufacturing drawing of Force Frame.....	128
Figure B.41 Isometric view of Force Frame #2.....	129
Figure B.42 Manufacturing drawing of Force Frame #2.....	129
Figure B.43 Isometric view of Limit Sensor L.....	130
Figure B.44 Manufacturing drawing of Limit Sensor L.....	130
Figure B.45 Isometric view of Scale Mount.....	131
Figure B.46 Manufacturing drawing of Scale Mount.....	131
Figure B.47 Isometric view of Wafer Table sub-assembly.	132
Figure B.48 Manufacturing drawing of Table (pg. 1 of 3).....	133
Figure B.49 Manufacturing drawing of Table (pg. 2 of 3).....	134
Figure B.50 Manufacturing drawing of Table (pg. 3 of 3).....	135

Figure B.51 Manufacturing drawing of modified Table.....	136
Figure B.52 Isometric view of PM Force Frame.	137
Figure B.53 Manufacturing drawing of PM Force Frame.	137
Figure B.54 Manufacturing drawing of Readhead Holder.	138
Figure B.55 Manufacturing drawing of Readhead Holder #2.	139
Figure B.56 Isometric view of Cable Carrier Plate.....	140
Figure B.57 Manufacturing drawing of Cable Carrier Plate.....	140
Figure B.58 Isometric view of Spacer.	141
Figure B.59 Manufacturing drawing of Spacer.	141
Figure B.60 Isometric view of modified Air Bushing Mounting Block.....	142
Figure B.61 Manufacturing drawing of modified Air Bushing Mounting Block.....	142
Figure B.62 Isometric view of Halbach Array sub-assembly.....	143
Figure B.63 Manufacturing drawing of Halbach 2D.....	144
Figure C.1 CAD model of coarse-fine stage testbed.	146
Figure C.2 Schematic of coarse-fine stage model.	147
Figure C.3 Reference trajectory of sinusoidal sweep case study; (a) Sweeping frequency, ϕ , (b) displacement, r , (c) acceleration, d^2r/dt^2 , and (d) magnitude of discrete Fourier transform of d^2r/dt^2	148
Figure C.4 Simulated ILC performance over iteration.	151
Figure C.5 Tunable convergence rate of the optimal inversion-based ILC by adjusting b . Gaussian output measurement noise (100 nm RMS) is added. Notice that even though the convergence rate	

is identical for $|1 - b|$, the steady-state error is different due to the noise as predicted by Eq. (5.24).
..... 152

Figure C.6 Comparison of tracking errors with and without output measurement noise (100 nm RMS). The RMS values of tracking errors from 201st to 300th iterations are plotted. The theoretical RMS tracking error as a function of b given in Eq. (5.24) is provided for reference. 153

Figure C.7 (a) Coarse-fine stage experimental set-up, (b) Block diagram for feedback controlled coarse-fine stage..... 154

Figure C.8 Frequency response functions (FRFs) used to construct the ILC update law – (a) Sen_1 [N/mm], (b) $G_{2,1}$ [mm/mm], and (c) $P_{2,2}$ [mm/N]; shaded regions represent the experimentally obtained system uncertainties. The dashed red lines represent conservatively selected nominal models, while the solid blue lines represent optimally selected nominal models for the uncertain system. 158

Figure C.9 Comparison of zero-phase robustness filter, Q , selected based on optimal and conservative selection of plant model..... 160

Figure C.10 Optimal inversion-based ILC update law for the coarse-fine stage using optimized model; (a) L_U and (b) L_E gains are applied to the previous iteration’s input and error signals, respectively. 160

Figure C.11 Optimal inversion-based (Opt-In) ILC update for sinusoidal sweep case study; RMS tracking error, RMS control input for coarse actuator (i.e., rotary motor), \mathbf{u}_{RM} , and RMS control input for fine actuator (i.e., voice coil actuator), \mathbf{u}_{VCA} , are shown..... 162

ABSTRACT

Scanning stages are characterized by repeated back and forth motions and are widely used in advanced manufacturing processes like photo-lithography, laser-scribing, inspection, metrology, 3D printing, and precision parts assembly, many of which are closely related to the semiconductor (i.e., integrated circuit) manufacturing industry. In order to deliver more high-performance semiconductor chips, i.e., to keep up with predictions made by Moore's Law, the scanning stages employed by the industry need to move faster while maintaining nanometer-level precision. Achieving these two goals simultaneously requires extensive use of thermal and vibration-induced error mitigation methods, because the motors, and subsequently the surrounding stage components, become heated and flexible parts of scanning stages are easily excited by their aggressive motions (with high acceleration/deceleration). Most of the available solutions tackle the heat and vibration mitigation problems separately, even though the two problems originate from one source, i.e., the large inertial loads generated by the scanning stage's actuators. Much benefit (e.g., size and cost reductions) can be achieved by considering the two problems simultaneously by addressing their root cause.

This dissertation proposes a design-based approach to simultaneously mitigate thermal and vibration-induced errors of scanning stages. Exploiting the repeated back-and-forth motions of scanning, permanent magnet (PM) based assist devices are designed to provide assist force needed during the motion reversal portions of scanning trajectories. The PM-based assist devices store the kinetic energy of the moving table during deceleration and release the stored energy when the table accelerates. Consequently, the force requirements of the primary actuator decrease, thus lowering its heat generation due to copper (resistive) losses. Moreover, the reaction forces borne by the PM assistive devices are channeled to the ground, bypassing the vibration isolated base upon which the scanning stage rests, thus reducing unwanted vibration. To increase the force density of the PMs, a 2D Halbach arrangement is adopted in a prototype scanning stage. Moreover, an efficient and low-cost servo system, optimized for versatility, is integrated into the scanning stage for automatic positioning of the PMs.

The designed magnet assisted scanning stage is an over-actuated system, meaning that it has more control inputs than outputs. For the best utilization of its actuators, a feedforward approach for optimal allocation of control efforts to its actuators is developed. The stage, controlled with the optimal feedforward control inputs, achieves significant reductions of actuator heat and vibration-induced errors when applied to typical scanning motions used in semiconductor manufacturing (silicon wafer processing). To further improve the positioning accuracy of the stage, an Iterative Learning Control (ILC) approach for over-actuated systems is developed, exploiting the repeated motion of scanning stages. The optimal ILC update law is designed, considering model and input force uncertainties, for robust monotonic convergence of tracking errors, and the resultant control force is efficiently allocated to multiple actuators. Applied to the magnet assisted scanning stage, the proposed ILC approach additionally reduces tracking errors arising from the mismatch between the model and actual system, thus significantly improving the positioning accuracy of the stage.

Chapter 1

Introduction

This doctoral dissertation is motivated by challenges faced by scanning stages, particularly those employed in the semiconductor manufacturing industry. In Section 1.1, semiconductor manufacturing processes and the use of scanning stages within the industry are reviewed. The challenges scanning stages must overcome to improve both quality and productivity in semiconductor manufacturing are then explained in Section 1.2. In Section 1.3, the outline of the rest of the dissertation is provided.

1.1 Use of scanning stages in semiconductor manufacturing

Motion stages are used to deliver precise and accurate positioning of tool and/or workpiece (e.g., silicon wafer, metal blank, circuit board, glass, film, etc.) in manufacturing processes, such as machining, substrate patterning, part assembly, and inspection (*Leu et al., 1993; Chou and Rao, 1997; Kim and Trumper, 1998; Stokowski and Vaez-Iravani, 1998; Altintas et al., 2011; Butler, 2011; Schmidt, 2012; Boeren et al., 2016*). A motion stage specifically designed for scanning (i.e., repeated back-and-forth motions) is called a scanning stage. Scanning stages are widely used in a wide range of processes such as photo-lithography, laser-scribing, metrology, micro-machining, additive manufacturing, and parts assembly (*3D Micromac; Desktop Metal; Park Systems; Gale et al., 1994; Schmidt et al., 2014*). However, many processes that utilize scanning stages are related to semiconductor (i.e., integrated circuit) manufacturing processes, which are schematically shown in Figure 1.1.

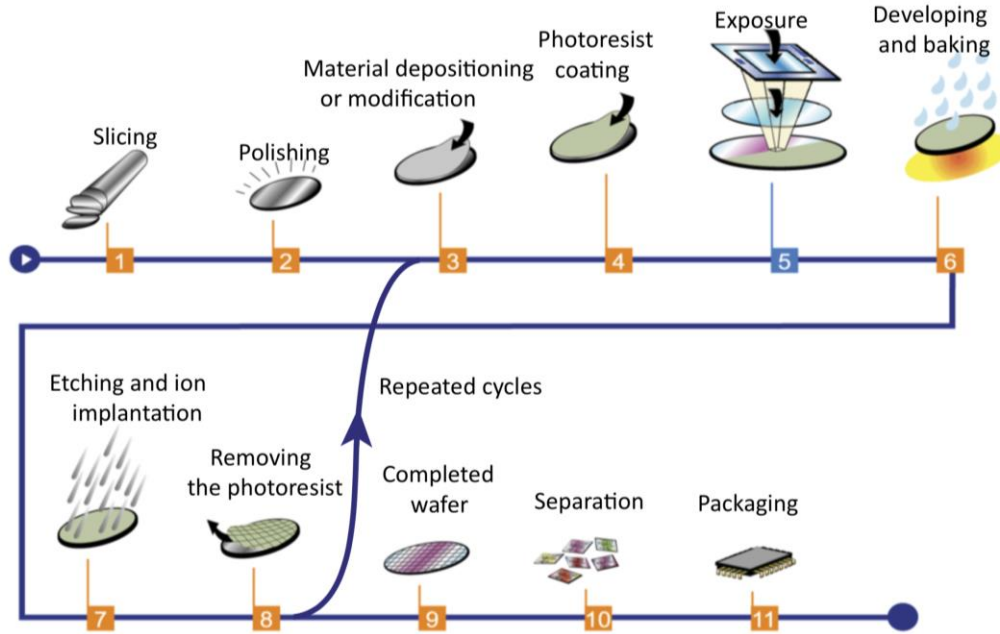


Figure 1.1 Flow of semiconductor manufacturing process (Schmidt et al., 2014).

Silicon wafers, serving as the substrate for semiconductor (i.e., integrated circuit) devices, are manufactured and prepared in steps (1) and (2). Thin film of materials is deposited and modified during step (3) via chemical/physical methods, followed by the photoresist coating in step (4). The circuit patterns are created with the photo-lithography process in step (5). The patterned photoresist passes through the development, etching, and removal processes as shown in steps (6) to (8). Once the patterned material layer is formed, the process quality is checked with inspection and metrology tools and the thin film coating and patterning processes (i.e., steps (3) to (8)) are repeated until all the desired layers are fabricated on the silicon wafer. Over 30 layers are typically needed for semiconductors used in today’s electronic devices, like the central processing unit of personal computers (*Intel*). After the completed wafer is produced in step (9), each die (i.e., integrated circuit chip) is separated from the wafer with micro-machining processes in step (10). The separated chips are packaged in step (11), such that each chip can be mounted on a printed circuit board for further integration into an electronic device. Among the steps highlighted, scanning stages play vital roles during the photo-lithography, inspection, metrology, micro-machining, and packaging processes. Their precision and speed determine the quality and quantity of devices being produced.

The photo-lithography process (step (5) of Figure 1.1) determines the number and minimum size of features on a semiconductor chip (*Schmidt et al., 2014*). Because very small features in nanoscale need to be printed, the semiconductor industry has adopted the wafer scanner concept, whose schematic is shown in Figure 1.2.

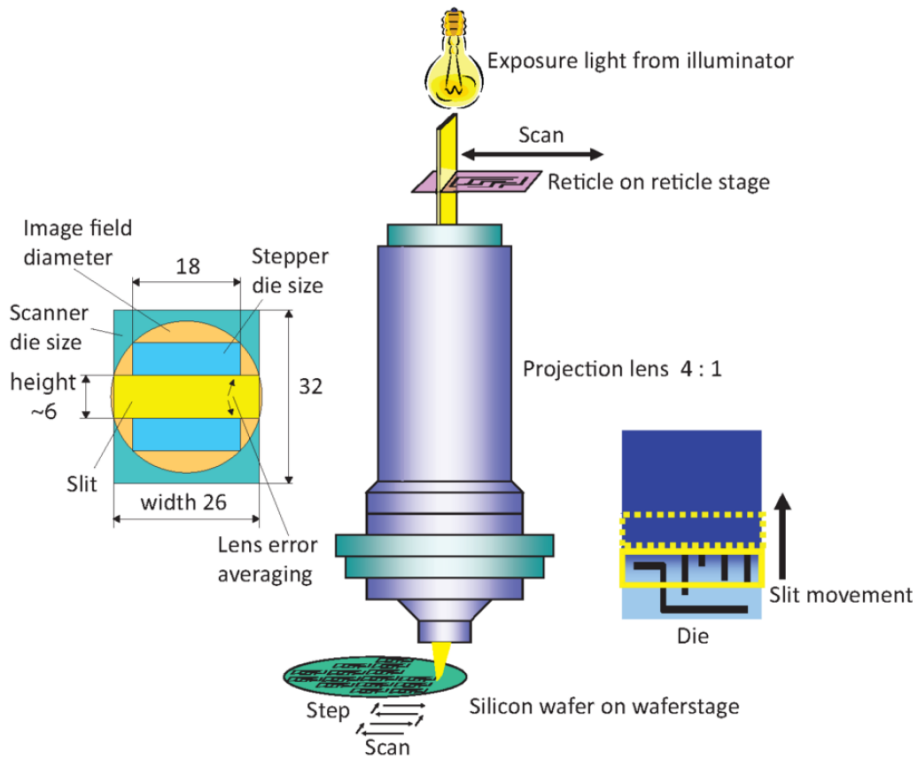


Figure 1.2 Schematic of photo-lithography wafer scanning principle (*Schmidt et al., 2014*).

The light passing through a reticle (i.e., master pattern) is projected on the photoresist coating on wafer. For practical concerns with manufacturing of the optical system (e.g., cost, size and light uniformity), a sub-section of the reticle image is transferred to the wafer at one time (*Schmidt et al., 2014*). Thus, the reticle and wafer stages scan the entire die area synchronously. After one die is scanned, the lithography equipment moves (i.e., steps) over to the next die area to scan. The scan and step process is repeated over the entire wafer surface as shown in Figure 1.3.

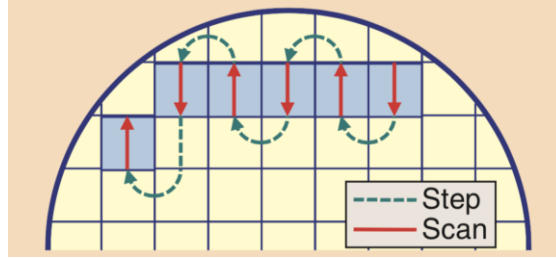


Figure 1.3 Scan and step motions of lithography process (Butler, 2011).

Typical velocity and acceleration profiles of the scanning motion of photo-lithography are shown in Figure 1.4. The stage quickly accelerates to the scanning speed and enters the scanning area, where the circuit image is optically projected. Before entering the scanning area, an error settling time is provided, such that the stage's tracking error from the transient portion (i.e., acceleration phase) settles below a threshold value. Two metrics are used to assess the stage's tracking performance during the constant velocity scanning: (1) moving average (MA) and (2) moving standard deviation (MSD) of tracking error (Butler, 2011). After reaching the end of scanning area, the stage quickly decelerates to prepare for the next scanning. Scanning speed and acceleration ranges for industrial wafer stages are $0.5 - 1 \text{ m/s}$ and $20 - 40 \text{ m/s}^2$, respectively, while the reticle stages typically travel four times faster because of the demagnification optics (Butler, 2011). Even though their specific displacement, velocity, and acceleration profile shapes and magnitudes may differ depending on the application, scanning stages employed by the rest of the semiconductor manufacturing processes (e.g., inspection, metrology, micro-machining, and packaging) need to carry out similar repeating back-and-forth motions as shown in Figures 1.3 and 1.4.

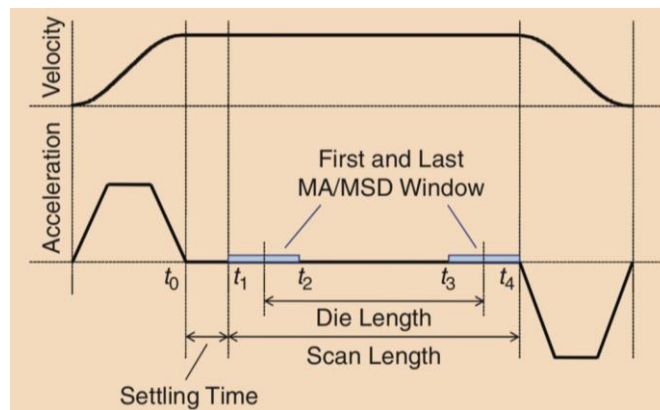


Figure 1.4 Typical velocity and acceleration profiles of lithography scanner (Butler, 2011).

Scanning stages that provide planar motions of workpiece/tool can be constructed using the magnetic levitation or multi-linear stage approaches (*Kim and Trumper, 1998; Poon and Novak, 2003; Erkorkmaz et al., 2010; Lu, 2012; Schmidt et al., 2014; Sandstrom et al., 2015*). The magnetic levitation stages (shown in Figure 1.5 for illustration) can provide planar motions using only one set of planar motors. Because the moving table is levitated by electromagnets, guiding elements are not needed. However, the actuation and control related hardware become expensive, because they need to cover the entire motion area. Some of the wafer stages of photo-lithography equipment use this approach to simplify the wafer swapping procedure between the wafer surface topology measurement and patterning processes (*Schmidt et al., 2014*).

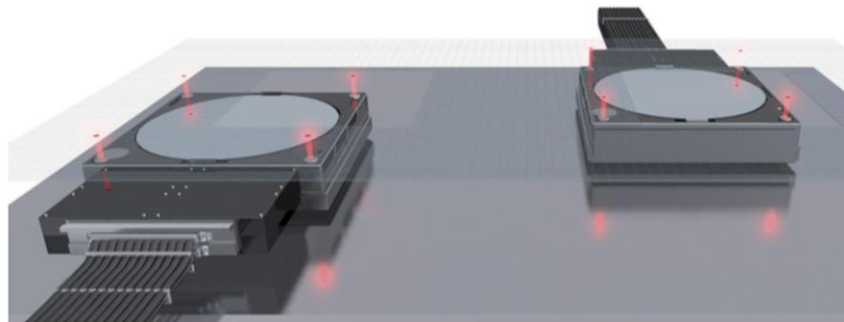


Figure 1.5 Magnetic levitation stages used in some photo-lithography equipment (*Schmidt et al., 2014*).

The multi-linear stage approach is a more popular and lower cost way to construct scanning stages. This approach is adopted by many scanning stages used in semiconductor manufacturing processes, e.g., inspection, metrology, micro-machining, packaging, and some photo-lithography applications. Two linear stages can be combined either in series or in parallel to achieve planar motions. Figure 1.6 shows an example of the series (i.e., stacked) approach, where the scanning axis is mounted on a gantry for silicon wafer processing. Because the scanning stage needs to be in motion throughout the entire manufacturing process, the stage having a lower moving mass is configured for scanning. In this construction, the tool is stationary, while the workpiece is moved by the stage.

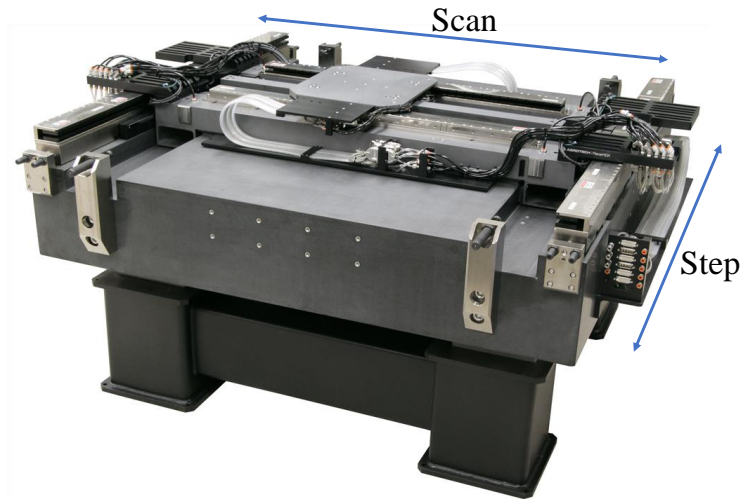


Figure 1.6 Stacked scanning stage for silicon wafer processing (*Aerotech Inc., (a)*).

If the tool is allowed to move, two linear stages can be arranged in parallel (i.e., two axes are split and arranged orthogonally) as shown in Figure 1.7. In this construction, either the top or the bottom axis can be configured for scanning, because both axes have similar moving masses.

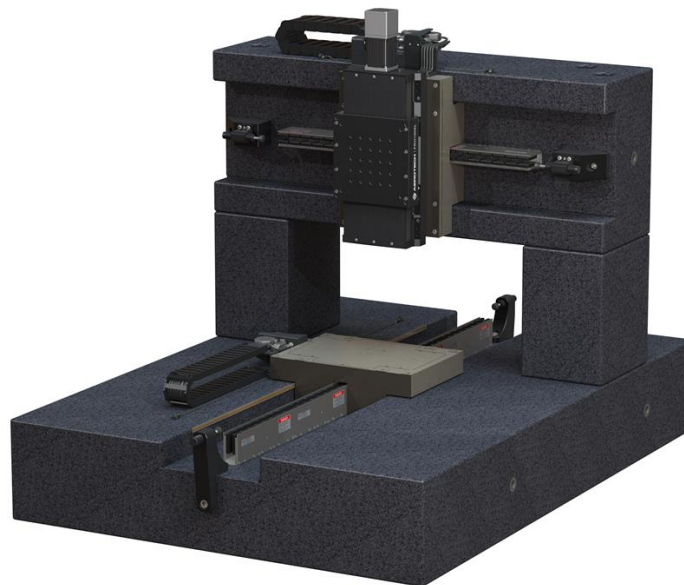


Figure 1.7 Split-axis motion stage. Either axis can be configured for scanning (*Aerotech Inc., (b)*).

1.2 Thermal and residual vibration problems in scanning stages

Since the inception of semiconductor manufacturing, the number of features in silicon integrated circuit has grown exponentially as observed and predicted by Moore's Law (*Moore, 1965; Mack, 2011*). With the rapid growth of the semiconductor industry, expressed by the cumulative revenue shown on the horizontal axis of Figure 1.8, the feature size of integrated circuit has shrunk, and the number of transistors embedded in each chip has grown as described in Figure 1.8 (a) and (b), respectively. Notice the two different scales used for the vertical axes. The feature size has grown by a factor of three, while the number of transistors being embedded in each chip has grown by a factor of eight. This suggests that the average chip size has also grown significantly. This stellar achievement is in part realized via advances made in positioning resolution and throughput (i.e., productivity) of scanning stages.

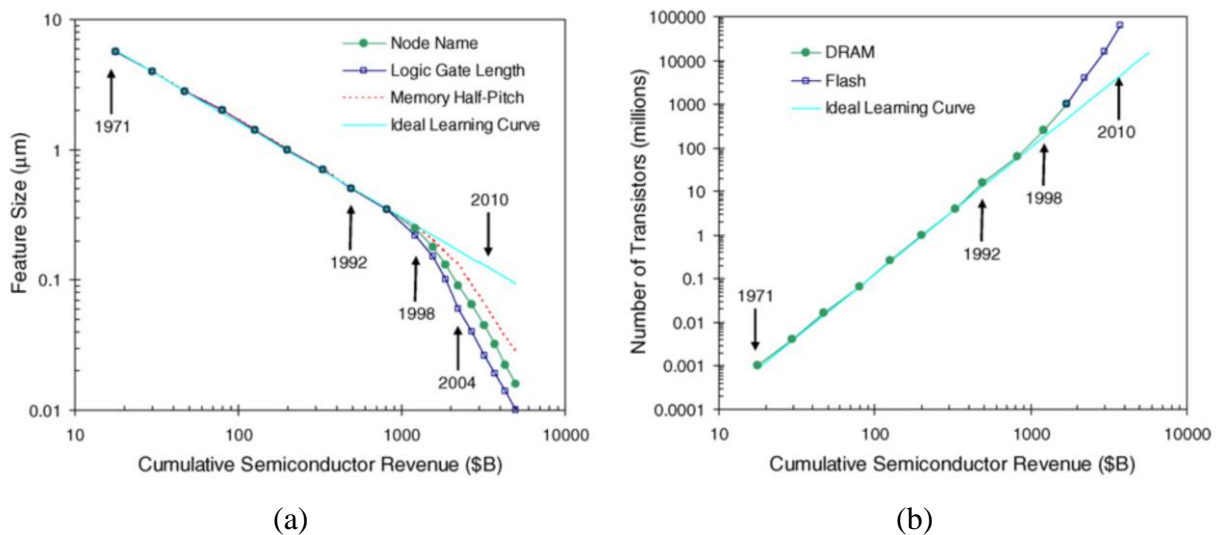


Figure 1.8 Historical trends of semiconductor manufacturing development on (a) reducing feature size, and (b) increasing number of transistors embedded in each chip (*Mack, 2011*).

Figure 1.9 describes a technical roadmap for deep ultraviolet (DUV) lithography equipment produced by ASML, the world's leading photo-lithography equipment manufacturer. The scanner resolution, which is quantified by overlay, improves over time, while the throughput described by wafers per hour (WpH) increases as well. Overlay is the relative positioning among the patterned layers (*Schmidt, 2012*). Key motivations behind improving the throughput are the equipment and operational costs. In order to fabricate patterns with finer resolution, multiple patternings are required, driving up the total number of photo-lithography processes (*Finders et al., 2009*;

Okazaki, 2015). Consequently, the number of all other processes (e.g., thin film coating, photoresist coating, development, etching, inspection and metrology) also need to be increased. Moreover, the semiconductor manufacturing takes place inside a cleanroom (i.e., fabrication facility), which is very costly to construct and maintain; thus, increasing throughput is considered a better solution than simply using a larger cleanroom and more process equipment. The following goals are imposed on scanning stages: (1) improve overlay by lowering the stage tracking error in the MA and MSD sense during scanning, and (2) increase throughput by lowering the non-scanning time (e.g., higher acceleration/deceleration and shorter settling time).

Application Node		190 WpH	230 WpH	250 WpH	>275 WpH	On product overlay	1 st Shipment
Logic	DRAM						
28	2H	NXT:1950i				7 nm	2009
	2M		NXT:1960Bi			6.5 nm	2011
				NXT:1965Ci		6.5 nm	2013
20/16 /14	2L			NXT:1970Ci		<5 nm	2013
10	1H				NXT:1980Di	<3.5 nm	2015
7	1M				NXT:next	2.5 nm	2017

Figure 1.9 Technical roadmap for deep ultraviolet (DUV) lithography equipment of ASML, the world’s leading lithography equipment manufacturer (McLaren, 2014).

One dilemma scanning stages face is the trade-off between improving throughput and positioning accuracy. Take the scanning stage schematic shown in Figure 1.10 as an example.

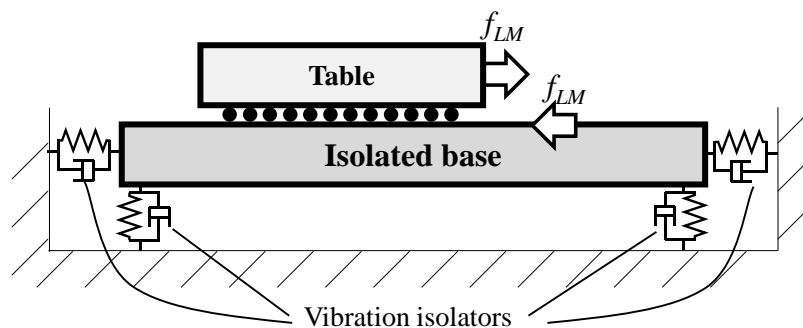


Figure 1.10 Schematic of scanning stage mounted on vibration isolated base.

The stage is mounted on an isolated base such that the adverse effects of ground vibration is attenuated via the vibration isolator's soft springs (*Rivin, 1995*). The moving table, driven by a linear motor, is controlled to track the reference trajectory that is relatively defined from the isolated base. When the stage is driven at a high acceleration/deceleration to reduce non-scanning time, at least two problems emerge. First, the large inertial load requires large electric current at the motor coil to produce the large linear motor force, f_{LM} . The large current leads to large copper (resistive) losses which scale with the square of motor current (*Kim et al., 2004*). The resultant heat leads to thermal errors in tool/workpiece positioning. Second, the inertial reaction load transmitted to the flexible parts creates excessive residual vibration, causing increased error settling time and/or worsened positioning during scanning (*DeBra, 1992*). Because the semiconductor manufacturing processes require extreme levels of positioning accuracy and throughput, both the increased heat and vibration of stage parts are detrimental to improving the manufacturing quality and quantity.

The simplest way to solve the heat and vibration problems is lowering the throughput, however this is against the overall goal set by the industry. More design and control elements are added to scanning stages to improve the positioning accuracy and throughput at the same time (i.e., cost and footprint of equipment increase). With magnetic levitation stages, employed by multi-million dollar process/equipment (e.g., high-end photo-lithography equipment), the cost increase associated with mitigating heat and vibration-induced problems is relatively small; hence they can get away with adopting less cost effective mitigation strategies. On the other hand, for multi-linear stages commonly used in less-expensive process/equipment, the counter measures to the heat and vibration-induced problems need to be very cost effective.

1.3 Outline of dissertation

This doctoral dissertation is motivated by challenges faced by the multi-linear stages for wafer scanning in reducing heat and vibration-induced errors. In this dissertation, scanning stage design and control solutions to simultaneously reduce heat and vibration-induced problems without overly increasing the implementation cost and equipment footprint are investigated. In Chapter 2, a literature review, starting with design-based approaches to solve the heat and vibration-induced problems, is provided. Based on the studies reviewed, designing an over-

actuated system with assist devices is found to be a promising approach to lower actuator heat and vibration-induced errors simultaneously. Control approaches often complement design-based approaches, to fully exploit the available actuators. Therefore, prior studies on control of over-actuated systems are reviewed, followed by the contributions of this dissertation with regard to both scanning stage design and control.

In Chapter 3, an over-actuated scanning stage design concept having a magnet-based assist device is proposed. In order to design a prototype stage, methods for sizing the stage components (e.g., magnet-based assist device and assistive device transmission) are studied. The over-actuated scanning stage is designed to lower the heat of actuators and residual vibration of flexible stage components, simultaneously. In Chapter 4, the designed over-actuated scanning stage is controlled to best utilize the multiple actuators using a feedforward scheme. The feedforward control scheme uses the optimal trajectory of assist devices to best allocate the actuators' control efforts, thereby minimizing the heat of the actuators. In Chapter 5, the designed scanning stage's performance is further improved, exploiting the repeating nature of semiconductor manufacturing, with an optimal Iterative Learning Control approach. In Chapter 6, conclusions and future work are provided. Appendices include bill of materials, CAD drawings for the designed over-actuated scanning stage with magnet-based assist devices, and validation of the proposed optimal Iterative Learning Control on a linear system. All the cited references are listed in the bibliography section.

Chapter 2

Literature Review

The heat and vibration-induced problems discussed in Chapter 1 are not unique to the scanning stages employed in the semiconductor industry. It is a problem shared by virtually any precision motion stage that requires high positioning accuracy and throughput. Therefore, many studies have investigated approaches to address the adverse effects of heat and vibration-related problems in motion stages. In Section 2.1, design-based approaches for reducing heat and vibration-induced errors are presented. Based on the review of design approaches, over-actuation with assist devices rises to the top because it mitigates the thermal and vibration-induced problems simultaneously without overly sacrificing capital investment and footprint of scanning stages. Control approaches are often used to complement design approaches as they lend ways for optimal use of a given design. Therefore, control approaches, that are relevant to the over-actuated scanning stage with assist devices and subject to heat and vibration-induced problems, are summarized in Section 2.2. In Section 2.3, addressing gaps found from the literature review, the key contributions of this dissertation are provided.

2.1 Design approaches for reducing temperature and vibration-induced errors

Mitigating thermal errors of positioning systems has received a lot of attention and several design approaches can be found. Examples of design-based approaches are symmetrical stage design (*Smith et al., 1987; Choi and Lee, 2005*), use of low thermal expansion materials (*Nomura and Suzuki, 1992; Holmes et al., 2000; Gao et al., 2006; Fan et al., 2007*), forced cooling (*Novak et al., 1997; Erkorkmaz et al., 2010*), addition of assist devices (*Schmidt, 2006; Wei, 2007; Brown and Ulsoy, 2013; Chen et al., 2016*), over-actuation (*Fesperman et al., 2012; Halevi et al., 2014; Duan and Okwudire, 2016b*) and light weighting of moving parts (*Van Herpen et al., 2014*). Symmetrical design of the stage leads to smaller thermal gradients; thus, scanning stages need to be designed to be as symmetrical as possible to lower thermal errors. Thermal expansions are

mitigated with the use of materials (e.g., invar and ZERODUR[®]) that have low thermal expansion coefficients. With the forced cooling approach, coolant is circulated to actively manage the temperature of stages. Assist devices are passive energy storage devices that can harvest and release energy as a function of the motion of the stage. By carefully selecting the assist device considering the operation of the equipment, the load on the actuators is distributed across operating points, thereby lowering actuator power needed to perform the same task. Over-actuation of stages distributes the load requirement to multiple actuators, thereby lowering heating of the main actuator. Light-weighting is effective in directly reducing the inertial loads and heat created by the actuators.

Several approaches have been presented in the literature for reducing vibration-induced errors due to actuation forces. They typically focus on reducing vibration as a means of improving tracking performance during positioning. The most common and widely utilized design examples are passive and active vibration absorbers (*Karnopp, 1995; Sun et al., 1995; Soong and Spencer, 2002*), eddy current dampers (*Sodano et al., 2006*), active balance masses and counter motion devices (*Poon and Novak, 2003; Van Schothorst et al., 2007; Wang et al., 2010; Schmidt, 2012*), and reaction force isolators (*Aerotech Inc., (a); Denkena et al., 2009; You and Ahn, 2014*). Passive vibration absorbers reduce resonance peaks that can lead to excessive vibrations, while the active absorbers use an external energy source to quickly remove (i.e., dampen) the sensed vibration. Balance masses and counter motion devices are used to cancel out inertial reaction forces transmitted to the flexible parts of stages via controlling the position of the balancing masses. Reaction force isolators are passive filters that mitigate the channeled reaction force from the actuators. In addition to actuator heat reduction, light-weighting (*Van Herpen et al., 2014*) reduces the inertial load transmitted to the isolated base (see Figure 1.10) as well, so the residual vibration of the base is mitigated.

Most of the reviewed approaches address one of the two problems (i.e., heating of the actuator and vibration) without considering the other. Many approaches discussed above may be used in combination to solve the thermal and vibration problems. However, combining approaches can overly increase footprint, equipment and operating costs, unless the solution approaches are judiciously selected to tackle the two problems in an efficient way. For example, the forced cooling and balance mass approaches can be combined to mitigate the temperature and vibration problems at the expense of large accessory loads and equipment (e.g., chillers, pumps, sensors, actuators and

supporting structures). Light-weighting is the only approach presented above, which solves the two problems at the same time. However, this may cause more easily excited vibration modes of the moving parts, which can deteriorate the positioning accuracy and control bandwidth of the system. Furthermore, most stages are already designed to have light moving parts, so the benefit of additional light-weighting may be marginal.

Observing the thermal and vibration reduction mechanism of the light-weighting approach, the temperature and vibration problems originate from the same source (i.e., inertial load for very high acceleration provided by the linear motor). Therefore, much synergistic benefit can be achieved if the inertial load provided by linear motor is mitigated without overly compromising the system-level performance (e.g., cost, throughput, vibration isolation and structural stiffness). On this perspective, adding assist devices or actuators to exploit the repeated back-and-forth (i.e., scanning) motions is a reasonable solution approach even though the reviewed implementations do not consider the scanning motions explicitly (*Schmidt, 2006; Wei, 2007; Fesperman et al., 2012; Brown and Ulsoy, 2013; Halevi et al., 2014; Duan and Okwudire, 2016b; Chen et al., 2016*). The reviewed assist device approaches lack the vibration mitigation, because they are mounted between the moving part and the stator (i.e., base). Similarly, the total sum of the inertial load provided by multiple actuators does not change; therefore, there is no reduction in vibration of flexible parts with the reviewed over-actuation approaches.

To reduce vibration caused by reaction force from the actuators, the motor stators can be placed on the ground (*Galburt, 2004*). Even though the actuator heat is not considered in the disclosed invention, the structural channel created by the ground mounted stator effectively suppresses excitation of isolated base caused by inertial loads. Following this approach, the assist devices or additional actuators can be mounted between the moving part and the ground such that vibration reduction is achieved together with heat reduction. With the ground-mounted assist devices or additional actuators, the inertial reaction force is channeled to the ground, keeping the vibration-isolated parts undisturbed. It must be noted that the vibration isolation performance of the stage must be preserved for precise positioning during actual manufacturing, even if additional elements (i.e., assist devices or actuators) are introduced into the overall system. For example, flexural hinges are employed to aid the alignment of motor stators and coils in the directions orthogonal to the stage travel and still maintain the vibration isolation in the disclosed invention by Galburt.

2.2 Complementary control approaches and tracking control of dynamic systems

In addition to the design-based approaches, control-based approaches are used to mitigate the thermal and vibration problems as they lend ways to gain the maximum benefit of given stage design. Examples of control-based approaches to mitigate thermal errors and vibration of flexible parts are optimal control of motor drives (*Morimoto et al., 1994*), optimal allocation of control inputs (*Härkegård and Glad, 2005; Jin, 2005; Luo et al., 2007; Johansen and Fossen, 2013; Duan and Okwudire, 2018*), thermal compensation (*Mayr et al., 2012*) and optimized input trajectories for vibration or heat reduction (*Li et al., 2009; Pellicciari et al., 2015; Sencer and Tajima, 2017; Duan et al., 2018*). The motor drives are controlled to minimize iron and copper losses such that the most efficient use of the given actuator and power amplifier design is achieved (*Morimoto et al., 1994*). For systems having multiple actuators, the control inputs are optimally allocated to maximize the system-level efficiency; thus, lowering resistive losses that generate heat. This can be achieved using feedback and/or feedforward control. Feedforward approaches are partially used for input allocation with the redistributed pseudoinverse (*Jin, 2005*), model predictive control (*Luo et al., 2007*) and virtual control approaches (*Härkegård and Glad, 2005; Johansen and Fossen, 2013*). By tracking a proxy function that evaluates the input allocation optimality in real-time, the optimal input allocation in a feedback sense can be achieved (*Duan and Okwudire, 2018*). Model-based or measurement-based thermal error compensation schemes are applied to mitigate thermal errors using the system model or temperature sensor measurement (*Mayr et al., 2012*). To reduce vibration of flexible parts or heat generated from actuators, the input trajectories can be optimized using knowledge of the system (*Li et al., 2009; Pellicciari et al., 2015; Duan et al., 2018*). To reduce residual vibration, optimized input trajectories containing attenuated frequency content can be used to avoid exciting vibration modes of system during rapid movement (*Sencer and Tajima, 2017*).

The design approaches can reduce vibration of flexible parts; however, they cannot eliminate the vibration-induced errors completely. When stages are driven with aggressive input trajectories, both feedback and feedforward control approaches are used to reduce tracking errors (*Heertjes et al., 2010; Butler, 2012; Iwasaki et al., 2012*). Because errors can be preemptively suppressed with feedforward approaches, precision scanning stages mostly adopt feedforward

approaches for tracking control, while feedback approaches are reserved for dealing with system uncertainty and unmodeled disturbance (*Bruijnen and Van Dijk, 2012*).

Inversion-based feedforward control approaches, which have been extensively studied by researchers, use the model of the system to generate the control signals (*Tomizuka, 1987; Van Den Braembussche et al., 1996; Clayton et al., 2009; Butterworth et al., 2012; Ramani et al., 2017; Duan et al., 2018; Van Zundert and Oomen, 2018*). Inversion-based feedforward control approaches can be applied to both the Single Input and Single Output (SISO) and Multiple Input and Multiple Output (MIMO) systems. Note that the direct inversion of the system model is not always possible, because non-minimum phase zeros, resulting from a high sampling rate, flexibility of the structure, non-collocated actuation, etc., are present in the system. Under such conditions, approximated inversion or filtered basis functions can be used to generate feedforward control signals (*Butterworth et al., 2012; Ramani et al., 2017; Duan et al., 2018*). For MIMO systems having the exact number of inputs and outputs (i.e., square MIMO systems), the same techniques used for the SISO system inversion can be applied. If the MIMO system is not square (i.e., system is either over-actuated or under-actuated), it can be made square with pre- and post-compensation in modeling before applying the square MIMO system inversion approaches.

Feedback control approaches use measured sensor data to create signals for suppressing tracking errors. With feedback, modeling errors and disturbances can be effectively suppressed, leading to superior tracking performance. Examples of time-domain feedback control are the disturbance observer (*Komada et al., 1991; Kempf and Kobayashi, 1999*) and adaptive control (*Xu and Yao, 2001; Tan et al., 2002; Butler, 2013*) schemes, which can be used in addition to the traditional PID-type controllers (*Åström and Hägglund, 2001*). Adaptive control approaches lend ways to identify model-system mismatches over time and the learned system dynamics can be used to tune feedforward controller for suppressing errors excited by the motion trajectories.

Building on the concept of learning system dynamics, Iterative Learning Control (ILC) approaches are used to improve tracking performance with past iteration's input and output data (*Arimoto et al., 1984; Kim and Kim, 1996; De Roover and Bosgra, 2000; Bristow et al., 2006*). Scanning stages need to carry out repeating tasks in manufacturing; therefore, much benefit can be obtained by applying the ILC framework to the stage. The ILC is an attractive approach that takes advantages of both the feedback and feedforward control, because tracking errors are preemptively suppressed as in feedforward, while model uncertainties and repeating disturbances

are learned and suppressed in the iteration-domain. Phase delays associated with feedback in the time-domain are not present with the ILC approaches, because entire trajectories are known from the previous iterations.

The ILC update laws are generated using PD-type, model inversion and cost optimization approaches (Arimoto *et al.*, 1984; Amann *et al.*, 1996; Lee *et al.*, 2000; Heertjes and Tso, 2007; De Roover and Bosgra, 2010; Barton and Alleyne, 2011; Kim and Zou, 2013; Van Zundert and Oomen, 2018). Among them, model inversion and cost optimization approaches are widely used to apply the ILC approach to MIMO systems. To assure error convergence rate to the ILC update law design, inversion-based approaches, which use the direct or approximated inverse model of the system, can be used (Van Zundert and Oomen, 2018). With the inversion-based ILC approaches, specifying error convergence rate without compromising the steady-state tracking performance is straightforward, because the errors from previous iterations can be partially compensated with user discretion in the next iteration (Harte *et al.*, 2005). Convergence rates can also be enforced in the frequency-domain ILC using a singular value-based design approach (Zsiga *et al.*, 2016). Existing work on inversion-based ILC focuses on their application to SISO or square MIMO systems. With pre- and/or post- compensation in modeling, inversion-based ILC can be applied to over-actuated MIMO systems, but the reviewed literature does not explicitly consider optimal allocation of control efforts (Ghosh and Paden, 2002; Ye and Wang, 2005; Yan *et al.*, 2012; Van Zundert and Oomen, 2018).

For optimality of the ILC update law, weighted-cost optimization using user-specified weights, often referred to as Norm Optimal ILC, is the most popular approach (Amann *et al.*, 1996; Lee *et al.*, 2000; Bristow *et al.*, 2006; Barton and Alleyne, 2011; Owens, 2012). In Norm Optimal ILC, the user-defined weight ratios among the objectives (i.e., tracking error, error convergence rate, and control efforts) determine the ILC performance, but the impact of weight ratios on achieving the desired balance is not clear; therefore, appropriate weights are selected on a trial-and-error basis. To address this shortcoming, the trade-off relationship among the weights in the Norm Optimal ILC approach has been investigated (Ge *et al.*, 2018), but their findings are only applicable to SISO systems, hence exclude over-actuated systems.

Robustness filters are often added to the ILC update law to guard against the update instability in the iteration domain due to the system model uncertainties (Bristow *et al.*, 2006) and numerous ways to represent model uncertainties for incorporation into the ILC update law design

have been investigated (*Van de Wijdeven et al., 2009; De Roover and Bosgra, 2010; Ge et al., 2018*). Addition of a robustness filter to the ILC update law makes the iteration-domain update more robust against the uncertainties in the model, but it lowers the steady-state (i.e., converged) tracking performance. Therefore, it is of interest to maintain the robustness filter gain as close to the unity as possible for better tracking. In linear systems, the frequency-domain method, that expresses system model uncertainties using both the magnitude and phase bounds of frequency response functions (FRF), provides a path to the least conservative ILC update law design (*Ge et al., 2018*). With the frequency-domain method for expressing model uncertainties, the system model used for inversion and the robustness filter can be selected to minimize the steady-state tracking errors.

Observing the reviewed literature, the over-actuated scanning stage with assist device can benefit from the use of optimal trajectories, control allocation and the inversion-based ILC to minimize heat and vibration-induced positioning errors. The input trajectory optimization and control allocation approaches lend ways to best utilize the given equipment design. Because same trajectories are repeated in manufacturing, the computational overhead required for optimization of motion trajectories is relatively low. The repeating nature of manufacturing can be exploited with the use of ILC framework, improving the positioning accuracy over the iteration-domain. Because the stage is over-actuated, the control efforts must be allocated optimally to the actuators and the optimality needs to be considered during the trajectory optimization and ILC update. To implement the ILC control framework on the actual machine, uncertainties associated with the system modeling need to be considered for the robust monotonic convergence of the solution.

2.3 Contribution of dissertation

The main contributions of dissertation are summarized below:

- A design-based concept of using assist devices to simultaneously reduce residual vibration of flexible parts and actuator-borne heat of scanning stages is proposed. The assist devices are mounted on the ground, so flexible parts of the stage are not disturbed. The presented design-based concept improves the constant velocity scanning performance (e.g., accuracy and precision), such that a higher throughput can be achieved (Chapter 3).
- The assist device concept is realized with a set of permanent magnets and automatic positioning systems are added to increase versatility of the assist device. Design and sizing

guidelines for the permanent magnet-based assist devices and their automatic positioning system for versatile use in scanning scenarios that have varying scan strokes/positions are proposed (Chapter 3).

- The proposed magnet assisted scanning stage is an over-actuated system. To best utilize the control efforts of the actuators, an energy optimal trajectory generation method for permanent magnet-based assist device is proposed. The proposed trajectory generation method explicitly minimizes the heat generated by the actuators. The vibration of isolated base, borne by the actuators to track the stage reference trajectory, is implicitly minimized (Chapter 4).
- The positioning performance of the designed scanning stage is further improved with Iterative Learning Control (ILC). An optimal inversion-based ILC framework for over-actuated systems is presented and implemented on the magnet assisted scanning stage. The optimal inversion-based ILC update law achieves the minimum steady-state tracking error in the presence of the system model uncertainties (Chapter 5).

Chapter 3

Design of an Over Actuated Scanning Stage with Permanent Magnet-based Assist Devices

The thermal and vibration problems of scanning stages are solved simultaneously with ground mounted assist devices in this chapter. The assist devices, that harvest the kinetic energy of the moving table and release it when the table re-accelerates toward the opposite direction, are realized with a set of permanent magnets. The permanent magnet-based assist devices are made versatile to varying scan strokes and positions with the addition of low-cost servo systems driven by a ball screw and a rotary motor.

The concept of using permanent magnet-based assist devices for scanning stages is explained in Section 3.1 and the systematic design of the permanent magnets is provided in Section 3.2. The automatic positioning mechanism and its sizing are shown in Section 3.3. Finally, the magnet-assisted scanning stage prototype design is shown in Section 3.4.

This chapter is partially based on the following publications:

- Yoon D, Okwudire C. *Magnet assisted stage for vibration and heat reduction in wafer scanning*. CIRP Annals. 2015; 64 (1); 381-384.
- Yoon D, Okwudire C. *Active assist device for simultaneous reduction of heat and vibration in precision scanning stages*. Precision Engineering. 2016; 46; 193-205.
- Okwudire C, Yoon D. *Magnet assisted stage for vibration and heat reduction in wafer scanning*. US Patent; 2018; 10077865.

3.1 Assist device for scanning stages

Typical motion profile of a scanning stage is shown in Figure 3.1; it is similar to the input trajectory used by photo-lithography scanners shown in Figure 1.3. The y -axis shown in Figure 3.1 advances in successive steps, while the x -axis shuttles back-and-forth (i.e., scans) repeatedly. The scanning motion of the x -axis is the focus of this dissertation and it consists of a constant velocity (CV) and motion reversal (MR) regions. The CV region of each scan is where the actual

manufacturing process (e.g., photo-lithography, metrology/inspection, or micro-machining) takes place, so positioning must be extremely precise. The MR regions are not useful to the actual manufacturing process. Therefore, they must be executed as fast as possible with high acceleration/deceleration to boost throughput, while ensuring that the precision of the CV regions is not compromised.

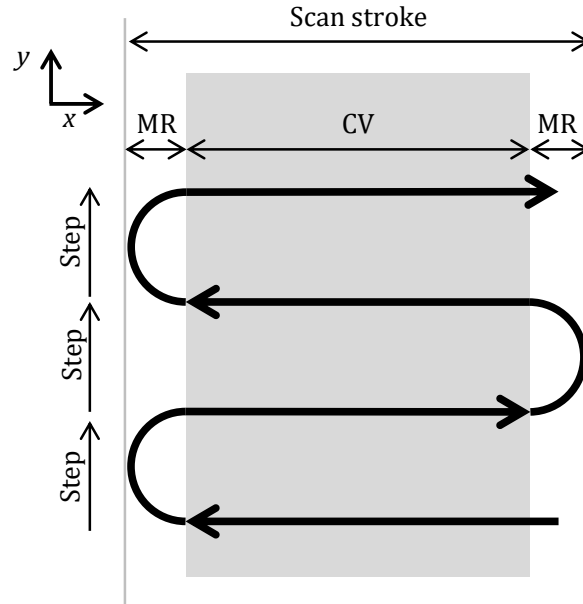


Figure 3.1 Typical scanning profile comprising step and scan motions. Each scan stroke can be divided into constant velocity (CV) and motion reversal (MR) regions.

Consider the schematic of the scanning stage shown in Figure 1.10 or the schematic shown in Figure 3.2 without the assist devices (ADs in short) in red color. The scanning table, actuated by linear motor force (f_{LM}), is mounted on a rigid base. The base is isolated from ground vibration using very soft springs to achieve the desired precision in the CV regions. However, the presence of the soft springs causes unwanted horizontal and rocking vibrations of the base due to the large inertial forces present during acceleration/deceleration in the MR regions. Upon arriving at the next CV region, the stage must wait for the residual vibration to settle before the manufacturing process resumes, thus slowing down the manufacturing process. Moreover, large inertial forces draw large electric currents from the motors, causing unwanted heat that compromises accuracy in the CV regions. Assist devices (ADs), shown as red dotted springs in Figure 3.2 can help reduce the magnitude of f_{LM} needed for acceleration/deceleration by harvesting and releasing some of the

kinetic energy of the table when it is in the MR regions, thus reducing motor heat (*Brown and Ulsoy, 2013*). Residual vibration can be reduced simultaneously by transmitting the reaction forces from the ADs directly to the ground, so that they do not disturb the vibration-sensitive base of the machine (*Galburt, 2004; Butler, 2011*). An ideal AD would store and release all the kinetic energy of the scanning table in the MR regions. Additionally, it would disengage completely from the table upon entering the CV region to stop the transmission of ground vibration to the table, and to prevent the actuators from doing unnecessary work against the AD to maintain the stage at constant velocity.

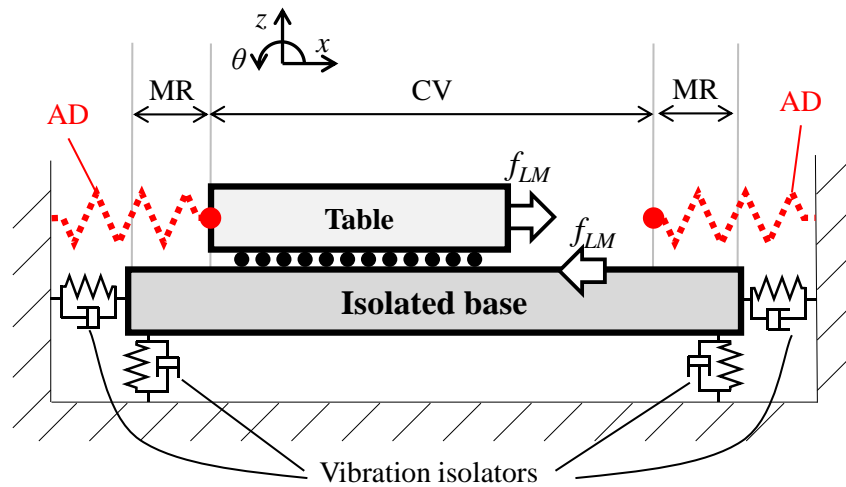


Figure 3.2 Schematic of scanning stage with assist device

The AD can be realized with a pair of repelling permanent magnets (PMs) (*Wei, 2007; Chen et al., 2016*). One PM is mounted to the moving table and the other located on the ground as shown in Figure 3.3 (a). The magnetic repulsion provides a nonlinear force (f_{PM}) to distance (d) relationship, which is schematically shown in Figure 3.3 (b). The stiffness (i.e., slope of the force to distance curve) provided by the magnetic repulsion is almost zero when the distance between the magnets is large, but it grows exponentially as the distance decreases. This smooth transition from zero stiffness to very high stiffness is ideal in precision scanning stages, because the AD made with the PM can smoothly engage and provide assist to the table as it enters the MR regions.

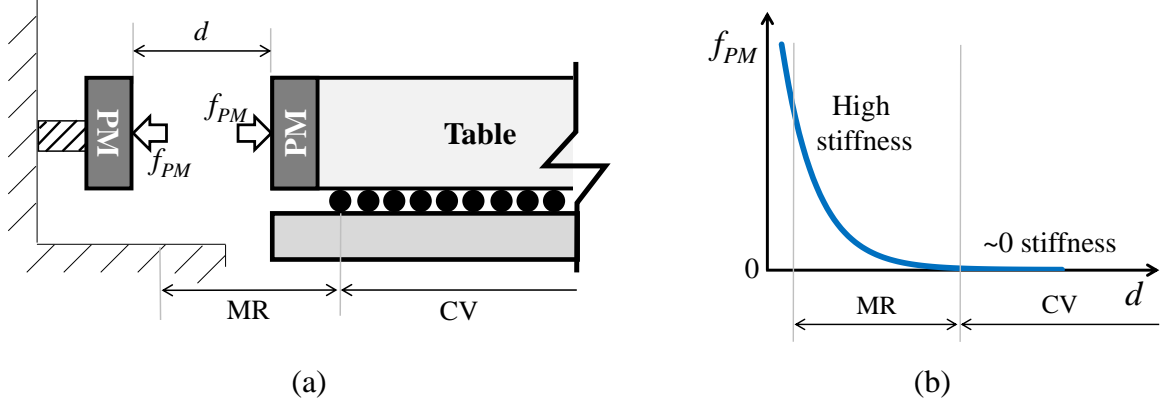


Figure 3.3 (a) Realization of magnet-based assist device shown for only one side of the table. (b) Characteristic force-distance relationship of a pair of repelling magnets.

As shown in Figure 3.4, two pairs of repelling PMs, i.e., PM_i ($i = \{1, 2\}$), are used to construct a complete set of ADs for the scanning axis. For each pair, one of the PMs is mounted to the table (with length l_T and position x_T), and the other PM is positioned in the MR region. Accordingly, the PM based ADs are effectively disengaged from the table when the table is in the CV regions; the magnetic repulsion is virtually zero (hence, the stiffness is also zero) due to the large distance between the PM pairs. On the other hand, much needed assist is provided as soon as the table enters either MR region.

Scanning motion profiles often have varying scan strokes/positions to access different regions of wafer. Therefore, assist force provided by fixed PMs (i.e., passive ADs), whose repulsion force has a very limited range, is suboptimal and ineffective, even if a robust design method is considered (Wei, 2007; Chen et al., 2016; Brown and Ulsoy, 2017). See Section 3.2, which illustrates the limited range of magnetic force. The effective force range is much less than 30 mm, so the fixed PMs are ineffective to the scanning stages that can handle 300 mm wafers. To solve drawbacks of the fixed PMs, actuators are added to actively control the ground mounted PMs' position (x_{PM1} and x_{PM2}). This way, the repulsion force of the AD becomes more effective, making it versatile to scan strokes/positions (i.e., the assist device is active). In addition, the PM assisted scanning stage can quickly adopt to different tasks, e.g., different scanning motion profiles and wafer diameters, like reconfigurable manufacturing systems (Koren et al., 1999). With given scanning motion profiles, PM positions can be optimized to deliver the optimal assist force for reducing the heat and vibration caused by the main actuator (i.e., linear motor).

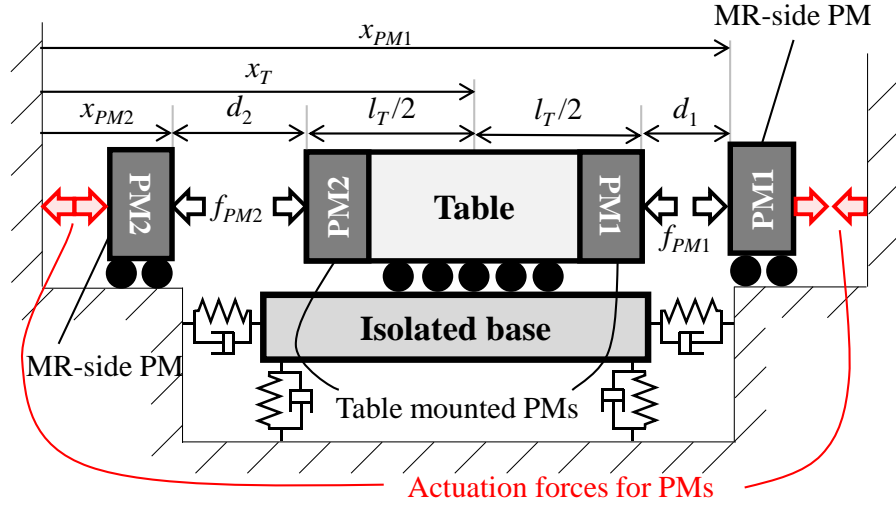


Figure 3.4 Schematic of scanning stage with movable magnet-based assist devices.

3.2 Design and sizing of permanent magnets

The permanent magnet-based ADs must be compact yet provide sufficient inertial force for rapid acceleration and deceleration to the scanning table in the MR regions. Therefore, a 2D Halbach arrangement, which is well-known to provide high force densities with rotating magnet poles (*Halbach, 1980; Moser et al., 2002; Lu, 2012*), is employed. As shown in Figure 3.5, the 2D Halbach array provides the highest force density among the array design candidates.

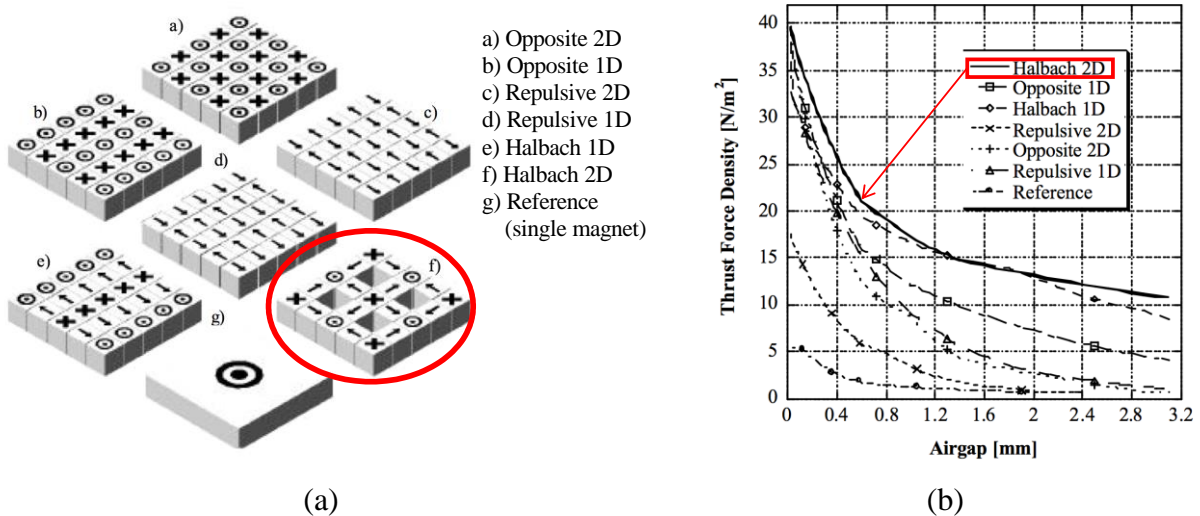


Figure 3.5 (a) Magnet array design candidates. (b) Force-distance relationship of a pair of repelling magnets with different magnet array designs (*Moser et al., 2002*).

A simplified Coulombian model is used to estimate the magnetic force between the two Halbach arrays for sizing purpose. Figure 3.6 (a) depicts the interaction between two magnetized surfaces (of dimension $a \times a$), based on the Coulombian model. cx_i , cy_i , and cz_i are respectively the x , y and z coordinates of the center of each surface ($i = 1, 2$). The equation describing the magnetic force vector (\vec{f}_{PM}) between the two magnetized surfaces is given by (Ravaud *et al.*, 2008)

$$\vec{f}_{PM} = \frac{\sigma_1^* \sigma_2^* a^2}{4\pi\mu_0} \int_{cy_1-a/2}^{cy_1+a/2} \int_{cx_1-a/2}^{cx_1+a/2} \frac{\vec{p}_{1,2}}{|\vec{p}_{1,2}|^3} dx_1 dy_1 \quad (3.1)$$

with the position vector ($\vec{p}_{1,2}$) expressed as

$$\vec{p}_{1,2} = (cx_2 - x_1)\vec{i} + (cy_2 - y_1)\vec{j} + (cz_2 - cz_1)\vec{k} \quad (3.2)$$

where $\mu_0 = 4\pi \times 10^{-7}$ H/m is the permeability of free space and σ^* is magnetic flux density of each surface, respectively. The simplified model uses averaged force over one of the magnetized surface; therefore, the computed force is less accurate when the distance between the two surfaces becomes small. For more accurate modeling of the repulsion force, a position vector from a point on the first surface to a point on the second surface needs to be used, instead of the position vector from the center of the first surface to a point on the second surface. This requires the quadruple integral to compute the force vector, instead of the double integral used in Eq. (3.1). Figure 3.6 (b) shows the magnetic pole arrangement of a 2D Halbach array, where N and S denote the North and South poles, respectively. The arrow direction indicates the N pole and there are no magnets in the grayed regions. With the Coulombian model of magnetized surfaces, the N pole has the positive flux density, while the S pole has the negative density of the same magnitude. The net force between two arrays at a given distance (d) can be computed by summing force vectors between all the magnetized surfaces of the two arrays. There are 42 magnetized surfaces in each 2D Halbach array (21 N and 21 S pole surfaces). To compute magnetic force of a 2D Halbach pair, total 1764 force vectors need to be summed.

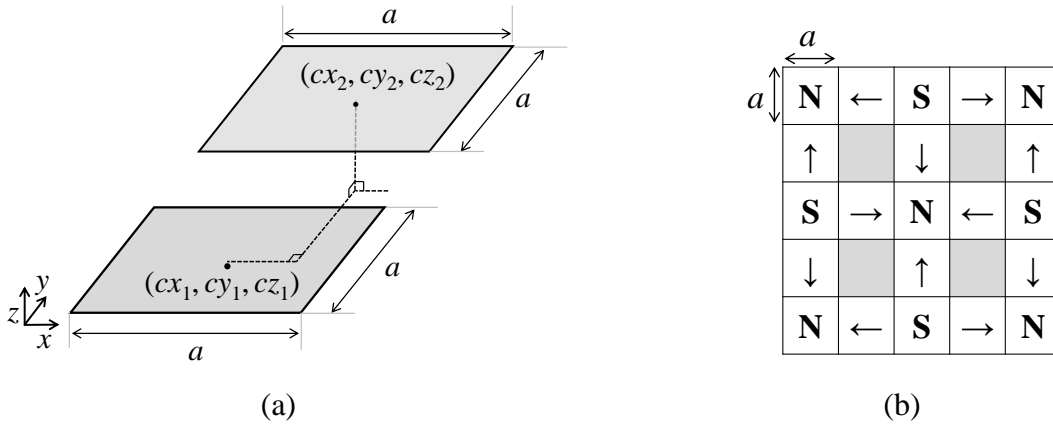


Figure 3.6 (a) Schematic of simplified Coulombian magnetic force model for determining force between two magnetized surfaces. (b) Magnetic pole arrangement for 2D Halbach array. Arrows indicate N pole direction. Gray spaces contain no magnets.

To validate the simplified Coulombian model approach for estimating the magnetic repulsion force, a commercial finite element analysis (FEA) software (COMSOL Multiphysics[®]) is employed. A screenshot of the half model mesh, exploiting the symmetry of the 2D Halbach array design, is provided in Figure 3.7.

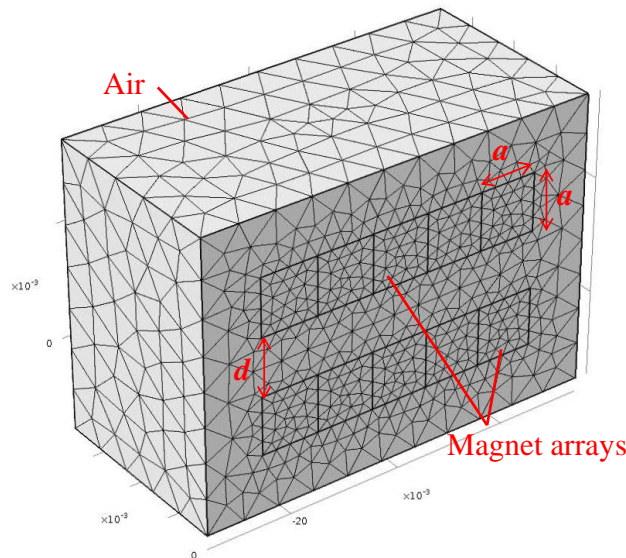


Figure 3.7 Finite element analysis (FEA) model for repelling 2D Halbach arrays. Half model of repelling magnet arrays is created and meshed using COMSOL Multiphysics[®].

Magnetic repulsion force between two 2D Halbach arrays is estimated with the simplified Coulombian model implemented in MATLAB[®] and the FEA software. The magnetic flux density

of $|\sigma^*| = 1.48$ T, for high-grade (e.g., N52) NdFeB magnets (*Ma et al., 2002*), and cuboidal magnets with $a = 10$ mm are used to estimate the force-distance relationship shown in Figure 3.8. The two methods result in similar force magnitudes. The simplified model can compute the force magnitude about 10 times faster than the FEA model, allowing more rapid model-based design process of the 2D Halbach array.

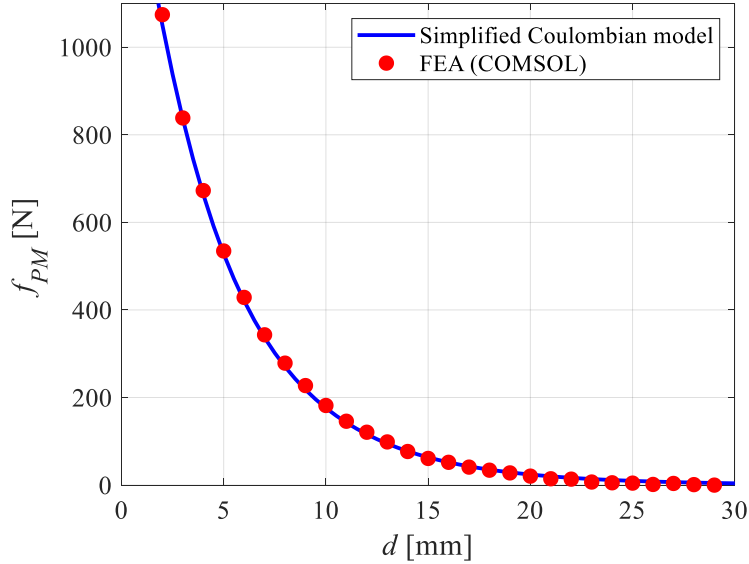


Figure 3.8 Comparison between magnetic force prediction.

The ideal PM-based assist device should provide all the required work to bring the moving table to a complete stop. The kinetic energy (E_K) of moving table (with mass, m_T , and scanning speed, v_{scan}) is

$$E_K = \frac{1}{2} m_T v_{scan}^2 \quad (3.3)$$

To bring the table to a complete stop, the PM needs to provide work (E_{PM}) given as

$$E_{PM} = \int_{d_{min}}^{d_{max}} |\vec{f}_{PM}(a, d)| dd \quad (3.4)$$

where d_{\min} and d_{\max} are the minimum and maximum distances between two PM arrays. The magnitude of repulsion force is a function of the cuboidal magnet dimension (a) and distance between the arrays (d).

As a feasibility test of the proposed PM array design, an existing motion stage with $m_T = 35$ kg and $v_{scan} = 0.5$ m/s is considered (Okwudire and Rodgers, 2013). As shown in Figure 3.9, a 2D Halbach array pair made with cuboidal magnets having $a = 9.8$ mm can provide all the work needed to completely stop the table from the 0.5 m/s scanning. The integration limits ($d_{\min} = 2$ mm and $d_{\max} = 30$ mm) are chosen to satisfy practical constraints. In order to avoid any collision during scanning, d_{\min} must be large enough to provide a safe distance. As shown in Figure 3.8, the magnetic force for $d > 30$ mm is virtually zero; thus, $d_{\max} = 30$ mm serves as the practical upper bound of d for any meaningful work.

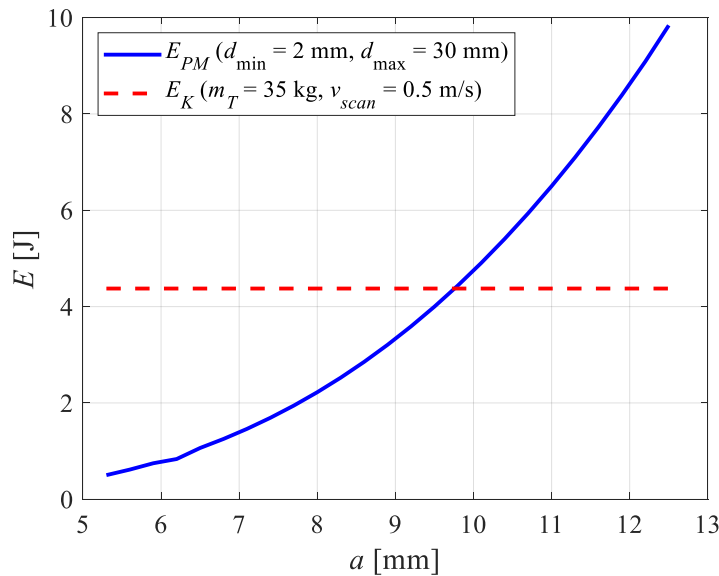


Figure 3.9 Sizing of 2D Halbach array for feasibility study using an existing motion stage.

For feasibility study of PM repulsion force measurement, N52-grade 9.53 mm (3/8", which is the closest available English fraction size sold) cuboidal permanent magnets are used to construct a pair of 2D Halbach arrays. One array is shown in Figure 3.10 (a), while a pair of PM arrays, mounted on the motion stage, is shown in Figure 3.10 (b).

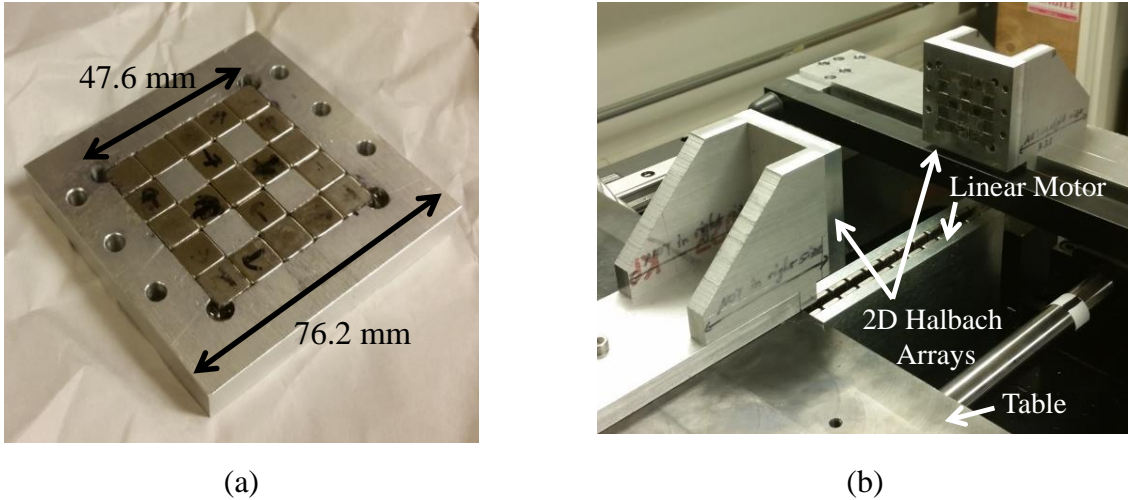


Figure 3.10 (a) Constructed 2D Halbach array for feasibility study. (b) A pair of 2D Halbach arrays installed on existing motion stage for feasibility study.

To measure the repulsion force between the PMs, the table is brought close to the MR-side PM with multiple approaching speeds. The linear motor (LM) current, which is a proxy to the motor force, required to keep the approaching speed constant is measured. The measured motor current is multiplied with the motor force constant to obtain the motor force as a function of distance between the PMs. The relationship is shown in Figure 3.11. The speed of approach has negligible effects on the measured repulsion force, signifying the eddy current damping between the two PM arrays is very small.

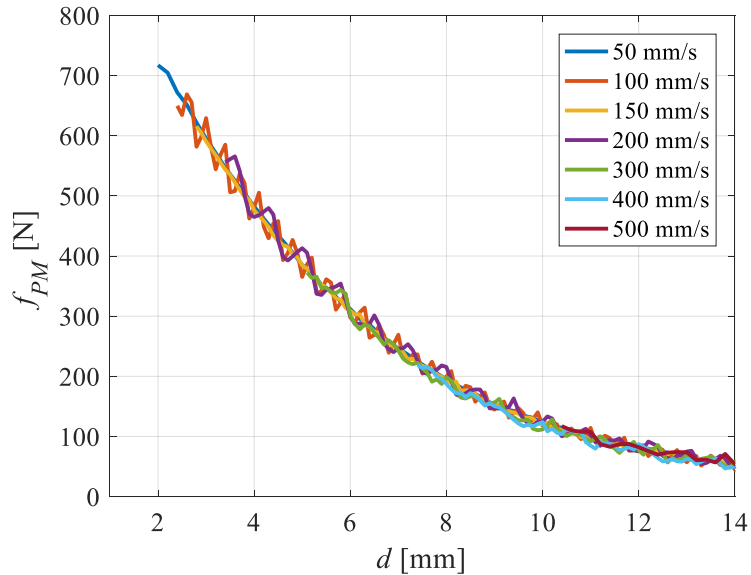


Figure 3.11 Measured magnetic force of a pair of prototype 2D Halbach arrays with different speeds of approach.

The measured vs. estimated PM repulsion force (based on the simplified Coulombian model) comparison is shown in Figure 3.12. The simplified model with $|\sigma^*| = 1.48$ T (N52-grade) case overestimates the measured force magnitude, while the overall shapes are similar. With the 5% lower σ^* magnitude ($|\sigma^*| = 1.41$ T), the estimated and measured force magnitudes become similar, suggesting that the actual PMs used to construct the 2D Halbach arrays may have lower flux densities than that listed (*K&J Magnetics, Inc.*).

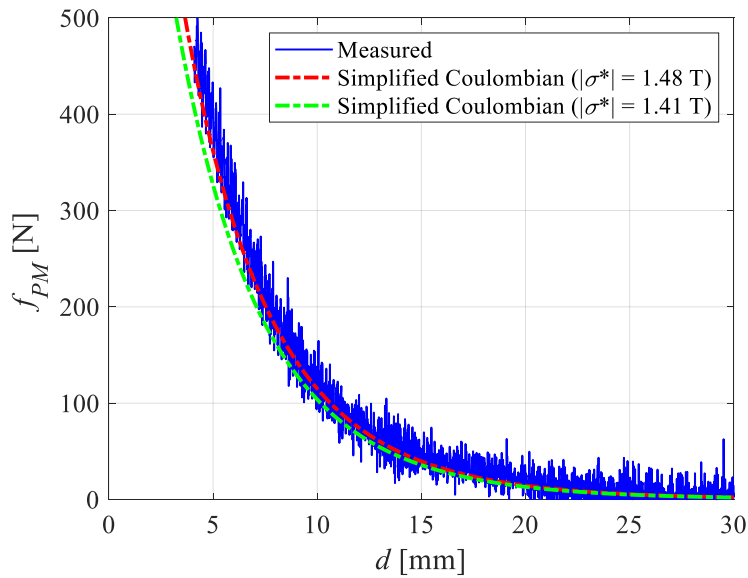


Figure 3.12 Comparison between predicted and measured magnetic force of a pair of 2D Halbach arrays.

3.3 Transmission design for automatic positioning of permanent magnets

The reviewed passive assist devices (e.g., permanent magnets and springs fixed to certain locations) lack versatility when scanning strokes/positions change over time. This deficiency can be overcome by adding efficient actuators to drive the ADs, making the stage an over-actuated system. In this over-actuation configuration, the assist devices serve as energy storage and transmission devices that can be exploited to achieve greater heating and vibration reductions of the scanning stages. The servo systems need to be quickly repositioned from one scanning position to another. Because they need not be active during the CV region, the PM positioning system can move at a lower speed than the scanning table; however, the PMs need to be repositioned for the next scan before the table arrives. To realize an inexpensive servo system, a ball screw driven by a rotary motor is employed. Compared to linear motors, rotary motors have lower cost and higher

thermal efficiency, due to the mechanical advantage of the ball screw (*Altintas et al., 2011*). Note that the lower positioning resolutions of rotary motors are acceptable, because they do not directly drive the scanning table.

The selection of the rotary motor is primarily based on size and torque constraints. It must be able to provide enough torque to support the magnetic repulsion force, while keeping a small enough profile to fit into the stage. The diameter of the screw can be selected based on the loading condition (e.g., peak magnetic force magnitude). Once the motor is selected, the power available to the servo system is fixed. However, the transmission ratio (i.e., lead) of the ball screw can be optimized to best allocate the power of the motor. Many studies have been done on selecting optimal gear ratios for load bearing, speed and acceleration of ball screw (*Kim and Park, 1990; Van de Straete et al., 1998; Cusimano, 2005*). However, for the purposes of this dissertation, the lead of the screw must be optimized for versatility, i.e., the ability of a PM-based AD to accommodate the widest range of scan strokes and positions using the given motor.

To further explain what is meant by versatility, let $x_{T,j}$ and $x_{T,j+1}$ ($j = \{1, 2, 3, \dots\}$) in Figure 3.13 (a) represent any two successive scan positions of the table where assist is to be provided by a given PM pair. To successfully provide the needed assist, the MR-side PM must be repositioned over distance ($\Delta = |x_{T,j+1} - x_{T,j}|$) during the travel time of the table moving from $x_{T,j}$ to $x_{T,j+1}$. Assuming trapezoidal velocity profiles for the table and PM, as shown in Figure 3.13 (b), the following condition must be satisfied:

$$t_a + t_b + t_c + t_d + t_e + t_f = t_1 + t_2 + t_3 \quad (3.5)$$

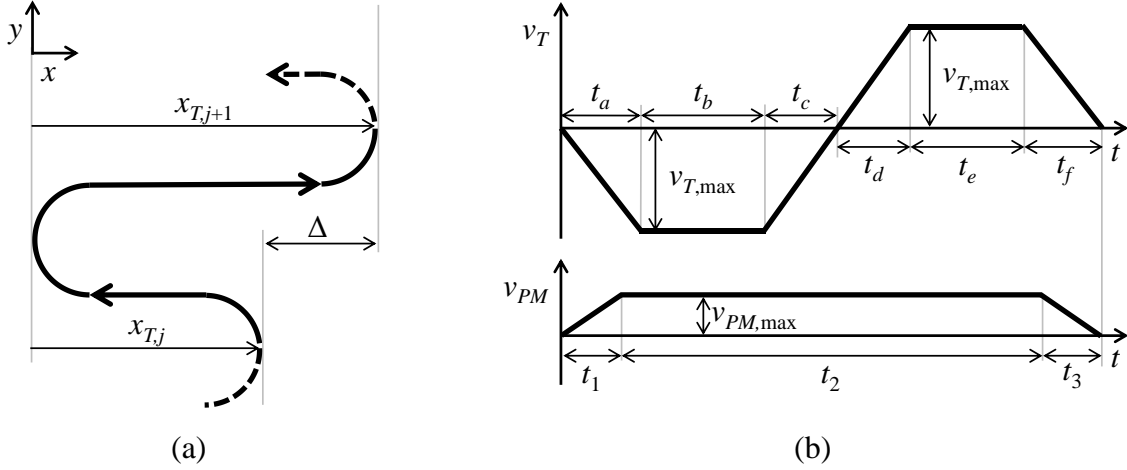


Figure 3.13 (a) Scan trajectory with varying scan strokes/positions, (b) Velocity profiles of scan table and PM during two successive scan strokes.

The time segments for the trajectory of table are given by

$$\begin{aligned}
 t_a = t_c &= \min \left(\frac{v_{T,max}}{a_{T,max}}, \sqrt{\frac{x_{T,j}}{a_{T,max}}} \right); t_b = \max \left(0, \frac{x_{T,j} - a_{T,max} t_a^2}{v_{T,max}} \right) \\
 t_d = t_f &= \min \left(\frac{v_{T,max}}{a_{T,max}}, \sqrt{\frac{|x_{T,j} \pm \Delta|}{a_{T,max}}} \right); t_e = \max \left(0, \frac{|x_{T,j} \pm \Delta| - a_{T,max} t_d^2}{v_{T,max}} \right)
 \end{aligned} \tag{3.6}$$

where $v_{T,max}$ and $a_{T,max}$ represent the maximum speed and acceleration of the table, which have been chosen because they represent the worst-case assist requirements of the table. Similarly, the time segments for the PM are given by

$$\begin{aligned}
 t_1 = t_3 &= \min \left(\frac{v_{PM,max}}{a_{PM,max}}, \sqrt{\frac{\Delta}{a_{PM,max}}} \right) \\
 t_2 &= \max \left(0, \frac{\Delta - a_{PM,max} t_1^2}{v_{PM,max}} \right)
 \end{aligned} \tag{3.7}$$

with $v_{PM,max}$ and $a_{PM,max}$ representing the maximum speed and acceleration of the PMs. They can be calculated based on the maximum rotational speed (Ω_{max}) and continuous torque limit (τ_{max}) of the rotary motor (RM);

$$v_{PM,max} = \frac{\Omega_{max} [\text{rpm}]}{60} l_s \quad (3.8)$$

$$a_{PM,max} = \left(\frac{\tau_{max} \eta}{SF} - \frac{f_{PM,max} l_s}{2\pi} \right) \frac{l_s}{2\pi} \left(m_n \frac{l_s^2}{4\pi^2} + I_s + I_m \right)^{-1} \quad (3.9)$$

where $f_{PM,max}$ represents the maximum assist force provided by the PM; l_s , SF , and η are respectively the lead, safety factor, and mechanical efficiency of the ball screw system; I_s and I_m represent the mass moments of inertia of the screw shaft and rotor (motor), respectively, and m_n is the mass of the nut (including the PM attached to it). It can be seen, by substituting Eqs. (3.6) – (3.9) into Eq. (3.5), that the repositioning distance Δ is a function of l_s and $x_{T,j}$, which could assume any value between $x_{T,min}$ and $x_{T,max}$, representing the minimum and maximum strokes of the scanning table. Arising from the \pm condition attached to Δ in Eq. (3.6), two solutions (i.e., Δ_1 and Δ_2) are available for a given l_s and $x_{T,j}$ set, because $|x_{T,j+1}|$ can either be larger or smaller than $|x_{T,j}|$. Accordingly, the optimal l_s is selected to maximize a versatility objective function (J_{vers}), defined as

$$\underset{l_s}{\text{maximize}} J_{vers} = \frac{1}{2(x_{T,max} - x_{T,min})} \int_{x_{T,min}}^{x_{T,max}} (\Delta_1(l_s, x_{T,j}) + \Delta_2(l_s, x_{T,j})) dx_{T,j} \quad (3.10)$$

representing the average value of Δ for all values of $x_{T,j} \in [x_{T,min}, x_{T,max}]$.

The design process laid out in this section is applied to a ball screw lead selection. Figure 3.14 shows a plot of J_{vers} vs. l_s , computed using the parameters given in Table 3.1. The parameters are based on the prototype magnet assisted scanning stage design, which is explained in depth in Section 3.4. The optimal lead is $l_s = 2.87$ mm, which corresponds to $J_{vers} = 63.0$ mm. However, the optimal lead may not be commercially available, because ball screws are typically sold in discrete

lead choices. In such case, the closest lead to the optimal lead can be selected, at the expense of slightly reduced versatility.

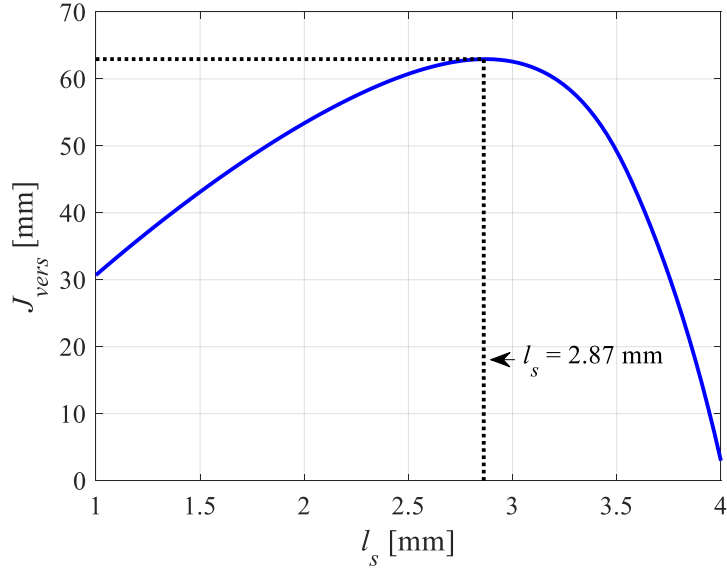


Figure 3.14 Versatility objective function (J_{vers}) vs. ball screw lead (l_s) for PM-assisted stage presented in Section 3.4.

Table 3.1 Parameters used in optimal lead selection for PM positioning servo presented in Section 3.4.

$\Omega_{\max} = 5500 \text{ rpm}$	$SF = 1.5$
$f_{PM,\max} = 600 \text{ N}$	$\eta = 0.9$
$m_n = 1.5 \text{ kg}$	$\tau_{\max} = 0.64 \text{ Nm}$
$a_{T,\max} = 35 \text{ m/s}^2$	$I_s = 3.01 \times 10^{-6} \text{ kg} \cdot \text{m}^2$
$v_{T,\max} = 1 \text{ m/s}$	$I_m = 1.63 \times 10^{-5} \text{ kg} \cdot \text{m}^2$
$x_{T,\min} = 0.05 \text{ m}$	$x_{T,\max} = 0.3 \text{ m}$

3.4 Design and construction of magnet-assisted scanning stage prototype

A prototype scanning stage with PM-based ADs is designed according to the concept laid out in Section 3.1. The PMs and automatic positioning systems are designed using the procedures presented in Sections 3.2 and 3.3, respectively. The CAD model of the prototype magnet assisted scanning stage is shown in Figure 3.15; it is designed to be able to handle a 300 mm silicon wafer with the maximum scanning speed and acceleration of 1 m/s and 35 m/s², respectively. The moving

mass of the stage is designed to be less than 15 kg, which is typical for air bearing guided linear stages for 300 mm wafer scanning applications (*Aerotech Inc. (a); Newport Corporation; Physik Instrumente*). The prototype stage's 360 mm \times 360 mm scanning table is guided by four air bushings (New Way Air Bearings, S302502), each mounted at the corner of the table and riding on a 25 mm precision ground shaft. A pair of linear shaft motors (Nippon Pulse, S250Q) with 600 N peak and 150 N continuous force (combined) is selected to drive the table to control both linear translations and any undesirable yaw motion of the table; each motor is powered by a PWM servo drive (Kollmorgen, AKD-P00306) in current mode. The table position is measured using linear encoders (Renishaw, RGSZ20 scale and T1000 readhead) with 4.88 nm resolution post-interpolation. The scanning table sits on a 900 mm \times 600 mm \times 100 mm granite base, which is suspended by four pneumatic isolators with automatic leveling (Bilz, BiAir[®] 0.5-ED).

Each PM is constructed using two adjacent 2D Halbach arrays, with N42-grade 7.9 mm (5/16") cuboidal NdFeB PMs, capable of providing the 600 N force needed to fully assist the linear motors (LMs). The N42-grade PMs are chosen because of their wider availability in size and lower price than the N52-grade ones. Each MR-side PM is actuated with a ball screw-driven servo system, which is installed on the ground through a bridge. The precision requirements of the servo system for PM are not tight, since they are not directly involved in manufacturing; micron-level positioning resolution is sufficient for them. Therefore, as shown in Figure 3.16, an inexpensive servo system, comprising a single linear guide (Misumi, SSEBZ13) and a 10 mm-diameter rolled ball screw (Misumi, BSSR1002) driven by a rotary stepper motor (Oriental Motor, NX620AC-3) is employed. The PM position is measured by a motor-built-in encoder providing 1 μ m resolution. Consequently, the stage becomes an over-actuated system, since both the linear and rotary motors provide the driving force to the table. Because the optimal lead, which is obtained with the design procedure presented in Section 3.3, is not commercially available, the closest lead ($l_s = 2$ mm) is selected. Subsequently, the versatility function (J_{vers}) is hit with a 15% penalty when compared to the optimal lead ($l_s = 2.87$ mm).

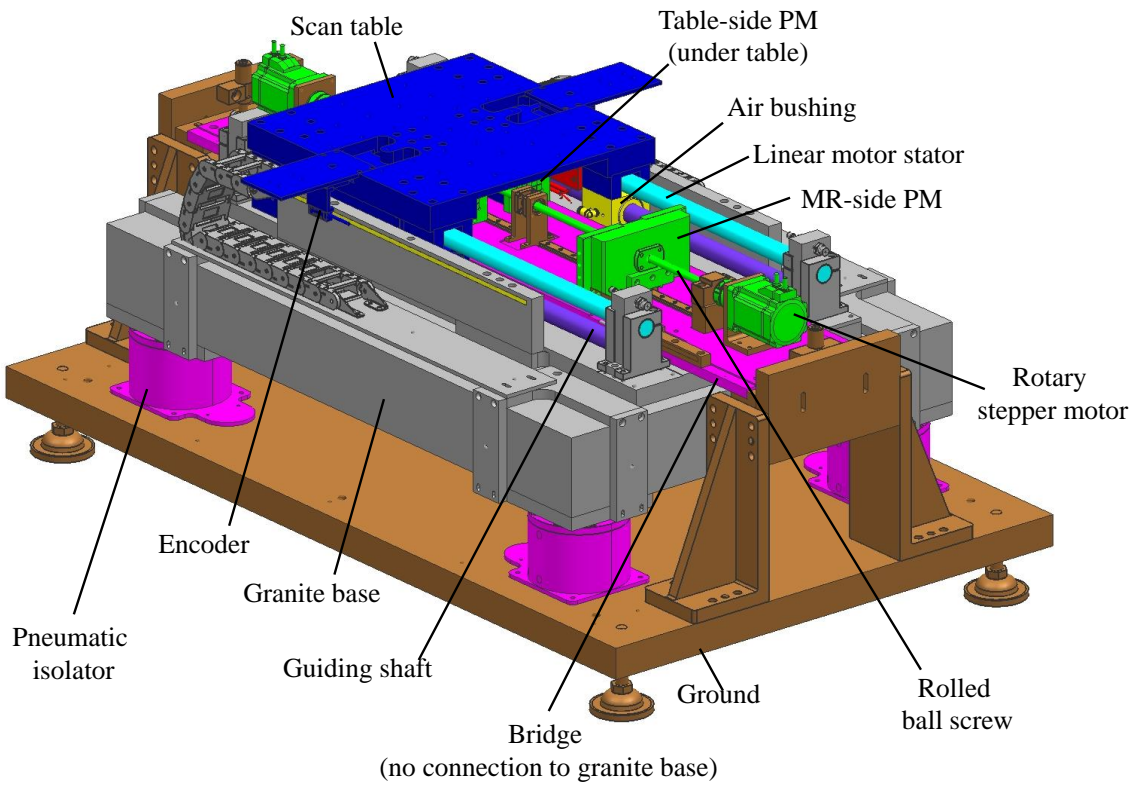


Figure 3.15 CAD model of prototype magnet assisted scanning stage.

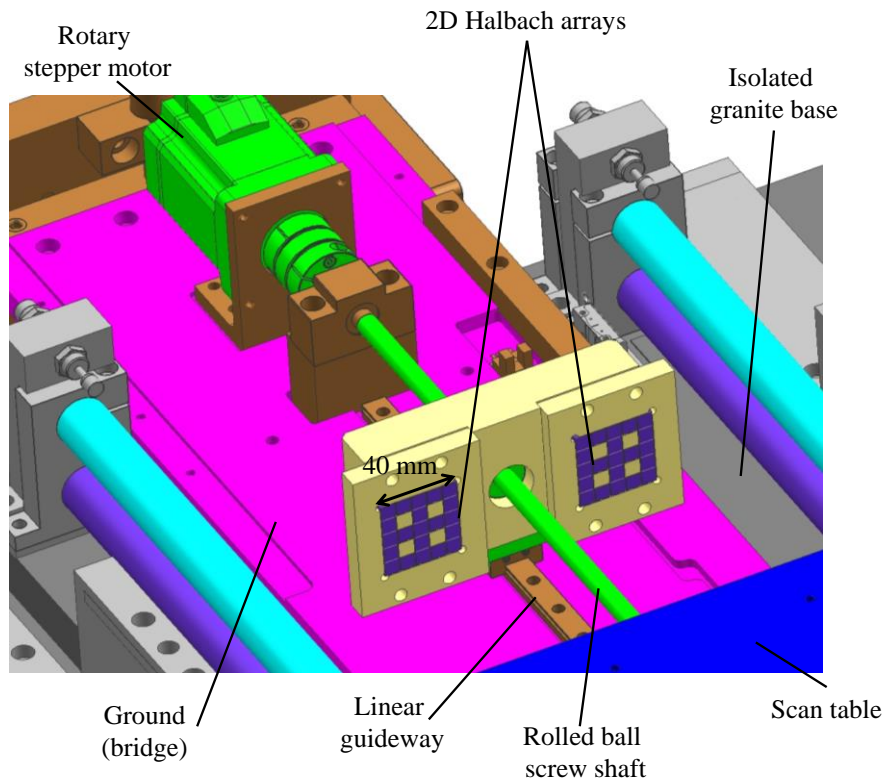
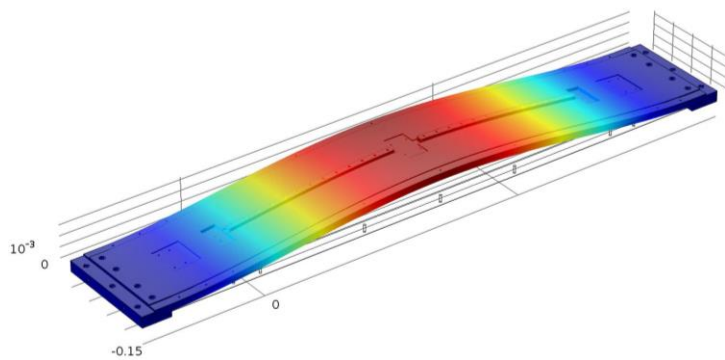
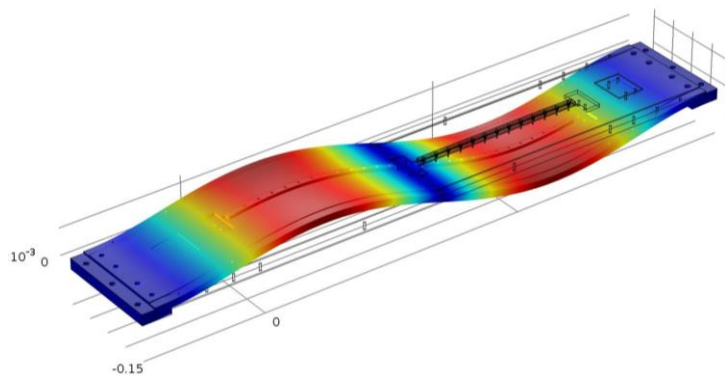


Figure 3.16 CAD model of MR-side PM mounted on bridge (connected to ground).

The PM positioning systems are mounted on a bridge directly connected to the ground (i.e., machine frame). Because the MR-side PMs move back-and-forth during scanning operations, the bridge can be excited by the motor torque and PM repulsion force. The ground vibration created by the PM positioning systems can be transmitted to the actual manufacturing on the isolated base; thus, the bridge is designed to have the 1st vibration mode at a frequency range one order of magnitude higher than the natural frequency of the vibration isolation system. Typical vibration isolation systems' cut-off frequency (i.e., natural frequency) is less than 10 Hz (*Rivin, 2003*). Modal analysis of the bridge using COMSOL Multiphysics[®] is shown in Figure 3.17. The steel bridge is fixed to the ground from the both ends and the 1st mode frequency is determined to be well above the cut-off frequency of typical isolation systems.



(a)



(b)

Figure 3.17 Vibration mode shapes of the ground bridge: (a) 1st mode at 66 Hz. (b) 2nd mode at 184 Hz.

The modal behavior of the scanning table is also analyzed using COMSOL Multiphysics® to ensure structural vibration modes remain in high frequency ranges, such that the feedback control bandwidth is not unduly sacrificed. The FEA results shown in Figure 3.18 suggests that the scanning table is very stiff and only the cantilever plates for mounting cable carriers are expected to be excited. The LM, PM, and encoder readhead mounting locations are not likely to vibrate and the entire table is expected to behave as a rigid body.

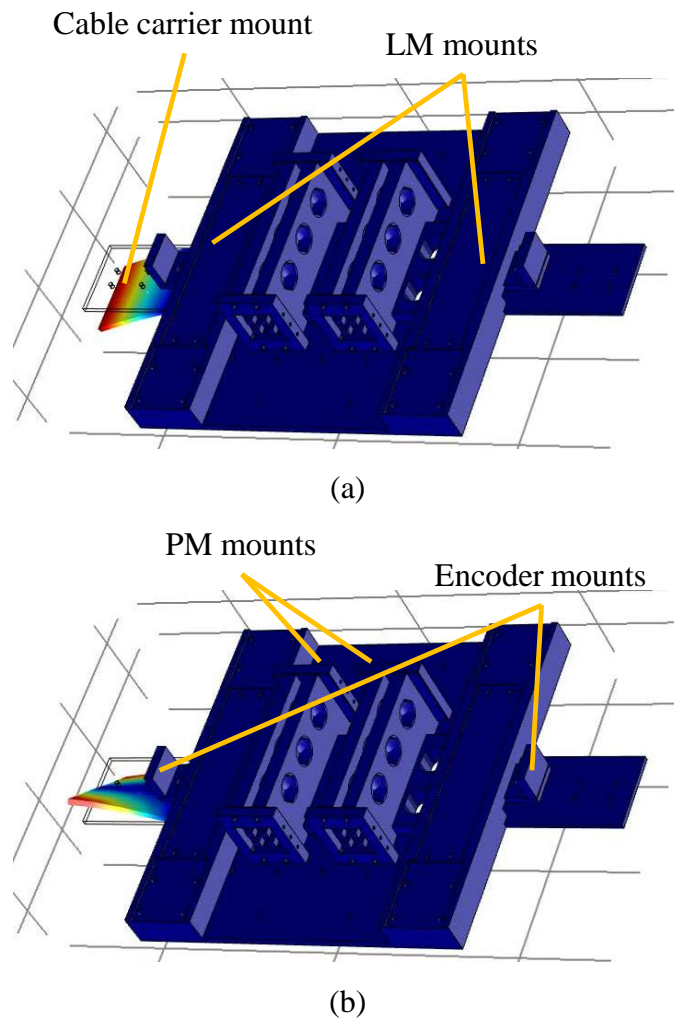


Figure 3.18 Vibration mode shapes of table: (a) 1st mode at 222 Hz. (b) 2nd mode at 844 Hz.

The constructed prototype magnet assisted scanning stage is shown in Figure 3.19, using commercially available components such as motors, encoders, bushings, linear motion guides, pneumatic vibration isolators and ball screw assemblies. Most of the structural components are custom designed and manufactured using either aluminum alloy or steel. A close-up view of the

MR-side PM assist device is shown in Figure 3.20, highlighting the compact PM-based AD and the low-cost servo system for automatic positioning. The MR-side PM is mounted on a bridge, as described above, which is not directly connected to the isolated base frame.

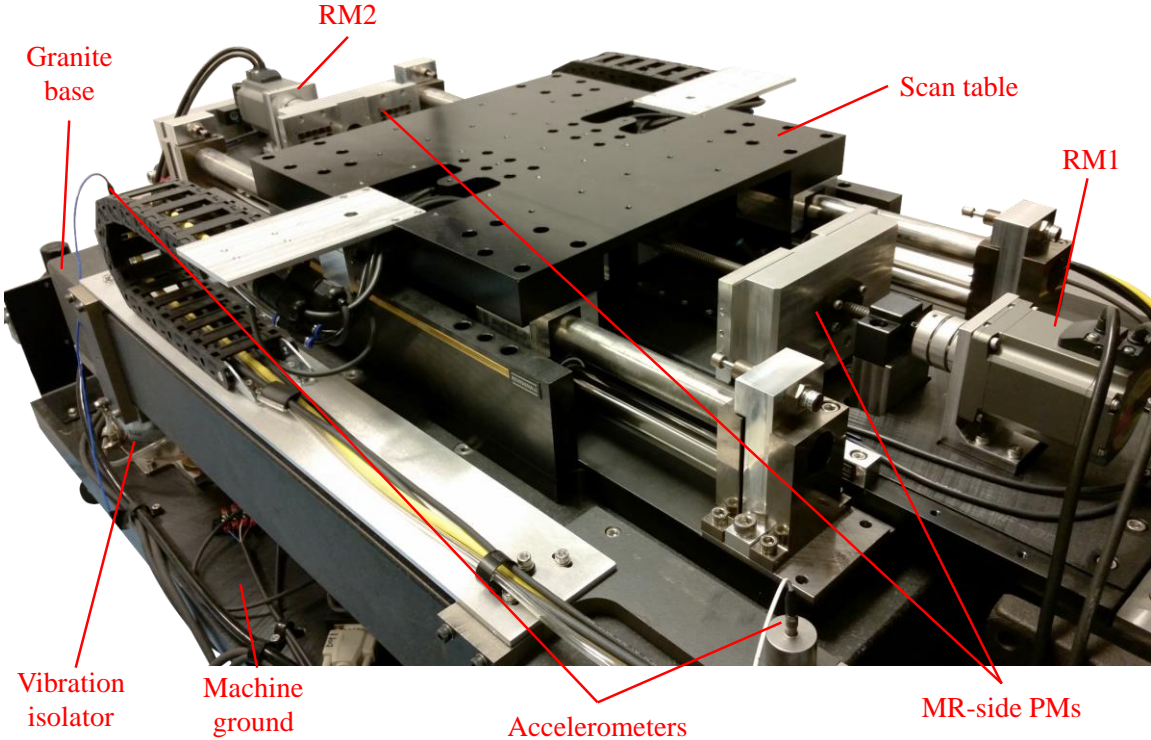


Figure 3.19 Constructed magnet assisted scanning stage.

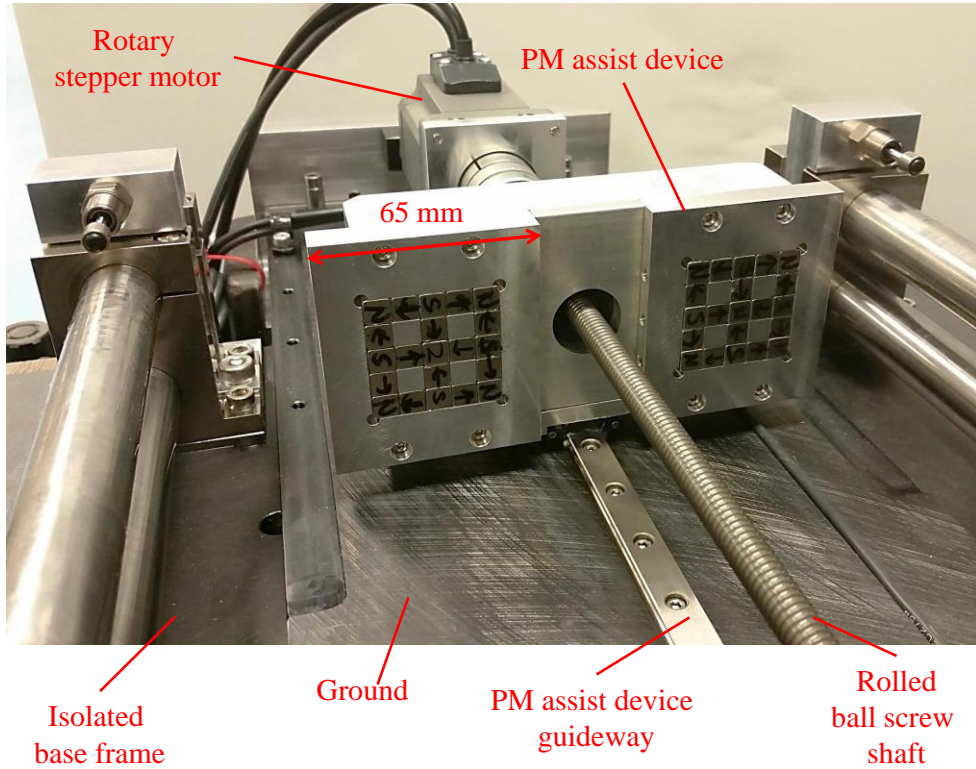


Figure 3.20 MR-side PM assist device.

The bottom view of the scanning table is shown in Figure 3.21. In the figure, the table side PMs are not yet mounted, but the cable carrier, air bushings and linear motor forcers are. As shown in Figure 3.18, the entire aluminum alloy structure is made very stiff and only the cantilever plates for mounting cable carriers are likely to be excited by motion commands. In Figure 3.22, the scanning table, with the table-side PMs mounted, is installed on the isolated base frame. The bill of materials for sourced machine components and custom designed parts is available in Appendix A. The custom designed parts' CAD drawings are listed in Appendix B.

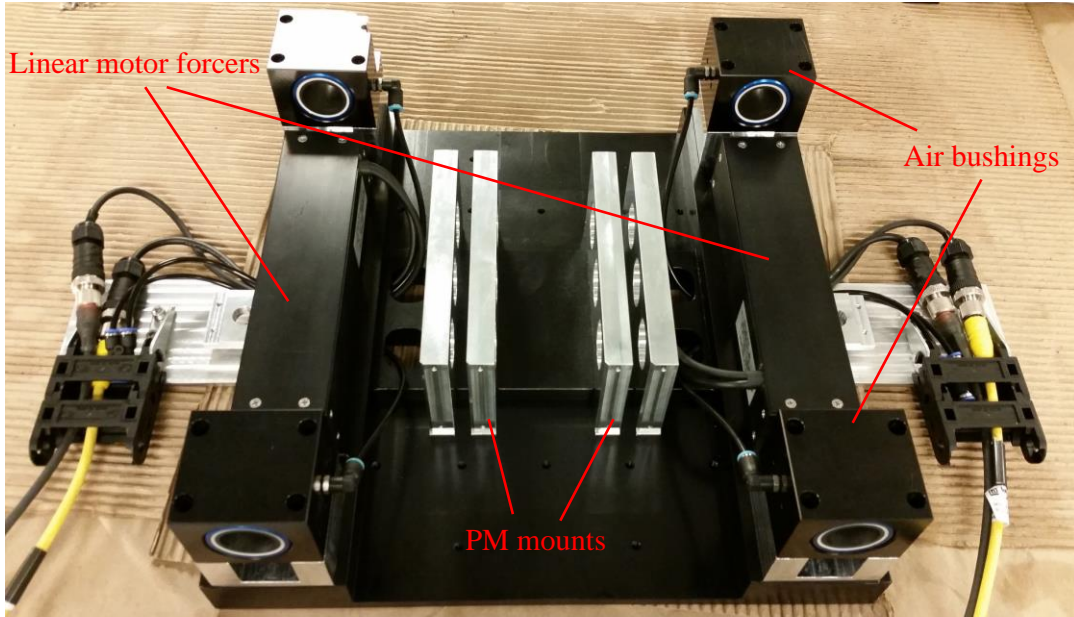


Figure 3.21 Bottom view of scanning table (without table-side PMs).

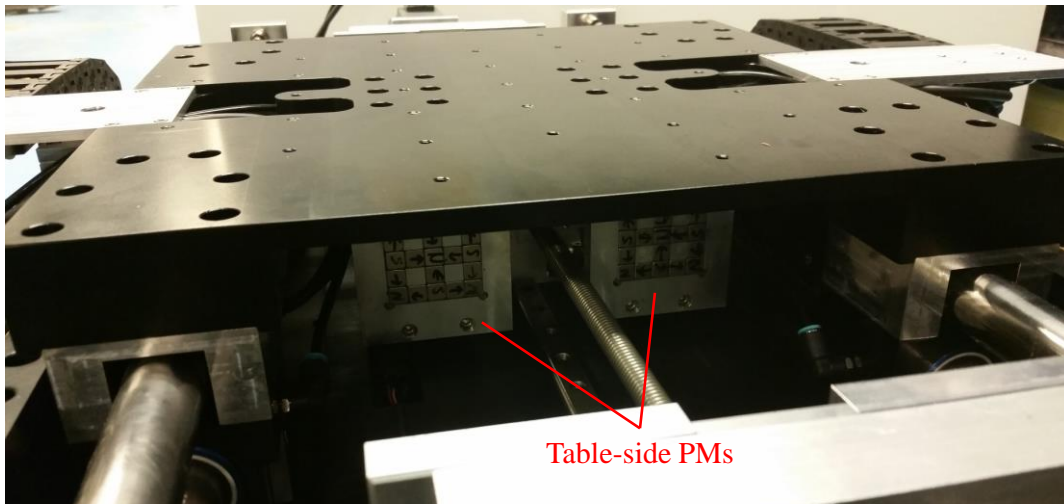


Figure 3.22 Scanning table installed on isolated base frame (with table-side PMs)

3.5 Chapter summary

A design-based concept of a scanning stage augmented with ground-mounted assist devices (ADs) to achieve simultaneous reduction of motor heat and vibration-induced errors is proposed. The ADs harvest the kinetic energy of moving table during the MR regions and release the stored energy for acceleration toward the opposite direction. The ADs are realized with repelling permanent magnets (PMs), which can be smoothly engaged and disengaged during scanning. The

PMs are designed to have high force densities by arranging multiple smaller PMs in the 2D Halbach array arrangement; a simplified Coulombian PM force model is used to aid the sizing of the array. To achieve versatility when the scan stroke and position changes during scan motions, a low-cost servo system, comprising a rotary motor and a ball screw, is employed; the lead of the ball screw is selected to maximize the versatility of assist. As a result, the rotary motors and linear motors can independently drive the table, i.e., the designed stage is over-actuated. A prototype of the proposed over-actuated scanning stage, capable of carrying a 300 mm silicon wafer with 1 m/s speed and 35 m/s² acceleration, is constructed. Optimal control of the over-actuated stage and its performance with regard to thermal and vibration-induced error reductions are discussed in the next two chapters.

Chapter 4

B-Spline based Optimal Trajectory Planning for Magnet-assisted Scanning Stage

Given a desired scan trajectory to follow, the magnet-assisted scanning stage presented in Chapter 3 can leverage three actuators – a linear motor and two rotary motors – to realize the motion. This chapter addresses the question of how to best allocate control efforts among the actuators, via trajectory planning for the permanent magnet-based (PM-based) assist devices (ADs), to minimize heat and vibration. A high-level control strategy of the stage is provided in Section 4.1. In Section 4.2, modeling of the stage for the purpose of optimal control effort allocation and identification of the model parameters are provided. In Section 4.3, a framework for optimal control allocation via trajectory planning is proposed. To lower computational costs of the optimization, it is proposed to parametrize the trajectories of PM-based ADs using B-splines; thus, an overview of the B-splines parametrization to represent motion trajectories is provided in Section 4.4. The trajectory optimization framework utilizing the B-splines is then presented in Section 4.5. A numerical case study, highlighting the benefit of optimizing the trajectories with the B-splines parameterization, is provided in Section 4.6. Finally, two experimental examples – 1) scanning for photo-lithography and 2) scanning for wafer inspection – are shown in Section 4.7, highlighting the simultaneous heat and vibration mitigation from the scanning stage with the proposed actively controlled PM-based ADs (i.e., active assist devices or AAD in short).

This chapter is partially based on the following publication:

- Yoon D, Okwudire C. *Active assist device for simultaneous reduction of heat and vibration in precision scanning stages*. Precision Engineering. 2016; 46; 193-205.

4.1 Control strategy overview of magnet assisted scanning stage

The magnet assisted scanning stage (presented in Chapter 3) is controlled using the strategy described by the block diagram shown in Figure 4.1; the stage has three inputs and one output. The PID-type feedback (FB) and model-based feedforward (FF) controllers are applied to the

linear motor for controlling x , measured by linear encoders, and the entire control scheme is implemented with a real time controller (dSPACE, DS1007) running at 10 kHz sampling frequency. Inside the feedforward controller, PM force and disturbance compensators are implemented to reject known disturbances. The role of the PM force compensator is to cancel the spill-over assistive forces in the CV region of each scan, based on the measured f_{PMi} curve of the PMs (see Section 4.2 for more details of the curve). The disturbance force compensator cancels out the position dependent disturbances such as the linear motor force ripple and cable carrier drag force. The PM positions are controlled by the rotary motors (RMs) via the PM position references ($x_{PM1,ref}$ and $x_{PM2,ref}$).

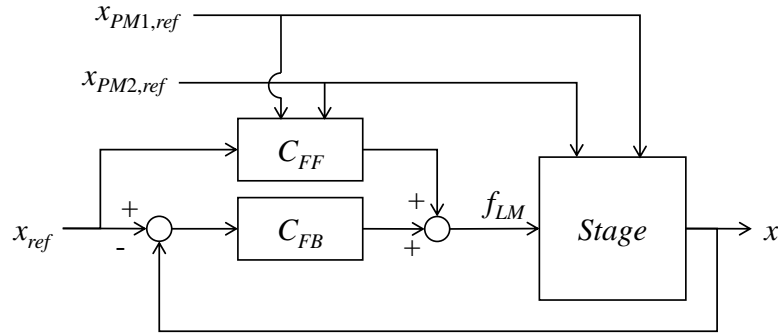


Figure 4.1 Control strategy of magnet assisted scanning stage. C denotes the controller transfer function and FF and FB denote feedforward and feedback, respectively.

4.2 System modeling and identification

For the purpose of optimally allocating control effort among the actuators, the scanning stage is modeled and its parameters identified. The control efforts for the motion stages are mostly determined by their rigid-body motion dominated by inertial and viscous damping forces. The equations of rigid body motion of the table and PMs (together with their ball screw actuators) of the scanning stage shown in Figure 3.19 are

$$m_T \ddot{x}_T(t) + b_T \dot{x}_T(t) = f_{LM}(t) - f_{PM1}(t) + f_{PM2}(t) \quad (4.1)$$

$$m_{PM1} \ddot{x}_{PM1}(t) + b_{PM1} \dot{x}_{PM1}(t) = f_{RM1}(t) + f_{PM1}(t) \quad (4.2)$$

$$m_{PM2} \ddot{x}_{PM2}(t) + b_{PM2} \dot{x}_{PM2}(t) = f_{RM2}(t) - f_{PM2}(t) \quad (4.3)$$

where m and b respectively denote equivalent masses and viscous damping coefficients, while the subscripts T and PM refer to the table and PMs, respectively; f_{RMi} ($i = 1, 2$) represent the equivalent rotary motor (RM) forces used to position the respective PM i . Eqs. (4.1) – (4.3) are derived based on the assumption that the motions of the isolated base are negligible compared to those of the table and PMs. It is, however, of interest to consider the scanning direction (x -axis) motion of the base (x_B) caused by horizontal motions of the ground (x_G) particularly within the CV region where high precision is desired (see Figure 4.2). Even though the horizontal vibration isolators of combined stiffness (k_B) and damping coefficient (b_B) are designed to reduce the transmission of x_G to x_B , the PMs create another channel for x_G to reach x_B through their equivalent stiffness (k_{PM}) arising from the magnetic repulsion forces. It is important to ensure that the presence of k_{PM} does not subvert the isolation of x_B from x_G .

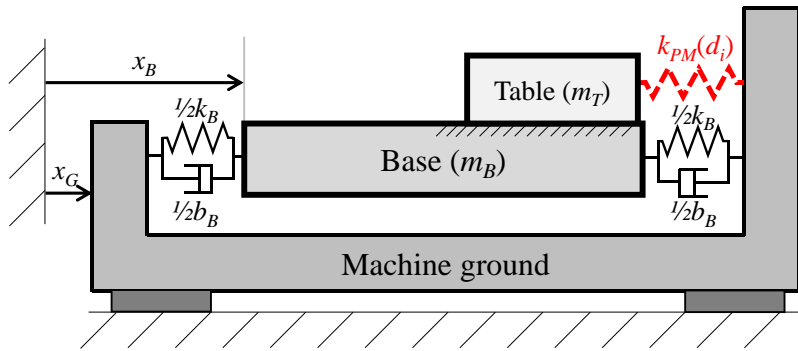


Figure 4.2 Representation of isolation system using a mass-spring-damper model.

For the purpose of analyzing the transmissibility of x_G to x_B , without loss of generality, assume that the table is at rest relative to the base, and that the connection between the table and base is rigid, due to the high bandwidth feedback controllers regulating the position of the table relative to the base. Accordingly, the equation of motion for the base is given by

$$\ddot{x}_B(t) + 2\zeta\omega_n\dot{x}_B(t) + \omega_n^2 x_B(t) = 2\zeta\omega_n\dot{x}_G(t) + \omega_n^2 x_G(t) \quad (4.4)$$

where ω_n and ζ are respectively the natural frequency and damping ratio of the isolation system (including the effect of the PMs), given by

$$\omega_n = \sqrt{\frac{k_B + k_{PM}}{m_B + m_T}} \quad (4.5)$$

$$\zeta = \frac{b_B}{2(m_B + m_T)\omega_n} \quad (4.6)$$

where m_B represents the mass of the isolated base. Note that the equivalent stiffness provided by the two PM pairs is nonlinearly related to the distance d_i between each PM pair. Observing the magnetic force-distance curve shown in Figure 3.11, f_{PMi} can be approximated as, for the purpose of capturing the overall relationship,

$$f_{PMi}(d_i) = \alpha_{PMi} e^{-\beta_{PMi} d_i} \quad (4.7)$$

where α_{PMi} and β_{PMi} are positive constants. Therefore, the stiffness provided by the PMs (k_{PM}) becomes

$$k_{PM} = -\frac{d}{d(x_B - x_G)} (-f_{PM1} + f_{PM2}) = \alpha_{PM1} \beta_{PM1} e^{-\beta_{PM1} d_1} + \alpha_{PM2} \beta_{PM2} e^{-\beta_{PM2} d_2} \quad (4.8)$$

based on the understanding that $d_1 = d_{1,0} - (x_B - x_G)$, $d_2 = d_{2,0} + (x_B - x_G)$ and $d_{i,0}$ represent the initial values of d_i (i.e., when $x_B = x_G = 0$) at the position of the table where k_{PM} is evaluated. The worst-case degradation of transmissibility in the CV regions due to the PM-based ADs occurs when the table is sandwiched between the two PM pairs such that $d_1 = d_2 = \delta_{CV}$. In this case, the table experiences the maximum PM stiffness given by

$$k_{PM,\max} = \alpha_{PM1} \beta_{PM1} e^{-\beta_{PM1} \delta_{CV}} + \alpha_{PM2} \beta_{PM2} e^{-\beta_{PM2} \delta_{CV}} \quad (4.9)$$

where δ_{CV} represents the smallest allowable distance between any two PM pairs when the table is in the CV region. The resonance frequency of an isolation system, given by

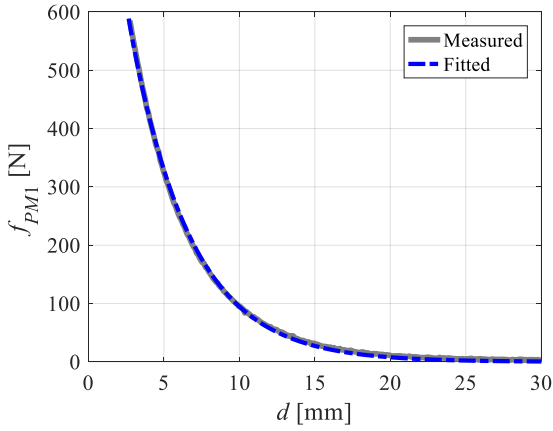
$$\omega_{res} = \omega_n \sqrt{1 - 2\zeta^2} \quad (4.10)$$

is commonly considered as a figure of merit for its vibration isolation quality (*Rivin, 1995*). Therefore, δ_{CV} can be selected to ensure that the worst-case percentage increase in resonance frequency (R) given by

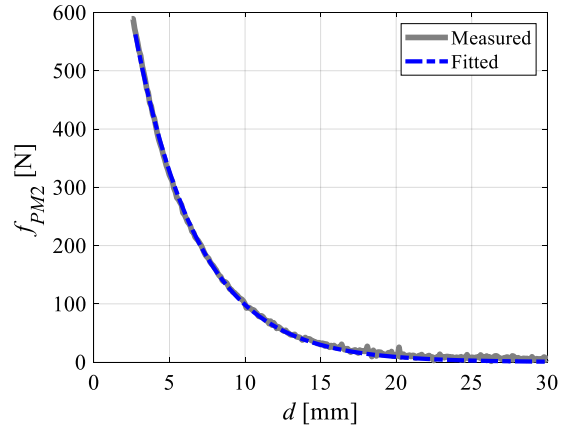
$$R = \left(\frac{\omega_{res}|_{k_{PM}=k_{PM,max}} - \omega_{res}|_{k_{PM}=0}}{\omega_{res}|_{k_{PM}=0}} \right) \times 100\% \quad (4.11)$$

is acceptably small, meaning that transmissibility is not unduly sacrificed by the introduction of the PM-based ADs.

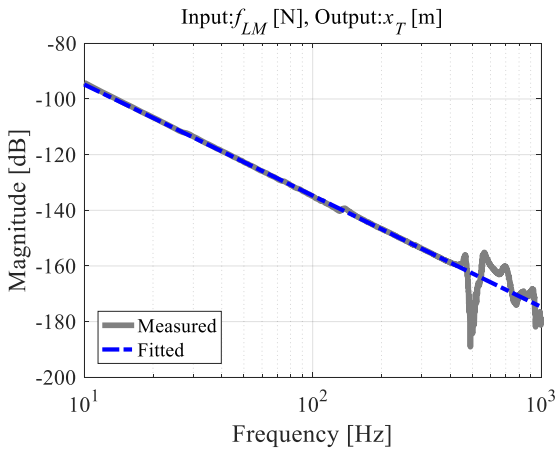
The measured and fitted force-distance relationships of the PM pairs are shown in Figure 4.3. The exponential force model given in Eq. (4.7) describes the measured relationship very well. To identify the table, PM*i* and isolated base model parameters, swept sinusoidal force inputs are respectively applied by the linear and rotary motors and the responses are recorded with encoders and accelerometers. The measured and fitted frequency response functions (FRFs) of the table, PM*i* and isolated base are shown in Figure 4.4 (only the magnitude responses are shown). During the fitting processes of table and PM*i*, low-frequency (i.e., < 300 Hz for the table and < 100 Hz for PM*i*) measurements are weighted more, because they are related to the system model explained above. For the isolated base model fitting, focus is on capturing the resonance behavior, which is the figure of merit for vibration isolation system. The identified model parameters are summarized in Table 4.1.



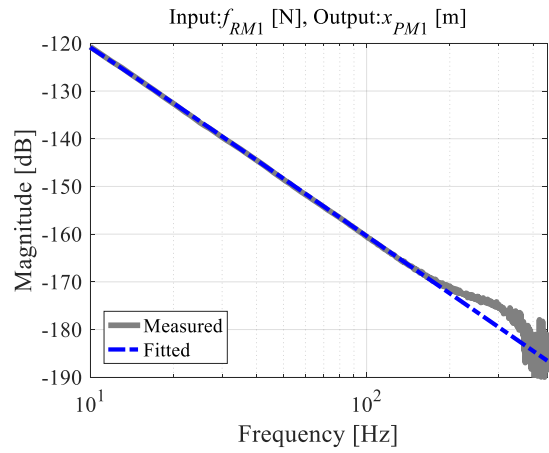
(a)



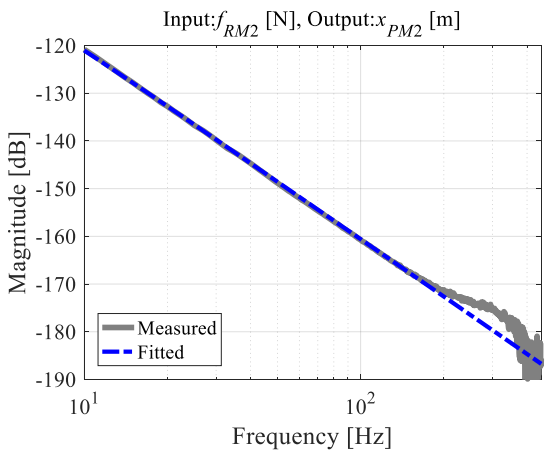
(b)

Figure 4.3 Measured and fitted PM repulsion force (f_{PM}) vs. distance (d) relationship; (a) PM1. (b) PM2

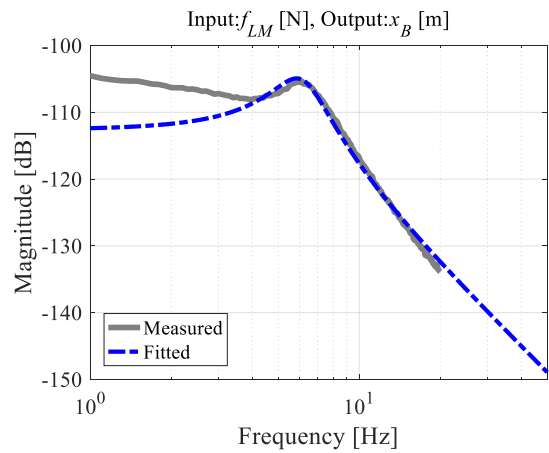
(a)



(b)



(c)



(d)

Figure 4.4 Measured and fitted frequency response functions from (a) f_{LM} to x_T , (b) f_{RM1} to x_{PM1} , (c) f_{RM2} to x_{PM2} , and (d) f_{LM} to x_B .

Table 4.1 Identified system parameters of stage. (The subscripts associated with each parameter listed in the first column is provided in parentheses in the first row).

	Table (T)	PM1 ($PM1$)	PM2 ($PM2$)	Base (B)
m [kg]	13.8	265	271	287
b [Ns/m]	123	562	567	4.68×10^3
k [N/m]	-	-	-	4.26×10^5
α [N]	-	1.14×10^3	1.08×10^3	-
β [1/m]	-	2.50×10^2	2.40×10^2	-

4.3 Optimal control allocation via PM trajectory optimization

With the fixed scanning table motion trajectory, because of manufacturing process requirements, the total force applied to table is also fixed. Thus, the optimal allocation of control efforts is achieved by generating optimal force profiles for the PM-based ADs. As presented in Section 3.2 and 4.1, the magnetic force profile is a function of the distances between the table-side and MR-side PMs. Consequently, the optimal control efforts allocation of the magnet assisted scanning stage involves the determination of $x_{PMi}(t)$ for any given $x_T(t)$ such that f_{LM} is reduced, as a means to reduce heat and vibration. Note, however, that there are costs associated with providing assist using the PM-based ADs. The rapid motion of the PMs, together with the larger f_{PMi} associated with providing assist for scan trajectories with variable strokes/positions increase f_{RMi} , which in turn generates heat in the rotary motors (RMs).

Representing the respective motion trajectories of the table and PMs as vectors $\mathbf{x}_T = [x_T(1) \dots x_T(n)]^T$ and $\mathbf{x}_{PMi} = [x_{PMi}(1) \dots x_{PMi}(n)]^T$ in discrete-time domain, with sampling interval T_s [s], the equivalent motor force signals necessary to track the trajectories can be derived from Eqs. (4.1) – (4.3) as

$$\mathbf{f}_{LM} = m_T \ddot{\mathbf{x}}_T + b_T \dot{\mathbf{x}}_T + \mathbf{f}_{PM1} - \mathbf{f}_{PM2} \quad (4.12)$$

$$\mathbf{f}_{RM1} = m_{PM1} \ddot{\mathbf{x}}_{PM1} + b_{PM1} \dot{\mathbf{x}}_{PM1} - \mathbf{f}_{PM1} \quad (4.13)$$

$$\mathbf{f}_{RM2} = m_{PM2} \ddot{\mathbf{x}}_{PM2} + b_{PM2} \dot{\mathbf{x}}_{PM2} + \mathbf{f}_{PM2} \quad (4.14)$$

where the dot accents on the vectors represent the discretized derivatives of respective motion trajectories. The magnetic force vectors (\mathbf{f}_{PM1} and \mathbf{f}_{PM2}) can be evaluated using Eq. (4.7) with the respective distance vectors (\mathbf{d}_1 and \mathbf{d}_2) given as

$$\mathbf{d}_1 = \mathbf{x}_{PM1} - \mathbf{x}_T - \frac{1}{2}l_T \begin{bmatrix} 1 \\ \vdots \\ 1 \end{bmatrix}_n \quad (4.15)$$

$$\mathbf{d}_2 = \mathbf{x}_T - \mathbf{x}_{PM2} - \frac{1}{2}l_T \begin{bmatrix} 1 \\ \vdots \\ 1 \end{bmatrix}_n \quad (4.16)$$

Note that each vector in Eqs.(4.12) – (4.16) is $n \times 1$ in size, where n is the number of data points in the discretized trajectories. Moreover, the equations assume that the servo dynamics of the LM and RMs can be ignored (i.e., they are of very high bandwidth) such that \mathbf{x}_T is the same as the desired trajectory of the table, which is known, and \mathbf{x}_{PMi} represent the desired trajectories of the PMs, which are to be determined. Considering the costs and benefits of the PM-based ADs, the optimal control objective is formulated as

$$J_{contr} = (1-w)\mathbf{f}_{LM}^T \mathbf{f}_{LM} + w(\mathbf{f}_{RM1}^T \mathbf{f}_{RM1} + \mathbf{f}_{RM2}^T \mathbf{f}_{RM2}) \quad (4.17)$$

where $w \in [0, 1]$ is a user-defined weight. It is reasonable to select $w \ll 0.5$ because the heat and vibration costs associated with the RMs are typically much smaller than those associated with the LM. This is because RMs are, in general, much more efficient than LMs (*Altintas et al., 2011; Duan and Okwudire, 2016b*), hence they generate much less heat for the same magnitude of force. Moreover, the heat generated by the RMs is distant from the manufacturing operation, compared to the heat generated by the LMs which are directly conducted to the table. Similarly, vibration of the machine ground caused by the reaction forces borne by the PMs is attenuated by the vibration isolators, whereas the reaction force caused by f_{LM} directly excites the machine base.

Based on the defined objective, \mathbf{x}_{PM1} and \mathbf{x}_{PM2} can be obtained by directly solving the constrained optimization problem formally given by

$$\begin{aligned}
& \text{minimize } J_{\text{contr}}(\mathbf{x}_{PM1}, \mathbf{x}_{PM2}) \\
& \text{s.t.} \\
& \delta_C - \min(\mathbf{d}_i) \leq 0 \\
& \delta_{CV} - \min(\mathbf{d}_{i,CV}) \leq 0 \\
& \max(|\dot{\mathbf{x}}_{PMi}|) - v_{PM,\max} \leq 0 \\
& \max(|\ddot{\mathbf{x}}_{PMi}|) - a_{PM,\max} \leq 0
\end{aligned} \tag{4.18}$$

where δ_C represents a safety gap (i.e., the minimum allowable distance between either PM pair to prevent collisions). The distance vectors $\mathbf{d}_{i,CV}$ are subsets of the vectors \mathbf{d}_i ; they correspond to the distances between the associated PM pairs when the table is in the CV regions. Accordingly, $\mathbf{d}_{i,CV}$ must be constrained by δ_{CV} to ensure that transmissibility is not unduly sacrificed by the PM-based ADs. Using the operator $|\cdot|$ to denote the absolute value of each vector element, the last two constraints ensure that the kinematic limits of the RMs, which are found using Eqs. (3.8) and (3.9), are not violated.

4.4 Overview of B-splines representation of motion trajectory

A direct approach can be taken to solve the optimization problem defined in Eq. (4.18) by treating every element of \mathbf{x}_{PMi} as an optimization variable (see Section 4.3 for details of the problem formulation). In this case, $2n$ variables must be optimized simultaneously using numerical optimization algorithms. The number of optimization variables can be halved by realizing that \mathbf{x}_{PM1} and \mathbf{x}_{PM2} are practically decoupled. This is based on the premise that, by design, as shown in Figure 3.4, the MR regions are separated by intervening CV regions for which no assist is needed. Nonetheless, n could still be very large in practice, thus making the numerical solution of the optimization challenging. A more computationally efficient solution approach, which employs basis-splines (or B-splines) to represent the trajectories, is proposed and evaluated in the rest of this chapter. B-splines, widely used for representing free-form curves, can be adopted to reduce the number of variables in solving for the optimal trajectories (*Wang and Horng, 1990; Pellicciari et al., 2015; Duan and Okwudire, 2016a*). In this section, an overview of B-splines is provided.

A B-spline curve $c(\tau)$ of degree r , can be expressed as a linear combination of basis functions, $N_{i,r}(\tau)$, and control points, $p(i)$ where $i = \{1, 2, \dots, k\}$, as (Piegl and Tiller, 2012)

$$c(\tau) = \sum_{i=1}^k N_{i,r}(\tau) p(i) \quad (4.19)$$

with $\tau \in [0,1]$ being the spline parameter. For a uniformly spaced knot vector $\mathbf{g} = [g(1) \dots g(r+k+1)]$ given by

$$g(\gamma) = \begin{cases} 0 & 1 \leq \gamma \leq r+1 \\ \frac{\gamma-r-1}{k-r+1} & r+2 \leq \gamma \leq k+1 \\ 1 & k+2 \leq \gamma \leq r+k+1 \end{cases} \quad (4.20)$$

$N_{i,r}(\tau)$ can be determined recursively from the expressions

$$N_{i,0}(\tau) = \begin{cases} 1 & g(i) \leq \tau < g(i+1) \\ 0 & \text{otherwise} \end{cases} \quad (4.21)$$

$$N_{i,j}(\tau) = \frac{\tau - g(i)}{g(i+j) - g(i)} N_{i,j-1}(\tau) + \frac{g(i+j+1) - \tau}{g(i+j+1) - g(i+1)} N_{i+1,j-1}(\tau), \quad j = \{1, 2, \dots, r\}$$

If the spline parameter $\tau \in [0,1]$ is discretized into n equally spaced points, resulting in a vector $\boldsymbol{\tau} = [\tau(1) \dots \tau(n)]^T$, a basis function matrix (\mathbf{N}_p) can be defined as

$$\mathbf{N}_p = \begin{bmatrix} N_{1,r}(\tau(1)) & \dots & N_{k,r}(\tau(1)) \\ \vdots & \ddots & \vdots \\ N_{1,r}(\tau(n)) & \dots & N_{k,r}(\tau(n)) \end{bmatrix} \quad (4.22)$$

Accordingly, Eq. (4.19) can be re-written in a matrix form as (Duan and Okwudire, 2016a)

$$\mathbf{c} = \mathbf{N}_p \mathbf{p} \quad (4.23)$$

where \mathbf{c} is the $n \times 1$ discretized curve vector and $\mathbf{p} = [p(1) \dots p(k)]^T$ is the control point vector. The derivative of $c(\tau)$ with respect to τ , denoted as $c'(\tau)$, is also a B-spline curve, but it has $k - 1$ control points, degree $r - 1$ and knot vector $\mathbf{g}_d = [g(2) \dots g(r+k)]$, obtained by dropping the first and last knots from the knot vector $\mathbf{g} = [g(1) \dots g(r+k+1)]$ of $c(\tau)$. The control point vector $\mathbf{p}_d = [p_d(1) \dots p_d(k-1)]^T$ of $c'(\tau)$ is related to \mathbf{p} by the derivative expression using their vector elements (Piegl and Tiller, 2012; Duan and Okwudire, 2016a);

$$p_d(i) = r \frac{p(i+1) - p(i)}{g(i+r+1) - g(i+1)}, \quad i = \{1, 2, \dots, k-1\} \quad (4.24)$$

Define $N_{i,r-1}(\tau)$ as the basis functions over the reduced knot vector \mathbf{g}_d , and assume that the spline parameter $\tau \in [0,1]$ represents time $t \in [0, T_{tot}]$ normalized by T_{tot} . Accordingly, using the chain rule, $\dot{c}(\tau)$, the time derivative of $c(\tau)$, can be written with respect to the control point velocity $p_v = p_d/T_{tot}$ as

$$\dot{c}(\tau) = \frac{1}{T_{tot}} c'(\tau) = \frac{1}{T_{tot}} \sum_{i=1}^{k-1} N_{i,r-1}(\tau) p_d(i) = \sum_{i=1}^{k-1} N_{i,r-1}(\tau) p_v(i) \quad (4.25)$$

whose discretized form is given by

$$\dot{\mathbf{c}} = \mathbf{N}_d \mathbf{p}_v = \mathbf{N}_d \mathbf{D}_v \mathbf{p} = \mathbf{N}_v \mathbf{p} \quad (4.26)$$

where \mathbf{N}_d and \mathbf{D}_v are defined as

$$\mathbf{N}_d = \begin{bmatrix} N_{1,r-1}(\tau(1)) & \cdots & N_{k-1,r-1}(\tau(1)) \\ \vdots & \ddots & \vdots \\ N_{1,r-1}(\tau(n)) & \cdots & N_{k-1,r-1}(\tau(n)) \end{bmatrix} \quad (4.27)$$

$$\mathbf{D}_v = \frac{r}{T_{tot}} \begin{bmatrix} g(r+2) - g(2) & 0 & \dots & 0 \\ 0 & \ddots & \ddots & \vdots \\ \vdots & \ddots & \ddots & 0 \\ 0 & \dots & 0 & g(r+k) - g(k) \end{bmatrix}^{-1} \begin{bmatrix} -1 & 1 & 0 & \dots & 0 \\ 0 & -1 & 1 & \ddots & \vdots \\ \vdots & \ddots & \ddots & \ddots & 0 \\ 0 & \dots & 0 & -1 & 1 \end{bmatrix}_{(k-1) \times k} \quad (4.28)$$

Following the same approach, higher order time derivatives in discretized form (i.e., $\ddot{\mathbf{c}}$, $\ddot{\mathbf{c}}$ and so forth) can be generated (Duan and Okwudire, 2016a).

One unique property of B-splines is their local property, meaning that the effect of changing control points is only on the nearby curve segments. Figure 4.5 (a) shows the columns of an illustrative basis function matrix ($i = 1, 2, \dots$), highlighting the spatial separation among the bases. Because the function values become zero outside their effective range, change of one control point has no effect on the curve segments located outside the range. This is illustrated with Figure 4.5 (b), where only the curve segments, pertaining to the relocated control point and its basis, are moved. In here, a 3rd order B-spline curve is described by 11 control points. While all other control points remain intact, only the 5th control point is lowered by 0.2. The effect of relocating the control point is only on the nearby segments. This local property is exploited to lower computational load when solving for the optimal PM trajectories for the rest of chapter.

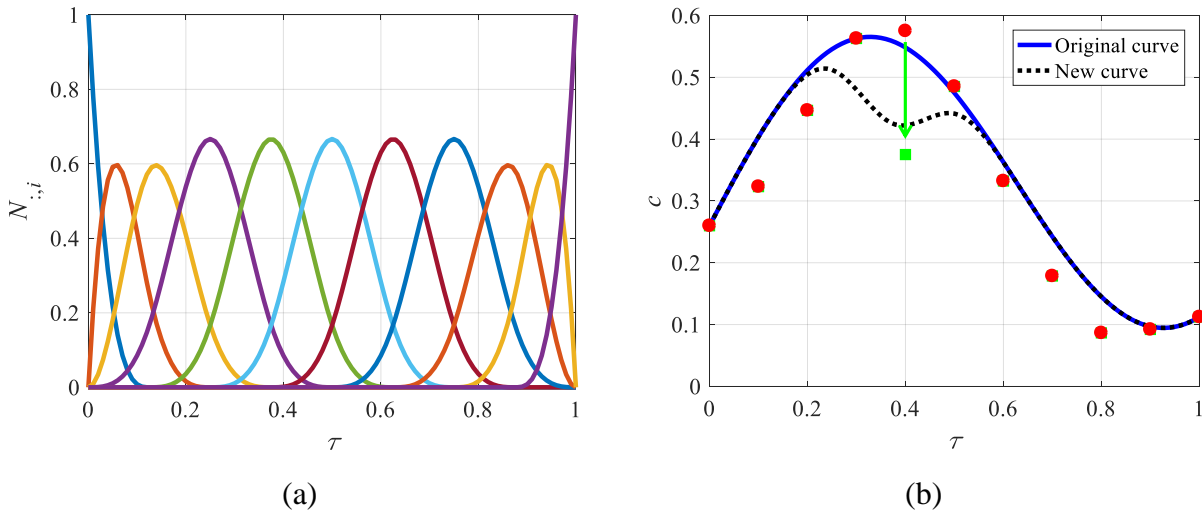


Figure 4.5 (a) Columns of basis function matrix showing the local property of B-splines. (b) Local property of B-splines; effect of changing a control point is only on nearby curve segments.

4.5 Optimization of B-spline-based trajectory for PMs

Using B-splines, x_{PMi} and their time derivatives can be represented as, in discrete-time domain (see Section 4.4 for overview of B-splines for representation of motion trajectory),

$$\mathbf{x}_{PMi} = \mathbf{N}_{pi} \mathbf{p}_{PMi} \quad (4.29)$$

$$\dot{\mathbf{x}}_{PMi} = \mathbf{N}_{vi} \mathbf{p}_{PMi} \quad (4.30)$$

$$\ddot{\mathbf{x}}_{PMi} = \mathbf{N}_{ai} \mathbf{p}_{PMi} \quad (4.31)$$

where \mathbf{p}_{PMi} are control point vectors for PMi trajectories (of size $n_{PMi} \times 1$) while \mathbf{N}_{pi} , \mathbf{N}_{vi} and \mathbf{N}_{ai} are basis function matrices for displacement, velocity and acceleration, respectively (again, see Section 4.4 for more details). The elements of \mathbf{p}_{PMi} can be used as optimization variables in place of the elements of \mathbf{x}_{PMi} , thus drastically reducing the size of the optimization problem, based on the fact that $n_{PMi} \ll n$. Note that, when represented as B-splines, the time derivatives of x_{PMi} are guaranteed to be smooth up to the $(r - 1)^{\text{th}}$ derivative, where r is the B-splines degree. Consequently, x_{PMi} and their derivatives can be down-sampled to smaller vectors based on \mathbf{N}_{pi} , \mathbf{N}_{vi} and \mathbf{N}_{ai} matrices calculated using a coarser (i.e., larger) value of T_s without sacrificing smoothness, as long as $r \geq 3$. Once the optimal \mathbf{p}_{PMi} vectors calculated using the coarser sampling are obtained, the original T_s can be employed to generate new \mathbf{N}_{pi} , \mathbf{N}_{vi} and \mathbf{N}_{ai} matrices, thereby up-sampling x_{PMi} and their derivatives back to the original resolution before implementation on the actual stage. The last two constraints of Eq. (4.18) are enforced using vectors of length n , which is computationally burdensome. Accordingly, the length of last two constraint vectors can be reduced by replacing $\dot{\mathbf{x}}_{PMi}$ and $\ddot{\mathbf{x}}_{PMi}$ by control point velocity and acceleration vectors, \mathbf{p}_{vi} and \mathbf{p}_{ai} , of respective lengths $n_{PMi} - 1$ and $n_{PMi} - 2$, given by

$$\mathbf{p}_{vi} = \mathbf{D}_v \mathbf{p}_{PMi} \quad (4.32)$$

$$\mathbf{p}_{ai} = \mathbf{D}_a \mathbf{D}_v \mathbf{p}_{PMi} \quad (4.33)$$

where \mathbf{D}_v and \mathbf{D}_a are time derivative operators expressed as

$$\mathbf{D}_v = \begin{bmatrix} h_p(1) & 0 & \dots & 0 \\ 0 & \ddots & \ddots & \vdots \\ \vdots & \ddots & \ddots & 0 \\ 0 & \dots & 0 & h_p(n_{PMi}-1) \end{bmatrix}^{-1} \begin{bmatrix} -1 & 1 & 0 & \dots & 0 \\ 0 & -1 & 1 & \ddots & \vdots \\ \vdots & \ddots & \ddots & \ddots & 0 \\ 0 & \dots & 0 & -1 & 1 \end{bmatrix}_{(n_{PMi}-1) \times n_{PMi}} \quad (4.34)$$

$$\mathbf{D}_a = \begin{bmatrix} h_v(1) & 0 & \dots & 0 \\ 0 & \ddots & \ddots & \vdots \\ \vdots & \ddots & \ddots & 0 \\ 0 & \dots & 0 & h_v(n_{PMi}-2) \end{bmatrix}^{-1} \begin{bmatrix} -1 & 1 & 0 & \dots & 0 \\ 0 & -1 & 1 & \ddots & \vdots \\ \vdots & \ddots & \ddots & \ddots & 0 \\ 0 & \dots & 0 & -1 & 1 \end{bmatrix}_{(n_{PMi}-2) \times (n_{PMi}-1)} \quad (4.35)$$

with $h_p(\cdot)$ and $h_v(\cdot)$ being the temporal spacing between vector elements of \mathbf{p}_{PMi} and \mathbf{p}_{vi} , respectively (see Section 4.4 for more details). Thus, with the adoption of B-splines, the constrained optimization problem of Eq. (4.18) simplifies to

$$\begin{aligned} & \text{minimize } J_{contr}(\mathbf{p}_{PM1}, \mathbf{p}_{PM2}) \\ & \text{s.t.} \\ & \delta_c - \min(\mathbf{d}_i) \leq 0 \\ & \delta_{CV} - \min(\mathbf{d}_{i,CV}) \leq 0 \\ & \max(|\mathbf{p}_{vi}|) - v_{PM,\max} \leq 0 \\ & \max(|\mathbf{p}_{ai}|) - a_{PM,\max} \leq 0 \end{aligned} \quad (4.36)$$

reducing the number of optimization variables from n to n_{PMi} .

Even with the reduced number of optimization variables facilitated by down-sampling and the adoption of B-splines, the size of the \mathbf{p}_{PMi} vectors can still be problematic for numerical solvers. Fortunately, because of the local property of B-splines (as explained in Section 4.4), a windowing technique can be applied to solve the optimization problem sequentially as smaller sub-problems. Let MRi represent the MR regions in a scan trajectory for which the acceleration direction of the table is the same (i.e., the MR regions associated with a given PMi pair), and let u_i represent the total number of MRi regions in a scan trajectory. Then, for $j = \{1, 2, \dots, u_i - q_{win} + 1\}$, a subset of the \mathbf{p}_{PMi} vectors, covering the j th to $(j + q_{win} - 1)$ th MRi regions can be optimized at a time (or window), where q_{win} is the number of MRi regions being optimized in each window.

4.6 Numerical example

The performance and computational costs associated with three solution approaches – 1) direct solution with down-sampling using Eq. (4.18), 2) B-splines-based solution with down-sampling using Eq. (4.36), and 3) B-splines-based solution with down-sampling and windowing using Eq. (4.36) – are comparatively evaluated in simulations using a simple scan trajectory, x_T , with the number of MR regions related to PM1 and PM2 given by $u_1 = 5$ and $u_2 = 6$, respectively, as shown in Figure 4.6. Its scan velocity and maximum acceleration are respectively 0.8 m/s and 20 m/s². For the solution process, $l_T = 0$ is assumed, for simplicity, because it is a constant offset value that does not make a difference in obtaining the optimal trajectories. Based on the original sampling interval ($T_s = 0.1$ ms) of x_T , $n = 30,001$, which is prohibitively large for the direct solution. Therefore, x_T is down-sampled by a factor of 20 (i.e., $T_s = 2$ ms).

For the direct approach, the down-sampled x_T is used to solve for \mathbf{x}_{PM1} and \mathbf{x}_{PM2} vectors separately, after which the optimal solutions are up-sampled back to the original $T_s = 0.1$ ms resolution using cubic spline interpolation. For the B-spline-based approach, with and without the windowing, the same down-sampled x_T is used to solve for the optimal \mathbf{p}_{PM1} and \mathbf{p}_{PM2} vectors separately. For both cases, B-spline parameters $n_{PM1} = n_{PM2} = 301$ and $r = 4$, are employed; additionally, $q_{win} = 2$ is employed for the windowed B-spline technique. The optimal solutions found with the down-sampled x_T are up-sampled back to the original resolution with an \mathbf{N}_p matrix generated using $T_s = 0.1$ ms. The numerical solutions for all three techniques are performed using the *fmincon* function of MATLAB[®], running on a computer having a 2.3 GHz quad-core processor and 8 GB memory. The system parameters for the scanning stage, summarized in Table 4.1, are used for the simulations. Additionally, $w = 10^{-4}$, $\delta_c = 1$ mm and $\delta_{CV} = 14.3$ mm are employed in Eqs. (4.18) and (4.36). Note that $\delta_{CV} = 14.3$ mm is calculated using Eq. (4.11) based on a change of resonance frequency from 5.7 Hz to 5.8 Hz (i.e., $R = 2\%$), indicating negligible loss of transmissibility due to the PM-based ADs.

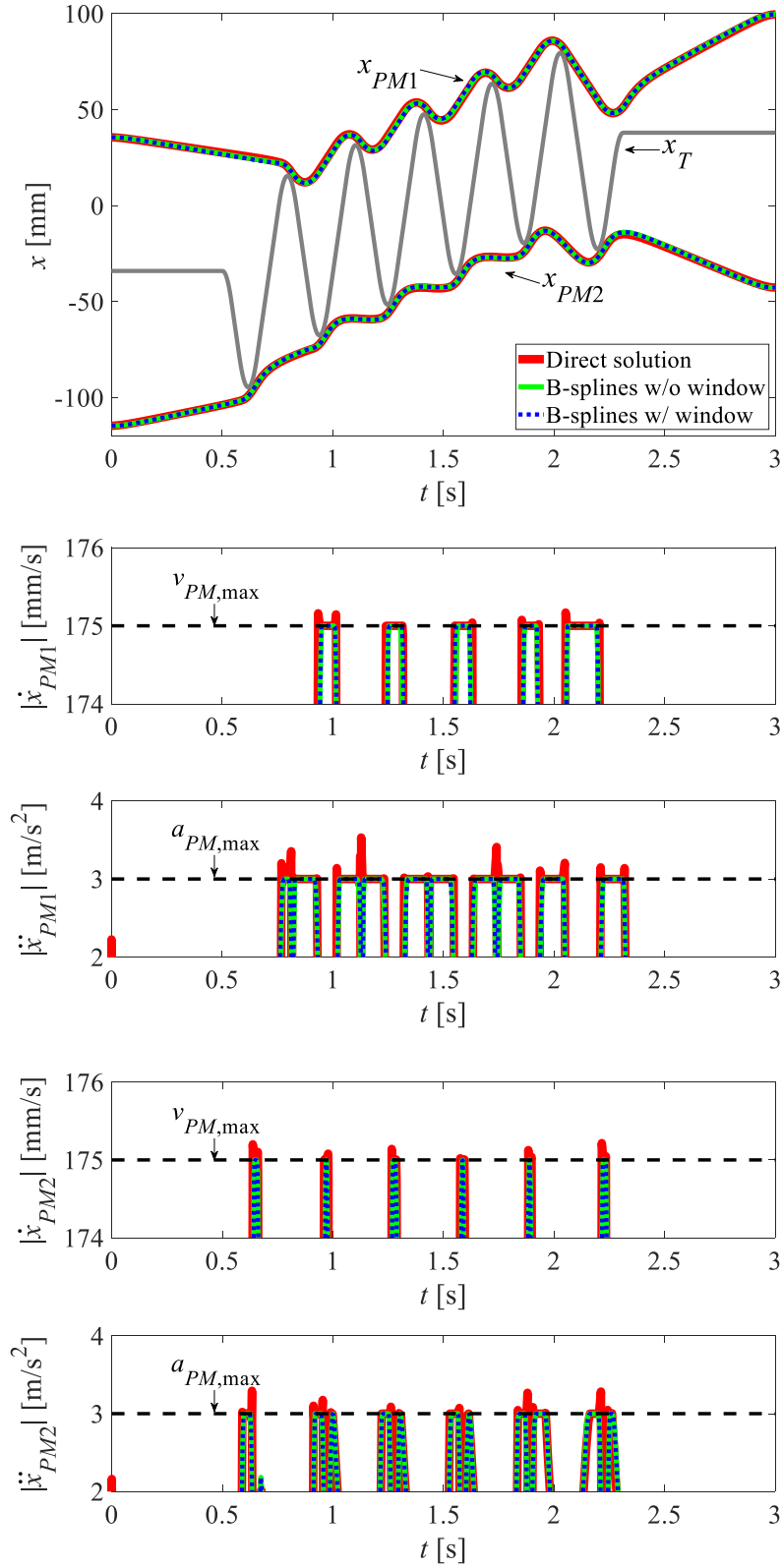


Figure 4.6 Optimal x_{PM1} and x_{PM2} , along with their time derivative profiles solved by three optimization approaches (direct, B-splines without windowing, and B-splines with windowing) in the original sampling resolution with $T_s = 0.1$ ms.

Figure 4.6 shows the optimal (up-sampled) x_{PMi} and their derivatives obtained by the three solution approaches, while the resulting computational times and optimal J_{contr} (based on the up-sampled vectors) are summarized in Table 4.2. Notice from Figure 4.6 that all x_{PMi} trajectories are very similar, and that the B-splines-based solutions are almost undistinguishable. However, the time derivative profiles of x_{PM1} show that while the kinematic constraints, $v_{PM,max} = 175$ mm/s and $a_{PM,max} = 3$ m/s², enforced during the optimization are satisfied by both B-spline-based solutions, are satisfied with both B-splines-based solutions, they are not satisfied by the direct approach after up-sampling; similar behaviors are observed for x_{PM2} . Notice from Table 4.2 that, even though the direct solution approach yields an optimal J_{contr} value that is only 0.4% lower than the J_{contr} values obtained using B-splines, it comes at the expense of significantly longer computation time and violation of constraints. Observe also that the B-spline technique with windowing achieves the same optimal J_{contr} values as the one without windowing, but its computational time is more than halved. Consequently, the windowed B-spline solution is adopted for the experimental validation of the PM-based ADs presented in following section.

Table 4.2. Comparison of computation times and objective function values (based on $T_s = 0.1$ ms) for the three optimization approaches (direct, B-splines without windowing, and B-splines with windowing).

	Direct	B-splines without windowing	B-splines with windowing
Computation time [s]	5,660	57	25
J_{contr} [N ²]	3.380×10^8	3.392×10^8	3.392×10^8

4.7 Experimental examples

The optimal control efforts allocation for the scanning stage designed in Chapter 3 is achieved with the optimal PM trajectories solved using the windowed B-splines approach presented in Section 4.5. The effectiveness of actively controlled PM-based ADs (i.e., active assist device, or AAD in short) is compared against the baseline (i.e., the case without PM-based ADs) and stationary PM-based ADs (i.e., passive assist device, or PAD in short) conditions, using two case studies from silicon wafer processing that reflect typical usage of scanning stages. To

determine the best locations for the stationary PM-based ADs (i.e., the PAD configuration), the constrained optimization shown in (4.36) is solved with $v_{PM,max} = a_{PM,max} = 0$.

The first case takes a representative scanning motion trajectory from photo-lithography process of 200 mm wafers. The second case uses a motion trajectory for silicon wafers topology inspection. For both cases, $T_s = 0.1$ ms is used for the actual stage implementation of the motion trajectories, but the optimization is carried out with 10 times down-sampling (i.e., $T_s = 1$ ms). The values of $w = 10^{-5}$, $\delta_c = 1$ mm, $\delta_{CV} = 14.3$ mm (corresponding to $R = 2\%$) are employed for both case studies.

4.7.1 Case study I: Scanning for photo-lithography

The first case study aims to replicate the scanning trajectories used in photo-lithography scanning processes of silicon wafers. A 200 mm diameter wafer with 25 mm \times 25 mm dies, shown in Figure 4.7, is assumed to be scanned using the step and scan profile shown in the figure. The scan portion (x -axis) of the trajectory, x_T , shown in Figure 4.8, has 0.5 m/s scan speed and 25 m/s² peak acceleration, with 25 ms settling time after each MR region; its step (y -axis) motions are not considered because they are outside the scope of this dissertation. The dotted lines inside the solid circle line of Figure 4.7, representing the boundary of wafer, are used to mark the edges of the dies. The scan tool (e.g., the light projection) starts its scanning from the upper left quadrant and ends the process at the lower right quadrant of the wafer. The beginning and ending portions of the trajectory are highlighted with blue dashed lines, revealing varying scanning strokes/positions, while the arrows are used to indicate the direction of scanning. The green colored squares indicate the dies being scanned during the trajectory portions highlighted in the figure.

The parameters for the windowed B-spline used to generate the optimal trajectories shown in Figure 4.8 are $n_{PM1} = n_{PM2} = 901$, $r = 5$ and $q_{win} = 2$, to ensure continuity up to the fourth derivative of x_{PMi} (i.e., snap). For simplicity, the averaged PM model parameters, $\alpha_{PM1} = \alpha_{PM2} = 1.10 \times 10^3$ N and $\beta_{PM1} = \beta_{PM2} = 2.45 \times 10^2$ m⁻¹, are used for the rest of this chapter.

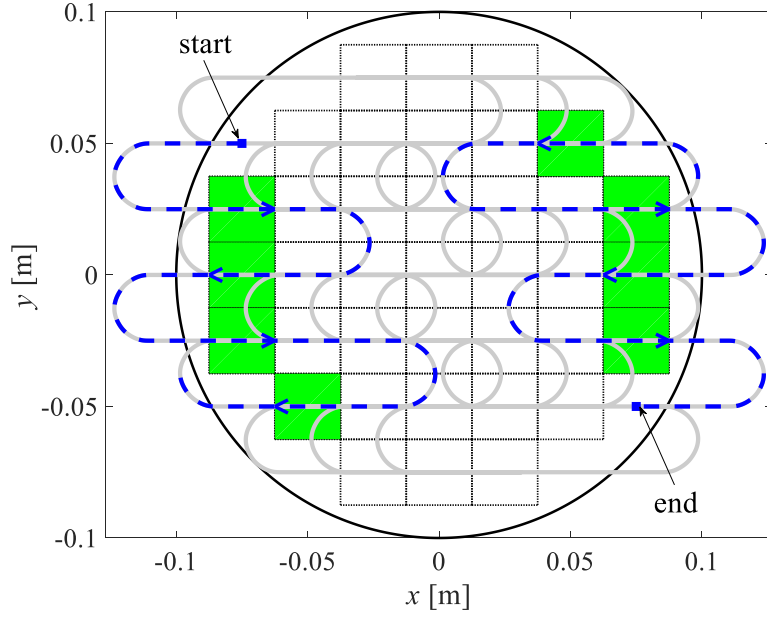


Figure 4.7 Step and scan profile for photo-lithography process of 200 mm silicon wafer.

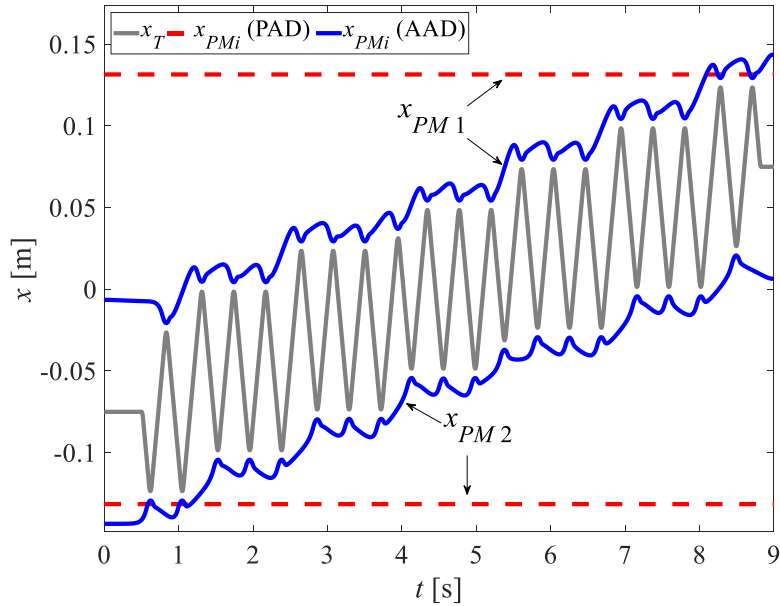


Figure 4.8 Scan trajectory of table and optimal PM trajectories for photo-lithography process of 200 mm silicon wafer.

The effectiveness of the optimal PM trajectories for the photo-lithography process scanning is shown in Figure 4.9. Three performance metrics are used to evaluate the comparative effectiveness of the PM-based ADs in the AAD configuration; they are: (1) the root-mean-square (RMS) values of \mathbf{f}_{LM} and \mathbf{f}_{RMi} , measured via the motor force commands; (2) the RMS values of the horizontal acceleration ($\mathbf{a}_{B,x}$), and the rotational acceleration ($\mathbf{a}_{B,\theta}$), of the isolated machine base,

measured using accelerometers (PCB Piezotronics, 393B05); and (3) the RMS value of the moving averaged (MA) position error within the CV regions (\mathbf{e}_{CV}) measured using the linear encoders. A moving average filter with the 10 ms width is utilized to filter the position error signal of table, as is common practice in wafer scanning applications (see Section 1.1). Table 4.3 summarizes the experimental results. With the AAD configuration, all the performance metrics improve over the Without AD case, except, obviously, in the terms of \mathbf{f}_{RMi} . Because the stationary PM-based ADs provide negligible assistance force for most of the scan positions and strokes, the PAD configuration does not improve the stage performance; the stage performance is virtually as same as the Without AD case. It must be noted that the tracking error is not zero even with the AAD configuration of the PMs is used, because vibration of the isolated base is still present; the base vibration and tracking error signals in Figure 4.9 show high correlation between the two signals. Another source of error is the model mismatch in the PM & disturbance force compensators of the feedforward controller (see Section 4.1). They create the MR region tracking errors and ripples (i.e., spikes) during the CV regions.

Table 4.3 Experimental results of scanning stage with photo-lithography process motion trajectory

	Without AD	With PAD	With AAD
RMS \mathbf{f}_{LM} [N]	161	157	102
RMS \mathbf{f}_{RM1} [N]	-	61	555
RMS \mathbf{f}_{RM2} [N]	-	28	528
RMS $\mathbf{a}_{B,x}$ [m/s ²]	0.570	0.539	0.385
RMS $\mathbf{a}_{B,\theta}$ [rad/s ²]	0.851	0.859	0.643
RMS MA(\mathbf{e}_{CV}) [nm]	93.7	93.5	74.7

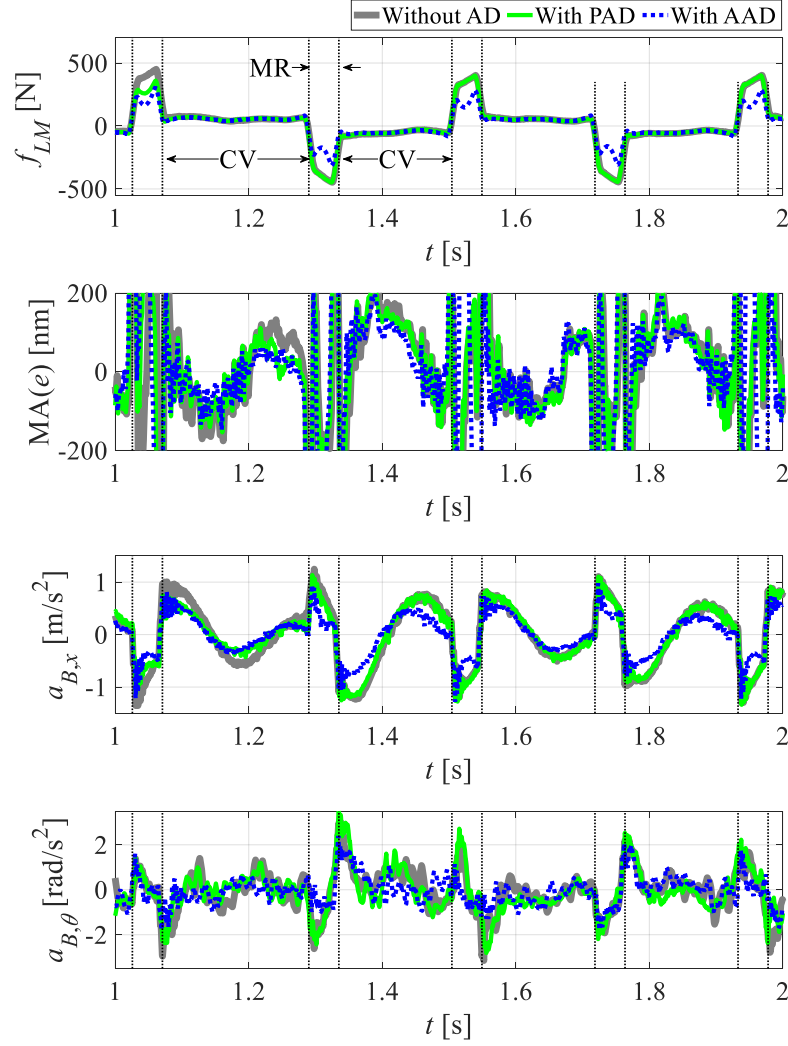


Figure 4.9 Measured signals for two configurations (Without and with AD) processing photo-lithography process motion trajectory.

4.7.2 Case study II: Scanning for wafer inspection

The second case study aims at replicating optical topology inspection processes of silicon wafers. Again, a 200 mm wafer diameter is used, but this time, its full length is scanned with 5 mm steps, as shown in Figure 4.10. Its scanning table trajectory, x_T , having 0.25 m/s scan speed and 10 m/s^2 peak acceleration with 50 ms settling time after each MR region is highlighted in Figure 4.11. The inspection tool starts its process from the bottom of wafer and ends at the top of the wafer. B-spline parameters, $n_{PM1} = n_{PM2} = 991$, $r = 5$ (for snap continuity) and $q_{win} = 2$, are used to generate the optimal PM trajectories (x_{PMi}).

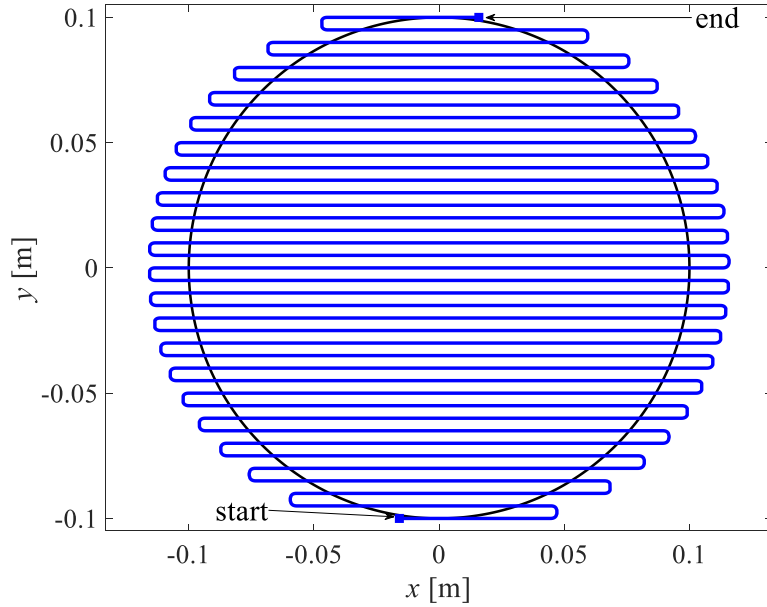


Figure 4.10 Step and scan profile for inspection of 200 mm silicon wafer.

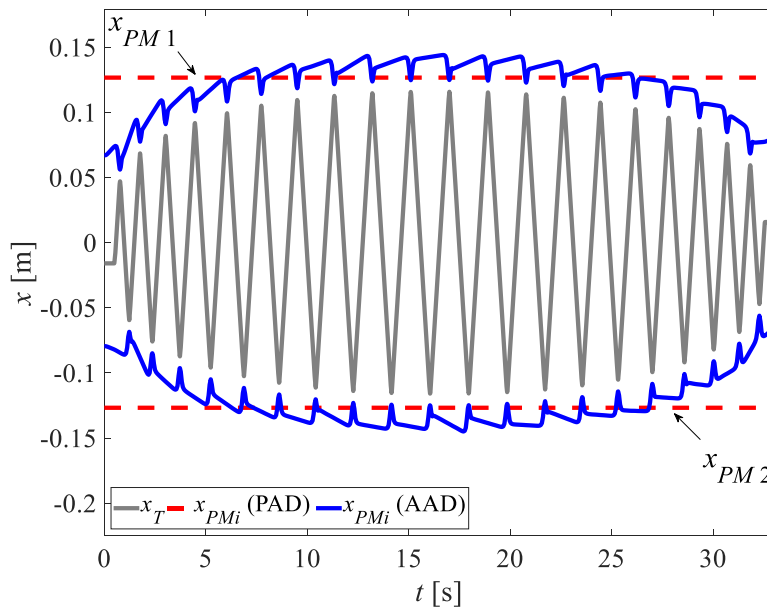


Figure 4.11 Scan trajectory of table and optimal PM trajectories for inspection of 200 mm silicon wafer.

The effectiveness of the optimal PM trajectories for wafer inspection scanning is shown in Figure 4.12. The same performance metrics as the photo-lithography scanning case are used to evaluate the comparative effectiveness of the PM-based ADs (the RMS metrics are summarized in Table 4.4). Like the photo-lithography scanning case, all the performance metrics (with the exception of f_{RMI}) improve from the Without the AD and the PAD cases.

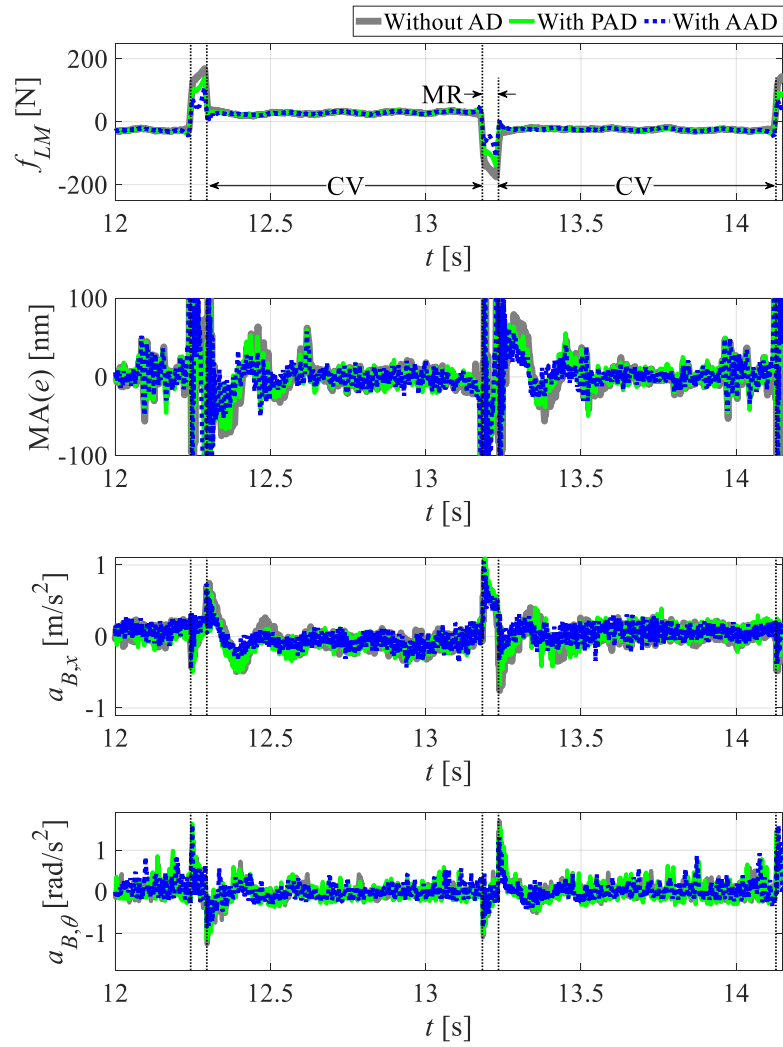


Figure 4.12 Measured signals for two configurations (Without and with AD) processing wafer topology inspection process motion trajectory.

Table 4.4 Experimental results of scanning stage with wafer topology inspection process motion trajectory.

	Without AD	With PAD	With AAD
RMS \mathbf{f}_{LM} [N]	45.1	42.3	31.1
RMS \mathbf{f}_{RM1} [N]	-	47	286
RMS \mathbf{f}_{RM2} [N]	-	22	289
RMS $\mathbf{a}_{B,x}$ [m/s ²]	0.201	0.191	0.164
RMS $\mathbf{a}_{B,\theta}$ [rad/s ²]	0.261	0.267	0.210
RMS MA(\mathbf{e}_{CV}) [nm]	20.7	19.2	13.6

4.7.3 Analysis of stage heat

The heat ($E_{heat,LM}$) generated by the LMs (note that two LM actuators in parallel are used to drive the scan table as shown in Figure 3.15) per scan cycle is given by

$$E_{heat,LM} = \frac{\mathbf{f}_{LM}^T \mathbf{f}_{LM}}{n_t \cdot K_{m,LM}^2} T_{tot} \quad (4.37)$$

where $K_{m,LM}$ is the equivalent motor constant of the LM pair in [N/(W)^{0.5}], n_t is the total number of sampled data for each scan cycle, which is 90,001 and 330,001 for Case studies I and II, and $T_{tot} = (n_t - 1)T_s$ is the total length of the trajectory, which is 9 s and 33 s, respectively. The equivalent motor constant for the LM pair, based on the motor specification provided by their manufacturer, is $K_{m,LM} = 21.40$ N/(W)^{0.5}. Accordingly, the LM heat generated per cycle for the Without AD, PAD, and AAD scenarios are 509 J, 484 J and 204 J for Case study I, and 167 J, 150 J, and 90 J for Case study II, respectively. In other words, the actively controlled PM-based ADs contribute a 60 % reduction in LM heat (in Case study I) and a 46% reduction in LM heat (in Case study II) over the Without AD scenarios, respectively. No information for calculating the heat of the RMs (stepper motors) is provided by their manufacturer. However, the relative impacts of the LM and RM heat can be visualized from the temperature distribution of the scan table and stage (shown in Figure 4.13), captured using an infrared (IR) thermometer (FLIR, E4 with 0.95 emissivity coefficient) after 40 consecutive scan cycles from thermal equilibrium at room temperature. It can be seen that, even though RMs heat up with repetitive assist motions of the PM-based ADs in the AAD configuration, their heat is locally confined and distant from the scan

table, even though no external cooling devices are employed. However, as seen in the IR images, the relatively large LM heat of the Without AD and PAD scenarios have a significant impact on the temperature gradient of the scan table, and hence could cause large thermal errors and other thermal problems such as hysteresis, drift, and creep, when compared to the AAD scenario (*Weck et al., 1995; Mayr et al., 2012*).

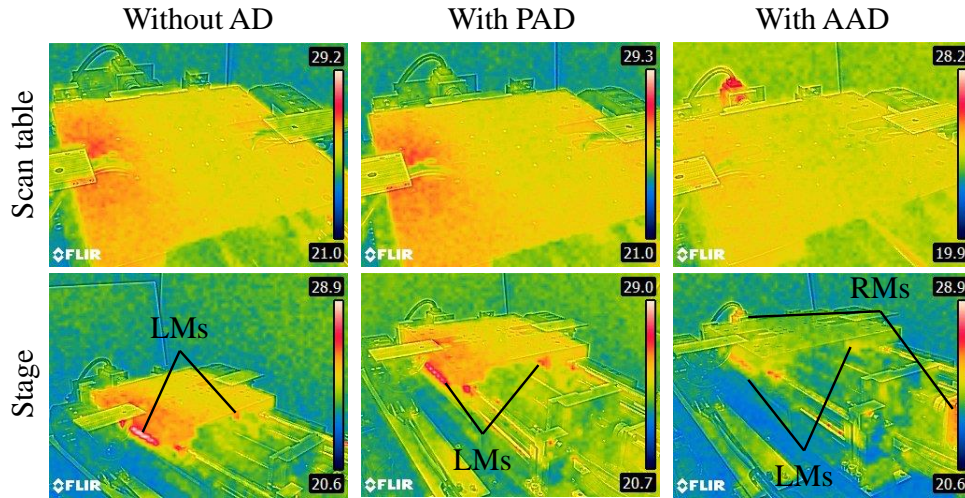
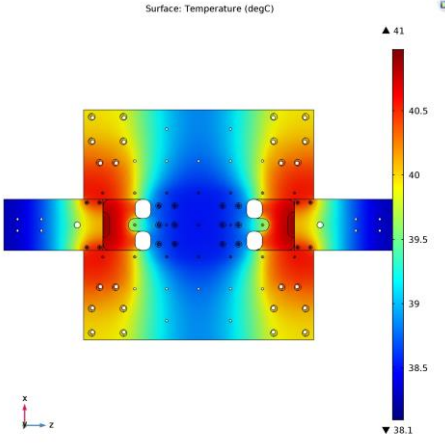
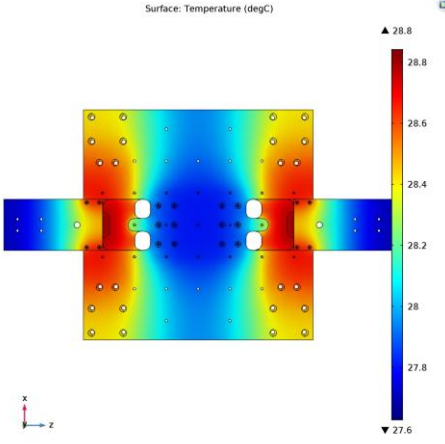
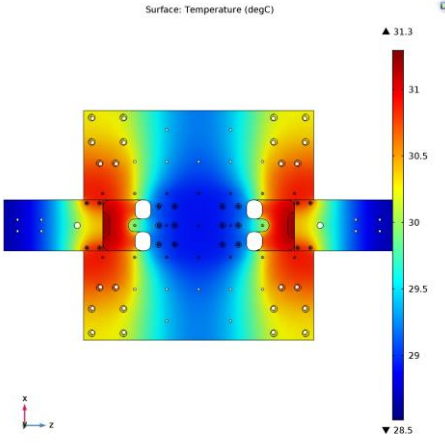
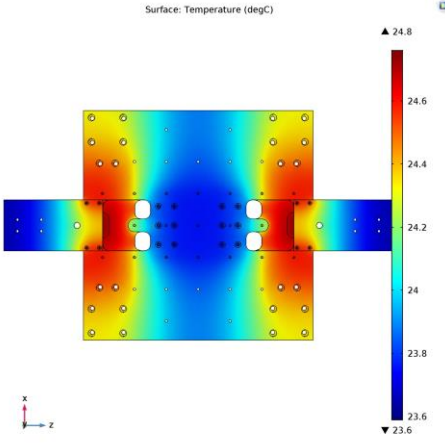
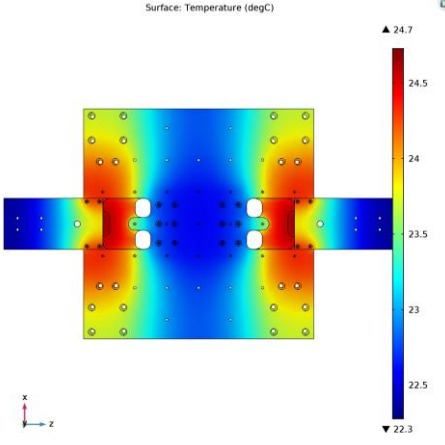
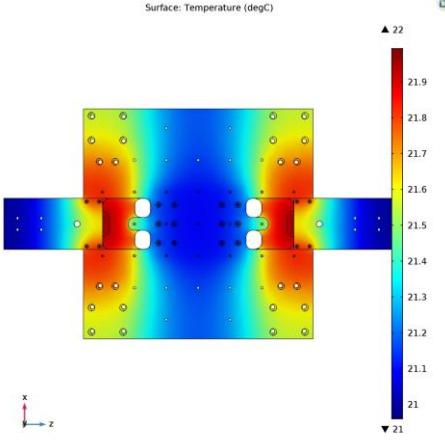


Figure 4.13 Surface temperature distribution of scan table and stage after 40 cycles of processing the photo-lithography scanning trajectory

Using the heat energy generated during scanning motions, the thermal equilibrium of the continuous use of scanning table can be estimated with an FEA software (i.e., COMSOL Multiphysics®). Table 4.5 compares the top views of table surface's temperature gradient when they reach the thermal equilibrium of continuous use for a range of assumed convective heat transfer coefficient (h). The range ($h = [5, 20]$ W/m²K) is based on a typical coefficient range for natural convection (i.e., without forced flow) of air (*Çengel and Boles, 2007*). Because the scanning motion of photo-lithography process from Case study I is more aggressive (i.e., its high acceleration/deceleration generates more heat), the wafer inspection scenario results are omitted, for the sake of brevity. The ambient temperature of 20°C is used throughout the simulation. It can be observed that the peak-to-peak surface temperature difference is more than halved when the actively controlled PM-based ADs are employed.

Table 4.5 Thermal equilibrium simulation of scanning table with the scanning motion for photo-lithography process with a range of convective heat transfer coefficients.

h [W/(m ² K)]	Without AD	With AAD
5		
10		
20		

4.8 Chapter summary

This chapter has tackled the question of how to best allocate control efforts among the actuators, via trajectory planning for the magnet assisted scanning stage designed and constructed in Chapter 3 to minimize heating and vibration. In order to preserve the vibration isolation performance during the manufacturing in CV regions, the PMs must be a safe distance away from the table during the manufacturing. The control efforts of three actuators – one linear motor and two rotary motors – are allocated using the optimal PM trajectories. In order to reduce computational burden during optimization, B-splines are used to represent the trajectories. The local property of B-splines is exploited to solve the optimization problem in smaller chunks. The effectiveness of the PM-based ADs is highlighted both numerically and experimentally using two wafer scanning scenarios – 1) photo-lithography scanning and 2) wafer inspection scanning. Up to 60% and 32% reductions in heat and vibration, respectively, are achieved when compared to the case without the proposed optimally controlled PM-based assist devices. Consequently, the measured tracking error during the CV regions is reduced by 20% and 34%, respectively, for the two manufacturing scenarios considered.

Chapter 5

Optimal Inversion-based Iterative Learning Control of Magnet Assisted Scanning Stage

The motor heat and vibration-induced tracking error are simultaneously mitigated with the optimal trajectory of PM-based ADs as shown in Chapter 4. Although significantly reduced, as seen in Section 4.7, some vibration-induced tracking errors still persist. One of the main causes for the residual tracking error is the mismatch between the system models and the actual system. For example, the dynamics of the isolation system is not considered during the PM trajectory optimization. In addition, the linear motor force is not zero; thus, creating residual vibration of the isolated base. In this chapter, exploiting the repeating nature of semiconductor manufacturing processes, an Iterative Learning Control (ILC) framework is proposed to learn the actual system dynamics in the iteration (i.e., trial) domain and create the optimal feedforward control signals that reduce the tracking error and still achieve the optimal control efforts allocation for the over-actuated magnet assisted scanning stage.

In Section 5.1, an overview of optimal inversion-based ILC for over-actuated systems is provided, highlighting the optimal control effort allocation and tunable learning convergence rate. Being a model-based approach, the inversion-based ILC is sensitive to modeling errors in guaranteeing monotonic convergence. A frequency-domain description of the model uncertainty is presented, and the knowledge of model uncertainty is considered during the ILC update law design procedure in Section 5.2. The proposed optimal inversion-based ILC framework for uncertain over-actuated systems has been validated with a linear system and key teachings are summarized in Section 5.3. In Section 5.4, the ILC framework is applied to the magnet assisted scanning stage, incorporating the nonlinear system dynamics (e.g., nonlinear PM-force curves) and input constraints (e.g., velocity and acceleration limits). In Section 5.5, an experimental case study, employing the photo-lithography scanning motion profile (shown in Section 4.7), is presented to highlight the effectiveness of the optimal inversion-based ILC.

This chapter is partially based on the following publication:

- Yoon D, Ge X, Okwudire C. *Optimal Inversion-based Iterative Learning Control for Over-Actuated Systems*. IEEE Transactions on Control Systems Technology. Under review.

5.1 Overview of optimal inversion-based ILC for over-actuated systems

The magnet assisted scanning stage is an over-actuated system. There are linear and rotary motors that provide actuation force to the scanning table, which is the only system output of interest. In this section, an inversion-based ILC approach, that achieves both the optimal control effort allocation and user-tunable learning convergence rate, is presented. This approach is presented in the broader context of linear systems.

5.1.1 Derivation of optimal inversion-based ILC update law

For over-actuated systems, the number of inputs, l , is larger than the number of outputs, m . The control input, $\mathbf{u} \in \mathfrak{R}^{lq \times 1}$, reference commands, $\mathbf{r} \in \mathfrak{R}^{mq \times 1}$, and full-rank model matrix for LTI system dynamics, $\mathbf{P} \in \mathfrak{R}^{mq \times lq}$, in the lifted domain with q discrete time steps are given as

$$\mathbf{u} = \begin{bmatrix} \mathbf{u}_1 \\ \vdots \\ \mathbf{u}_l \end{bmatrix}; \mathbf{r} = \begin{bmatrix} \mathbf{r}_1 \\ \vdots \\ \mathbf{r}_m \end{bmatrix}; \mathbf{P} = \begin{bmatrix} \mathbf{P}_{1,1} & \cdots & \mathbf{P}_{1,l} \\ \vdots & \ddots & \vdots \\ \mathbf{P}_{m,1} & \cdots & \mathbf{P}_{m,l} \end{bmatrix} \quad (5.1)$$

where the subscripts are used to denote the degrees of inputs, outputs and references, e.g., \mathbf{u}_1 denotes the control input vector of actuator 1. (See *Bristow et al., 2006* for construction of system dynamics matrices in the lifted domain). For the remainder of this chapter, bold upper- and lower-case symbols are respectively used to denote lifted domain matrices and discrete time domain column vectors. The tracking error, $\mathbf{e} \in \mathfrak{R}^{mq \times 1}$, is given as

$$\mathbf{e} = \mathbf{r} - (\mathbf{P}\mathbf{u} + \mathbf{n}) \quad (5.2)$$

where the output measurement noise, $\mathbf{n} \in \mathfrak{R}^{mq \times 1}$, is assumed to be $\mathbf{0}$ for the derivation of ILC update law in this section (the effects of $\mathbf{n} \neq \mathbf{0}$ are considered in Section 5.1.2). The tracking error of next iteration (i.e., $k + 1^{\text{st}}$ iteration) can be computed as shown in Eq. (5.3), with the subscripts denoting the iteration index.

$$\mathbf{e}_{k+1} = \mathbf{e}_k - \mathbf{P}(\mathbf{u}_{k+1} - \mathbf{u}_k) \quad (5.3)$$

The control effort is optimally allocated if a quadratic objective function, J , given as

$$J = \mathbf{u}_{k+1}^T \mathbf{S} \mathbf{u}_{k+1} \quad (5.4)$$

where \mathbf{S} is the user-selected control effort ratio matrix, is minimized for the next iteration subject to the user-prescribed tracking error of the next iteration. Thus, the tracking error is cast as the equality constraint using the error learning matrix, \mathbf{B} (*Harte et al., 2005*). The selection of \mathbf{B} specifies the error in the next iteration;

$$\mathbf{e}_{k+1} = (\mathbf{I} - \mathbf{B}) \mathbf{e}_k \quad (5.5)$$

where \mathbf{I} is the identity matrix. Enforcing the equality constraint of (5.5) on minimizing (5.4), the following optimization is obtained:

$$\begin{aligned} & \underset{\mathbf{u}_{k+1}}{\text{minimize}} \quad J = \mathbf{u}_{k+1}^T \mathbf{S} \mathbf{u}_{k+1} \\ & \text{s.t.} \quad (\mathbf{I} - \mathbf{B}) \mathbf{e}_k - \mathbf{e}_{k+1} = \mathbf{0} \end{aligned} \quad (5.6)$$

To solve the optimization problem given in (5.6), J is augmented with the Lagrange multiplier, λ^T ; thus, providing the augmented objective function, J_C .

$$J_C = \mathbf{u}_{k+1}^T \mathbf{S} \mathbf{u}_{k+1} + \lambda^T (\boldsymbol{\varepsilon} - \mathbf{P} \mathbf{u}_{k+1} + \mathbf{P} \mathbf{u}_k) \quad (5.7)$$

$$\boldsymbol{\varepsilon} = \mathbf{e}_k - \mathbf{e}_{k+1} = \mathbf{B} \mathbf{e}_k \quad (5.8)$$

By minimizing J_C , the optimal control input, \mathbf{u}_{k+1} , that satisfies the mapped tracking error, \mathbf{e}_{k+1} , can be found. The optimization solution is obtained by setting the partial derivatives of J_C with respect to \mathbf{u}_{k+1} and $\boldsymbol{\lambda}^T$ equal to $\mathbf{0}$;

$$\frac{\partial J_C}{\partial \mathbf{u}_{k+1}} = 2\mathbf{S}\mathbf{u}_{k+1} - \mathbf{P}^T\boldsymbol{\lambda} = \mathbf{0} \quad (5.9)$$

$$\frac{\partial J_C}{\partial \boldsymbol{\lambda}} = \boldsymbol{\varepsilon} - \mathbf{P}\mathbf{u}_{k+1} + \mathbf{P}\mathbf{u}_k = \mathbf{0} \quad (5.10)$$

Combining Eqs. (5.9) and (5.10), an expression for $\boldsymbol{\lambda}$ is obtained;

$$\boldsymbol{\lambda} = 2(\mathbf{P}\mathbf{S}^{-1}\mathbf{P}^T)^{-1}(\boldsymbol{\varepsilon} + \mathbf{P}\mathbf{u}_k) \quad (5.11)$$

Note the use of full rank matrix property of \mathbf{P} to obtain Eq. (5.11) from Eqs. (5.9) and (5.10), i.e., the system is based on the weighted pseudoinverse (*Horn and Johnson, 1985; Laub, 2005*). If \mathbf{P} is not full-rank, model approximation techniques can be used to resolve the inversion problem (*Ye and Wang, 2005; van Zundert and Oomen, 2018*). Equation (5.11) is substituted into Eq. (5.9) to solve for \mathbf{u}_{k+1} . As a result, the optimal inversion-based ILC update law is given as

$$\mathbf{u}_{k+1} = \mathbf{S}^{-1}\mathbf{P}^T(\mathbf{P}\mathbf{S}^{-1}\mathbf{P}^T)^{-1}(\mathbf{B}\mathbf{e}_k + \mathbf{P}\mathbf{u}_k) \quad (5.12)$$

The ILC update law can be separated into two learning gains, \mathbf{L}_U and \mathbf{L}_E , to be applied to the input and tracking error vectors from the previous iteration, respectively (*Bristow et al., 2006*);

$$\mathbf{u}_{k+1} = \mathbf{L}_U\mathbf{u}_k + \mathbf{L}_E\mathbf{e}_k \quad (5.13)$$

where \mathbf{L}_U and \mathbf{L}_E are given as

$$\mathbf{L}_U = \mathbf{S}^{-1} \mathbf{P}^T (\mathbf{P} \mathbf{S}^{-1} \mathbf{P}^T)^{-1} \mathbf{P} \quad (5.14)$$

$$\mathbf{L}_E = \mathbf{S}^{-1} \mathbf{P}^T (\mathbf{P} \mathbf{S}^{-1} \mathbf{P}^T)^{-1} \mathbf{B} \quad (5.15)$$

This inversion-based ILC update law, incorporating the user-selected input ratio and convergence rate, allows non-causal and optimal allocation of control inputs using the model of plant dynamics and input/output measurements from the previous iteration.

The proposed optimal inversion-based (Opt-In for short) ILC selects the control input that minimizes the control efforts (i.e., two-norm of input signal vectors) from infinitely many input candidates. Consequently, the goal of the optimal inversion-based ILC is as same as the PM trajectory optimization framework presented in Chapter 4, as the both methods seek to minimize the control efforts (i.e., motor force) subject to the modeled system dynamics. In addition to the control efforts allocation, the ILC approach enables the learning of system dynamics (both modeled and unmodeled), such that the tracking performance improves over iterations.

5.1.2 Tunable monotonic error convergence rate of optimal inversion-based ILC

With the tracking error mapping matrix, \mathbf{B} , the tracking error convergence rate can be explicitly specified by the user. For monotonic convergence of tracking error, the following inequality must be satisfied;

$$\|\mathbf{I} - \mathbf{B}\|_2 < 1 \quad (5.16)$$

where $\|\cdot\|_2$ denotes the two-norm of a matrix inside the operator, i.e., the largest singular value of the matrix (*Laub, 2005*). A simple way of specifying the error convergence rate is to select $\mathbf{B} = b\mathbf{I}$, where b is a user-selected gain for directly controlling the matrix norm of $(\mathbf{I} - \mathbf{B})$. For instance, the ILC update converges with only one iteration, if the model and plant have matching dynamics and $b = 1$ (*Harte et al., 2005*).

In this section, the effect of bounded output measurement noise on the tracking performance of Opt-In ILC is analyzed since the noise is not explicitly considered during the ILC update law derivation in Section 5.1.1. More in-depth analysis accounting for iteration-varying

disturbances can be carried out following the procedures in (Gunnarsson, and Norrlöf, 2006; Oomen and Rojas, 2017). Substituting Eq. (5.2) into the ILC update law given in Eq. (5.13), the control input of next iteration, under the presence of noise, is computed as

$$\mathbf{u}_{k+1} = (\mathbf{L}_U - \mathbf{L}_E \mathbf{P}) \mathbf{u}_k + \mathbf{L}_E \mathbf{r} - \mathbf{L}_E \mathbf{n}_k \quad (5.17)$$

where \mathbf{n}_k is the iteration-varying noise signal. Assuming $\mathbf{B} = b\mathbf{I}$ with $0 < b < 2$ to satisfy the condition given in Eq. (5.16), the tracking error due to the output measurement noise can be iteratively computed. Based on the initial iteration tracking error, \mathbf{e}_1 , and control input, \mathbf{u}_1 , the second iteration control input, \mathbf{u}_2 , and tracking error, \mathbf{e}_2 , are respectively computed as

$$\mathbf{u}_2 = (1-b)\mathbf{L}_U \mathbf{u}_1 + \mathbf{L}_E (\mathbf{r} - \mathbf{n}_1) \quad (5.18)$$

$$\mathbf{e}_2 = (1-b)\mathbf{r} - (1-b)\mathbf{P}\mathbf{u}_1 + b\mathbf{n}_1 - \mathbf{n}_2 \quad (5.19)$$

Advancing another iteration, the control input and tracking error become

$$\mathbf{u}_3 = (1-b)^2 \mathbf{L}_U \mathbf{u}_1 + (1-b)\mathbf{L}_E (\mathbf{r} - \mathbf{n}_1) + \mathbf{L}_E (\mathbf{r} - \mathbf{n}_2) \quad (5.20)$$

$$\mathbf{e}_3 = (1-b)^2 \mathbf{r} - (1-b)^2 \mathbf{P}\mathbf{u}_1 + (1-b)b\mathbf{n}_1 + b\mathbf{n}_2 - \mathbf{n}_3 \quad (5.21)$$

and so on. For further analysis, suppose the noise signal as Gaussian white with standard deviation, σ_k . Using the root sum square method of standard deviation of noise signals (Devore, 2011), the steady-state tracking error is quantified with

$$\text{stdev}(\mathbf{e}_\infty) = \sqrt{\sigma^2 + b^2 \sigma^2 + (1-b)^2 b^2 \sigma^2 + (1-b)^4 b^2 \sigma^2 + \dots} \quad (5.22)$$

where the $\text{stdev}(\cdot)$ operator computes the standard deviation of signal in its argument and $\sigma = \sigma_1 = \sigma_2 = \dots$ is assumed. The geometric series shown in Eq. (5.22) becomes

$$\text{stdev}(\mathbf{e}_\infty) = \sqrt{\frac{2}{2-b}}\sigma \quad (5.23)$$

providing an analytical expression for quantifying the steady-state tracking error. Because the presumed noise signal is Gaussian, the standard deviation and RMS value are the same; i.e.,

$$\text{RMS}(\mathbf{e}_\infty) = \sqrt{\frac{2}{2-b}}\sigma \quad (5.24)$$

If the fastest error convergence rate is selected (i.e., $b = 1$), the RMS value of steady-state tracking error is amplified by a factor of $\sqrt{2}$ relative to the RMS value of the noise signal. The effect of noise on \mathbf{e}_∞ decreases as b approaches 0 at the expense of convergence rate. Both the tracking error and convergence rate deteriorate simultaneously if $b > 1$. Therefore, if slower convergence is acceptable, $b < 1$ should be selected because $b > 1$ amplifies measurement noise.

5.2 Incorporation of system model uncertainty

In general applications, the actual plant dynamics, \mathbf{P}_T , is different from the nominal model, and the stability of ILC is based on the learning gains, \mathbf{L}_U and \mathbf{L}_E . To guarantee ILC update stability when the actual plant dynamics is concerned (i.e., robust monotonic convergence), the following inequality must be satisfied (*Bristow et al., 2006*);

$$\|\mathbf{L}_U - \mathbf{L}_E \mathbf{P}_T\|_2 < 1 \quad (5.25)$$

However, when the model deviates a lot from the actual plant, the convergence rate may be adversely affected, and the ILC update stability criterion in (5.25) may not be satisfied unless a Q -filter is employed (*Bristow et al., 2006*). Numerous ways to represent model uncertainty for incorporation into the ILC update law design have been investigated (*Van de Wijdeven et al., 2009; De Roover and Bosgra, 2010; Ge et al., 2018*). It is proposed to adopt a frequency domain method to express system model uncertainties using both the magnitude and phase bounds of FRF (*Ge et al., 2018*). This way, the use of large matrices for ILC performance analysis, which requires large

computational power, is avoided. The adopted FRF based model uncertainty description is used to determine the optimal nominal model and Q -filter for Opt-In ILC, that minimize the steady-steady error.

For sufficiently long time-intervals, the lifted domain matrix for a SISO system can be approximated by its frequency response function (FRF) via discrete Fourier transform (DFT); in which case, inverse discrete Fourier transform (IDFT) is used to transform from frequency back to the time domain (*Gorinevsky, 2002; Van de Wijdeven et al., 2009*). For the remainder of this chapter, upper-case italic letters are used to denote the equivalent FRFs of the system dynamics described by bold upper-case letters (i.e., lifted domain matrices). For example,

$$P_{1,1}(e^{j\theta}) \underset{IDFT}{\overset{DFT}{\rightleftharpoons}} \tilde{\mathbf{P}}_{1,1} \cong \mathbf{P}_{1,1} \quad (5.26)$$

where θ represent frequency and \sim is used to denote the approximation. The FRF matrices represent the MIMO system dynamics; e.g.:

$$P(e^{j\theta}) = \begin{bmatrix} P_{1,1}(e^{j\theta}) & \dots & P_{1,l}(e^{j\theta}) \\ \vdots & \ddots & \vdots \\ P_{m,1}(e^{j\theta}) & \dots & P_{m,l}(e^{j\theta}) \end{bmatrix} \quad (5.27)$$

For the nominal SISO FRF, $P_{1,1}$, the FRF of the actual plant, $P_{T,1,1}$, can lie anywhere between the upper and lower bounds of the system model uncertainty. The solid black lines of the Bode plot shown in Figure 5.1(a) represent the upper and lower bounds of the uncertainty for the magnitude and the phase, respectively. The gray shaded regions in between the solid lines represent models within the uncertainty bounds. At each discretized frequency, the magnitude and the phase uncertainties can be used to construct a set of system model candidates, $P_{C,1,1}$, on the Nyquist plot, as shown in Figure 5.1 (b). The blue squares shown on Figure 5.1 (b) represent the elements of $P_{C,1,1}$ at the frequency highlighted by the red solid lines in Figure 5.1 (a) (*Ge et al., 2018*). Thus, at each frequency, $\theta_i; i = 1, 2, \dots, q$, the following inequalities hold;

$$Mag_{\min,1,1}(e^{j\theta_i}) \leq |P_{T,1,1}(e^{j\theta_i})| \leq Mag_{\max,1,1}(e^{j\theta_i}) \quad (5.28)$$

$$Phase_{\min,1,1}(e^{j\theta_i}) \leq \angle P_{T,1,1}(e^{j\theta_i}) \leq Phase_{\max,1,1}(e^{j\theta_i}) \quad (5.29)$$

where $|\cdot|$ and \angle are used to denote the magnitude and phase of a complex number, respectively. The magnitude and phase uncertainty bounds are represented with $Mag_{\min,1,1} \in \mathfrak{R}$, $Mag_{\max,1,1} \in \mathfrak{R}$, $Phase_{\min,1,1} \in \mathfrak{R}$ and $Phase_{\max,1,1} \in \mathfrak{R}$. Note that the number of discretized frequencies is denoted by q , which is the length of the reference trajectory (Gorinevsky, 2002).

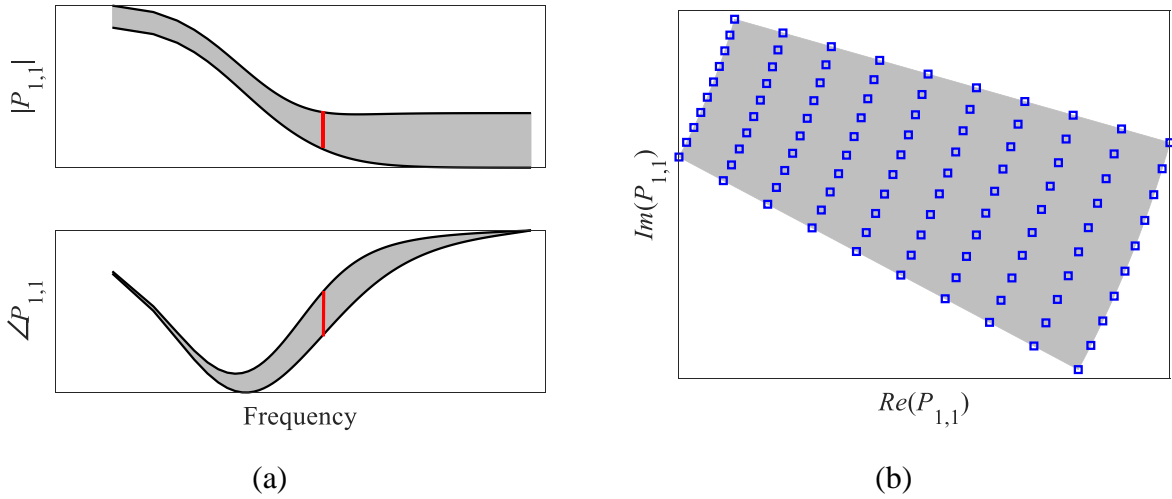


Figure 5.1 (a) Bode plot for illustrating system model uncertainty, (b) mesh grid for system model candidates on Nyquist plot at frequency highlighted in (a). In this illustration, P_C consists of 100 elements (i.e., grid points).

In order to generate the ILC update law (i.e., \mathbf{L}_U and \mathbf{L}_E and their equivalent frequency domain matrices, L_U and L_E) and robustness filter (Q -filter), the plant model must be available. Following the system model uncertainty definitions described above, the optimal plant model, P , can be selected to satisfy the robust monotonic convergence (RMC) criterion and minimize the steady-state tracking error. In case the RMC constraint in Eq. (5.25) cannot be satisfied by the selection of optimal P alone, the Q -filter can be incorporated. Note that the steady-state tracking error, E_∞ , is given as (Bristow et al., 2006)

$$E_\infty(e^{j\theta_i}) = \left[I - \underbrace{P_C (I - QL_U + QL_E P_C)^{-1} QL_E}_H \right] R \quad (5.30)$$

where the frequency argument, $e^{j\theta_i}$, is omitted in Q , L_U , L_E , R and P_C , for the sake of conciseness. The following constrained optimization is solved to minimize the tracking errors against the worst-case uncertainty at each frequency, θ_i , using the set of model candidates, P_C :

$$\begin{aligned} \text{minimize}_{P, Q} J_s &= \max \left(\left[I - H(P, Q) \right]^T \left[I - H(P, Q) \right] \right) \\ \text{s.t.} \quad & \left\| Q \left[L_U(P) - L_E(P) P_C \right] \right\|_2 < \frac{1}{\gamma} \end{aligned} \quad (5.31)$$

where $\max(\cdot)$ operator computes the maximum value of the set and $\gamma \geq 1$ is the safety factor that helps account for the approximations involved in DFT. The robust ILC update laws, L_U and L_E , are obtained with the optimal P such that they provide monotonically convergent update with the minimum steady-state tracking error; i.e.,

$$u_{k+1} = Q(L_U u_k + L_E e_k) \quad (5.32)$$

In MIMO systems, there are $m \times l$ input-output relationships; therefore, a full factorial design must be taken to construct P_C for the MIMO system optimization. In other words,

$$P_C = \left\{ P_{C,1}, P_{C,2}, \dots, P_{C, (v_M)^{m \cdot l} \cdot (v_P)^{m \cdot l}} \right\} \quad (5.33)$$

where v_M and v_P are the number of discrete grid points used to represent the magnitude and phase uncertainties, respectively (see Figure 5.1(b) for an illustration where $v_M = v_P = 10$, totaling 100 grid points for each frequency):

5.3 Validation of optimal inversion-based ILC using a coarse-fine stage testbed

The Opt-In ILC for over-actuated system presented in Sections 5.1 and 5.2 has been validated using a coarse-fine stage testbed. Both numerical and experimental studies are conducted to highlight the strength and effectiveness of the proposed approach. The results are summarized in Appendix C and important teachings are:

- Opt-In ILC allocates the control efforts to the actuators with user-specified weights and system models. The weights can be selected to minimize heat.
- The simple way of specifying the error convergence rate presented in Section 5.1.2 ($\mathbf{B} = b\mathbf{I}$) requires $b \leq 1$ as not to amplify the system output measurement noise, which is bound to occur in practice.
- Optimal selections of plant model for inversion and robustness filter (i.e., Q -filter), with the knowledge of system model uncertainty, enable the learning of the system dynamics in wider ranges of frequency. The solved ILC update law is less conservative than the one based on intuition. Consequently, the steady-state tracking error is reduced, when compared to the conservative selections of model and robustness filter.

5.4 Application of optimal inversion-based ILC to magnet assisted scanning stage

The model for the magnet assisted scanning stage for the purpose of optimal allocation of control efforts (presented in Section 4.2) assumes that the isolated base displacement is negligible during the scanning motions, because x_B is much smaller than x_T . This leads to the assumption that the table displacement (x_T) is as same as the tool/workpiece displacement (x), which is measured by sensors (i.e., linear encoders), for the subsequent trajectory optimization. This assumption of stationary base ($x_B = 0$) is reasonable for the purpose of control efforts allocation as seen in Chapter 4. However, to achieve the tracking performance with the nm-level precision, the vibration of the base (even if in the order of μm) needs to be accurately captured and effectively suppressed. However, modeling the vibration behavior of isolated base with such high accuracy and precision can be troublesome because the pneumatic vibration isolators with leveling devices employed in the scanning stage show nonlinear and parameter-varying behavior as a function of x_B , i.e., magnitude of excitation (Ryaboy, 2014). Additionally, the identified model parameters for the PM

trajectory optimization and the feedforward controller (e.g., cable carrier disturbance, motor force ripple, PM force curve, etc.) have uncertainties.

In this section, the unmodeled dynamics behavior of stage and the model mismatch are learned to provide better tracking performance, using the teachings of the Opt-In ILC approach presented in Sections 5.1 and 5.2. The proposed approach from the previous sections assumes no input constraints and linear system dynamics, which cannot be directly applied to the magnet assisted scanning stage. For example, the stage has nonlinear magnetic force-distance relationships (as shown in Figure 4.3) and there are input constraints such as the PM trajectory velocity and acceleration limits, which are discussed in Section 4.3. Thus, the stage model is revisited to find an optimal inversion-based ILC approach that can handle the system nonlinearities and the input constraints.

A two-stage process is used to deal with the nonlinearities and the input constraints. The total actuation force, consisting of the linear motor and the permanent magnet forces, are calculated based on an ILC framework similar to the approach presented in Sections 5.1 and 5.2 above. Then, the combined force is distributed (i.e., allocated) using an approach similar to the approach used in Chapter 4, based on knowledge of the system dynamics. This is analogous to the squaring method for non-square MIMO system (*Van Zundert and Oomen, 2018*)

Let us first consider the stage dynamics, described with the block diagram shown in Figure 5.2, which includes both the table and the isolated base. The tool/workpiece displacement (x) is measured using linear encoders, by taking the difference between the table and base displacements;

$$x = x_T - x_B \quad (5.34)$$

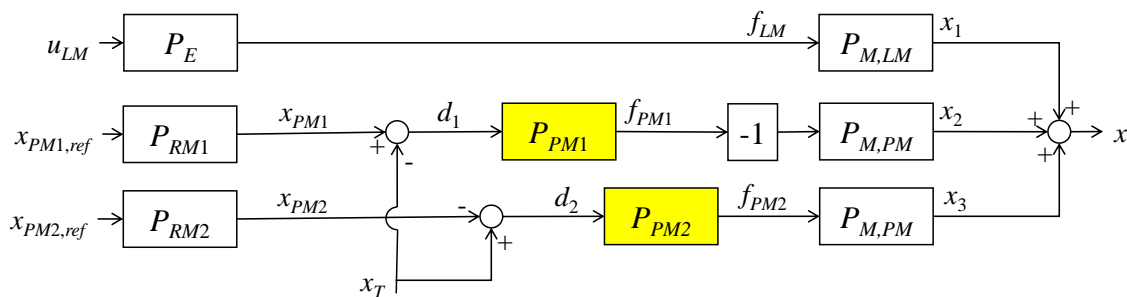


Figure 5.2 Dynamics model of the magnet assisted scanning stage; yellow blocks indicate nonlinear transfer functions (i.e., nonlinear magnetic force and distance relationships).

The blocks in Figure 5.2 denote the transfer functions. The tool or workpiece displacement can be controlled by three actuators – one linear motor (LM) and two rotary motors (RMs). The LM force command (u_{LM}) passes through the amplifier's electrical dynamics, described by P_E , to generate the actual LM force (f_{LM}). The generated LM force directly drives the tool or workpiece displacement via $P_{M,LM}$. On the other hand, the PM reference trajectories ($x_{PMi,ref}$ where $i = 1, 2$) pass through the RM servo dynamics, described by P_{RMi} , to generate the actual PM displacement (x_{PMi}), creating the distance (d_i) between the table (x_T) and PM (x_{PMi}). The PM repulsion force is, then, generated based on the distance, with the nonlinear relationships given in P_{PMi} , subsequently driving the tool or workpiece displacement via $P_{M,PM}$. Assuming linear system dynamics of the stage described with $P_{M,LM}$ and $P_{M,PM}$, the three displacements (x_1 , x_2 and x_3) are summed as shown with the block diagram in Figure 5.2. Yellow blocks are used to indicate the nonlinear transfer functions (i.e., the nonlinear magnetic force and distance relationships).

The stage dynamics ($P_{M,LM}$ and $P_{M,PM}$) are further described with a two-mass model, consisting of the base and table, connected with springs/dampers/forces as shown in Figure 5.3. The two PM forces are summed and replaced with one PM force ($f_{PM} = f_{PM1} + f_{PM2}$), because the two PMs are not engaged with the table simultaneously by design. For the purpose of dynamics analysis, the ground vibration (x_G) is ignored and the vibration isolation system is described with a spring/damper system, with stiffness (k_B) and damping coefficient (b_B). Between the isolated base and table, only the damping (with coefficient, b_T) exists. The LM provides the equal and opposite direction force between the base and table. The PM force is directly applied to the table from the ground, bypassing the isolated base.

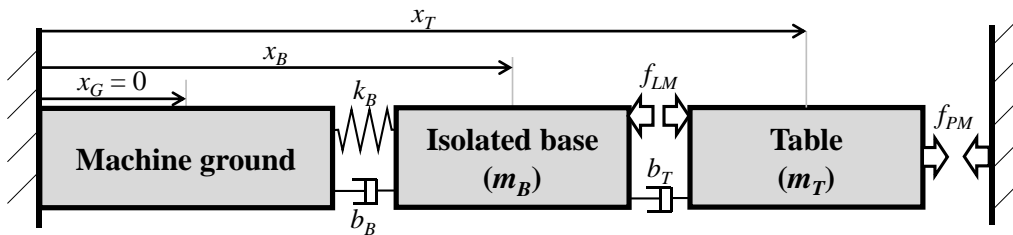


Figure 5.3 Schematic of the magnet assisted scanning stage for the purpose of ILC model analysis.

The equation of motion for the linear system described with Figure 5.3 above is given as

$$\begin{bmatrix} m_B & 0 \\ 0 & m_T \end{bmatrix} \begin{bmatrix} \ddot{x}_B \\ \ddot{x}_T \end{bmatrix} + \begin{bmatrix} b_B + b_T & -b_T \\ -b_T & b_T \end{bmatrix} \begin{bmatrix} \dot{x}_B \\ \dot{x}_T \end{bmatrix} + \begin{bmatrix} k_B & 0 \\ 0 & 0 \end{bmatrix} \begin{bmatrix} x_B \\ x_T \end{bmatrix} = \begin{bmatrix} -1 \\ 1 \end{bmatrix} f_{LM} + \begin{bmatrix} 0 \\ 1 \end{bmatrix} f_{PM} \quad (5.35)$$

Following transfer functions are generated based on Eq. (5.35);

$$P_{T,LM} = \frac{x_T}{f_{LM}} = \frac{m_B s^2 + b_B s + k_B}{m_B m_T s^4 + (b_T m_T + b_B m_T + b_T m_B) s^3 + (b_B b_T + k_B m_T) s^2 + b_T k_B s} \quad (5.36)$$

$$P_{T,PM} = \frac{x_T}{f_{PM}} = \frac{m_B s^2 + (b_B + b_T) s + k_B}{m_B m_T s^4 + (b_T m_T + b_B m_T + b_T m_B) s^3 + (b_B b_T + k_B m_T) s^2 + b_T k_B s} \quad (5.37)$$

$$P_{B,LM} = \frac{x_B}{f_{LM}} = \frac{-m_T s}{m_B m_T s^3 + (b_B m_T + b_T m_B + b_T m_T) s^2 + (b_B b_T + k_B m_T) s + b_T k_B} \quad (5.38)$$

$$P_{B,PM} = \frac{x_B}{f_{PM}} = \frac{b_T}{m_B m_T s^3 + (b_B m_T + b_T m_B + b_T m_T) s^2 + (b_B b_T + k_B m_T) s + b_T k_B} \quad (5.39)$$

where the subscripts T and B denote the table and base, respectively. The linear encoders measure the displacement (x), thus the transfer functions for the stage dynamics ($P_{M,LM}$ and $P_{M,PM}$) are given as

$$P_{M,LM} = P_{T,LM} - P_{B,LM} \quad (5.40)$$

$$P_{M,PM} = P_{T,PM} - P_{B,PM} \quad (5.41)$$

The Bode plots of the transfer functions, given in Eqs. (5.36) – (5.42) above, are shown in Figure 5.4 with the model parameters identified from Chapter 4. Figure 5.4 (a) shows the Bode plots when the table displacement is taken as the output of interest; the LM and PM forces have similar effectiveness in creating the table displacement. Figure 5.4 (b) shows the Bode plots when the base displacement is taken as the output of interest. For the most of frequency range, PM force is more effective in reducing the base displacement (i.e., vibration). As can be seen from Figure 5.4 (b) and Eqs. (5.38) and (5.39), the PM force induces larger magnitude of base vibration at a low frequency range ($< \sim 1$ Hz). In fact, Eq. (5.39) indicates that $P_{B,PM}$ has a finite DC gain ($1/k_B$), because the PM force is between the ground and table. This DC gain, however, should not be of a

concern, because the PMs are not designed to provide the low-frequency force components (i.e., frequency approaching the DC component) for tracking. The PM is meant to deliver inertial loads during high acceleration/deceleration for MR regions, which contain high-frequency range components. Figure 5.4 (c) shows the Bode plots when the tool/workpiece displacement is taken as the output of interest. All the units used for the magnitude in Figure 5.4 (a) – (c) are [m/N]. Figure 5.4 (d) shows the difference between $P_{M,LM}$ and $P_{B,PM}$ where the LM and PM are respectively used as the input. The difference between the two transfer functions is very small. The phase difference is negligible across the frequency range, except near the resonance of the vibration isolation system. As the frequency increases, the magnitude difference approaches the mass ratio between the table and base, which is also small.

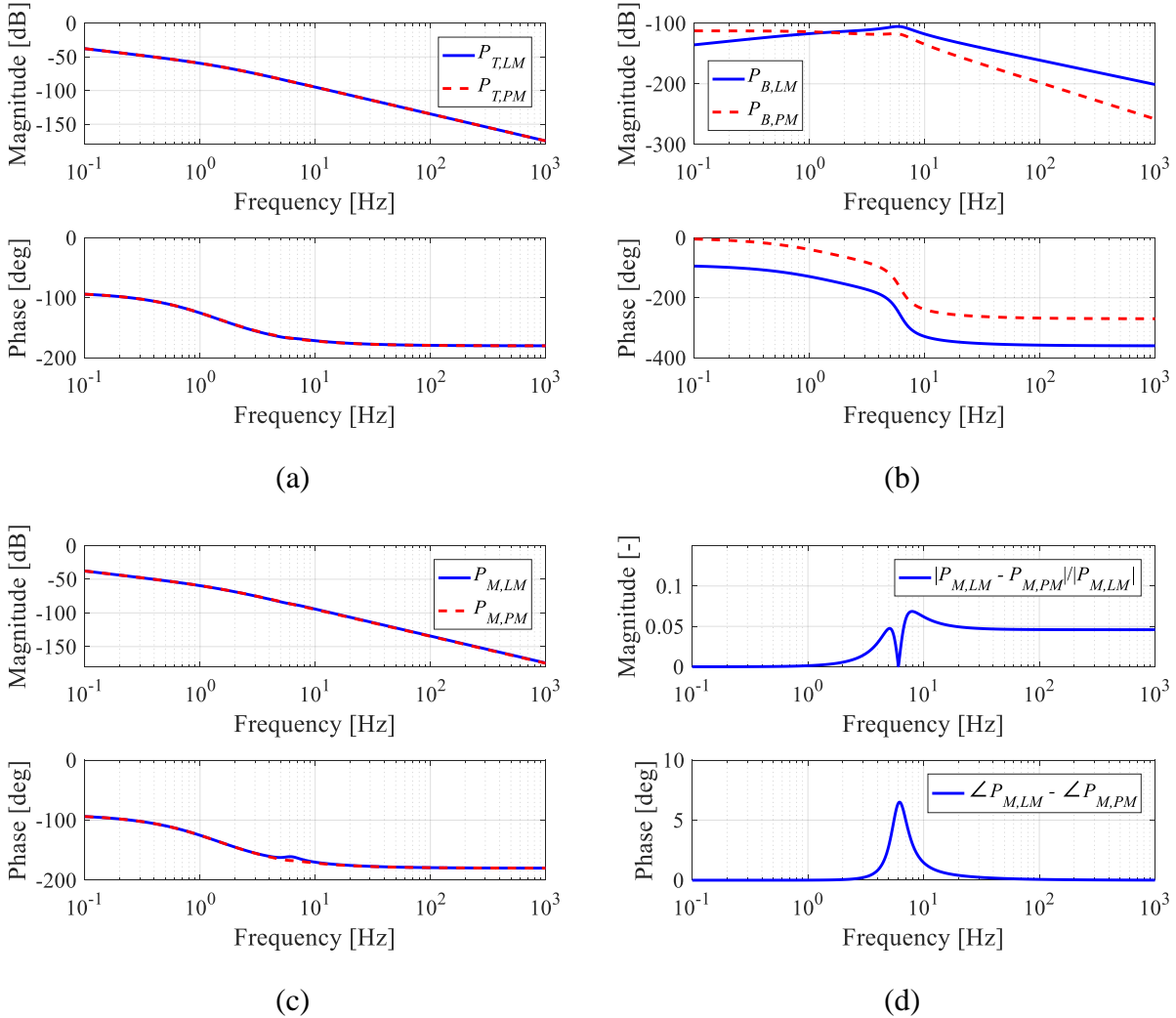


Figure 5.4 Simulated frequency response functions when (a) x_T is output, (b) x_B is output, (c) $x_T - x_B$ is output. (d) Magnitude and phase differences between $P_{M,LM}$ and $P_{M,PM}$. The magnitude unit is [m/N]

The transfer functions that describe the relative displacement between the table and base (i.e., displacement for actual manufacturing) with the LM and PM force inputs are similar in terms of the magnitude and phase of FRFs. Thus, it is proposed to have only one system dynamics model (i.e., transfer function, P_M) used to describe the stage behavior for both the LM and PM force inputs for the purpose of ILC update law generation; the magnitude and phase differences between the two models ($P_{M,LM}$ and $P_{M,PM}$) can be lumped into the description of model uncertainties because they exhibit very similar frequency responses. Figure 5.5 shows the simplified block diagram of the original model shown in Figure 5.2. In here, the stage's reference displacement, x_{ref} , replaces the table displacement, x_T (like Chapter 4), because the difference between the actual system (x_T) and the simplified model (x_{ref}) can be lumped into the PM force model uncertainties, as well.

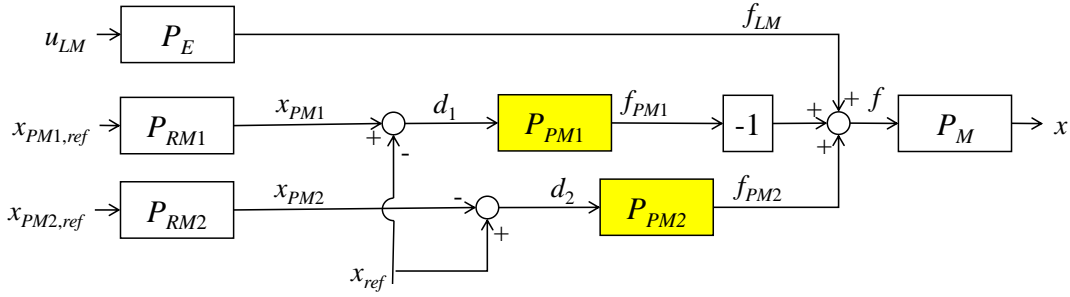


Figure 5.5 Simplified dynamics model of the magnet assisted scanning stage; yellow blocks indicate nonlinear transfer functions (i.e., nonlinear magnetic force and distance relationship).

With the simplified model of the system, the system can be treated as a SISO system. Thus, the ILC update law for the stage can be generated with the direct inversion of P_M . After solving the optimal f , the system models such as P_E , P_{PMi} and P_{RMi} are used to allocate the actuator inputs following the similar procedure as provided in Chapter 4. In the lifted-time domain representation, the ILC update is carried out with

$$\mathbf{f}_{k+1} = \mathbf{f}_k + \mathbf{P}_M^{-1} \mathbf{e}_k \quad (5.42)$$

using $\mathbf{B} = \mathbf{I}$, as in Eq. (5.8), for the fastest convergence under the perfect model scenario. In order to maintain the monotonic convergence of tracking error, the following inequality must be

satisfied, meaning the next iteration's tracking error must be less than or equal to the current iteration;

$$\|\mathbf{e}_{k+1}\|_2 \leq \|\mathbf{e}_k\|_2 \quad (5.43)$$

Similar to the robust monotonic convergence criterion given in (5.25), the following inequality must be satisfied for the entire range of system model candidates (\mathbf{P}_C);

$$\|\mathbf{I} - \mathbf{P}_M^{-1} \mathbf{P}_C\|_2 < 1 \quad (5.44)$$

The ILC update structure becomes, with the inclusion of the robustness filter (i.e., Q -filter);

$$\mathbf{f}_{k+1} = \mathbf{Q}(\mathbf{f}_k + \mathbf{P}_M^{-1} \mathbf{e}_k) \quad (5.45)$$

Due to the input force uncertainty, stemming from the simplification made with the table displacement and the PM force model uncertainty, the actual input force applied to the stage is described with

$$\mathbf{f}_{k+1} = \mathbf{Q}(\mathbf{I} + \mathbf{D})(\mathbf{f}_k + \mathbf{P}_M^{-1} \mathbf{e}_k) \quad (5.46)$$

where \mathbf{D} is the relative input force uncertainty. Combining the model and input force uncertainties, the following equation that describes the tracking error of the next iteration is provided;

$$\mathbf{e}_{k+1} = (\mathbf{I} - \mathbf{P}_C \mathbf{Q} \mathbf{P}_M^{-1} - \mathbf{P}_C \mathbf{Q} \mathbf{D} \mathbf{P}_M^{-1}) \mathbf{e}_k + \mathbf{P}_C (\mathbf{I} - \mathbf{Q} - \mathbf{Q} \mathbf{D}) \mathbf{f}_k \quad (5.47)$$

Using the frequency-domain representation of Eq. (5.43), $|e_{k+1}| \leq |e_k|$, and the triangle inequality, the following inequality must be satisfied during the ILC update for RMC for all frequency.

$$\left(\left| (1 - P_C Q P_M^{-1} - P_C Q D P_M^{-1}) E_k \right| + \left| P_C (1 - Q - Q D) F_k \right| \right) \gamma \leq |E_k| \quad (5.48)$$

where $\gamma \geq 1$ is the safety factor accounting for the approximations involved with conducting the analysis in the frequency rather than the lifted domain. A similar constraint is discussed in Eq. (5.31) in Section 5.2. For given model and input force uncertainties, P_C and D , and the nominal model, P_M , the robustness filter, Q , can be maximized such that the steady-state tracking error is minimum (Bristow *et al.*, 2006). Formally stated,

$$\begin{aligned} & \text{Maximize } |Q| \\ & \text{s.t. } \left(\left| (1 - P_C Q P_M^{-1} - P_C Q D P_M^{-1}) E_k \right| + \left| P_C (1 - Q - Q D) F_k \right| \right) \gamma \leq |E_k| \end{aligned} \quad (5.49)$$

After solving for the optimal input force to be applied to the table for the next iteration, the force can be allocated to the three inputs, (f_{LM} , f_{PM1} and f_{PM2}). In order to enforce the velocity and acceleration limits of the RMs, the control allocation optimization must be carried out in the time domain. Dropping the iteration subscript ($k+1$) for conciseness, the following equality in the discrete time domain must be satisfied;

$$\mathbf{f} = \mathbf{f}_{LM} - \mathbf{f}_{PM1} + \mathbf{f}_{PM2} \quad (5.50)$$

With user-specified weights for the actuators, an objective function ($J_{allocate}$) using the two-norm of weighted sum of control inputs is minimized;

$$J_{allocate} = \begin{bmatrix} \mathbf{f}_{LM} \\ \mathbf{f}_{RM1} \\ \mathbf{f}_{RM2} \end{bmatrix}^T \begin{bmatrix} \mathbf{I} & 0 & 0 \\ 0 & w_1 \mathbf{I} & 0 \\ 0 & 0 & w_2 \mathbf{I} \end{bmatrix} \begin{bmatrix} \mathbf{f}_{LM} \\ \mathbf{f}_{RM1} \\ \mathbf{f}_{RM2} \end{bmatrix} \quad (5.51)$$

where $w_1 \ll 1$ and $w_2 \ll 1$ are weights used for the optimization. The objective function is like J_{contr} shown in (4.36). The difference between J_{contr} and $J_{allocate}$ is that \mathbf{f} used for $J_{allocate}$ is based on the ILC update, whereas \mathbf{f} used for J_{contr} is based on the simple model expressed with Eq. (4.1) that

does not accurately capture all the dynamic behavior of the system. As in Chapter 4, B-splines are adopted to reduce the optimization dimension. The B-splines representation of the inputs are

$$\mathbf{x}_{PM1,ref} = \mathbf{N}_P \mathbf{p}_{PM1}; \mathbf{x}_{PM2,ref} = \mathbf{N}_P \mathbf{p}_{PM2}; \mathbf{u}_{LM} = \mathbf{N}_E \mathbf{p}_E \quad (5.52)$$

where \mathbf{N}_E and \mathbf{p}_E are the basis function matrix and control points for the LM force command, respectively. Exploiting the linear system dynamics, filtered B-splines are used to more accurately simulate the time domain responses (*Ramani et al., 2017*), meaning the PM positioning servo controllers are rightly assumed not to have perfect tracking;

$$\mathbf{x}_{PM1} = \tilde{\mathbf{N}}_{P1} \mathbf{p}_{PM1}; \mathbf{x}_{PM2} = \tilde{\mathbf{N}}_{P2} \mathbf{p}_{PM2}; \mathbf{f}_{LM} = \tilde{\mathbf{N}}_E \mathbf{p}_E \quad (5.53)$$

where $\tilde{\mathbf{N}}_{P_i}$ and $\tilde{\mathbf{N}}_E$ are filtered basis function matrices for the RM servo and electrical dynamics, respectively. Following the control efforts description presented in Chapter 4, the RM control efforts, considering the servo dynamics with the filtered B-splines, are provided with

$$\mathbf{f}_{RM1} = m_{PM1} \tilde{\mathbf{N}}_{A1} \mathbf{p}_{PM1} + b_{PM1} \tilde{\mathbf{N}}_{V1} \mathbf{p}_{PM1} + \mathbf{f}_{PM1} \quad (5.54)$$

$$\mathbf{f}_{RM2} = m_{PM2} \tilde{\mathbf{N}}_{A2} \mathbf{p}_{PM2} + b_{PM2} \tilde{\mathbf{N}}_{V2} \mathbf{p}_{PM2} - \mathbf{f}_{PM2} \quad (5.55)$$

where $\tilde{\mathbf{N}}_{V_i}$ and $\tilde{\mathbf{N}}_{A_i}$ are the servo's filtered basis function matrices for velocity and acceleration, respectively. Like the optimization problem given in (4.36), the control allocation optimization after applying the ILC update is found by

$$\begin{aligned}
& \text{minimize } J_{\text{allocate}}(\mathbf{p}_{PM1}, \mathbf{p}_{PM2}, \mathbf{p}_E) \\
& \text{s.t.} \\
& \mathbf{f}_{LM} - \mathbf{f}_{PM1} + \mathbf{f}_{PM2} - \mathbf{f} = 0 \\
& \delta_c - \min(\mathbf{d}_i) \leq 0 \\
& \delta_{CV} - \min(\mathbf{d}_{i,CV}) \leq 0 \\
& \max\left(\left|\tilde{\mathbf{N}}_{Vi} \mathbf{p}_{PMi}\right|\right) - v_{PM,\max} \leq 0 \\
& \max\left(\left|\tilde{\mathbf{N}}_{Ai} \mathbf{p}_{PMi}\right|\right) - a_{PM,\max} \leq 0
\end{aligned} \tag{5.56}$$

5.5 Experimental example

In this section, the optimal inversion-based ILC with control efforts allocation approach presented in Section 5.4 is applied to the magnet assisted scanning stage. Three cases are considered for comparison;

- 1) ILC with optimal Q -filter presented in Section 5.4 with \mathbf{p}_{PMi} configured to provide no assist for the initial iteration (Start w/o assist).
- 2) ILC with optimal Q -filter presented in Section 5.4 with \mathbf{p}_{PMi} configured to provide assist using the control allocation approach presented in Chapter 4 for the initial iteration (Start from baseline).
- 3) Without ILC and \mathbf{p}_{PMi} are solved using the control allocation approach presented in Chapter 4 (w/o ILC).

The allocation weights of $w_1 = w_2 = 1/200$ are used, which are equivalent to setting $w = 1/201$ in Chapter 4. The minimum gap during the CV regions constraint of $\delta_{CV} = 15$ mm is used, while the PM positioning servo's speed and acceleration limits are 175 mm/s and 3.3 m/s², respectively. The reference motion trajectory is as same as in Case study I (i.e., scanning motion for photo-lithography) from Chapter 4 (Figure 4.7 and Figure 4.8).

The model uncertainties are obtained from the measured FRFs from the stage and the dynamics analyses (i.e., the FRFs shown in Figure 5.4). To find the magnitude and phase bounds, varying sinusoidal force inputs (15 N to 300 N) are applied to the table by the linear motor. After obtaining the response bounds based on the force inputs, $\pm 6\%$ magnitude and $\pm 8^\circ$ phase uncertainties are added, respectively (see Figure 5.4 for difference between $P_{M,LM}$ and $P_{M,PM}$ of the modeled system). The system model uncertainties (shaded regions) and nominal model (blue lines) used for the ILC update law generation are shown in Figure 5.6.

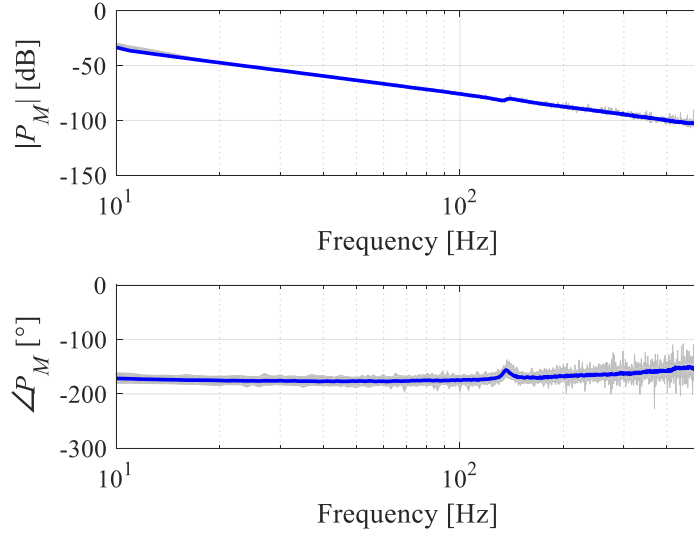


Figure 5.6 Frequency response function used to construct the ILC update law and optimal robustness filter. Shaded regions represent the experimentally obtained system uncertainties that include the modeling error.

The PM force model uncertainties are based on the measured force-distance relationships with $\pm 3\sigma$ (standard deviation) as shown in Figure 5.7. The upper and lower bounds are fitted with the same exponential equation structure as presented in Eq. (4.7). Because of the nonlinear PM force curves, D must be computed every ILC iteration using the uncertainty bounds, i.e., Q -filter is no longer constant over the iteration domain. The input force uncertainty is computed using

$$\mathbf{f}_{C,k} = \mathbf{f}_{LM,k} - \mathbf{f}_{PM1,C,k} + \mathbf{f}_{PM2,C,k} \quad (5.57)$$

where the subscript C and k denote the input force candidates and the previous iteration data, respectively. The measured input force and its uncertainty region for the 15th iteration data for the Start w/o assist case are shown in Figure 5.8 (a), where the shaded regions represent the uncertainty. The measured force signal is shown with the solid blue line. The measured uncertainty region is converted into the frequency domain via DFT to estimate the uncertainty candidate (D_C) in the frequency domain;

$$D_{C,k} = \frac{F_{C,k}}{F_k} - 1 \quad (5.58)$$

The uncertainty candidate's magnitude is shown in Figure 5.8 (b) using the 15th iteration data from the Start w/o assist case. The optimal Q -filter, solved for the 15th iteration for the Start w/o assist case using (5.49), is shown in Figure 5.9. The optimal Q -filter gain is maximized; thus, the minimum tracking error is expected at the steady-state (*Bristow et al., 2006*). See Appendix C for more detail on the impact of optimal Q -filter on the steady-state tracking performance.

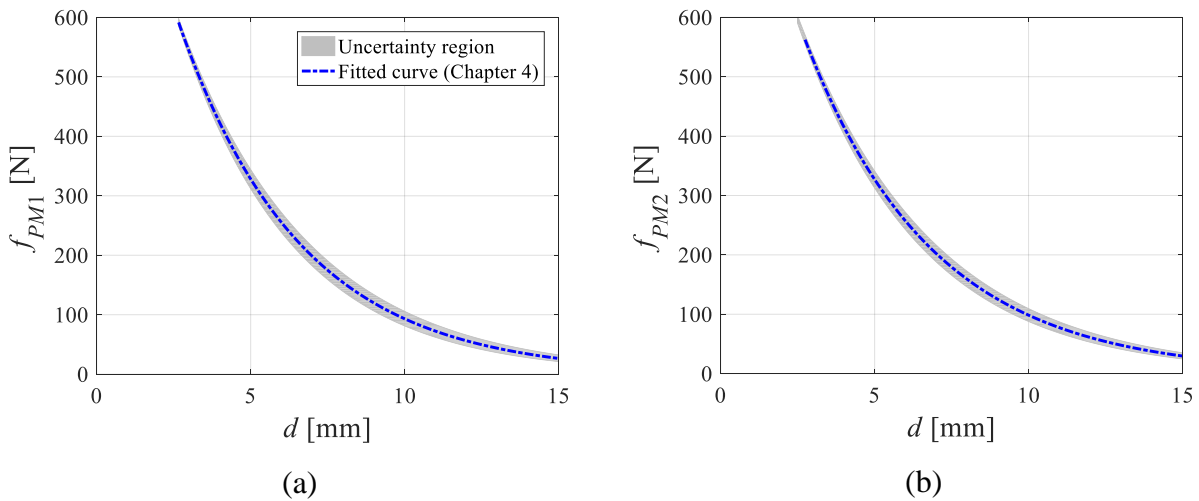


Figure 5.7 PM repulsion force uncertainty regions and fitted force curve presented in Section 4.2; (a) PM1. (b) PM2

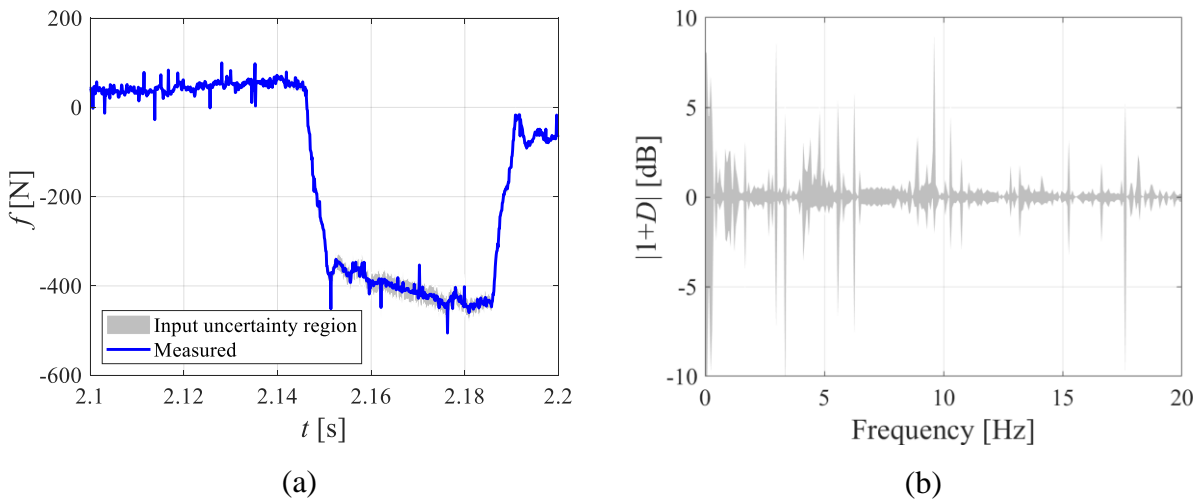


Figure 5.8 (a) Input force uncertainty based on the PM repulsion force uncertainty and previous iteration's input signals. (b) Input force uncertainty is converted into the frequency domain via DFT.

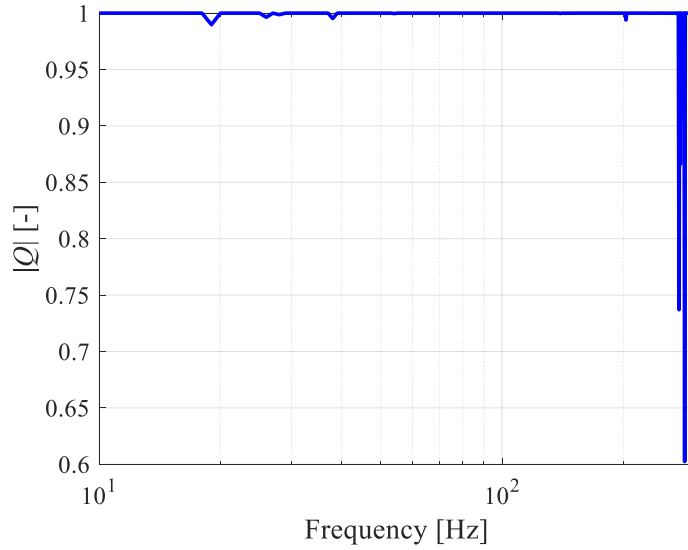


Figure 5.9 Optimized robustness filter, Q , selected based on the model and input force uncertainties for the 15th iteration of the Start w/o assist case.

Figure 5.10 (a) and (b) show the RMS tracking error, for the entire duration of motion trajectory and during the CV regions. The ILC cases return almost the same performance, even though it takes more iterations for the Start w/o assist case to converge. The presented ILC approach achieves extra 30% reductions in RMS tracking on top of the benefits of having the optimally controlled PM-based ADs (i.e., AAD configuration) shown in Chapter 4.

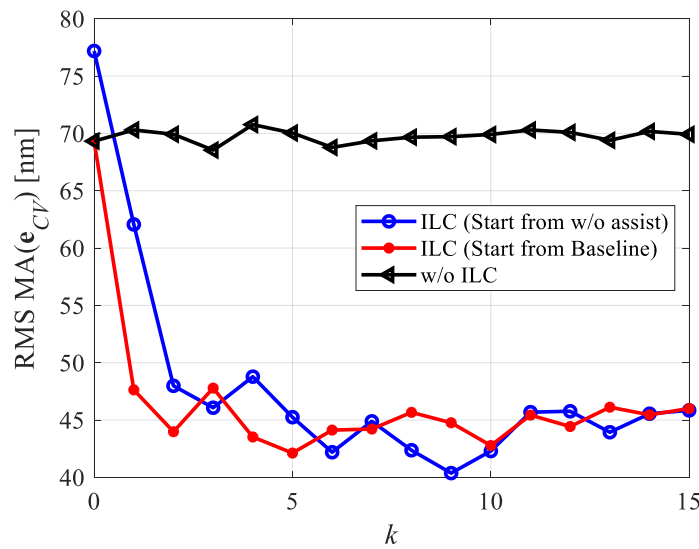


Figure 5.10 RMS MA tracking error during the CV regions.

The RMS LM forces for the three cases are compared in Figure 5.11. Because the model and parameters used in Chapter 4 are useful in capturing the overall control efforts requirement, the differences among the cases are very small. All the cases' LM control force in the RMS sense is within 1% of each other.

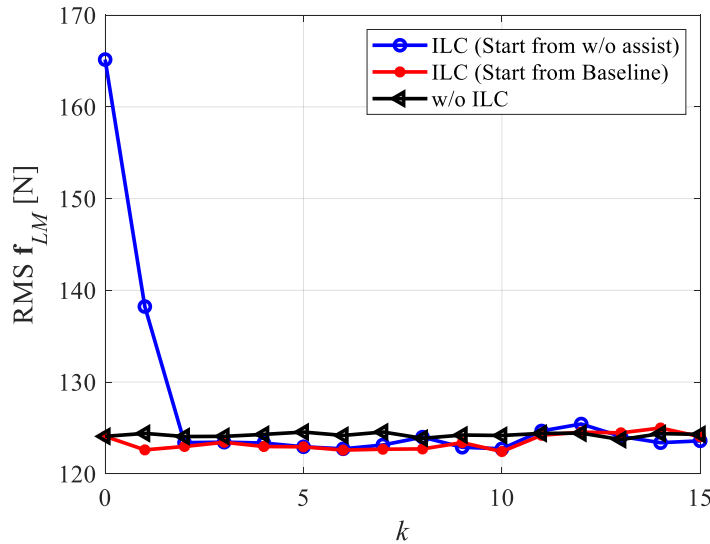


Figure 5.11 RMS linear motor force.

A portion of PM reference trajectories are shown in Figure 5.12 (a) and (b). All the ILC cases converge to the virtually identical trajectory, while the solution based on Chapter 4 is slightly different. Nonetheless, all the PM trajectory solutions are very similar, especially during the CV regions, highlighting the usefulness of the simple stage model in Eq. (4.12). However, the simple model is not adequate in estimating the force needed for tracking with a high accuracy, as the simulated force signal is noticeably different from the more accurate signal obtained with the ILC framework as shown in Figure 5.13. The feedforward control signal obtained with the ILC approach can effectively suppress tracking errors arising from the motion-induced vibration of the base, linear motor force ripple, amplifier dynamics, etc.

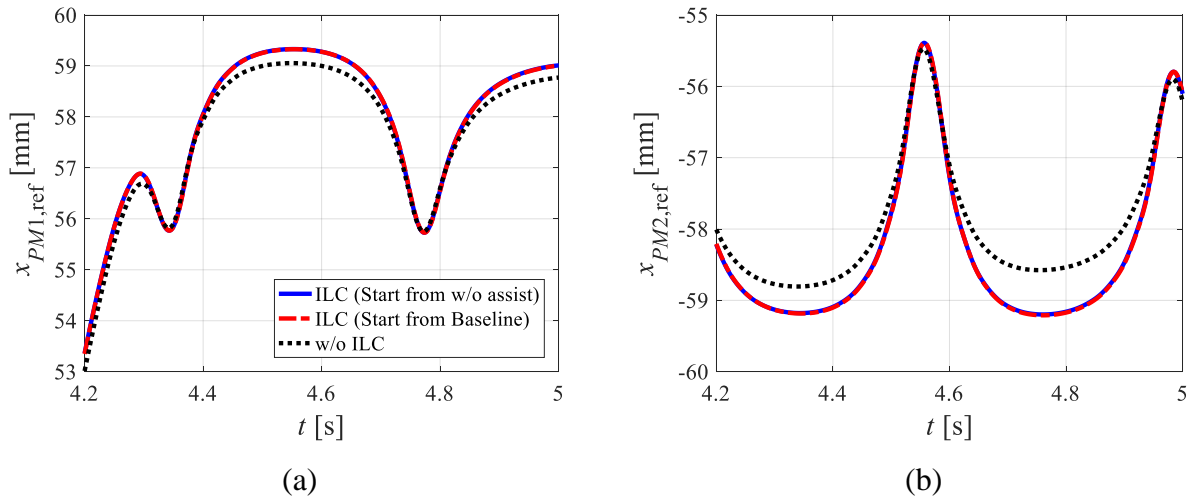


Figure 5.12 Reference motion trajectories of PM-based ADs for the 20th iteration; (a) PM1, (b) PM2.

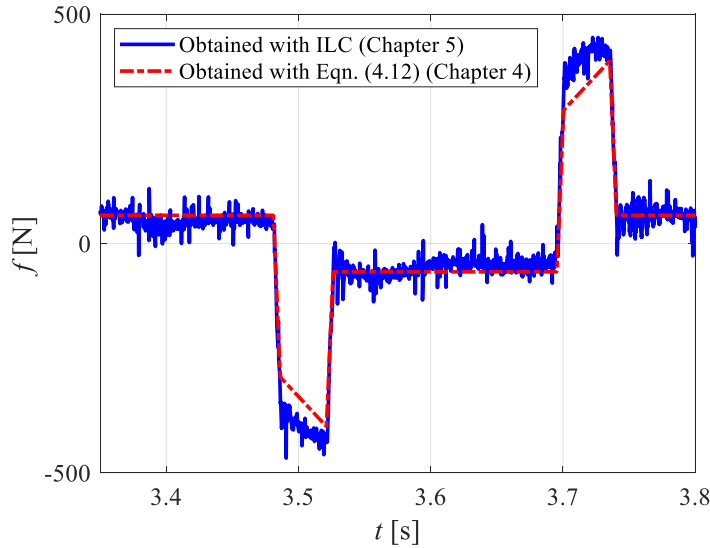


Figure 5.13 Force applied to table used for control input allocation.

5.6 Chapter summary

An optimal inversion-based ILC framework, considering the model uncertainties of system, is proposed in this chapter. The proposed inversion-based ILC framework allows explicitly selectable error learning convergence rate. The knowledge of system dynamics and model uncertainties is exploited to generate the ILC update law that achieves the minimum steady-state tracking error with the optimal control effort allocation. The proposed optimal inversion-based ILC approach has been validated on a coarse-fine stage, and the teachings are used to apply the

proposed ILC approach to the magnet assisted scanning stage. Because the internal dynamics exhibits nonlinear behaviors, a simplified model is developed to convert the stage, for the purpose of generating the ILC update law, into a SISO linear system, using a squaring method. The total force applied to the table is determined with the ILC framework and the control efforts allocation is carried out using the stage model. An experimental example is provided to highlight the effectiveness of the proposed ILC approach. The optimal inversion-based ILC applied to the magnet assisted scanning stage achieves more than 30% reductions in tracking error, on top of what is already achieved with the actively controlled PM-based ADs, while maintaining the optimal control efforts allocation. The optimal control effort allocation method presented in Chapter 4 generates a good starting point for the initial trial of the ILC update, because it can capture the majority of load required to drive the stage; the ILC update converges faster than the case without the initial allocation.

Chapter 6

Conclusion and Future Work

This doctoral dissertation has proposed a design-based method to simultaneously mitigate actuator heat and vibration-induced errors of scanning stages with permanent magnet-based assist devices. Unlike most design methods available in the literature that solve the two problems independently, simultaneous consideration of the two problems, which originate from a common source (i.e., large inertial load during motion), led to a compact design with efficient use of resources. The magnet assisted scanning stage design is accompanied by an optimal control framework, which involves optimal allocation of the control efforts for mitigating actuator heating via trajectory planning and Iterative Learning Control (ILC) for improving tracking errors. The proposed method is readily applicable to linear-stage type scanning stages, which are widely employed by the semiconductor manufacturing industry.

The repelling permanent magnet (PM) arrays are used to provide assistive force to the scanning table; one PM array is mounted on the table, while the other array is located on the ground for channeling the reaction forces to the ground. The PM-based assist devices (ADs) store and release the kinetic energy of the moving table during the deceleration portions of the motion and the stored energy is effectively released during the acceleration portions of the motion as the table moves toward the opposite direction. Because the PM repulsion force sharply decreases as the distance between the PM pair increases, the PM-based ADs are practically decoupled from the table during the constant velocity (CV) scanning, where manufacturing takes place. Consequently, the main actuator of the stage (i.e., linear motor) needs to produce much less force to deliver high acceleration/deceleration and the copper losses are drastically mitigated. The reduced linear motor force, hence the reduced vibration of isolated base, mitigates the tracking error during the CV scanning. To increase the magnetic force density, a 2D Halbach arrangement is adopted and the PM arrays are designed to be able to produce all the inertial load required for the main actuator's force requirement. The PM-based ADs are made versatile to changing scan strokes and positions

with a low-cost servo system, realized with a ball screw-driven sub-stage. The optimal lead for maximizing the versatility of ADs is found by maximizing the achievable travel distance from one assist position to another for a given rotary motor and a set of scanning motion trajectories. With the stage design concept and the PM array and screw pitch optimizing frameworks, a prototype magnet-assisted scanning stage for semiconductor manufacturing, capable of carrying a 300 mm silicon wafer at the 1 m/s and 35 m/s² velocity and acceleration limits, respectively, is constructed. It must be noted that the addition of the actively controlled PM-based ADs to the prototype stage increases about 100 mm length to each end (200 mm total) in size and about \$5,000 in cost, which are small compared to the overall size of stage (> 900 mm in length) and construction cost (> \$40,000, excluding the real-time controller).

The over-actuated scanning stage with magnet assist, having one linear motor and two rotary motors, is controlled with optimal PM trajectories for control efforts allocation. In order to estimate the control force requirements, a simple model of the system, comprising moving mass, viscous losses, and magnetic repulsion force, is constructed and the parameters are identified. The optimal PM trajectories, parameterized with B-splines for gaining computational efficiency, minimize the actuators' heat. Two experimental case studies, comprising photo-lithography and inspection scanning motions, are used to highlight the effective use of the optimal PM trajectories in reducing heat and vibration-induced errors.

Finally, an optimal inversion-based ILC framework for over-actuated systems, which enforces a user-tunable error convergence rate, is proposed. The proposed ILC framework uses frequency domain analysis and optimization tools to solve for the ILC update law, ensuring the robust monotonic convergence of tracking errors against given (or known) model uncertainties. The residual tracking errors, stemming from the vibration of isolated base due to non-zero linear motor force during the acceleration/deceleration and model mismatch from the feedforward controllers, are subsequently mitigated with the proposed optimal inversion-based ILC framework. The optimal PM trajectories generated previously serve as a good starting point for the ILC approach, because the converged solution can be obtained with only one iteration.

The works presented in this dissertation have been published in the following journal articles and patent:

- Yoon D, Okwudire C. *Magnet assisted stage for vibration and heat reduction in wafer scanning*. CIRP Annals. 2015; 64 (1); 381-384.

- Yoon D, Okwudire C. *Active assist device for simultaneous reduction of heat and vibration in precision scanning stages*. Precision Engineering. 2016; 46; 193-205.
- Yoon D, Ge X, Okwudire C. *Optimal Inversion-based Iterative Learning Control for Over-Actuated Systems*. IEEE Transactions on Control Systems Technology. Under review.
- Okwudire C, Yoon D. *Magnet assisted stage for vibration and heat reduction in wafer scanning*. US Patent; 2018; 10077865.

The stage design method and the prototype constructed can be readily used in many manufacturing settings such as 3D printing and flat panel display manufacturing. However, more rigorous analyses and appropriate design modifications must be carried out if the working environment is under vacuum or generates ferrous particles. The vacuum environment may render the air bushings and the NdFeB magnets incompatible and the ferrous particles, generated from manufacturing processes, can accumulate near the PM arrays. Thus, it must be noted that the prototype stage serves as a demonstration tool for the combined actuator heat and vibration reduction method using the ADs and not the only realization of the proposed design method.

Depending on the severity of thermal and vibration problems, the proposed design method can eliminate needs for other temperature and vibration control approaches, e.g., forced cooling and counter motion devices. Should there need further reductions of the actuator-borne heating and vibration, the existing approaches, reviewed in Chapter 2, can be used to complement the design method proposed in this dissertation. Because the actuator heating and vibration of isolated base are already reduced drastically with the proposed actively controlled PM-based ADs, budgetary requirement for the existing approaches can be significantly lower than the case without the ADs.

From the experimental case studies shown in Chapter 4, the tracking error reductions are lower than the vibration reductions of the isolated base (e.g., the photo-lithography scanning case study shows 32% reduction in vibration, whereas the tracking error reduction is only 20%), because of short constant velocity scanning portions of the motions. However, the reduced vibration still provides additional benefits to manufacturing equipment, which are not directly captured by the case studies. The reduced vibration of isolated base leads to reduced vibrational disturbances to the manufacturing tools and surrounding machine components, e.g., metrology

probes and optical systems, thus, the quality of manufacturing is expected to improve more than the measured tracking error improvement

The simultaneous consideration of the heat and vibration reductions has led to the reduced temperature gradient (i.e., thermal errors) of the scanning table and tracking errors using a simple industrial feedback control structure, as shown in Chapter 4. With the ILC framework proposed in Chapter 5 for improving the tracking errors, one may see that the vibration reductions by design in Chapter 3 may not be needed after all. However, it must be noted that the ILC framework cannot suppress the vibration; it only provides a better tracking performance under repeating disturbances. As stated above, the reduced vibration of isolated base brings additional benefit of lowering vibrational disturbances to surrounding machine components, which can potentially improve the manufacturing quality more than the tracking error of stage. In this situation, the vibration reduction feature of the proposed design can greatly benefit the stage users/designers, without solely relying on the ILC framework to improve the manufacturing quality.

The presented work has specifically focused on the scanning axis of scanning stages, however there are many applications that require stepping (e.g., point-to-point positioning for photo-lithography, inspection, metrology, micro-machining, and 3D printing processes). The magnet assisted stage design as presented can be used for many stepping applications, where the actuator heating and vibration of isolated base can be mitigated. But, its impact on reducing heat and vibration would be much less because the repeating back-and-forth motions, for harvesting and releasing the energy using the magnetic field, can no longer be exploited. The deficiency in heat and vibration mitigation methods in the stepping axis has been addressed with preliminary works using a scale decouplable coarse-fine stage prototype (*Yoon et al., 2017; Yoon and Okwudire, 2018*), but more in-depth investigation is required to refine the solution approaches and the full-scale (e.g., 300 mm wafer) implementation.

The proposed inversion-based ILC framework has used a simple diagonal error learning matrix structure (i.e., $\mathbf{B} = b\mathbf{I}$). Different matrix structures may lead to better steady-state performances, but more rigorous analysis tools need to be developed to assess the implication of using the different matrix structures. In addition, a nonlinear ILC framework that does not require extensive computational resources can be investigated, potentially eliminating needs for the two-stage process presented in Section 5.4.

APPENDICES

Appendix A

Bill of Materials of Magnet Assisted Scanning Stage Prototype

Bill of materials shown in Table A.1 includes all the purchased and custom-made parts used to construct the magnet assisted scanning stage shown in this dissertation. Control related hardware (e.g., the real-time controller and PWM amplifiers used) list is omitted from this table.

Table A.1 Bill of materials of magnet assisted scanning stage prototype.

Vendor	Name	Model #	Quantity	Note
Bilz	Membrane Air Springs	BiAir0.5-ED	4	Including re-levelers
K&J Magnetics	Permanent magnet	B555	168	N42 grade 5/16" PM cube
Misumi	Dowel Pins	MSTH10-70	2	Undersized, One End Tapped (H7)
Misumi	Adjustment Pads	FJGM16-75-R	4	Nonslip Type
Misumi	Flat Washers	SPWF12	4	
Misumi	Lifting Eye Bolts	CHi12	4	
Misumi	Spring Washers	SSLW6	5	
Misumi	Dowel Pins	MSTH10-25	20	Undersized, One End Tapped (H7)
Misumi	Dowel Pins	MSTH10-60	4	Undersized, One End Tapped (H7)
Misumi	Adjusting Bolts	AJKTNF12-50	2	Knurled head with Hex Socket
Misumi	Blocks for Adjusting Bolts	AJKC12-12	2	Standard Type
Misumi	Miniature Linear Guides Standard Blocks	SSEBZ13-320	2	Light Preload, Precision Class L Configurable Type
Misumi	Precision Angle Plates	BIKF250-A120-B75-X40-F40-Y195-G40	4	Plates - Cast Iron/Aluminum Casting/Stainless Casting, Configurable Hole Position,
Misumi	Coupling	SCXW34-6-14	2	High Positioning Accuracy Disc, Clamping / Keyway
Misumi	Support Units	BSW8S	2	
Misumi	Rolled Ball Screw	BSSR1002-388	2	Thread Diameter 10- Lead 2, 4 or 10 - Precision Grade C7 or C10
Misumi	Dowel Pins	MSHT6-35	4	Undersized, One End Tapped (h7)

Misumi	Support Units	BUR6	2	Round Type, Support Side with Retaining Ring
Misumi	Hex Socket Set Screws	MSSF4-5	24	Shaped Tips
Misumi	Crush Pads	PACK-SEPNS4	1	
Misumi	Shock Absorbers	MAKC1210M	4	Preset Dampening
Misumi	Shaft supports	SHWTM25_60	8	T-shaped - Side slit
Misumi	Lifting Eye Bolts	CHI6	4	
Misumi	Cable Carreirs	MHPUS206-38-16-A	2	Flap Open-Close Type
NEWWAY air bearings	25 mm ID Air Bushing	S302502	4	Air bushing, diameter = 25 mm
NEWWAY air bearings	Bushing mounting block	S8025P02	4	Air bushing mounting block
Nippon Pulse Motor	Linear Servomotor	S250Q-ST500-HA	2	Shaft Diameter 25mm, Acceleration Force 300N
Oriental Motor	Rotary Motor	NX620A	2	Tuning-Free Servo Motor & Driver
Renishaw	Tonic Dual O/P Interface X20	DOP0020A10A	3	10 MHz
Renishaw	Tonic Readhead	T1000-30A	3	RGSZ20
Renishaw	RGSZ-S Scale Kit 100 mm	A-9420-0010	1	
Renishaw	TGSZ-S Tonic Scale	A-9420-0048	2	480 mm
	Granite Base	-		600 mm × 900 mm × 100 mm
	Table	WT_001	1	Moving table
	Force Frame	WT_002	4	Plates for mounting Halbach arrays
	Readhead Holder	WT_003	2	Horizontal part of encoder read head mount
	Readhead Holder 2	WT_004	2	Vertical part of encoder read head mount
	Cable Carrier Plate	WT_005	2	Horizontal plate for mounting cable carrier (moving side)
	Spacer	WT_006	4	Spacer for air bushing mounting blocks
	Connecting Plate	MF_001	1	Long horizontal bridging plate for mounting PM tables
	Nut Mounting Block	MF_002_002	2	Bottom part of ball screw nut attachment
	Nut Mounting Plate	MF_003_002	2	Top part of ball screw nut attachment
	Fixed Side Plate	MF_004	2	Block for mounting fixed side bearing for ball screw

	Support Side Plate	MF_005	2	Plate for mounting support side bearing for ball screw
	Step Motor Holder	MF_006	2	L bracket for stepper motor mounting
	Machine Frame Base	MF_007	1	Machine frame plate (big and heavy)
	Force Frame	MF_008	2	L shaped intermediate connector between bridge and the machine frame
	Force Frame 2	MF_009	2	Intermediate connector between bridge and the machine frame (vertically movable)
	Limit Sensor L	MF_010	2	L shaped plate for limit switch (blocks light)
	Scale Mount	MF_011	1	Scale mount for measuring base frame vibration
	Halbach 2D	HA_001	8	
	Block	BF_002	1	Base frame
	Scale Block	BF_003	2	Encoder scale mount
	Bumper Block	BF_004	4	Bumper mount
	Base Frame Connecting Plate	BF_005	2	Granite mounting
	Base Frame Connecting Plate	BF_006	2	Granite mounting
	Air Spring Mount	BF_007	2	Isolator mounting
	Air Spring Mount 2	BF_008	2	Isolator mounting
	Base Frame Connecting Plate 3	BF_009	8	Granite mounting
	Cable Carrier Plate	BF_010	2	Mounting cable carriers (fixed)
	Encoder Readhead Mount	BF_011	1	Mounting encoder read head for measuring baseframe vibration
	Spacer	BF_012	4	Spacer for shaft mounts

Appendix B

CAD Drawings of Magnet Assisted Scanning Stage Prototype

The CAD drawings for the custom designed parts and sub-assemblies for the magnet assisted scanning stage prototype are provided. In B.1, parts related to the isolated base are presented. The ground of scanning stage (i.e., machine frame) is assembled with the parts shown in B.2. Parts related to the scanning table and the 2D Halbach array are listed in B.3 and B.4, respectively.

B.1 CAD drawings for Base Frame

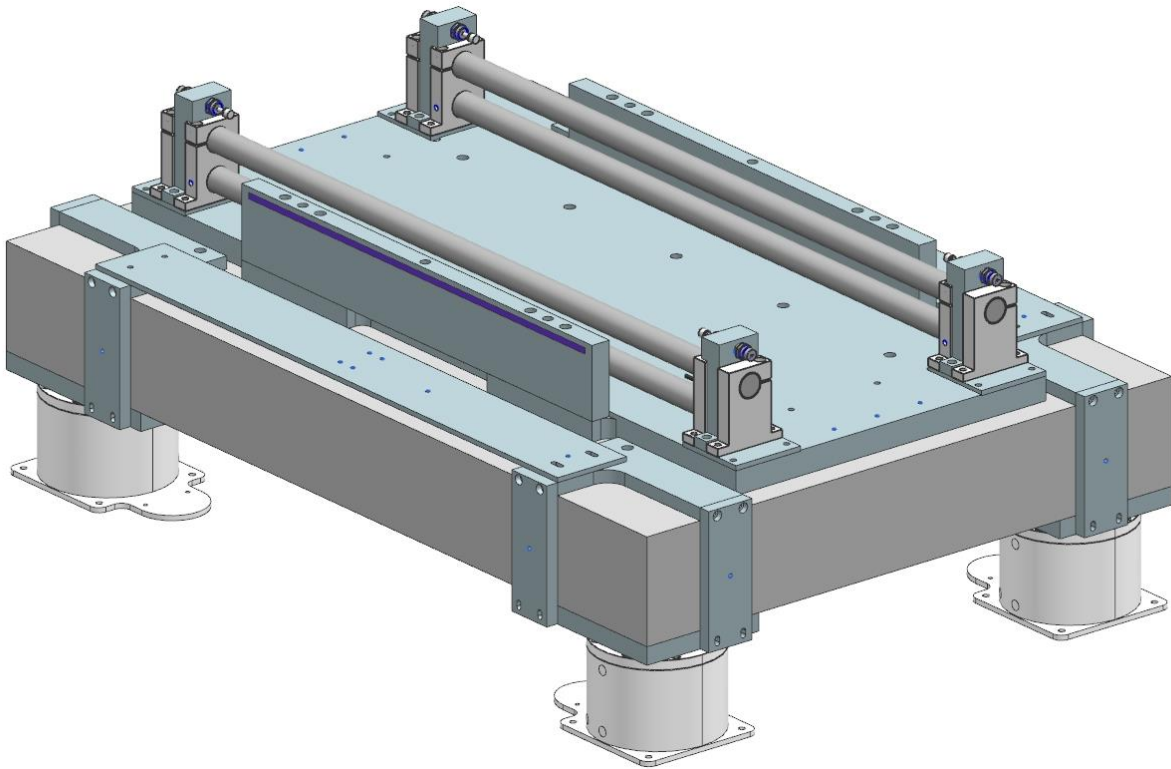


Figure B.1 Isometric view of Base Frame sub-assembly.

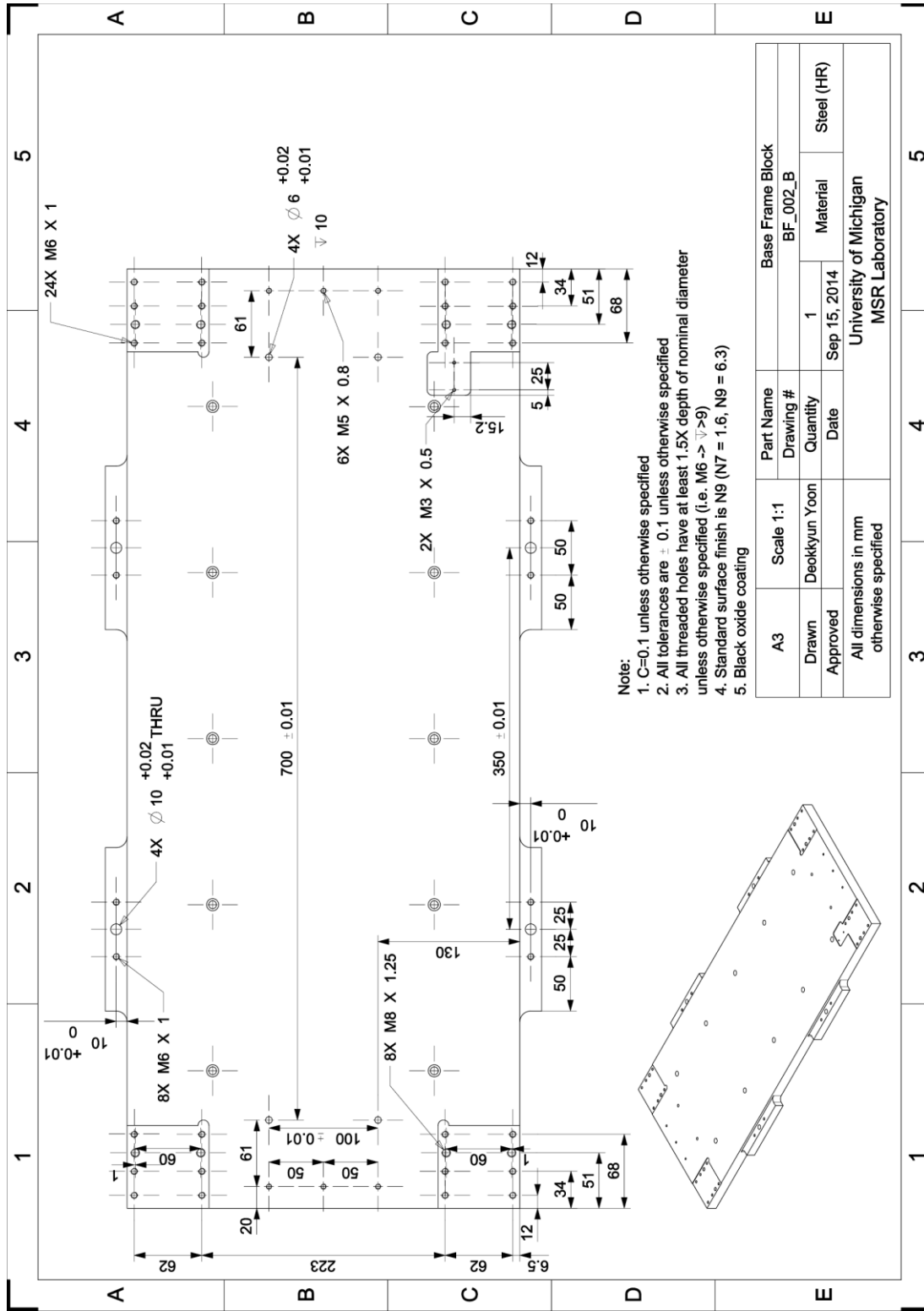


Figure B.3 Manufacturing drawing of Base Frame Block (pg. 2 of 2).

B.1.2 Scale Block

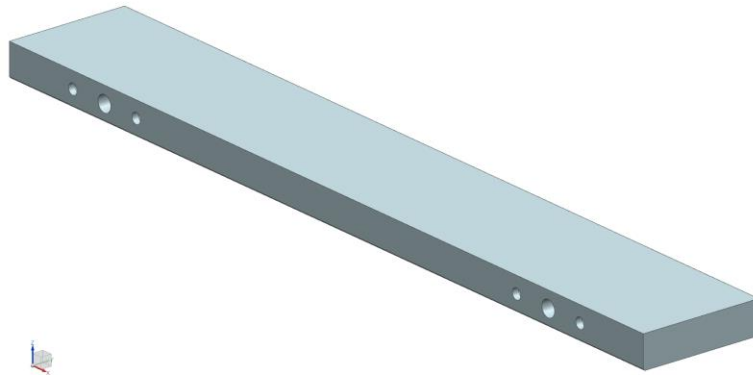


Figure B.4 Isometric view of Scale Block.

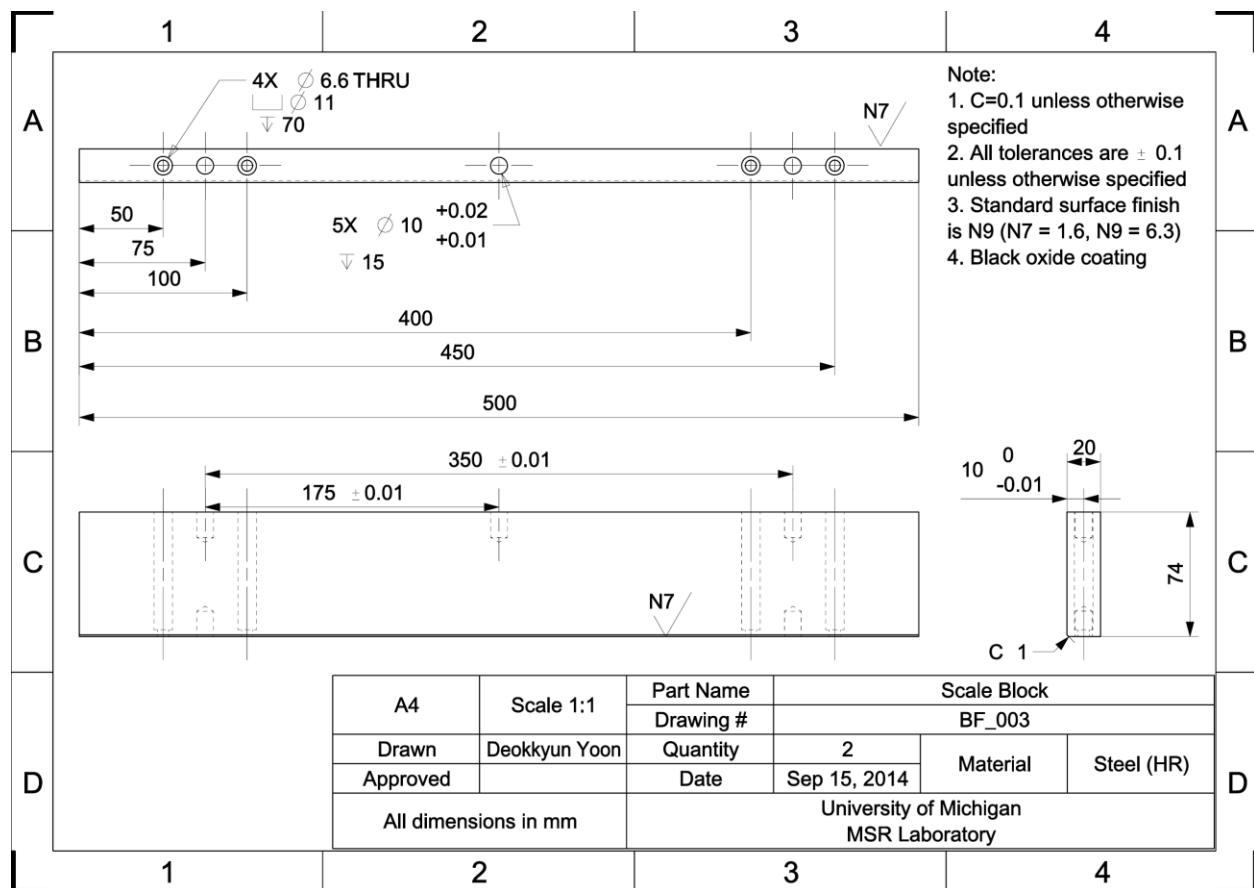


Figure B.5 Manufacturing drawing of Scale Block.

B.1.3 Bumper Block

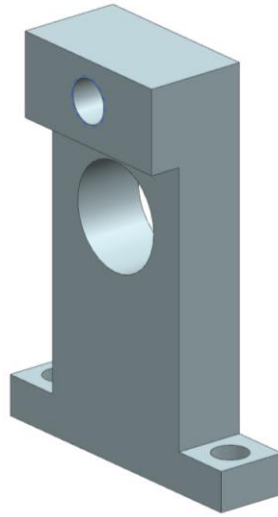


Figure B.6 Isometric view of Bumper Block.

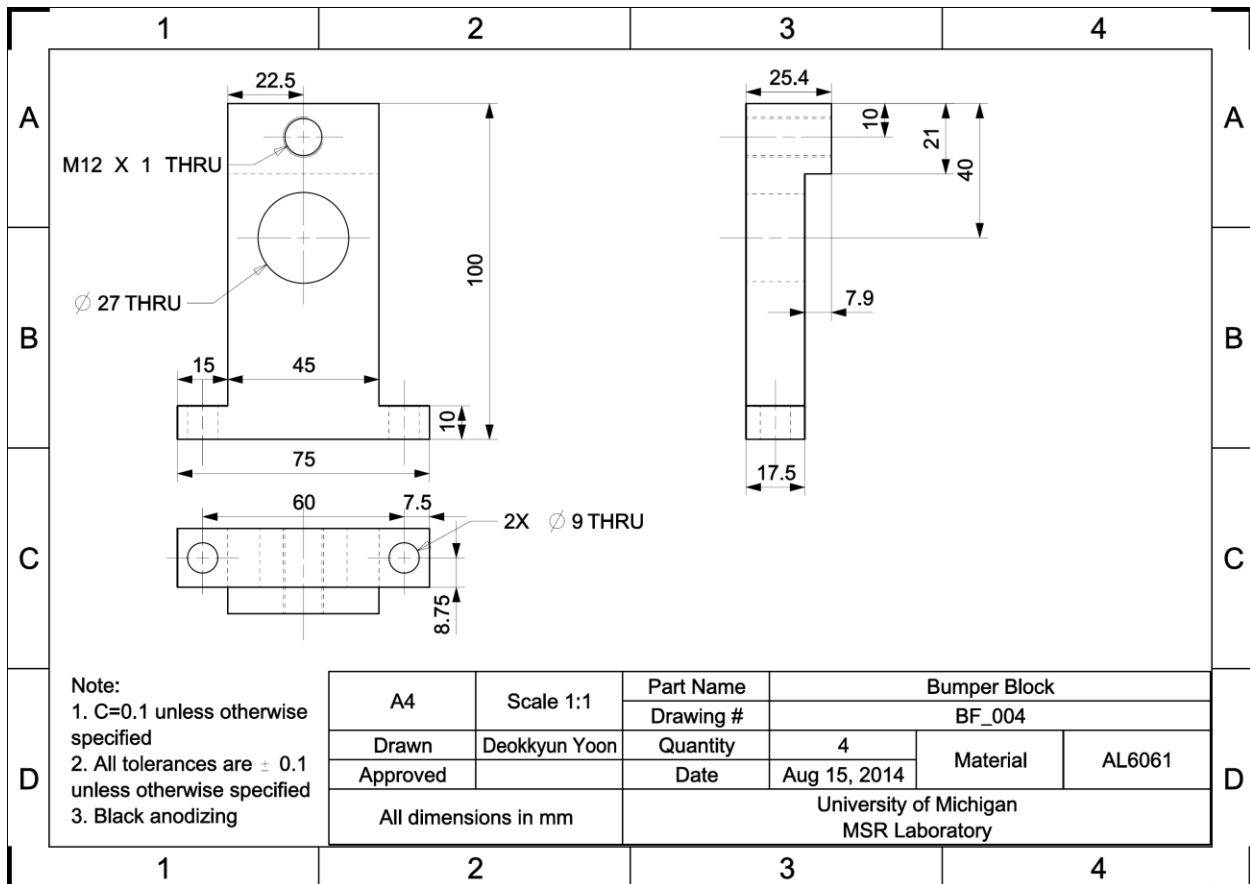


Figure B.7 Manufacturing drawing of Bumper Block.

B.1.4 Base Frame Connecting Plate #1

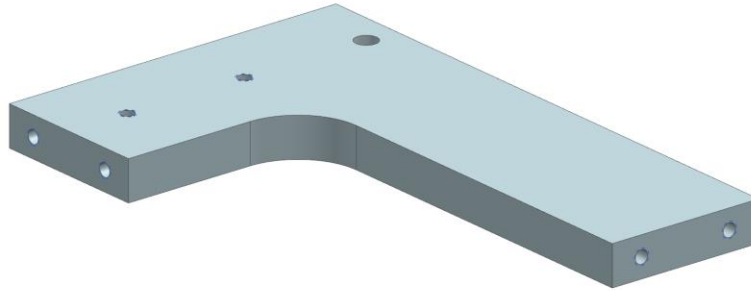


Figure B.8 Isometric view of Base Frame Connecting Plate #1.

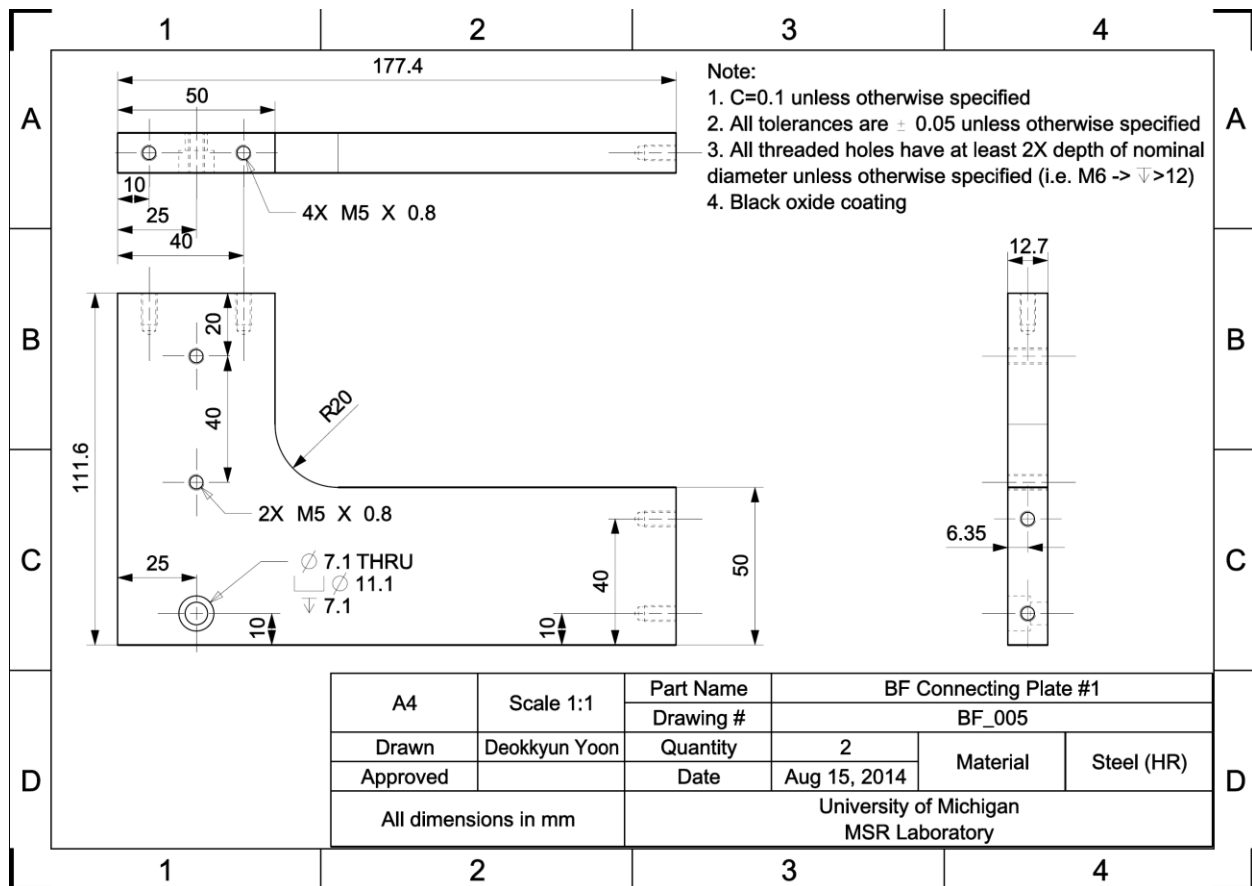


Figure B.9 Manufacturing drawing of Base Frame Connecting Plate #1.

B.1.5 Base Frame Connecting Plate #2

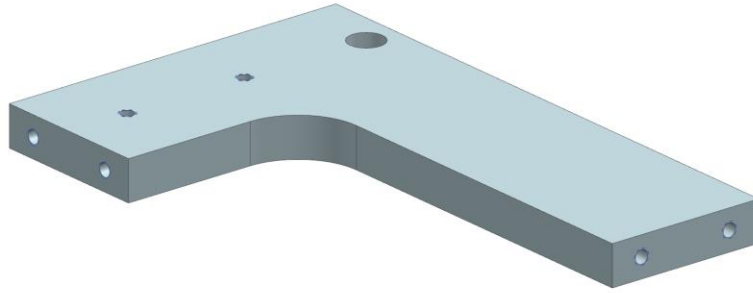


Figure B.10 Isometric view of Base Frame Connecting Plate #2.

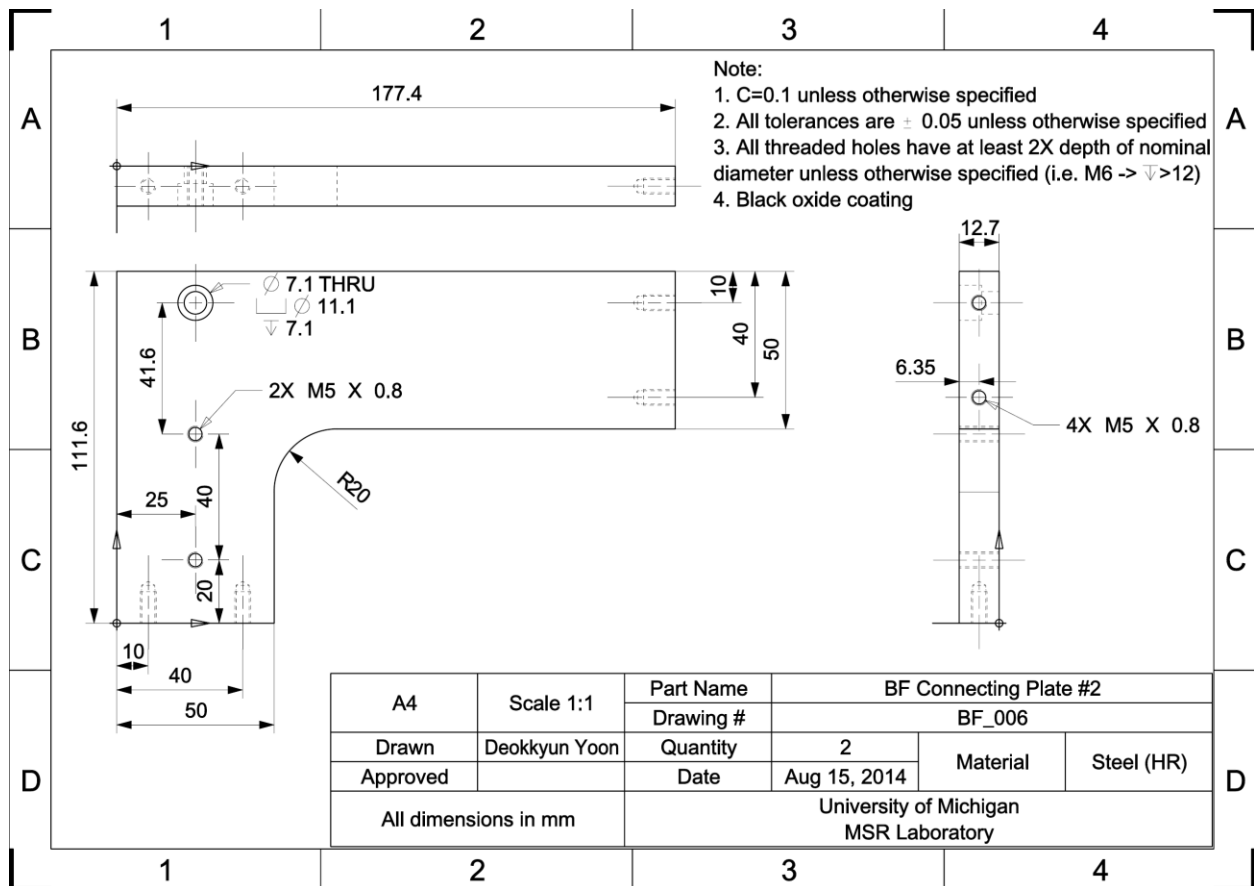


Figure B.11 Manufacturing drawing of Base Frame Connecting Plate #2.

B.1.6 Base Frame Connecting Plate #3

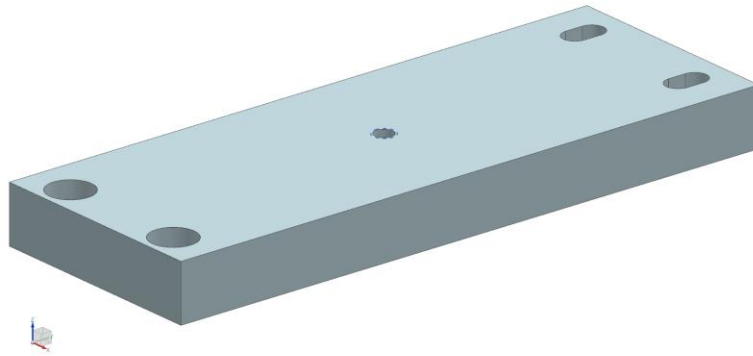


Figure B.12 Isometric view of Base Frame Connecting Plate #3.

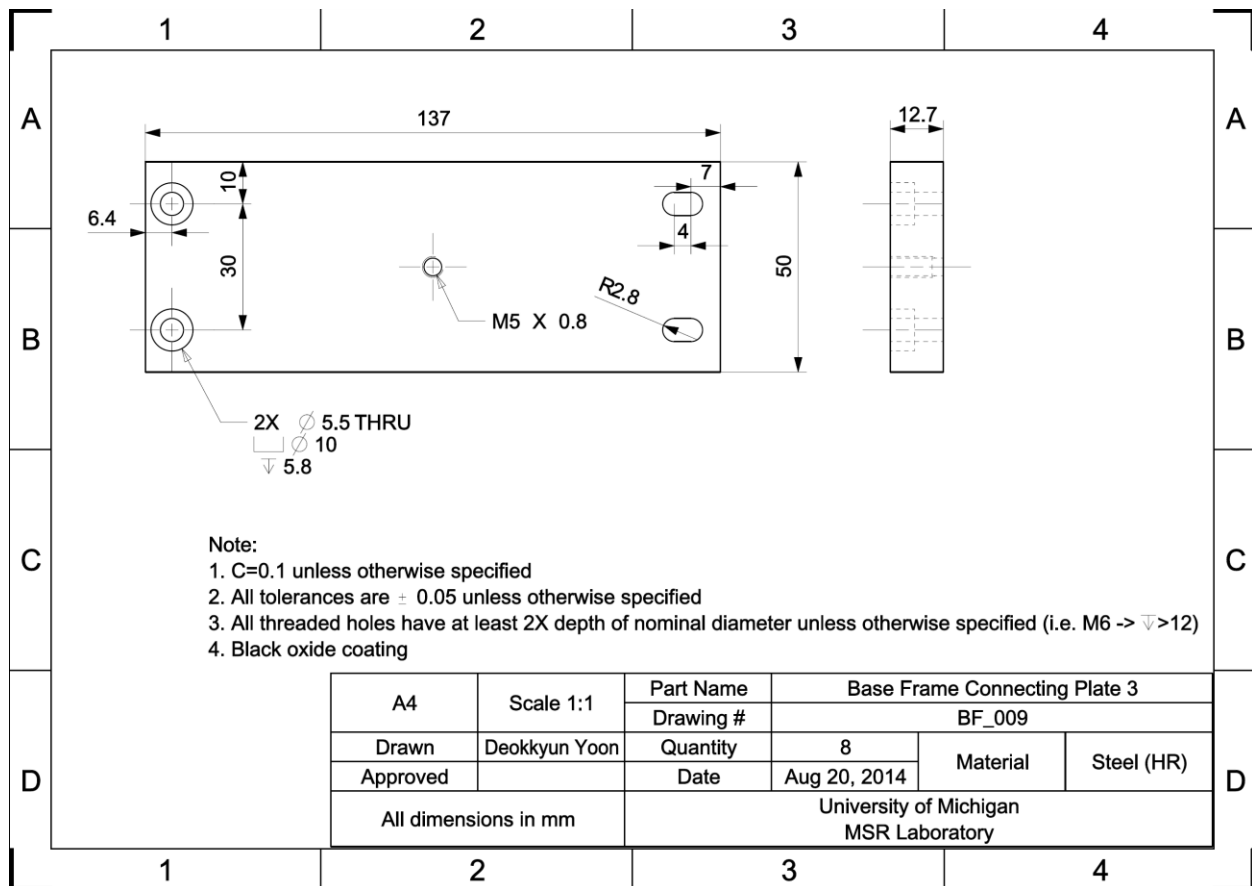


Figure B.13 Manufacturing drawing of Base Frame Connecting Plate #3.

B.1.7 Air Spring Mount #1

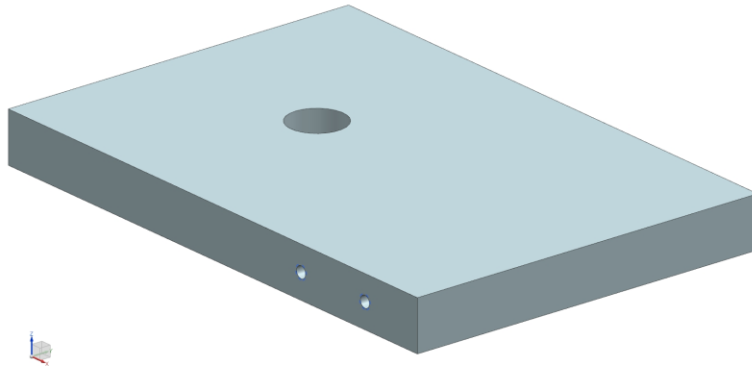


Figure B.14 Isometric view of Air Spring Mount #1.

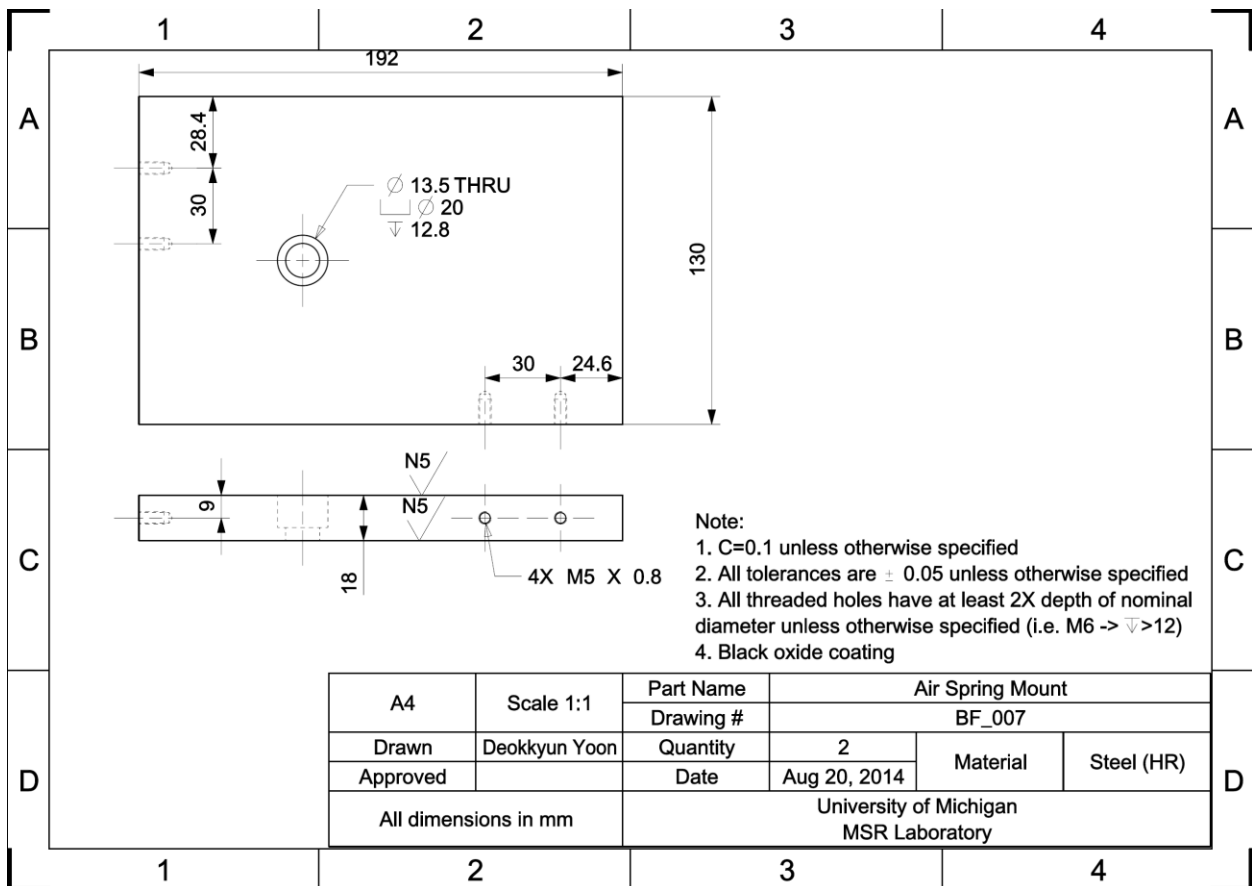


Figure B.15 Manufacturing drawing of Air Spring Mount #1.

B.1.8 Air Spring Mount #2

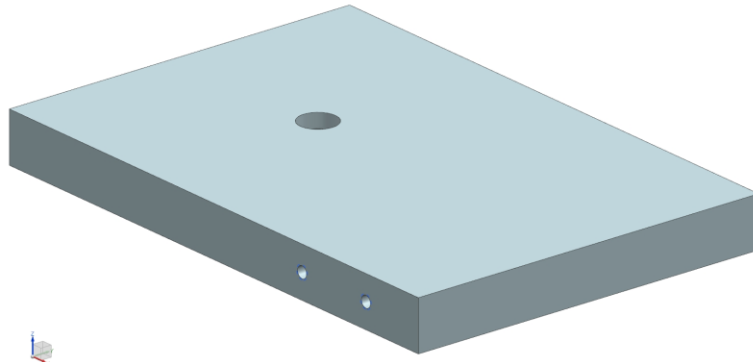


Figure B.16 Isometric view of Air Spring Mount #2.

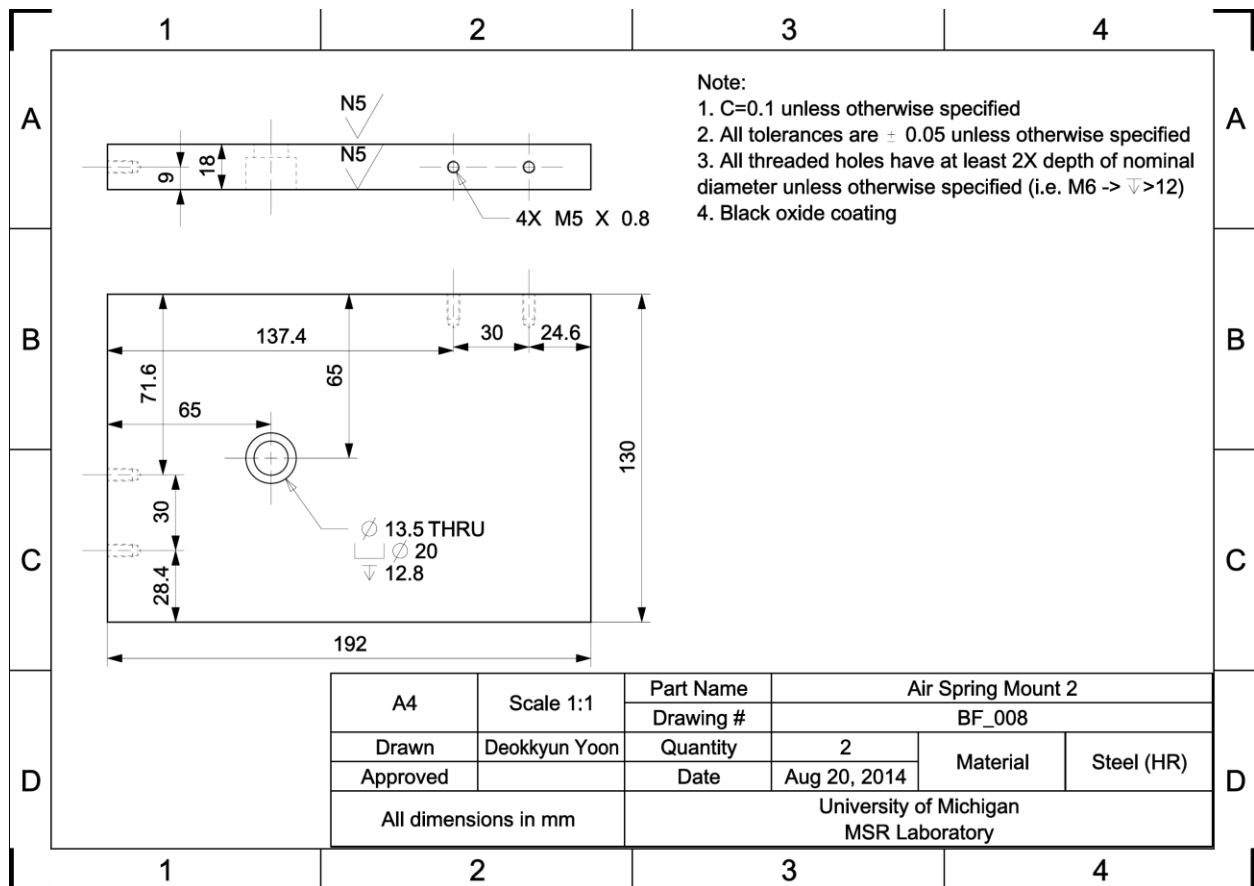


Figure B.17 Manufacturing drawing of Air Spring Mount #2.

B.1.9 Cable Carrier Plate

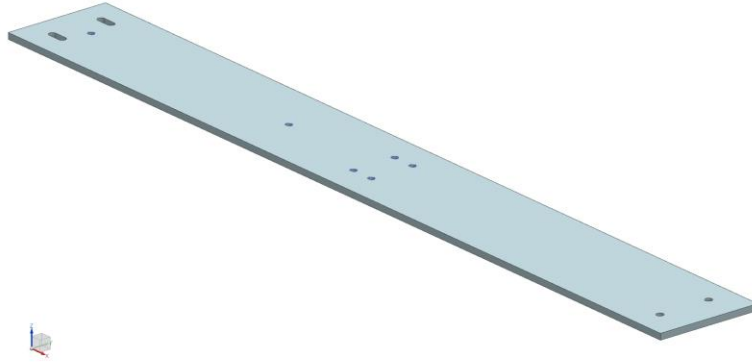


Figure B.18 Isometric view of Cable Carrier Plate.

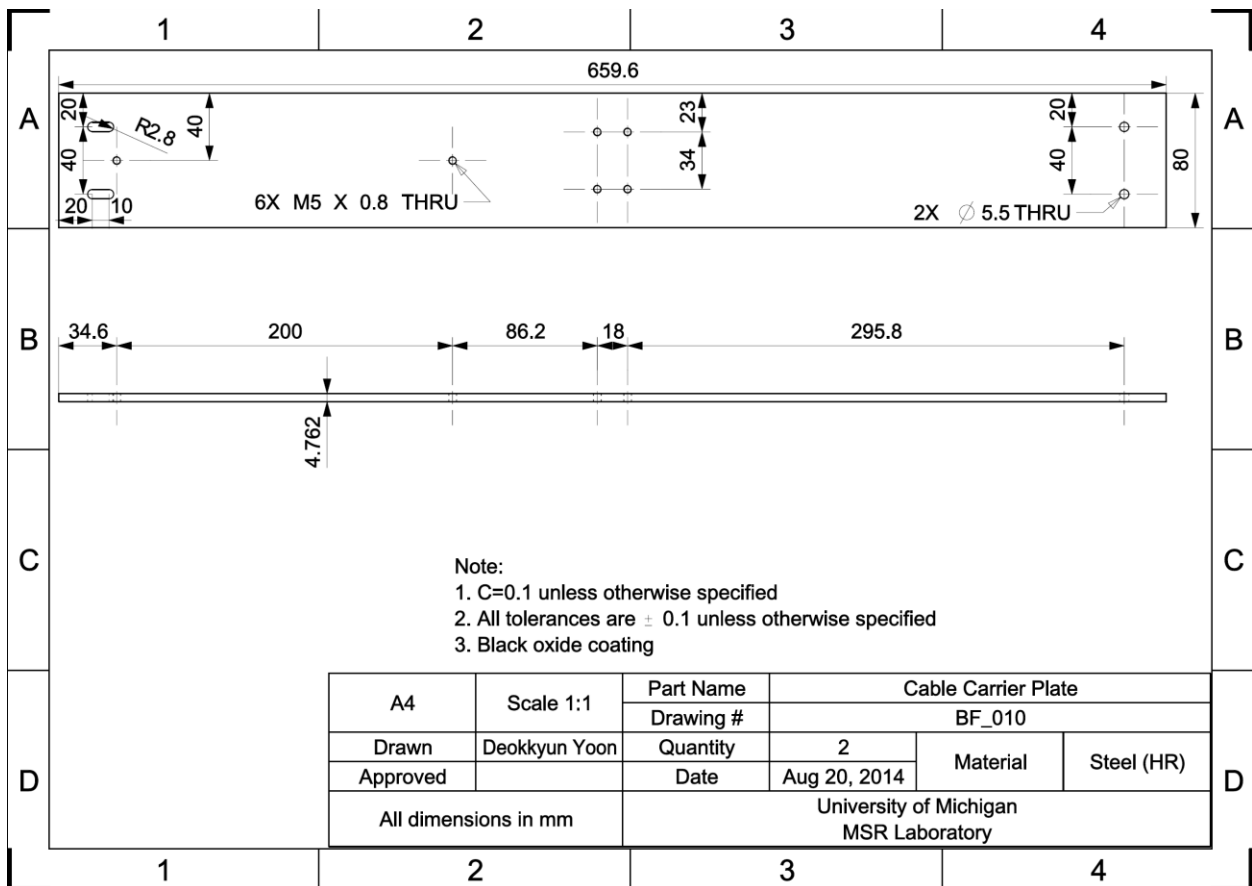


Figure B.19 Manufacturing drawing of Cable Carrier Plate.

B.1.10 Encoder Readhead Mount

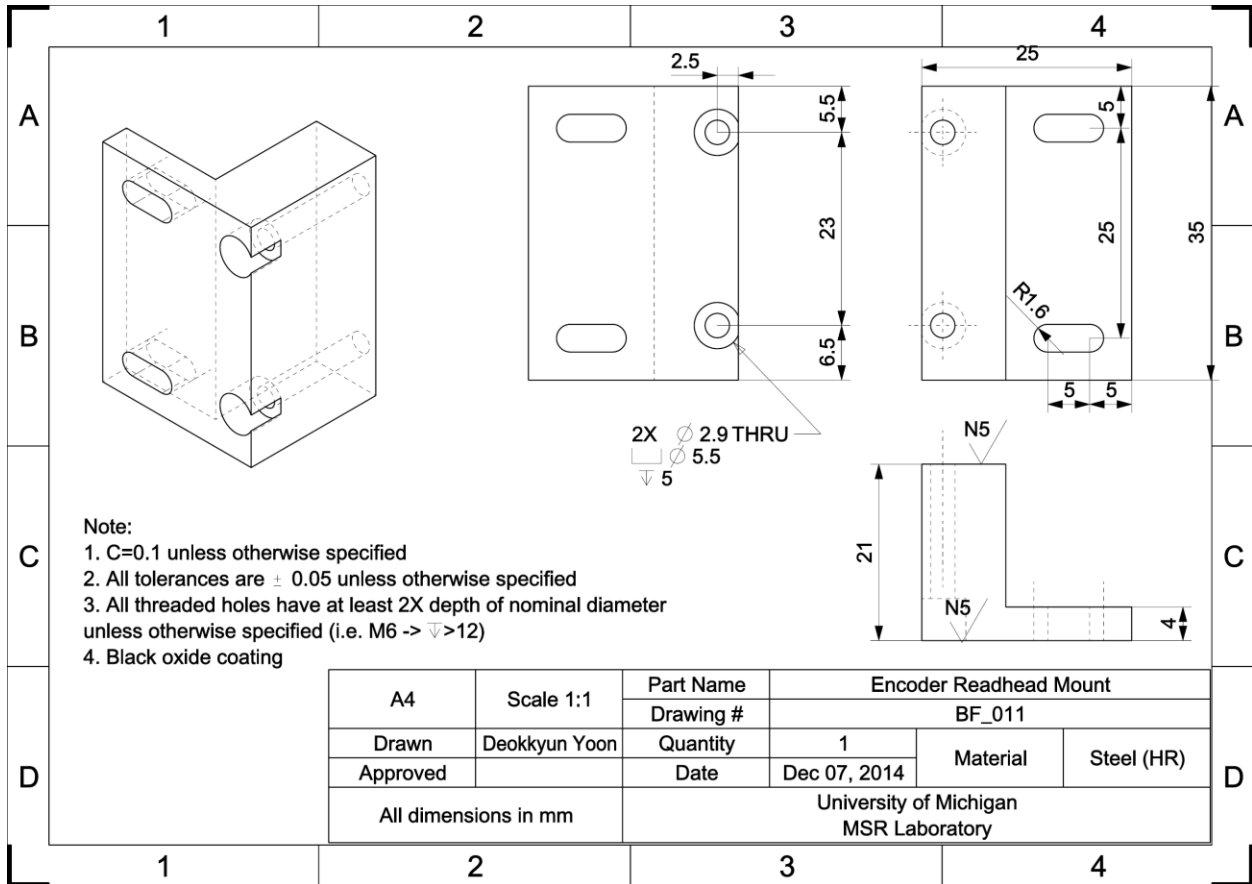


Figure B.20 Manufacturing drawing of Encoder Readhead Mount.

B.1.11 Spacer

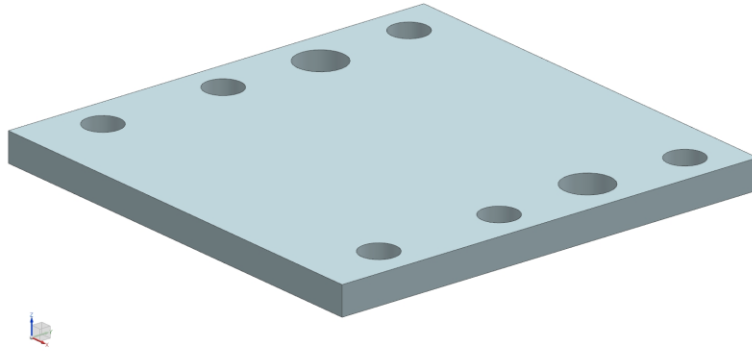


Figure B.21 Isometric view of Spacer.

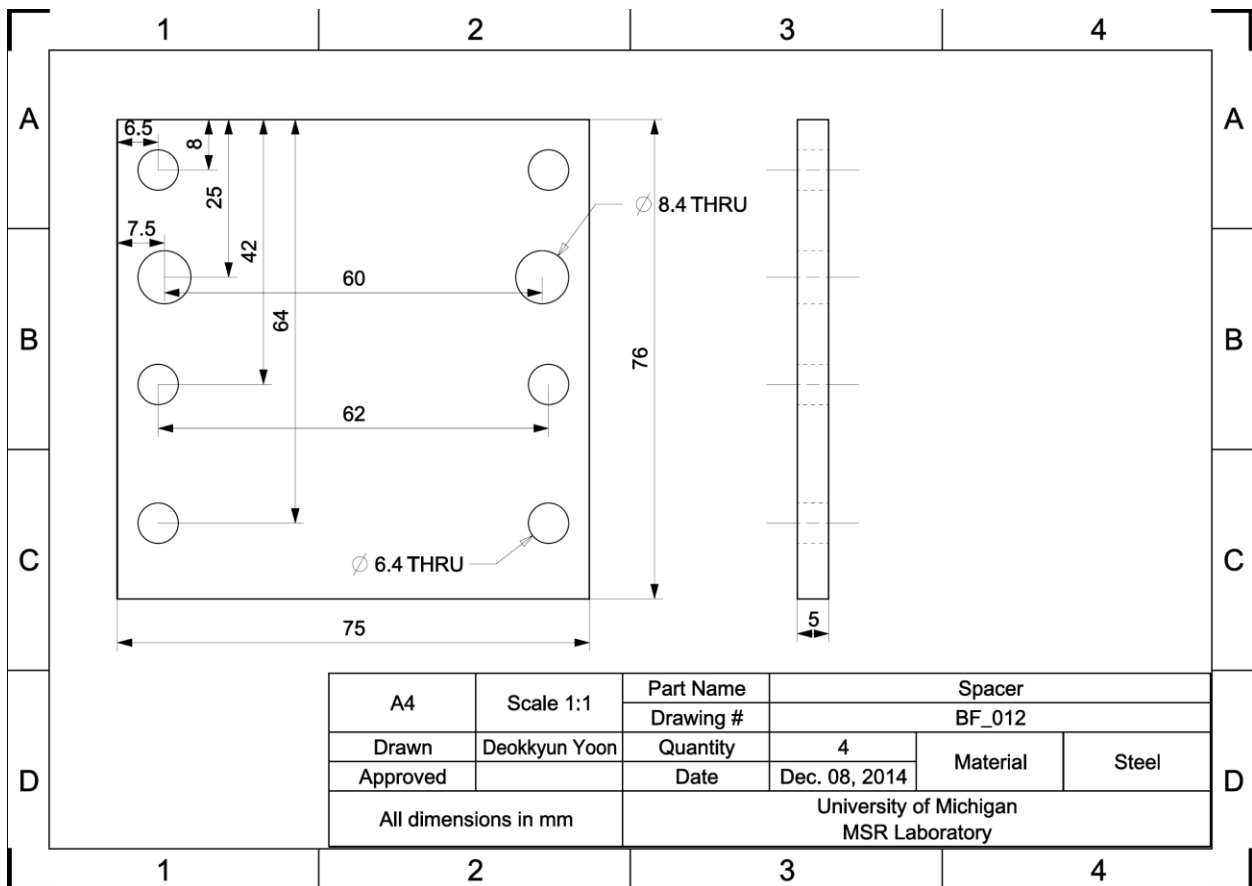


Figure B.22 Manufacturing drawing of Spacer.

B.1.12 Shaft Support (modification)

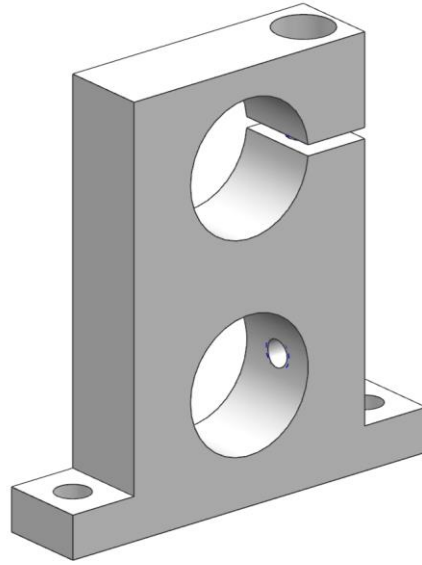


Figure B.23 Isometric view of modified Shaft Support.

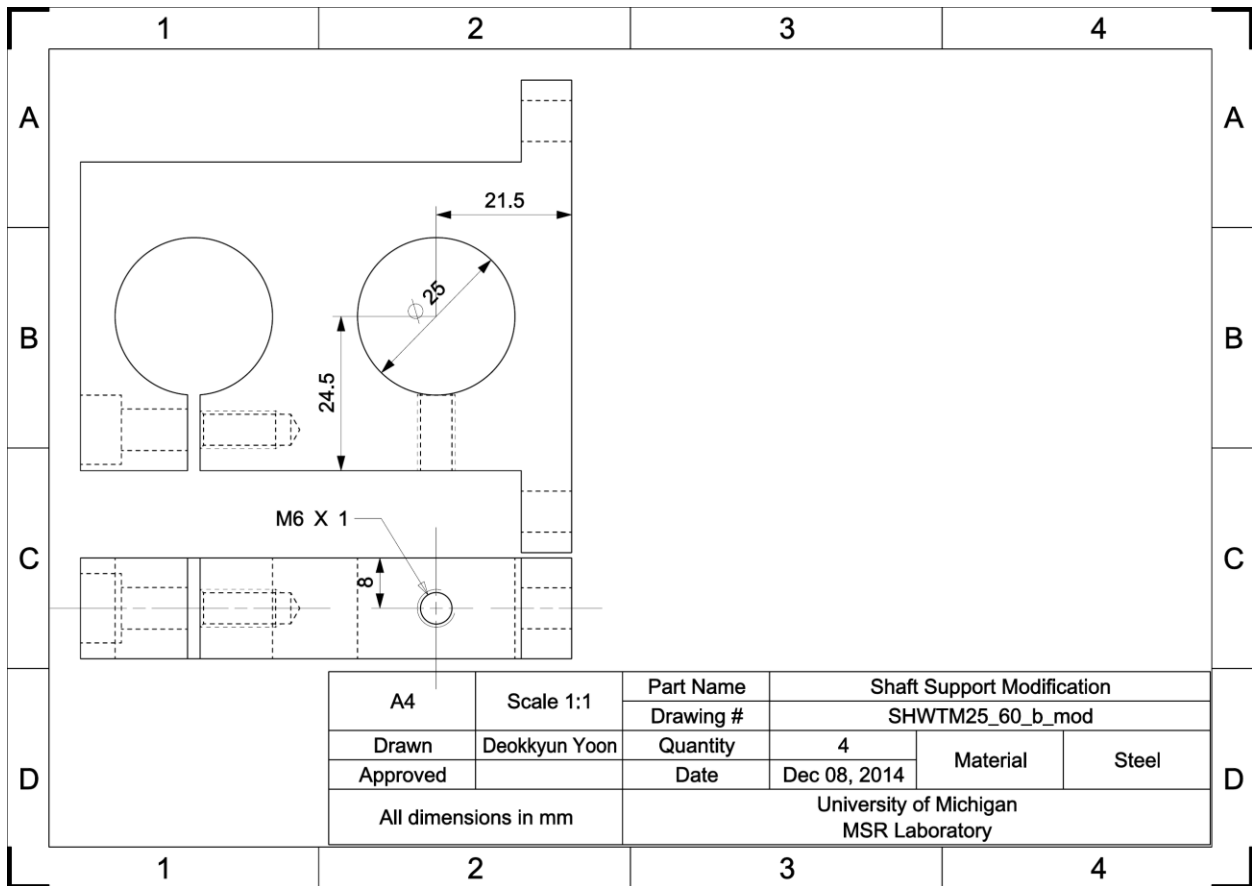


Figure B.24 Manufacturing drawing of modified Shaft Support.

B.2 CAD drawings for Machine Frame

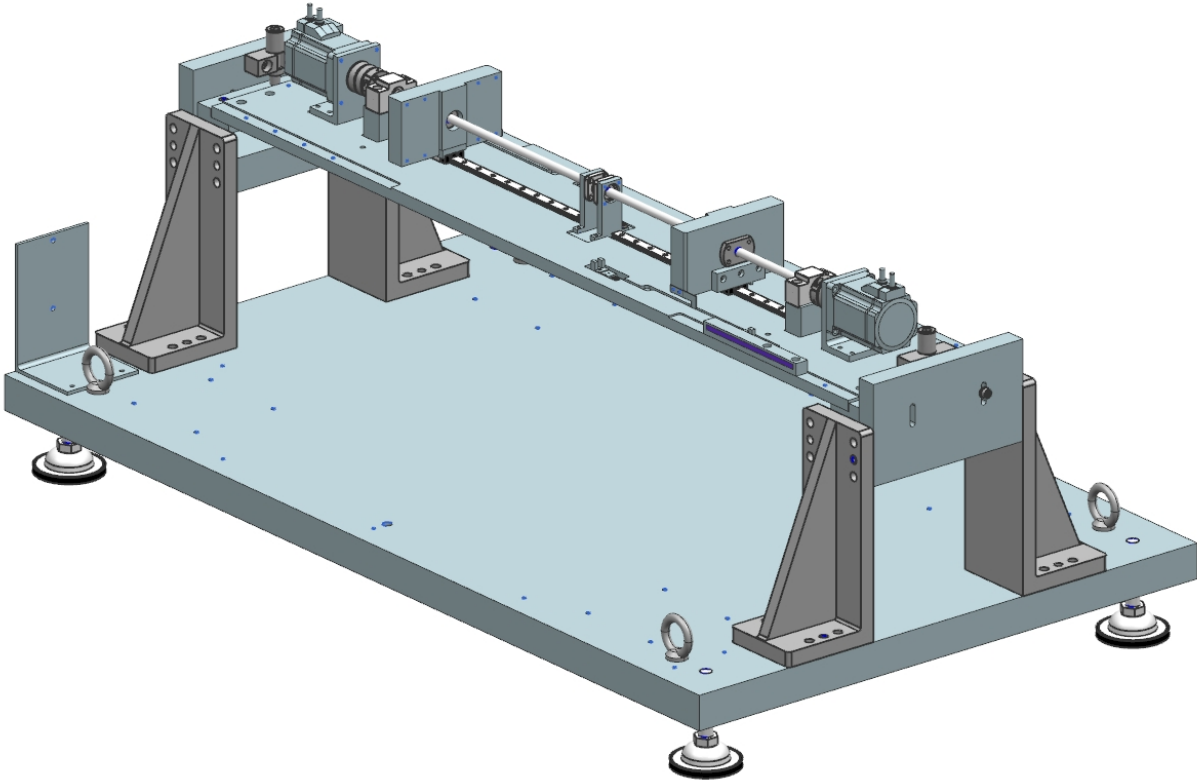


Figure B.25 Isometric view of Machine Frame sub-assembly.

B.2.1 Connecting Plate

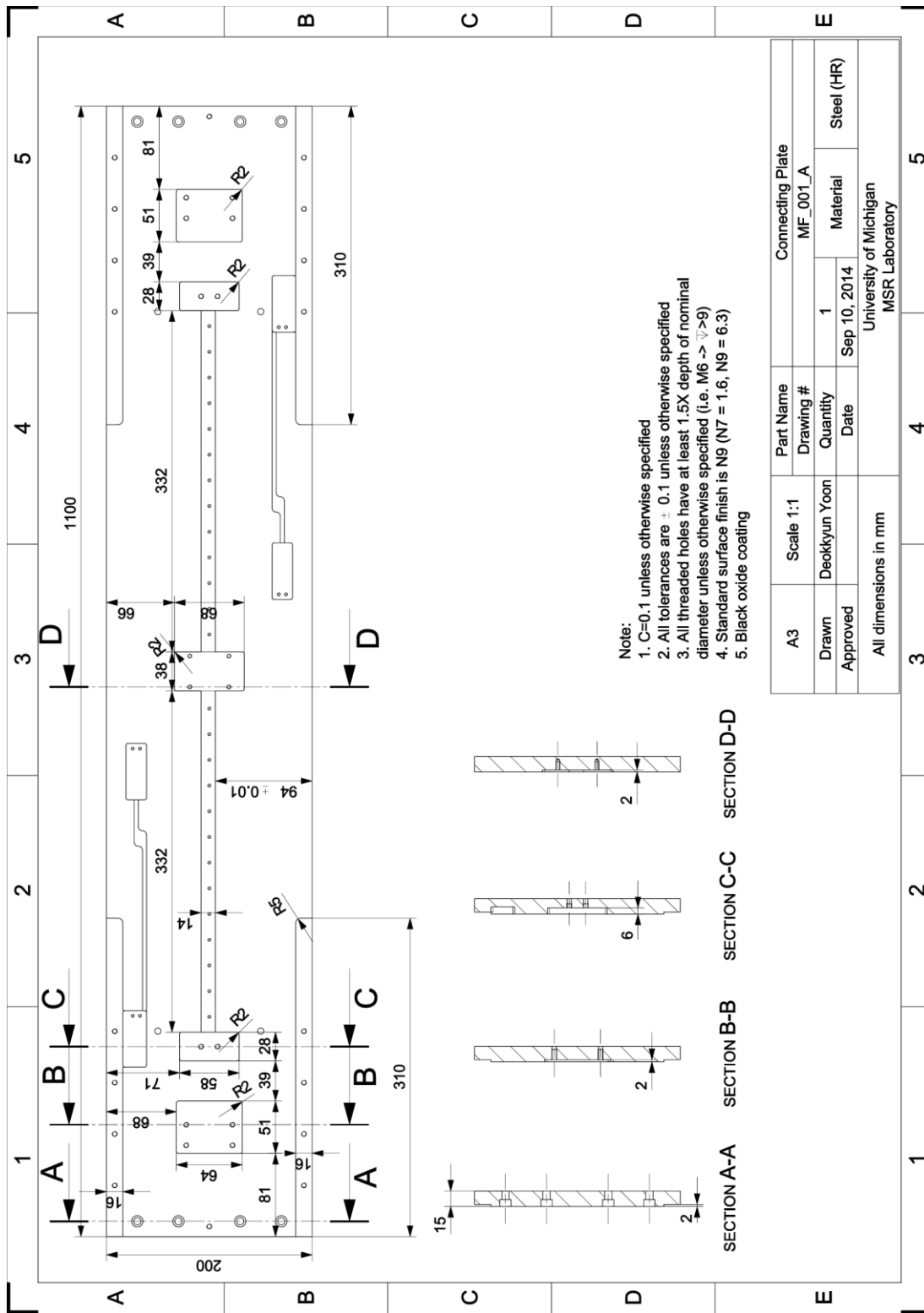


Figure B.26 Manufacturing drawing of Connecting Plate (pg. 1 of 3).

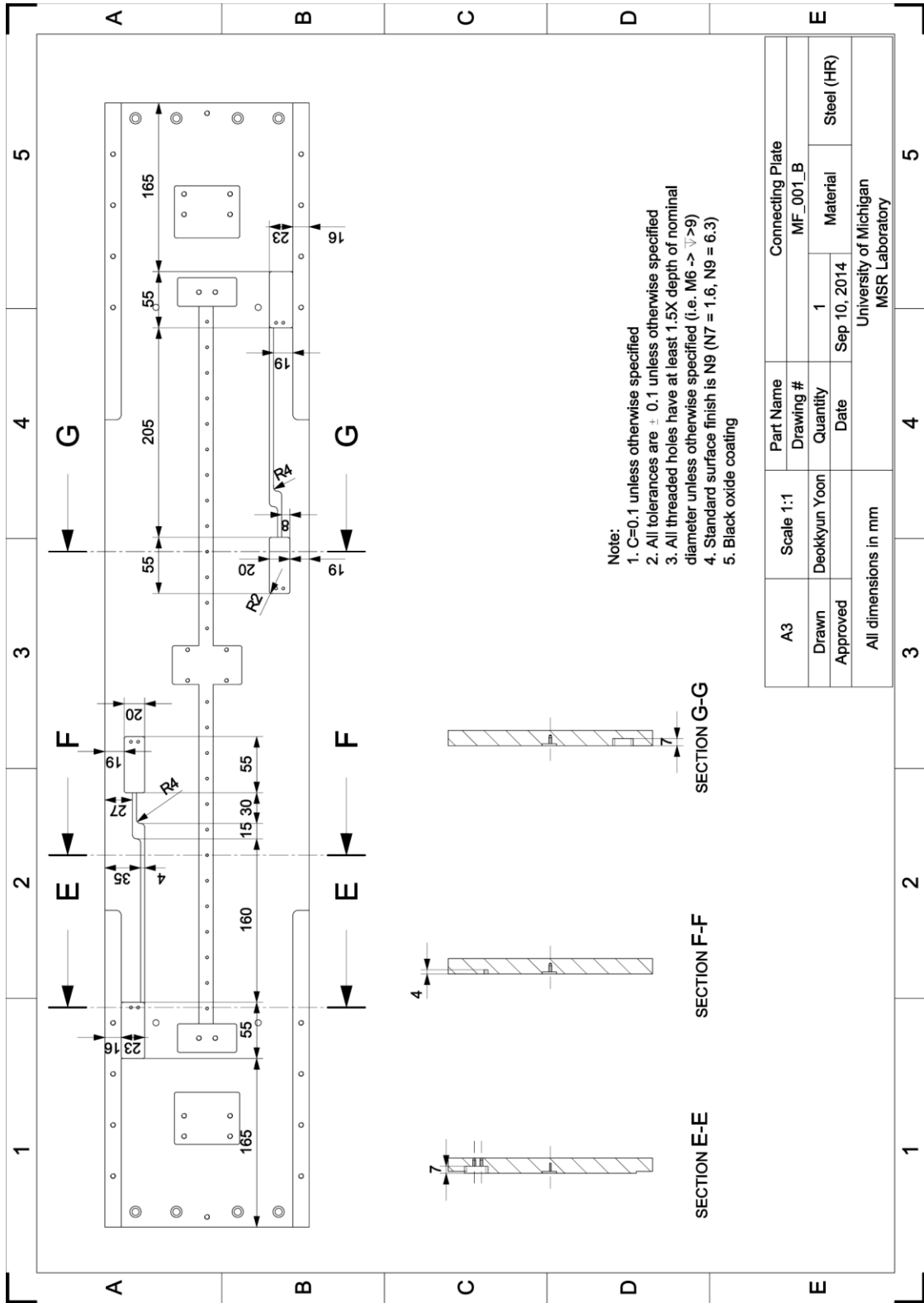
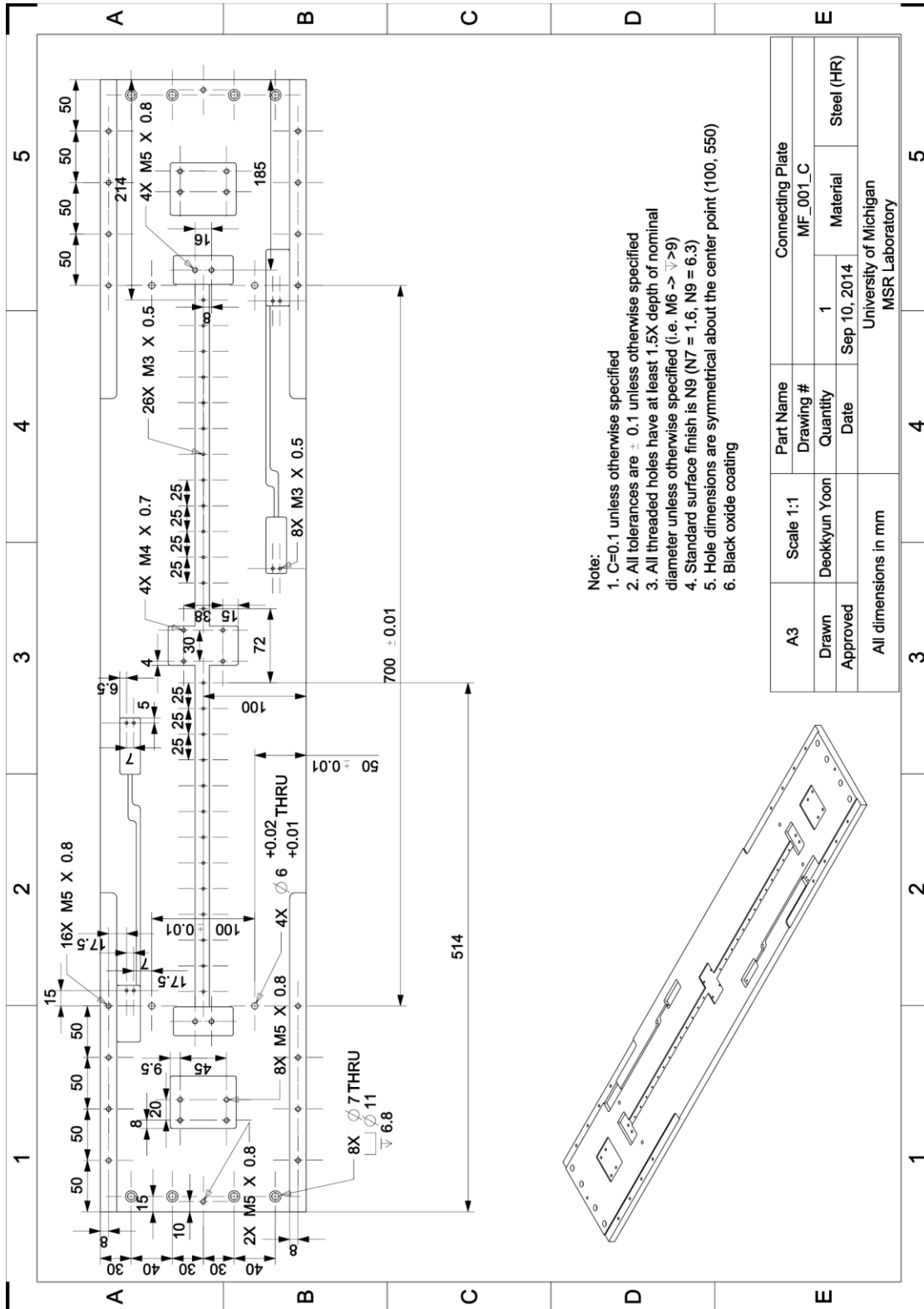


Figure B.27 Manufacturing drawing of Connecting Plate (pg. 2 of 3).



- Note:
1. C=0.1 unless otherwise specified
 2. All tolerances are ± 0.1 unless otherwise specified
 3. All threaded holes have at least 1.5X depth of nominal diameter unless otherwise specified (i.e. M6 \rightarrow ∇ >9)
 4. Standard surface finish is N9 (N7 = 1.6, N9 = 6.3)
 5. Hole dimensions are symmetrical about the center point (100, 550)
 6. Black oxide coating

A3	Scale 1:1	Part Name	Connecting Plate	
Drawn	Deokkyun Yoon	Drawing #	MF_001_C	
Approved		Quantity	1	Material
All dimensions in mm		Date	Sep 10, 2014	Steel (HR)
		University of Michigan MSR Laboratory		

Figure B.28 Manufacturing drawing of Connecting Plate (pg. 3 of 3).

B.2.2 Nut Mounting Block

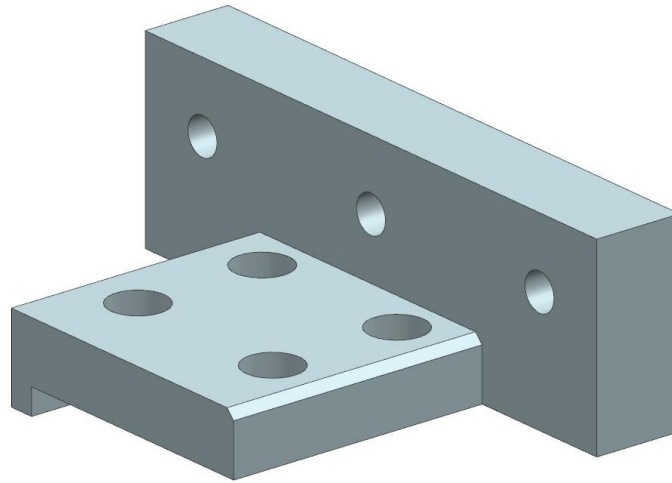


Figure B.29 Isometric view of Nut Mounting Block.

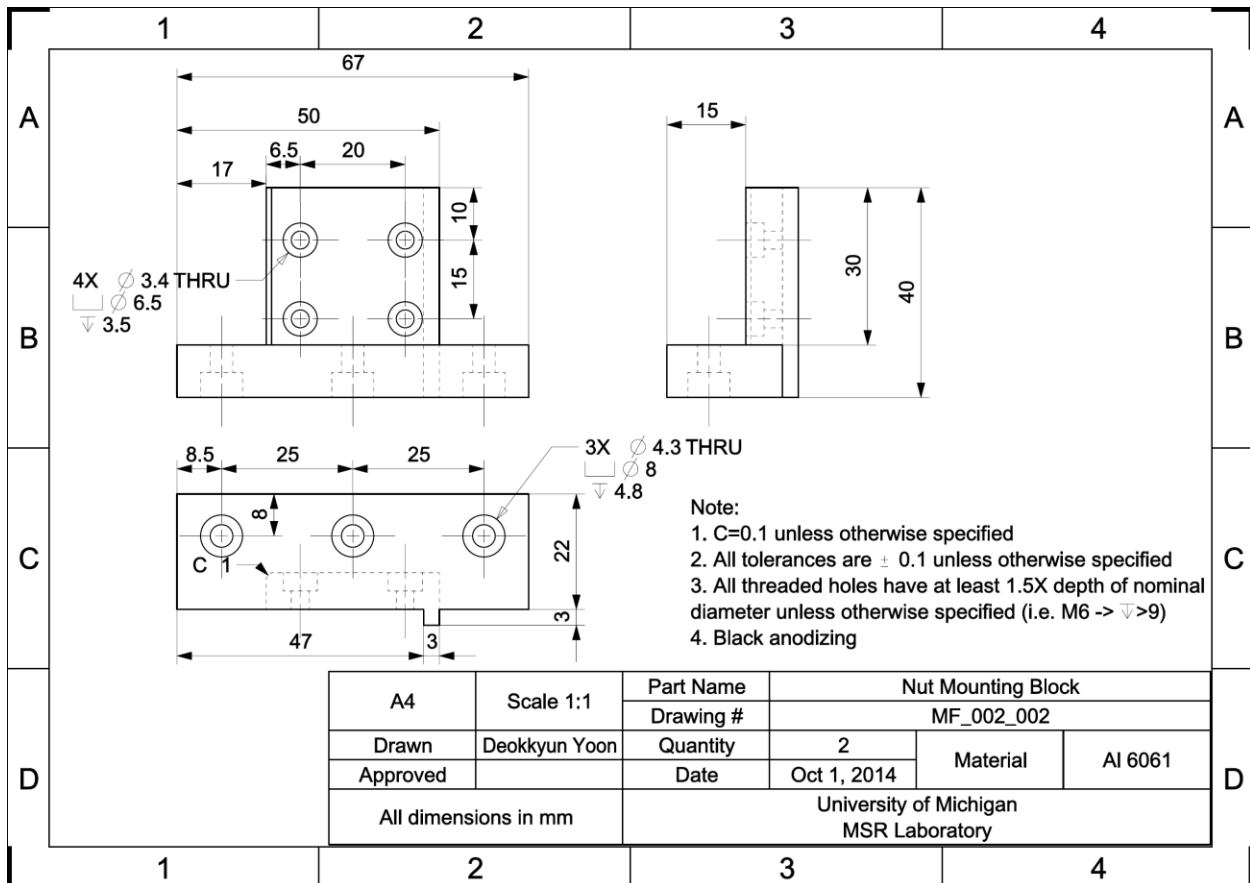


Figure B.30 Manufacturing drawing of Nut Mounting Block.

B.2.3 Nut Mounting Plate

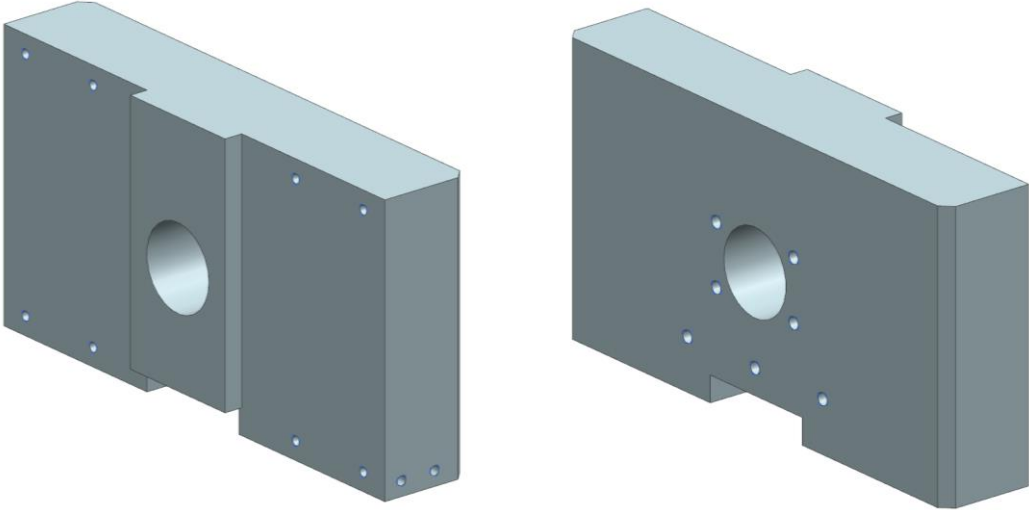


Figure B.31 Isometric views of Nut Mounting Plate.

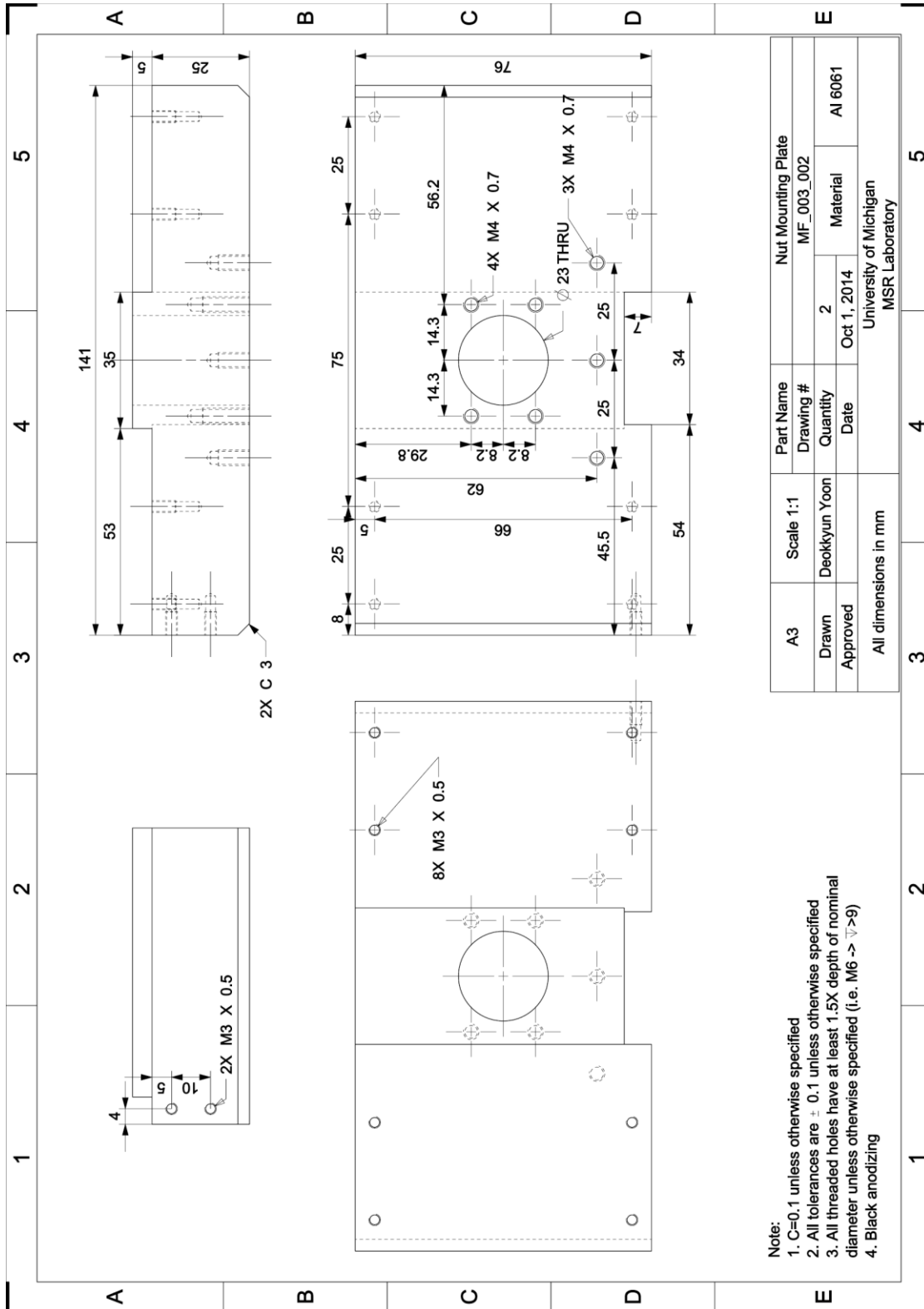


Figure B.32 Manufacturing drawing of Nut Mounting Plate.

B.2.4 Fixed Side Plate

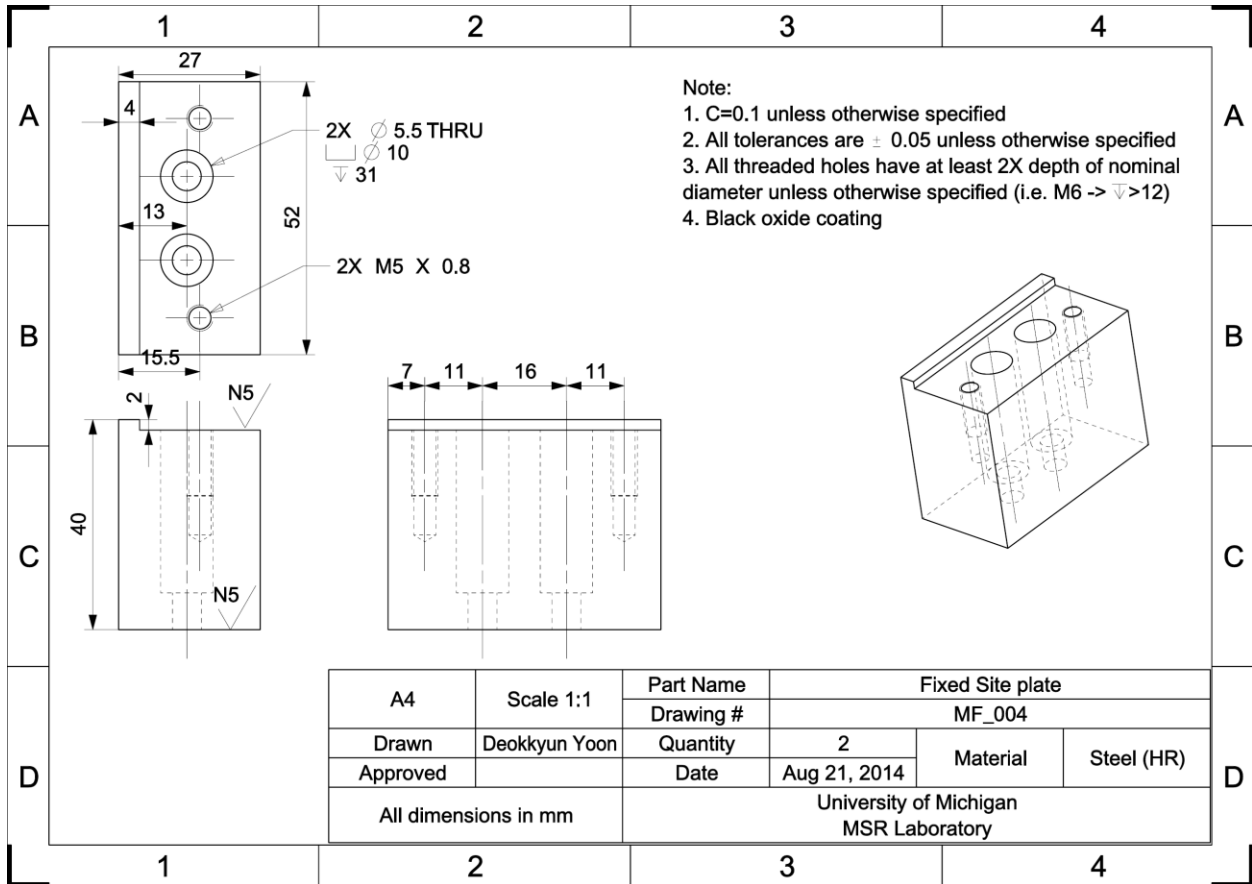


Figure B.33 Manufacturing drawing of Fixed Side Plate.

B.2.5 Support Side Plate

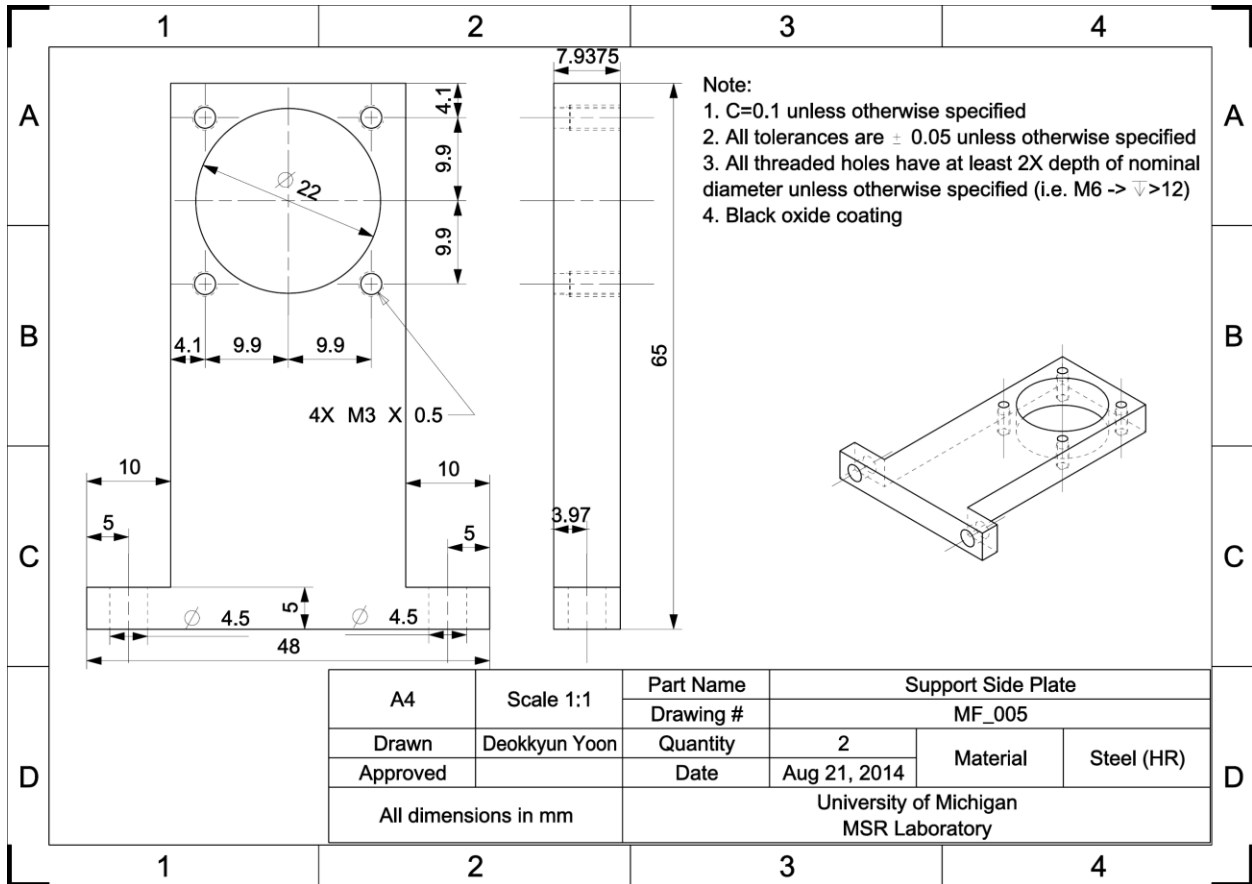


Figure B.34 Manufacturing drawing of Support Side Plate.

B.2.6 Step Motor Holder

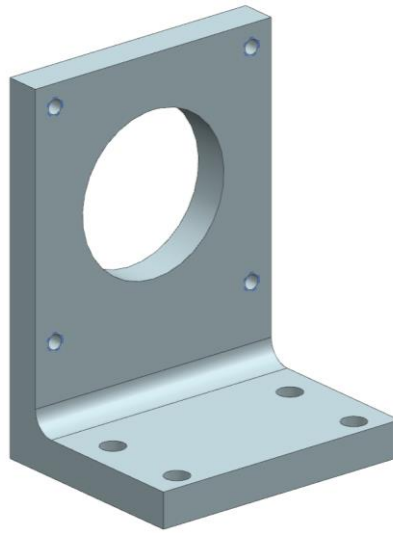


Figure B.35 Isometric view of Step Motor Holder.

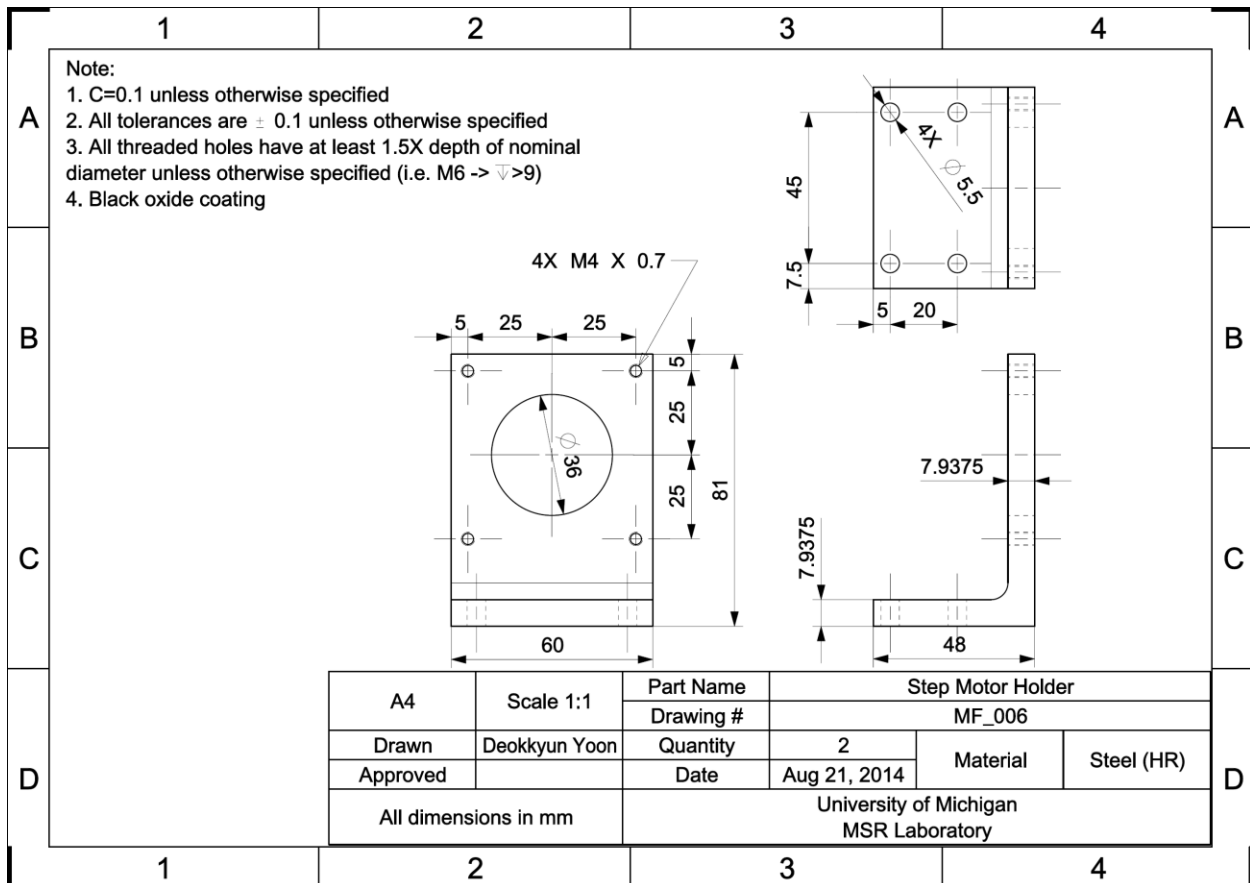


Figure B.36 Manufacturing drawing of Step Motor Holder.

B.2.7 Machine Frame Base

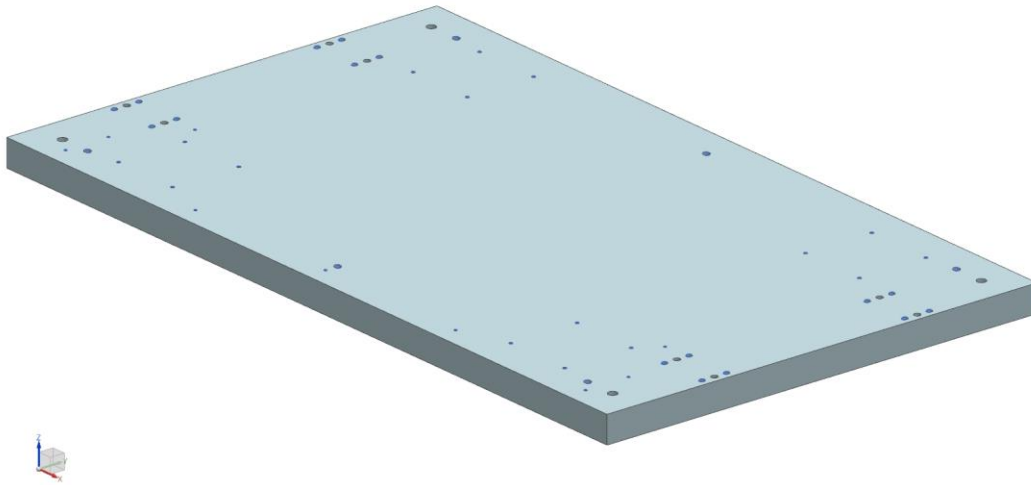


Figure B.37 Isometric view of Machine Frame Base.

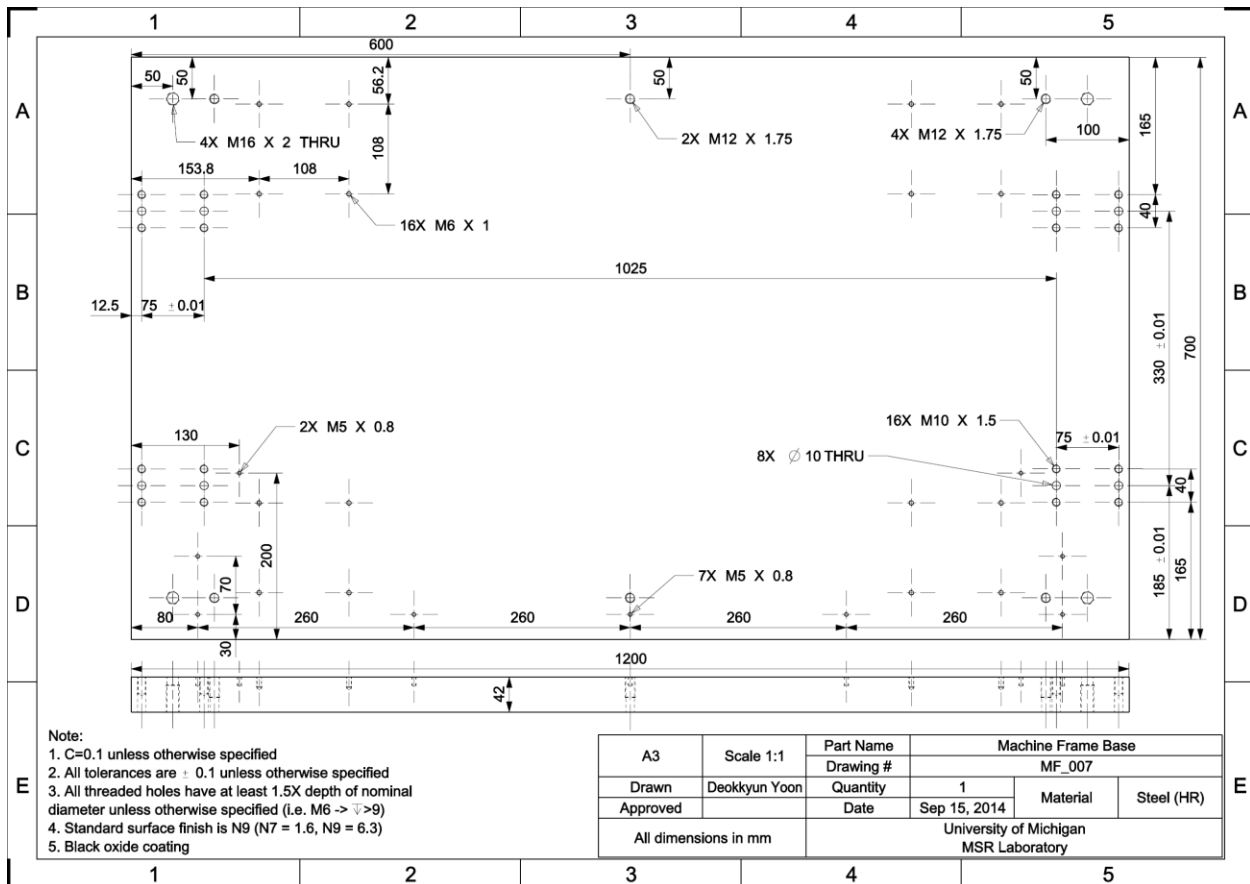


Figure B.38 Manufacturing drawing of Machine Frame Base.

B.2.8 Force Frame

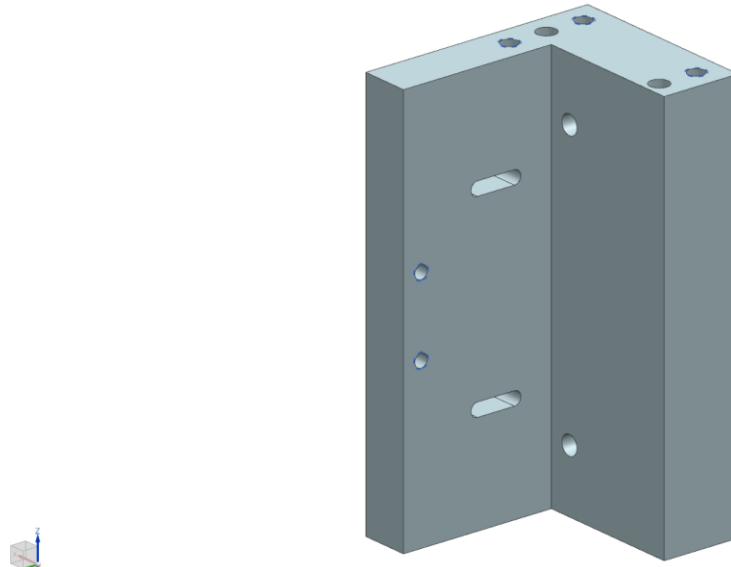


Figure B.39 Isometric view of Force Frame.

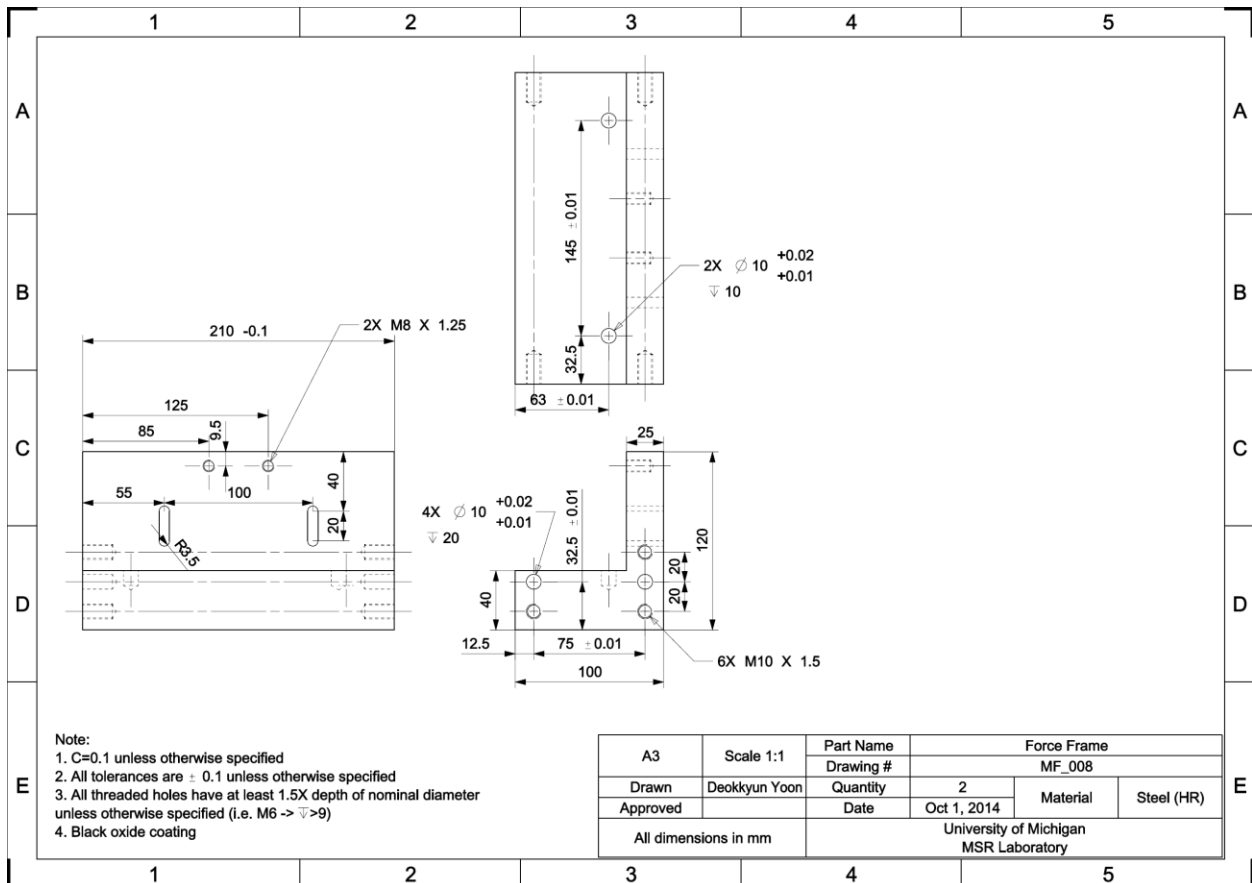


Figure B.40 Manufacturing drawing of Force Frame.

B.2.9 Force Frame #2

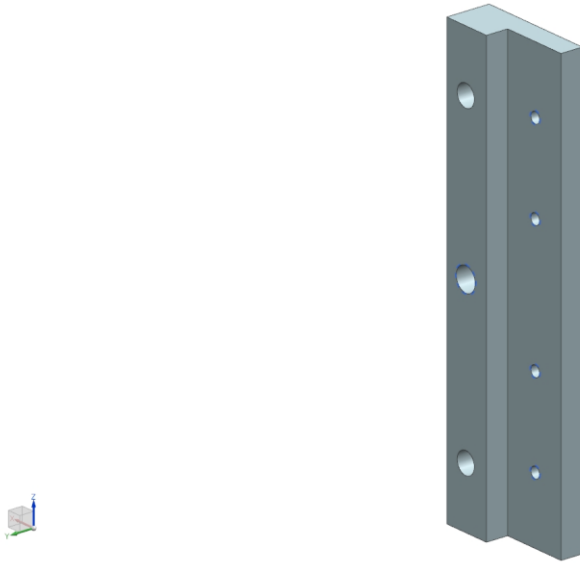


Figure B.41 Isometric view of Force Frame #2.

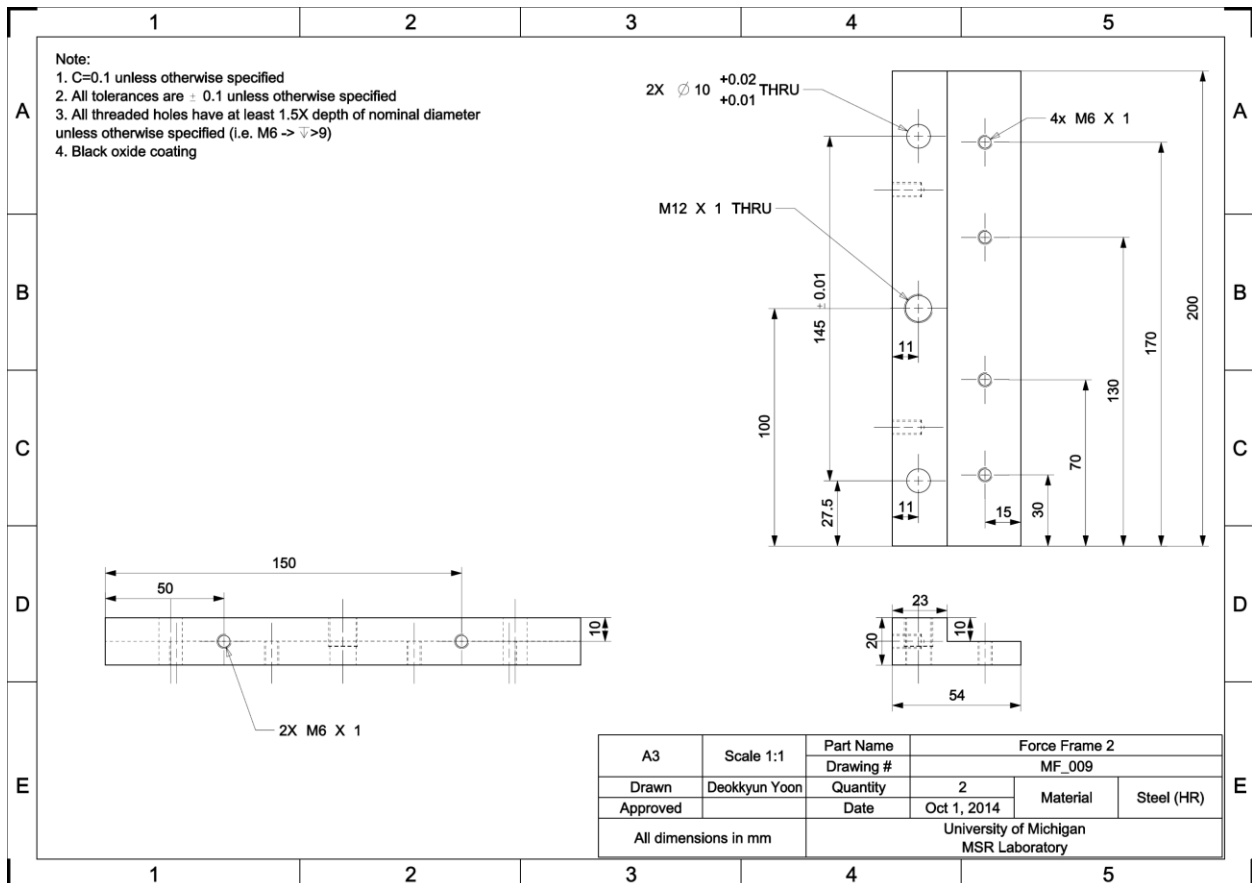


Figure B.42 Manufacturing drawing of Force Frame #2.

B.2.10 Limit sensor L

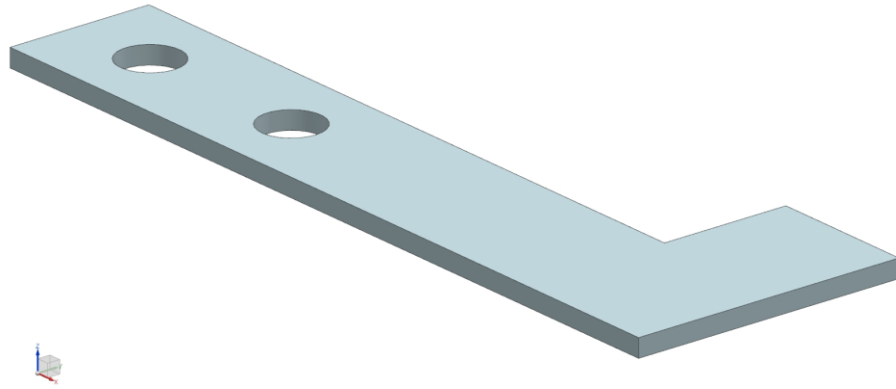


Figure B.43 Isometric view of Limit Sensor L.

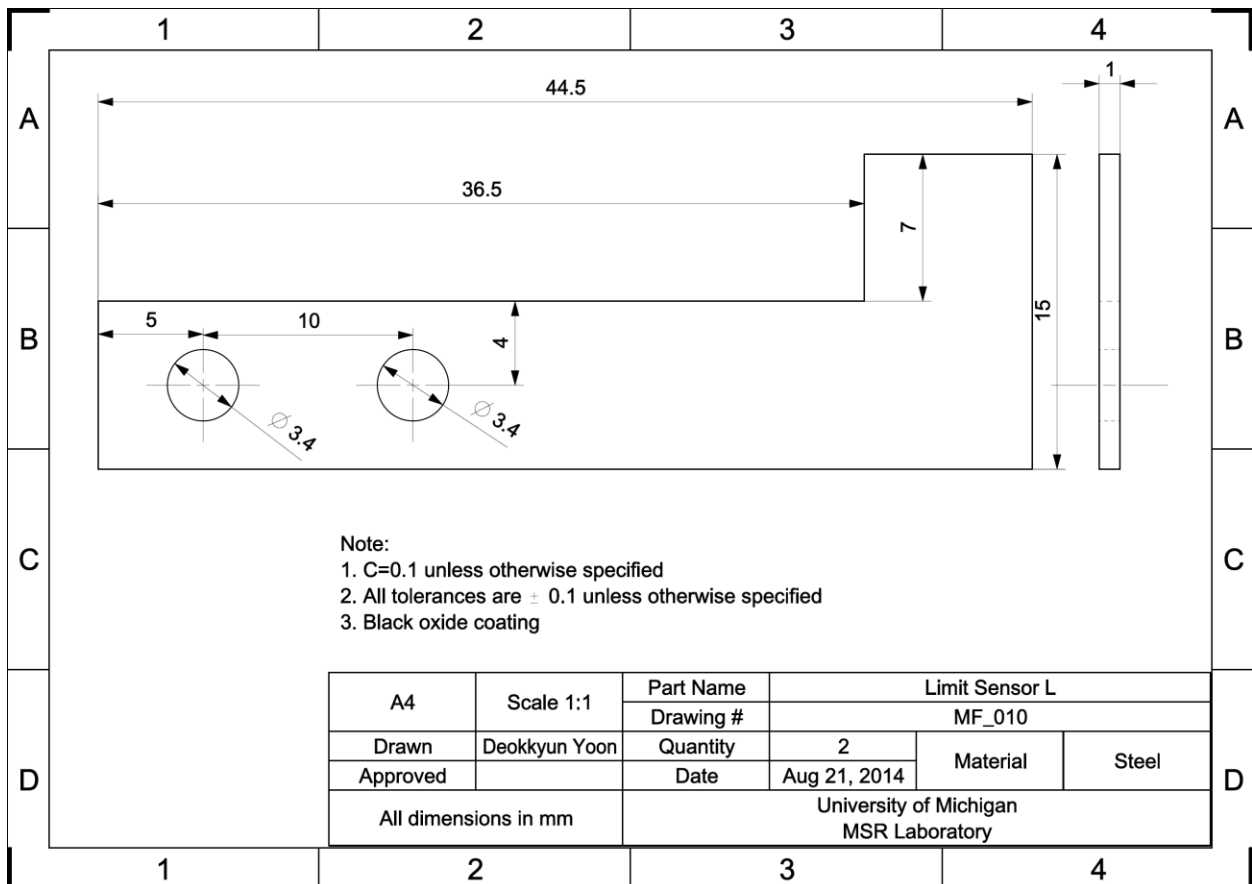


Figure B.44 Manufacturing drawing of Limit Sensor L.

B.2.11 Scale Mount

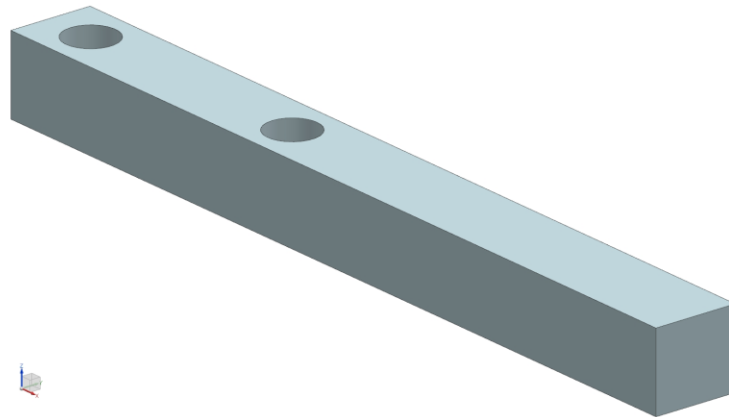


Figure B.45 Isometric view of Scale Mount.

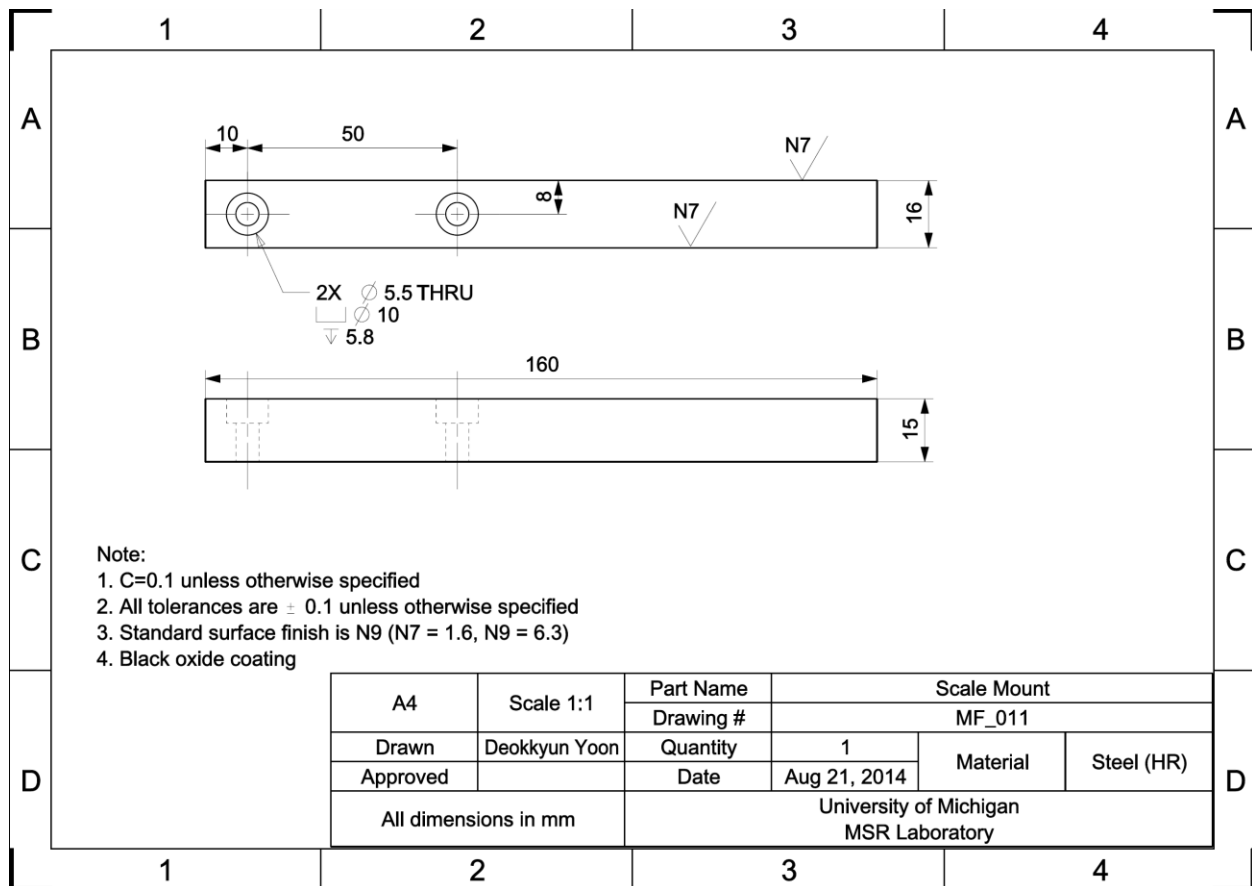


Figure B.46 Manufacturing drawing of Scale Mount.

B.3 CAD drawings for Wafer Table

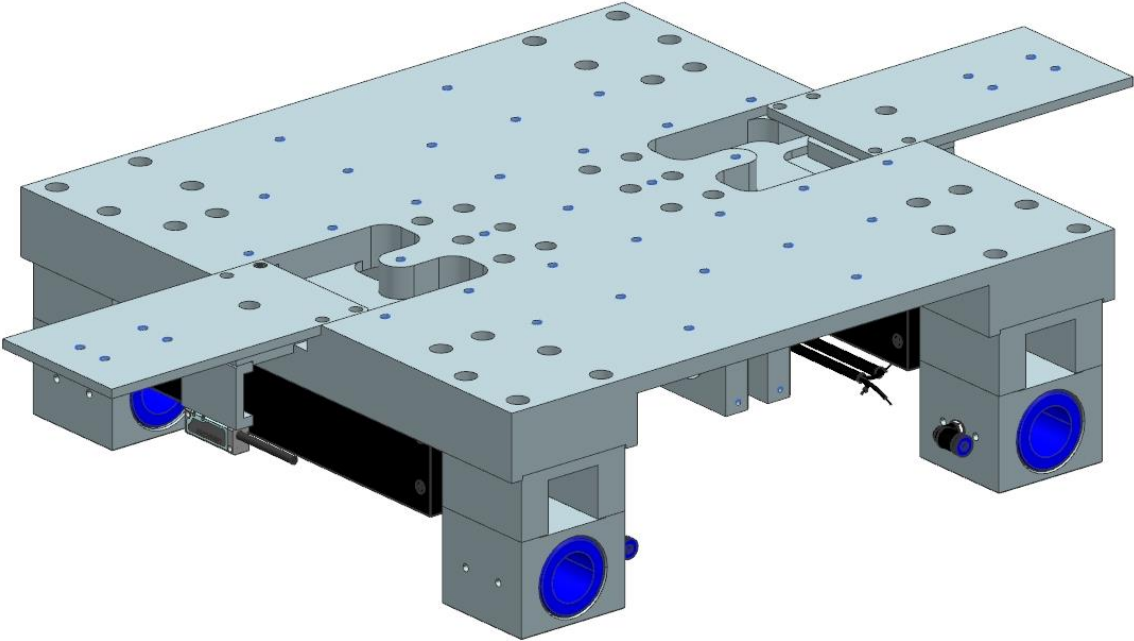


Figure B.47 Isometric view of Wafer Table sub-assembly.

B.3.1 Table

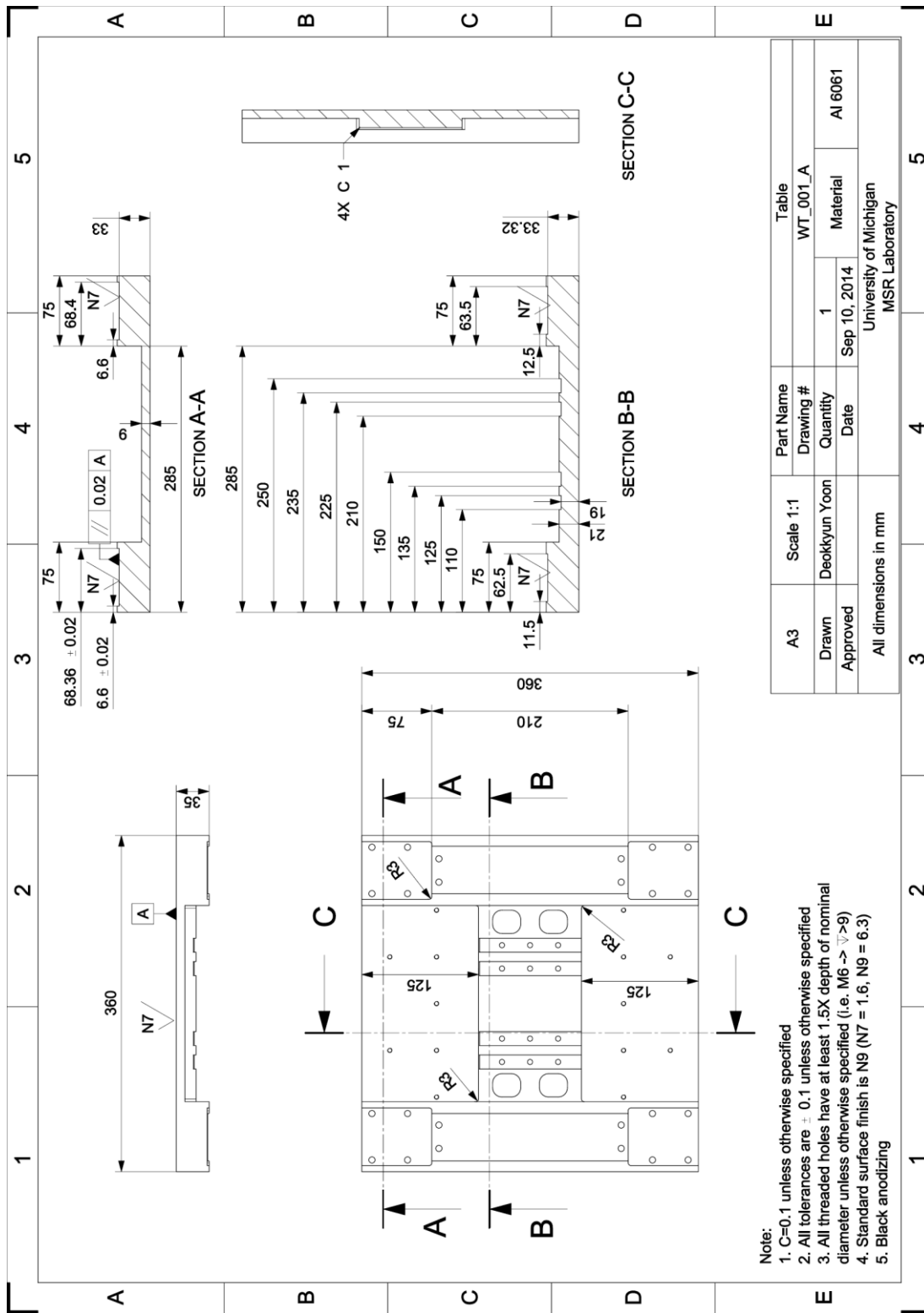


Figure B.48 Manufacturing drawing of Table (pg. 1 of 3).

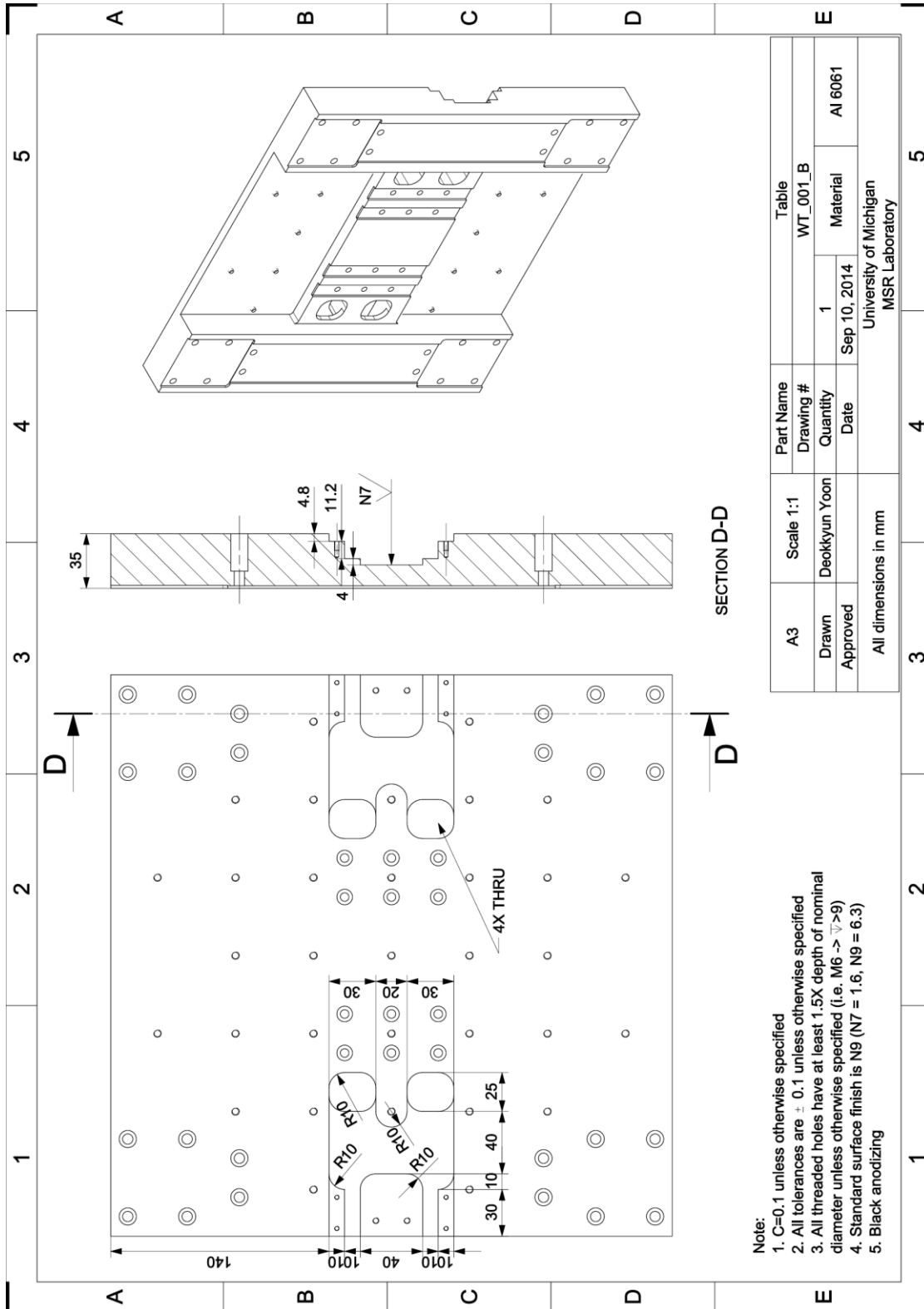


Figure B.49 Manufacturing drawing of Table (pg. 2 of 3).

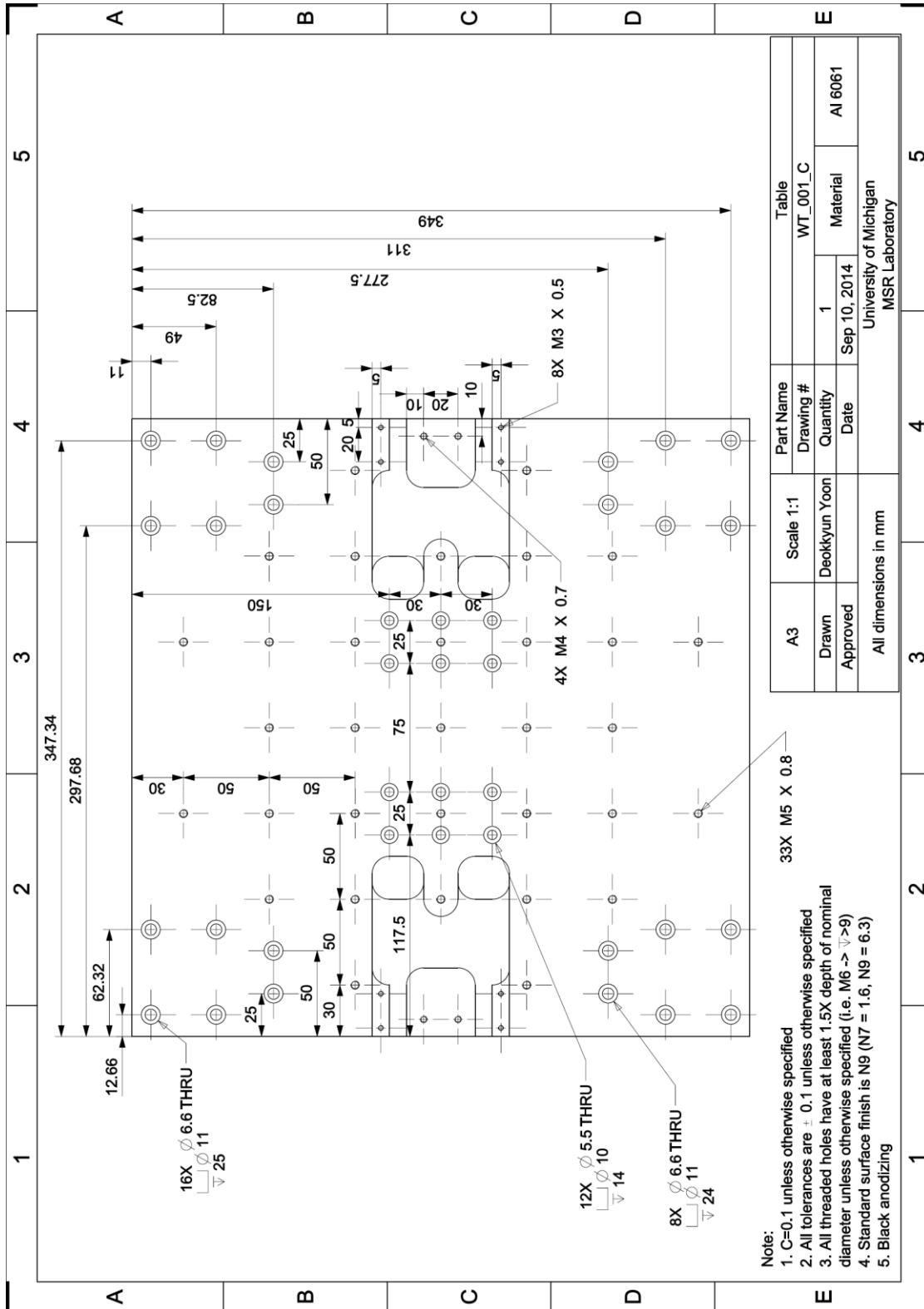


Figure B.50 Manufacturing drawing of Table (pg. 3 of 3).

B.3.2 Table (modification)

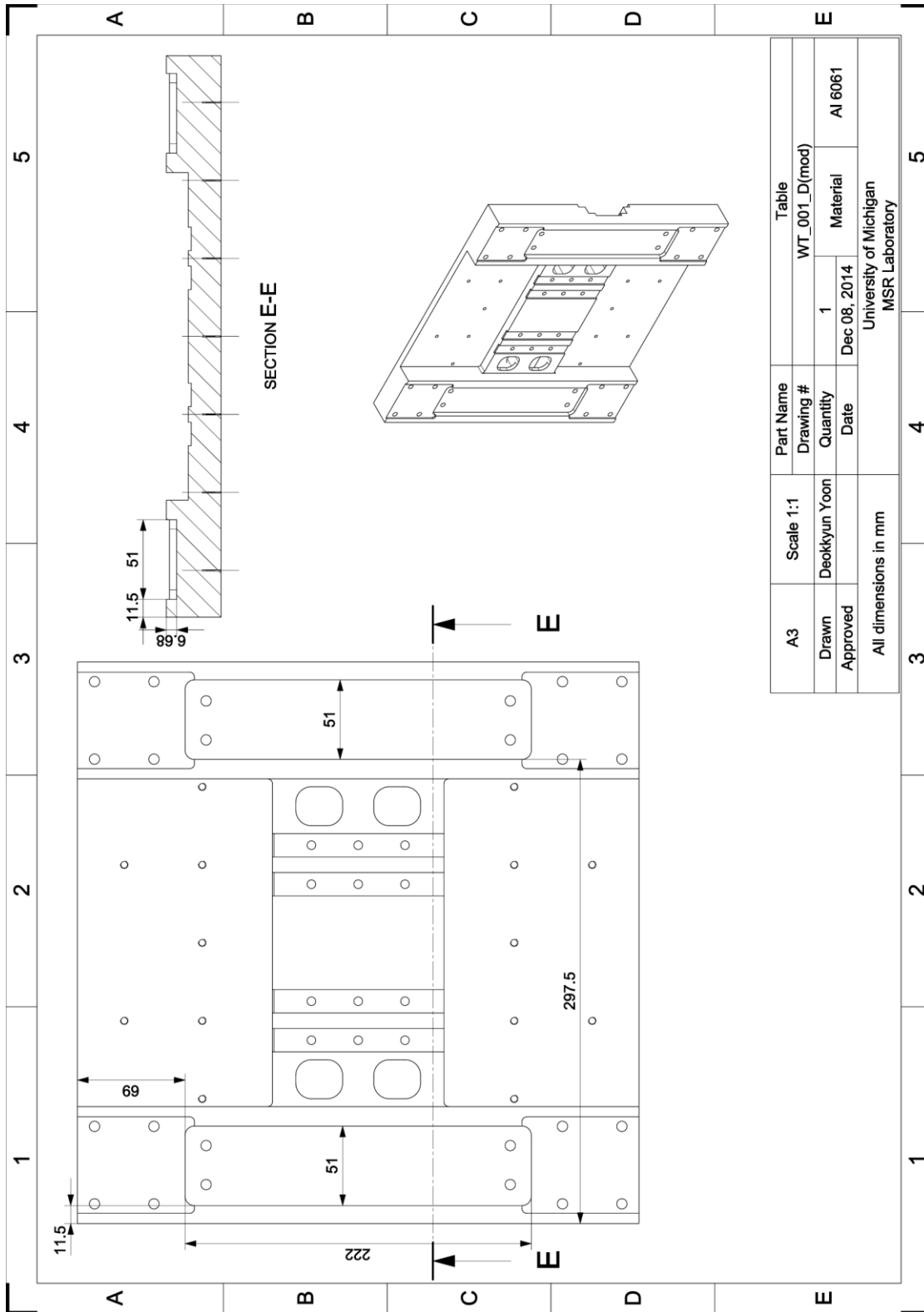


Figure B.51 Manufacturing drawing of modified Table.

B.3.3 PM Force Frame

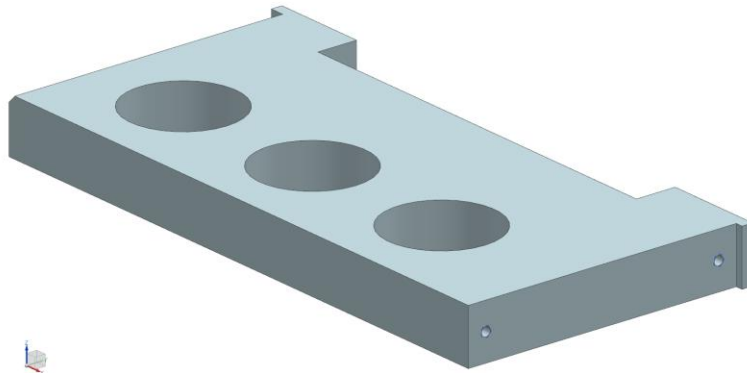


Figure B.52 Isometric view of PM Force Frame.

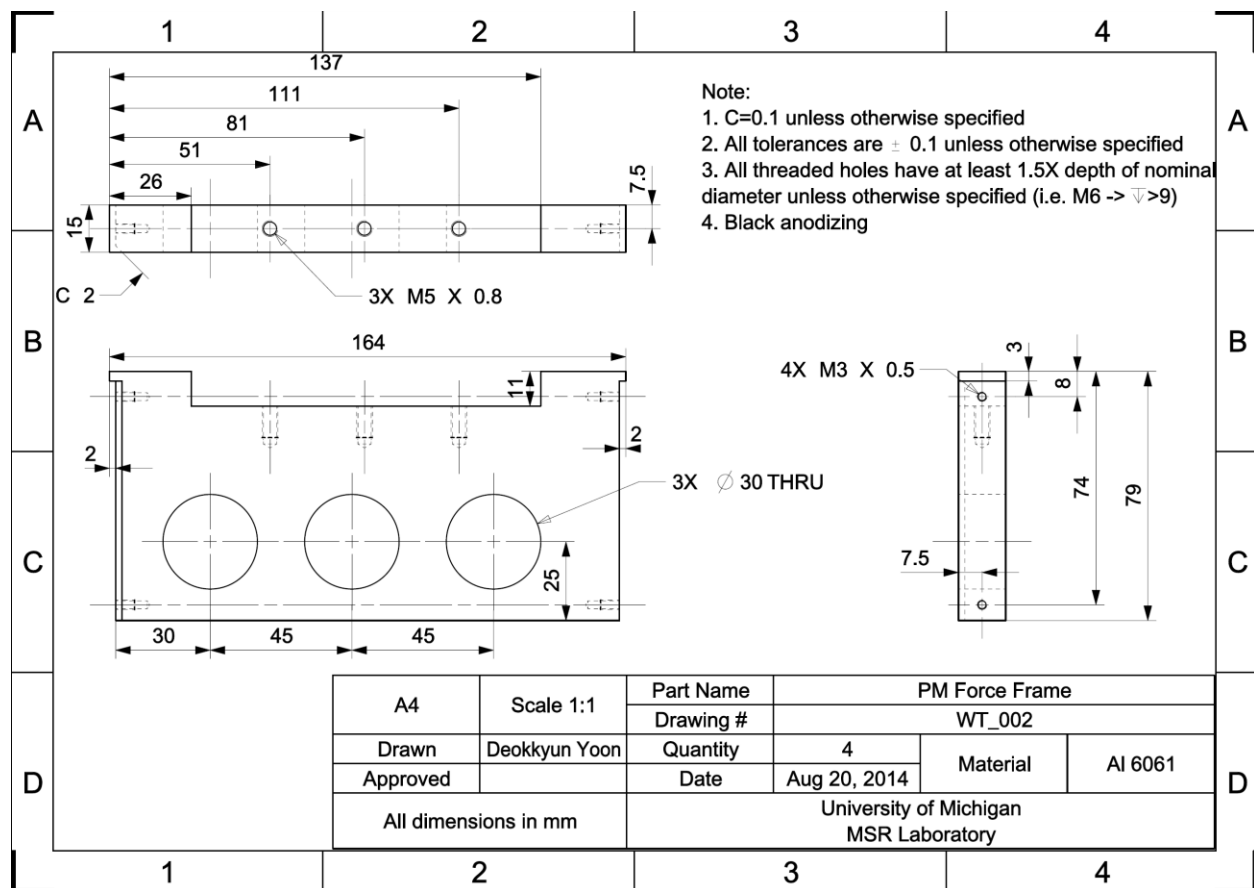


Figure B.53 Manufacturing drawing of PM Force Frame.

B.3.4 Readhead Holder

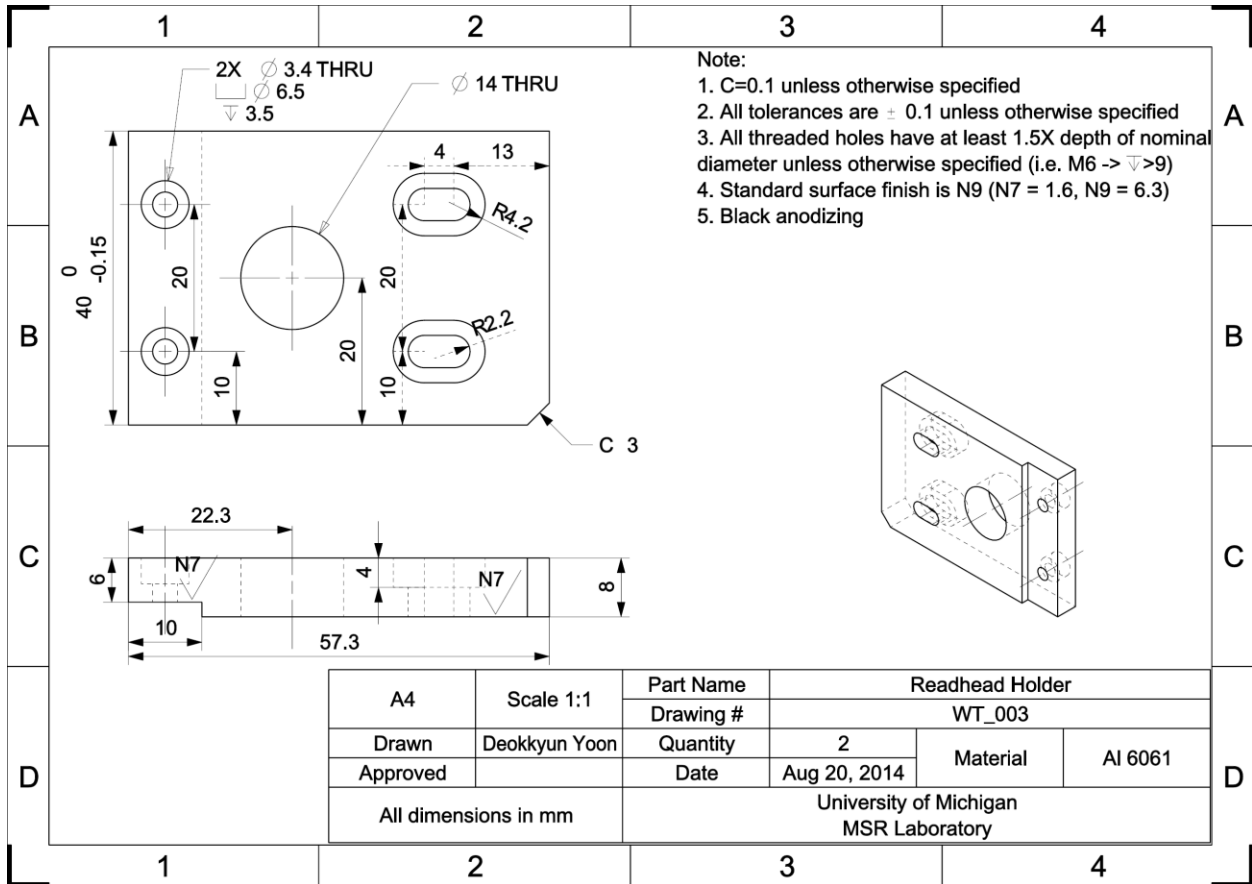


Figure B.54 Manufacturing drawing of Readhead Holder.

B.3.5 Readhead Holder #2

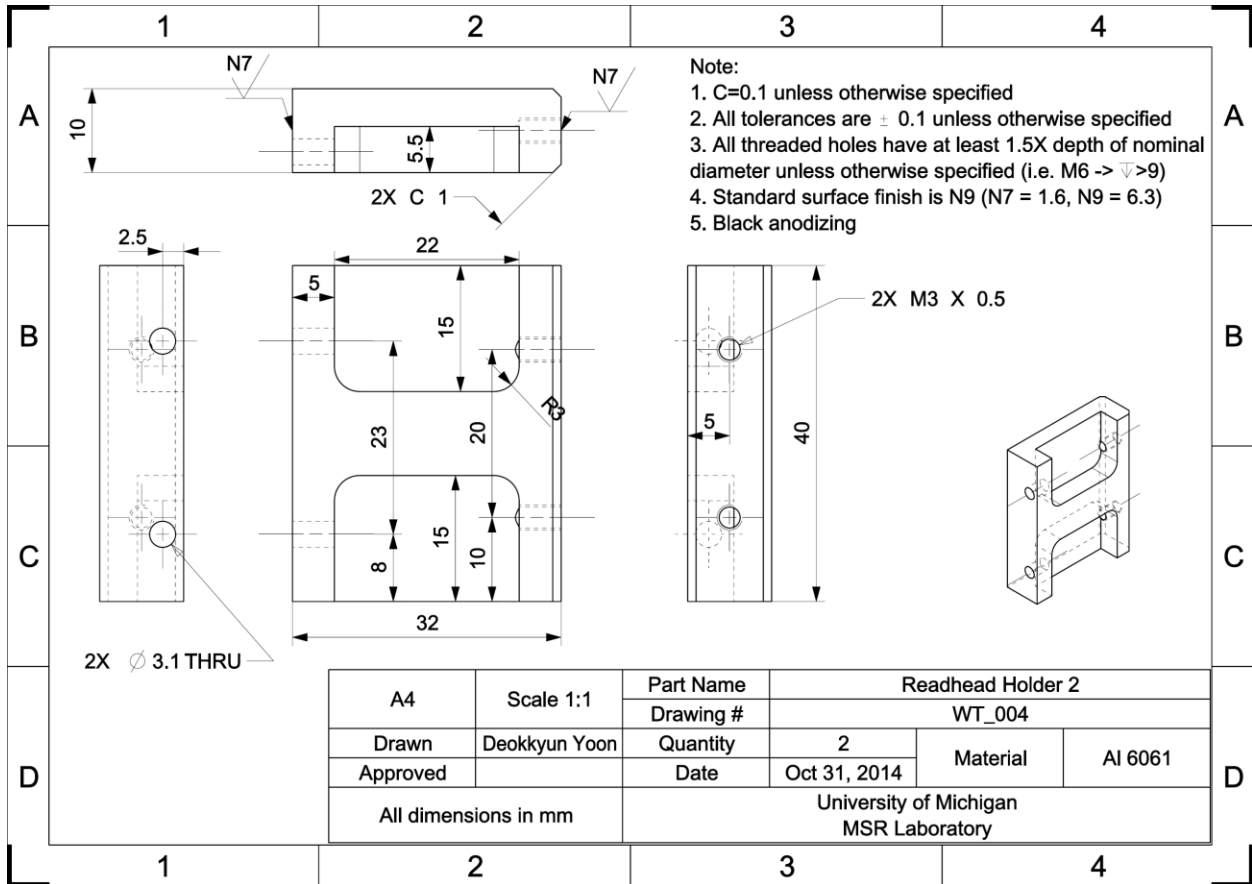


Figure B.55 Manufacturing drawing of Readhead Holder #2.

B.3.6 Cable Carrier Plate

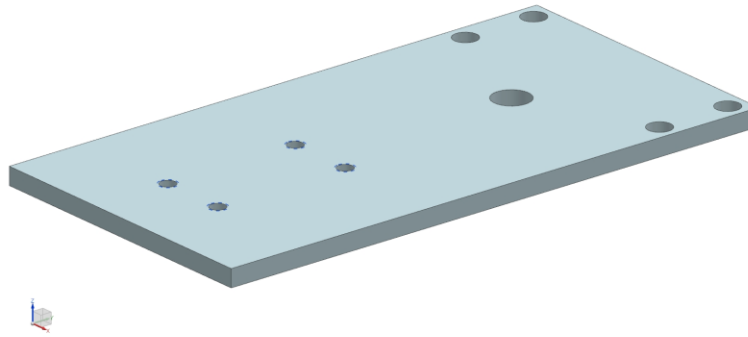


Figure B.56 Isometric view of Cable Carrier Plate.

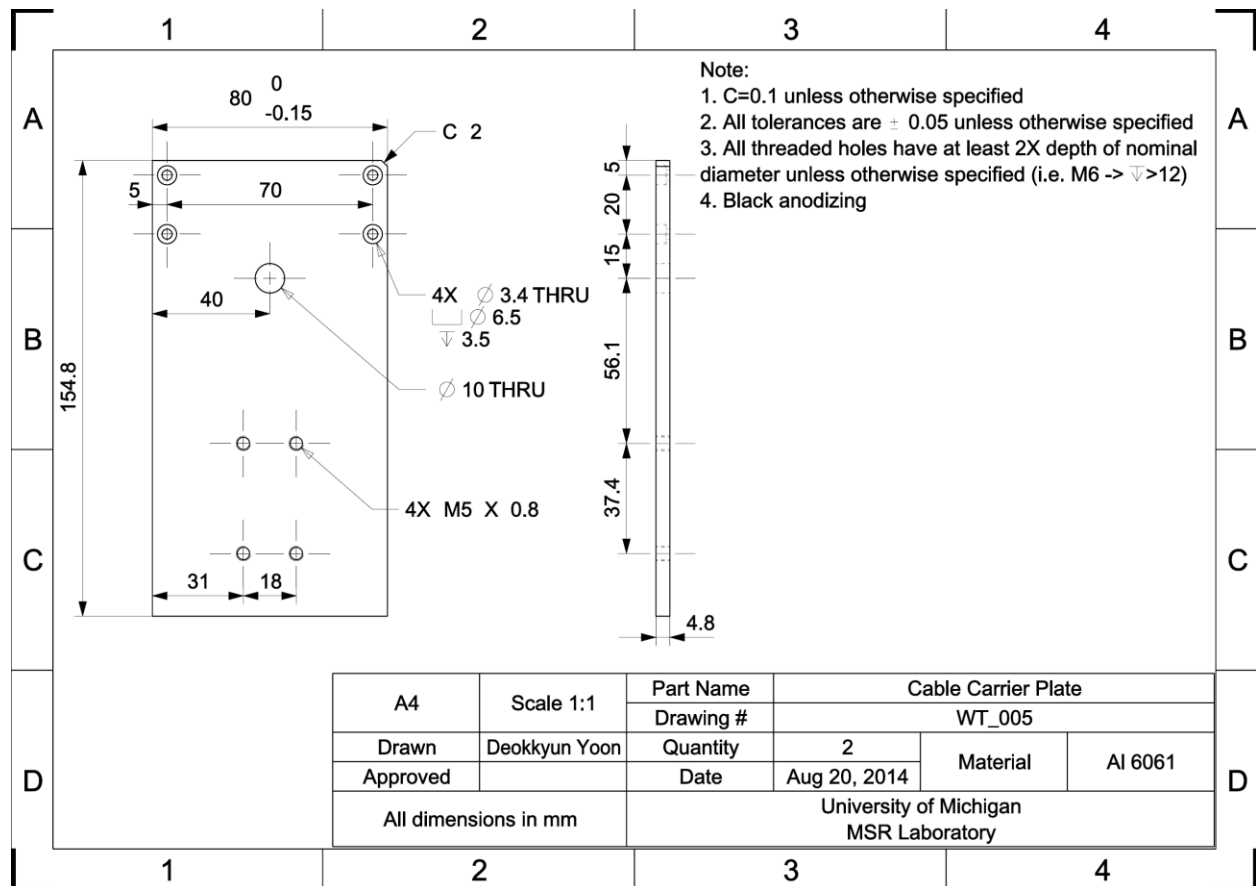


Figure B.57 Manufacturing drawing of Cable Carrier Plate.

B.3.7 Spacer

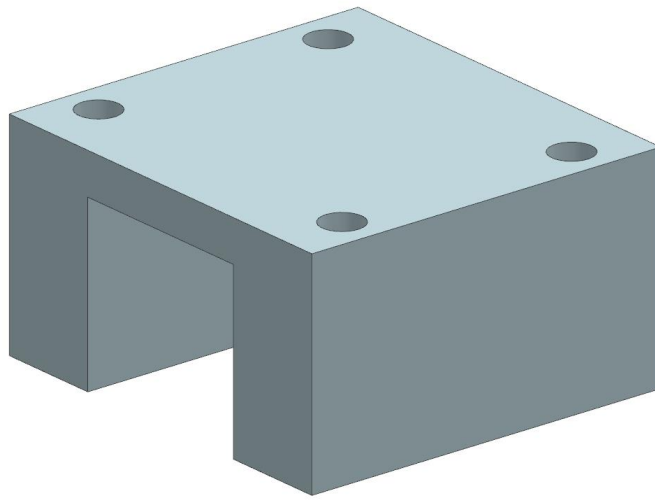


Figure B.58 Isometric view of Spacer.

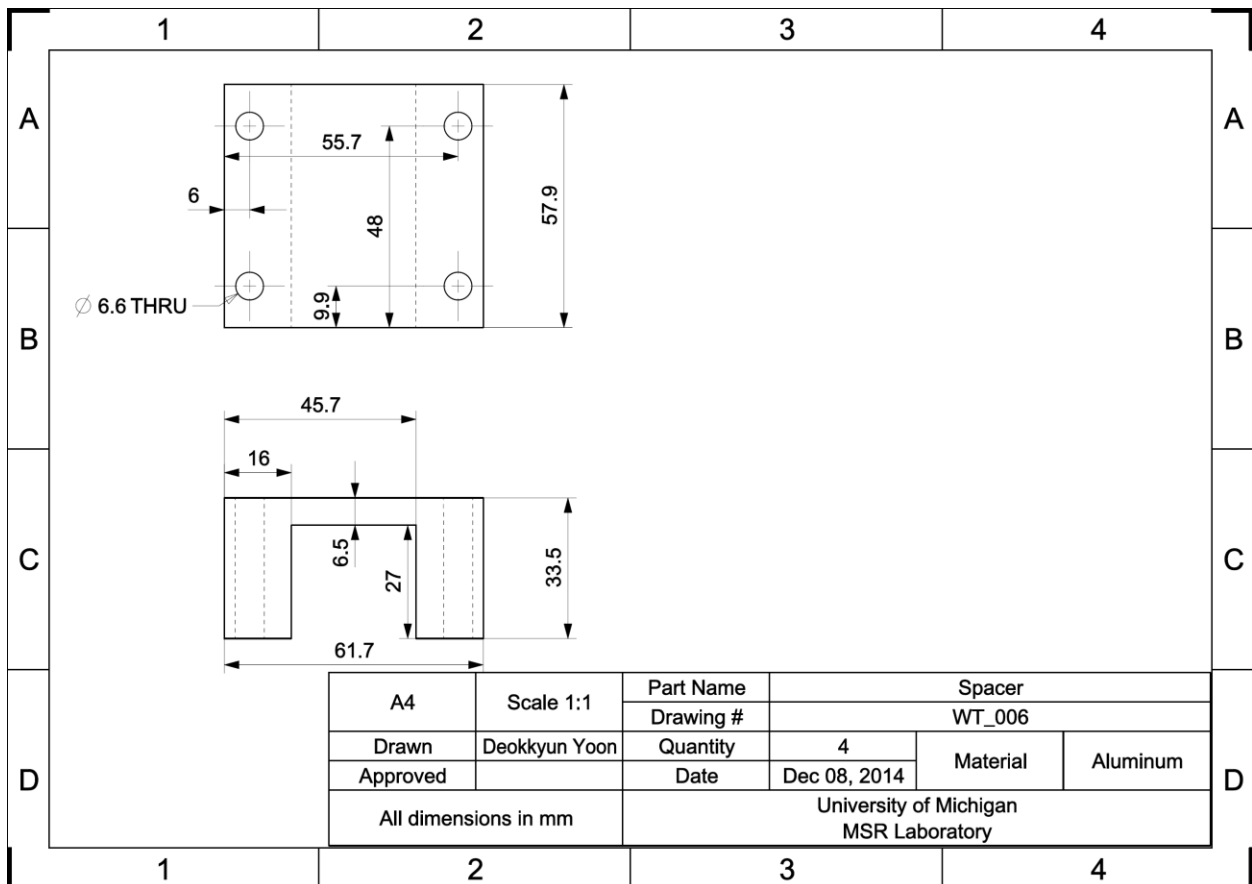


Figure B.59 Manufacturing drawing of Spacer.

B.3.8 Air Bushing Mounting Block (modification)

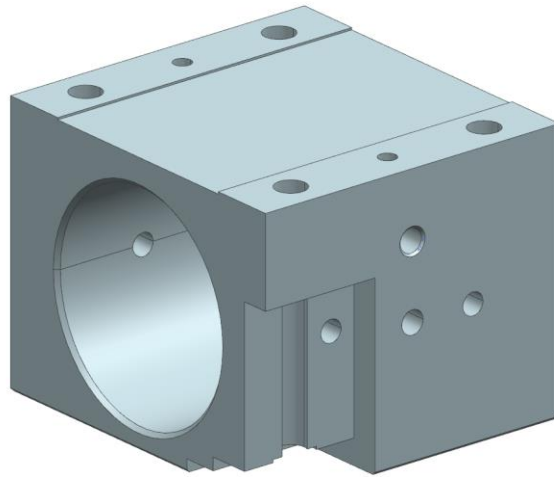


Figure B.60 Isometric view of modified Air Bushing Mounting Block.

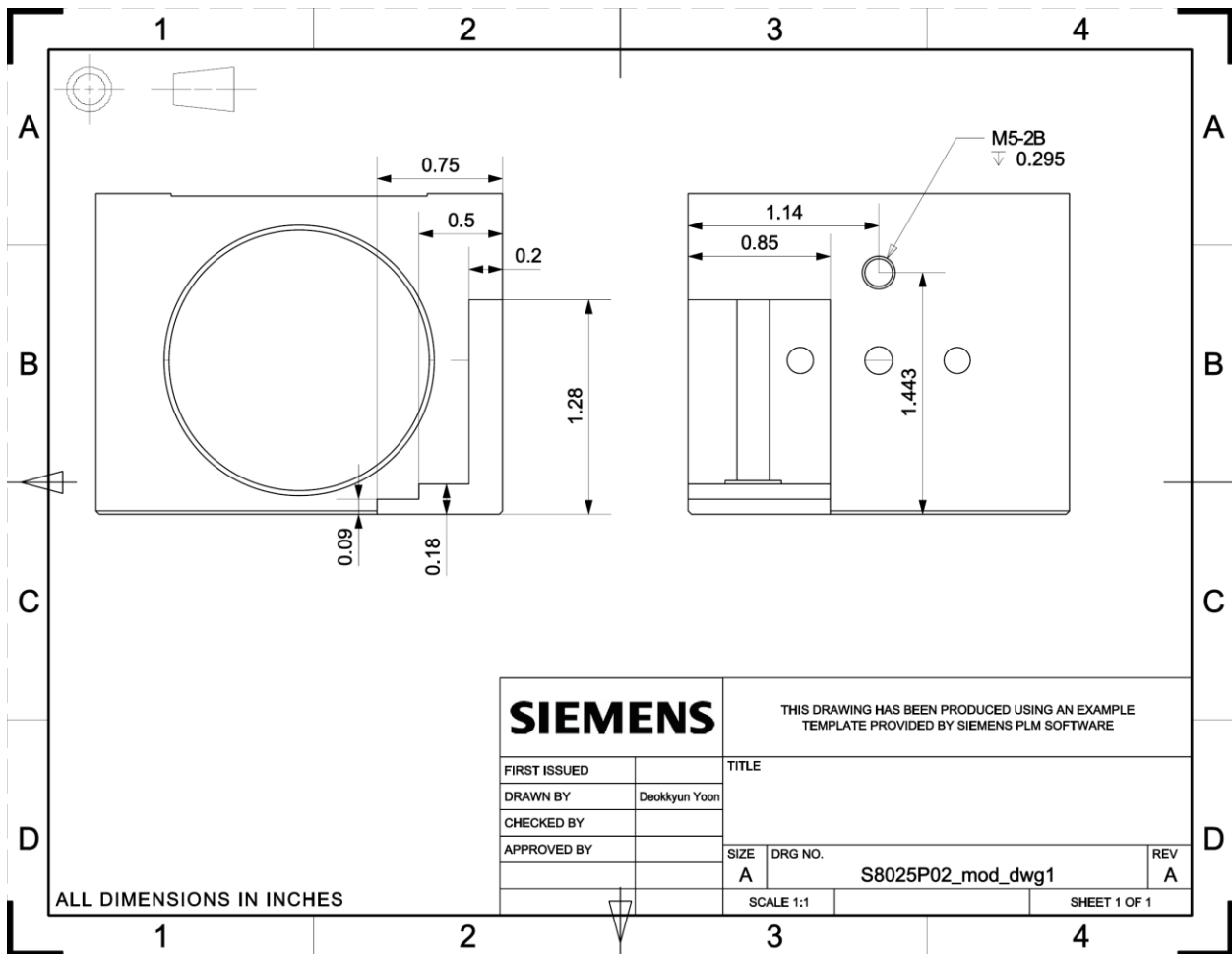


Figure B.61 Manufacturing drawing of modified Air Bushing Mounting Block.

B.4 CAD drawing for Halbach Array

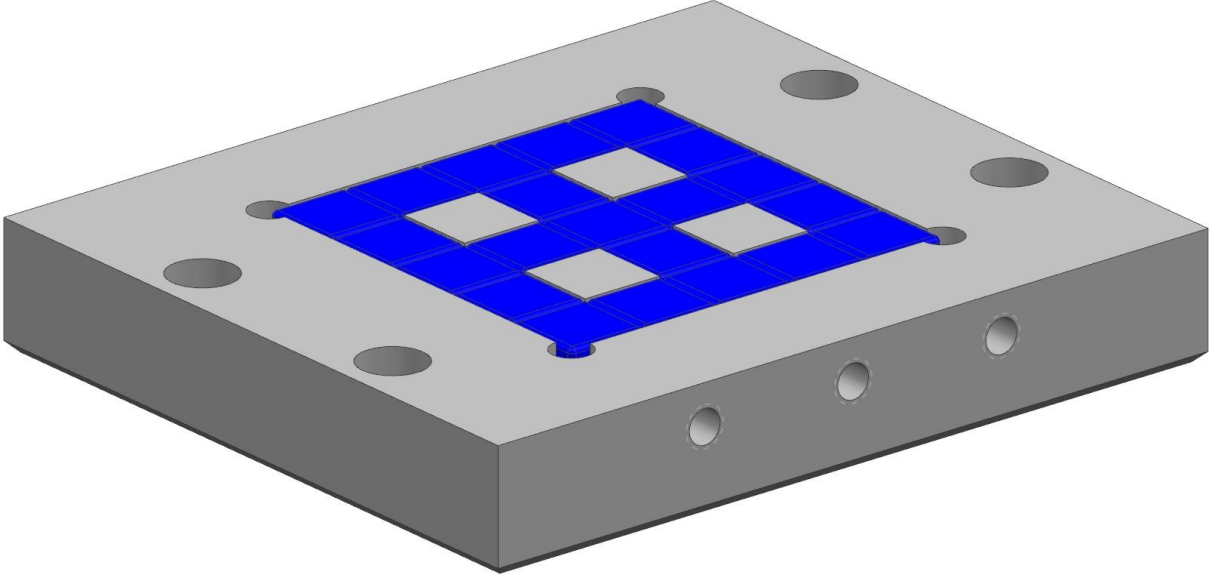


Figure B.62 Isometric view of Halbach Array sub-assembly.

B.4.1 Halbach 2D

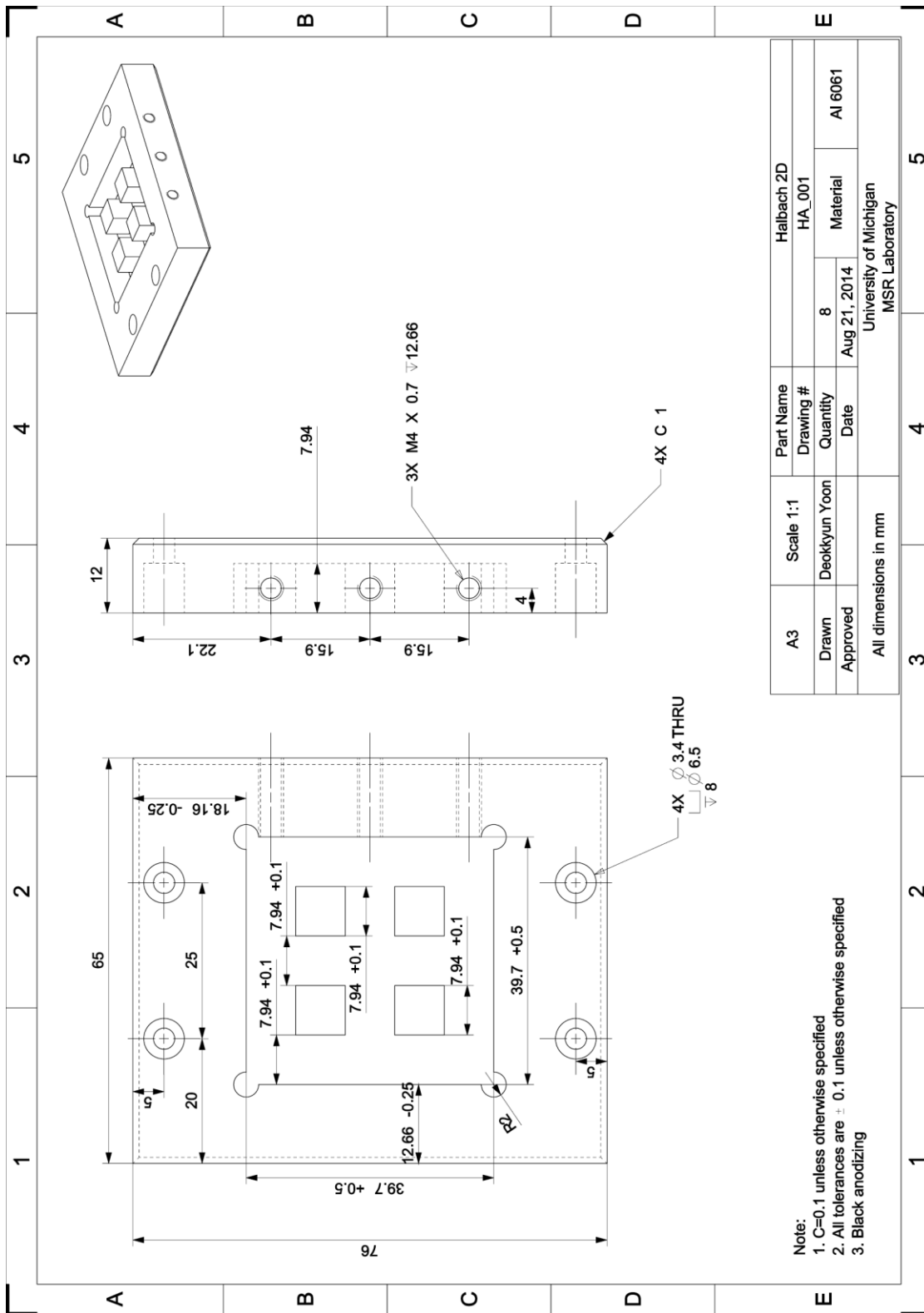


Figure B.63 Manufacturing drawing of Halbach 2D.

Appendix C

Validation of Optimal Inversion-based ILC

The optimal inversion-based (Opt-In for short) ILC approach for over-actuated systems proposed in Sections 5.1 and 5.2 is validated with a coarse-fine stage testbed. The coarse-fine stage used here is a linear system. Thus, it serves as the validation tool for the proposed ILC approach. In C.1, an overview of the coarse-fine stage is provided. Numerical and experimental validations of the proposed Opt-In ILC approach are shown in C.2 and C.3, respectively.

C.1 Coarse-fine stage and reference trajectory

C.1.1 Overview of coarse-fine stage

Coarse-fine stages achieve high precision positioning with multiple actuators stacked in series and are widely used in manufacturing applications where very precise positioning is required (*Elfizy et al., 2005*). The coarse actuators are designed to deliver low-precision, but long-range positioning, while the fine actuators are selected to provide high-precision, but short-range motion (*Kim et al., 2004*). Simulation and experimental validation of the proposed optimal inversion-based ILC approach is carried out on a coarse-fine stage testbed, whose CAD model is shown in Figure C.1. The fine stage is a flexure-guided stage with 0.6 mm thick leaf springs and 0.4 mm stroke, constructed using Al 7075 alloy. The position of the fine stage relative to the ground is measured by a linear encoder (Renishaw, T1000 readhead and RGSZ20 scale) having a post-interpolation resolution of 4.88 nm (on dSPACE, DS3002). A voice coil actuator (Moticont, LVCM-022-013-01), powered by a linear amplifier (Trust Automation, TA115) is employed to drive the fine stage. For the coarse stage, a commercial linear ball-screw stage (Aerotech, ATS110-050) having 5 mm lead is utilized. The coarse stage is powered by a PWM amplifier (Aerotech, Soloist CP10) and the stage position is measured with a built-in rotary encoder having a post-quadrature resolution of 100 nm. The equivalent motor constants for the voice coil actuator (VCA) and rotary motor

(RM), based on the motor specifications, are $K_{M,VCA} = 1.50 \text{ N/W}^{0.5}$ and $K_{M,RM} = 62.8 \text{ N/W}^{0.5}$, respectively.

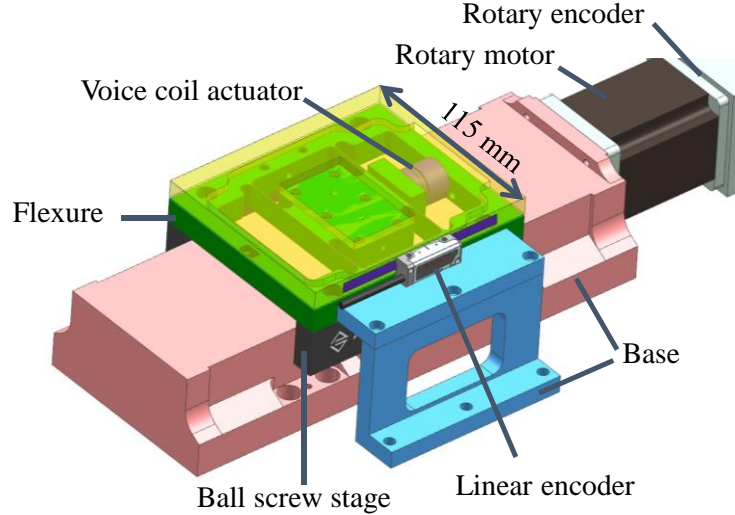


Figure C.1 CAD model of coarse-fine stage testbed.

C.1.2 Modeling of coarse-fine stage

The coarse-fine stage shown in Figure C.1 is modeled using the schematic shown in Figure C.2 where the coarse stage (CS) carries the fine stage (FS) on top of it. The output of the FS, x_2 , is the desired position output of the coarse-fine stage. In Figure C.2, the masses of coarse and fine stages are respectively denoted by m_1 and m_2 ; the stiffness and viscous damping coefficient between the two stages are k and c , while coefficient of viscous damping between the ground and CS is b . The task of optimal inversion-based ILC boils down to optimally (i.e., efficiently) allocating the coarse and fine actuator inputs, u_1 and u_2 , respectively, while iteratively improving tracking precision at a prescribed error convergence rate.

The transfer functions, $P_{1,1}$, $P_{2,1}$, $P_{1,2}$ and $P_{2,2}$, are respectively used to describe the transfer function relationships from u_1 to x_1 , u_1 to x_2 , u_2 to x_1 and u_2 to x_2 (i.e., with each input-output pair considered exclusively). The transfer functions are defined as

$$P_{1,1}(s) = \frac{m_2 s^2 + cs + k}{Den(s)}; P_{1,2}(s) = \frac{m_2 s^2}{Den(s)} \quad (C.1)$$

$$P_{2,1}(s) = \frac{cs + k}{Den(s)}; P_{2,2}(s) = \frac{m_1 s^2 + bs}{Den(s)} \quad (C.2)$$

where the denominator, $Den(s)$, is

$$Den(s) = m_1 m_2 s^4 + (b m_2 + c m_1 + c m_2) s^3 + (bc + k m_1 + k m_2) s^2 + b k s \quad (C.3)$$

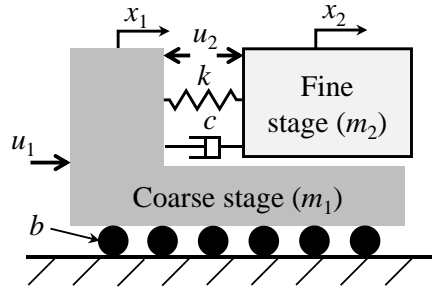


Figure C.2 Schematic of coarse-fine stage model.

The model parameters (used in Section C.2 for simulation studies) based on the coarse-fine stage testbed are provided in Table C.1

Table C.1 Model parameters for simulation case studies.

m_1 [kg]	m_2 [kg]	b [Ns/m]	k [N/m]	c [Ns/m]
39.3	0.5	60	10^5	45

C.1.3 Reference trajectory

For the rest of Appendix C, a reference trajectory consisting of sinusoidal sweep motions is used. The sweeping frequency, ϕ , exponentially increases as shown in Figure C.3 (a) and the reference trajectory, r , shown in Figure C.3 (b) is computed, in mm, with

$$r = -\frac{30000}{\pi^3 \phi^3} \cos(2\pi\phi t) + \frac{30000}{27\pi^3} \quad (C.4)$$

From a practical standpoint, r could be viewed as a single-axis component of a two-axis coarse-fine stage traversing a spiral path with monotonically decreasing speed. The acceleration of reference trajectory in both time and frequency domains are shown in Figure C.3 (c) and (d), respectively. The frequency contents of the reference trajectory obtained via DFT indicate that its spectral power is mostly concentrated inside a low frequency (< 200 Hz) range.

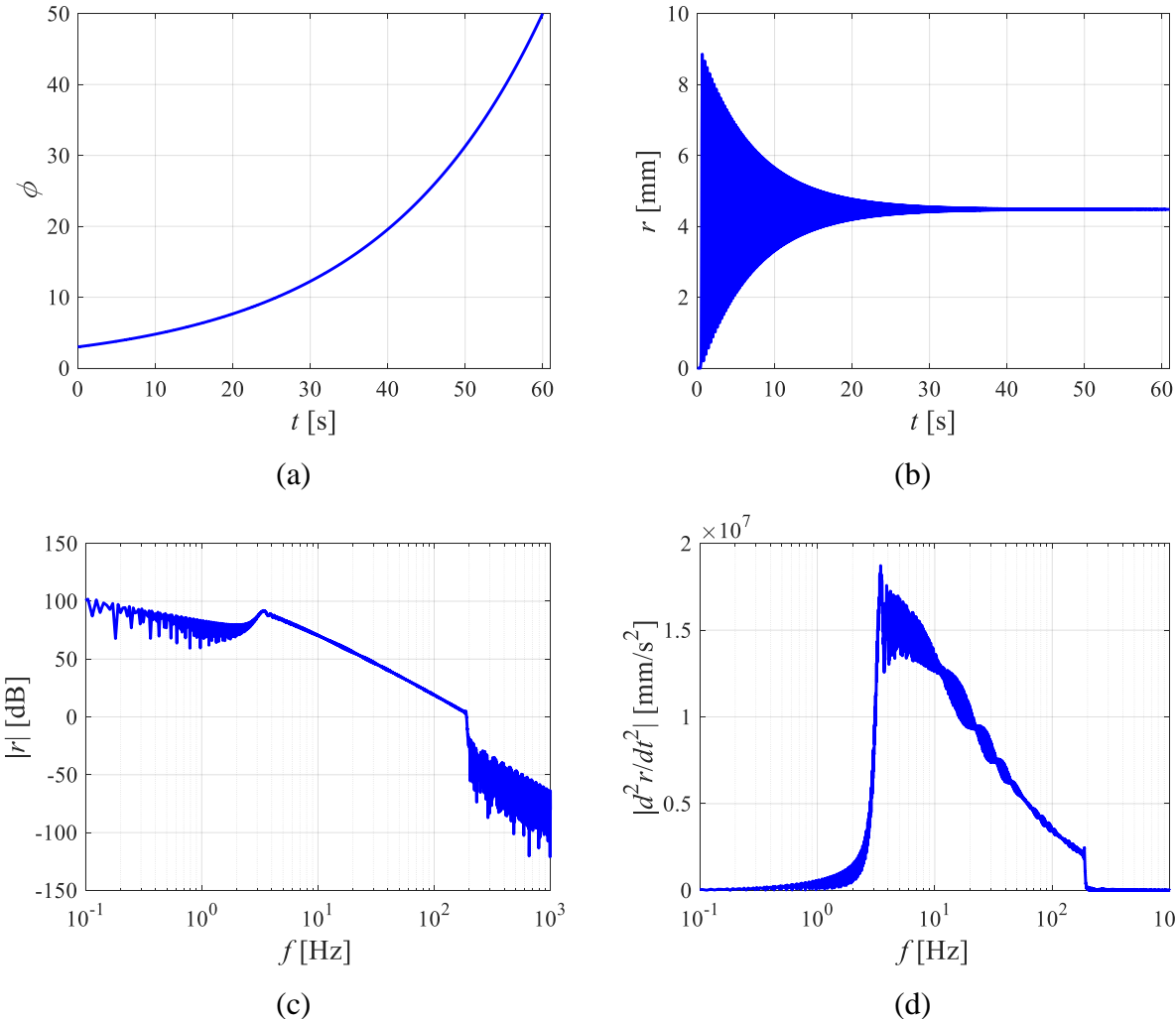


Figure C.3 Reference trajectory of sinusoidal sweep case study; (a) Sweeping frequency, ϕ , (b) displacement, r , (c) acceleration, d^2r/dt^2 , and (d) magnitude of discrete Fourier transform of d^2r/dt^2 .

C.2 Numerical examples

C.2.1 Optimal control effort allocation

The goal of the simulation studies presented in this section is to validate the proposed optimal inversion-based ILC in the absence of model uncertainty with regard to: (1) optimal control effort allocation; (2) convergence rate and steady-state error in the presence of noise. All the simulation results presented are implemented on MATLAB[®] with the sampling interval of 0.01 s. Based on the coarse-fine stage testbed, the non-square system dynamics is given as

$$\mathbf{e} = \mathbf{r} - \mathbf{y}; \mathbf{y} = \mathbf{x}_2 = \underbrace{\begin{bmatrix} \mathbf{P}_{2,1} & \mathbf{P}_{2,2} \end{bmatrix}}_{\mathbf{P}} \begin{bmatrix} \mathbf{u}_1 \\ \mathbf{u}_2 \end{bmatrix} \quad (\text{C.5})$$

Since there are two actuators and two sensors, a straightforward way of implementing inversion-based ILC without dealing with the challenges of over-actuation is to square the system up to a dual-input dual-output system (*Semba et al., 1999*);

$$\mathbf{e}_{Sq} = \begin{bmatrix} \mathbf{r} \\ \mathbf{r} \end{bmatrix} - \mathbf{y}_{Sq}; \mathbf{y}_{Sq} = \begin{bmatrix} \mathbf{x}_1 \\ \mathbf{x}_2 \end{bmatrix} = \underbrace{\begin{bmatrix} \mathbf{P}_{1,1} & \mathbf{P}_{1,2} \\ \mathbf{P}_{2,1} & \mathbf{P}_{2,2} \end{bmatrix}}_{\mathbf{P}_{Sq}} \begin{bmatrix} \mathbf{u}_1 \\ \mathbf{u}_2 \end{bmatrix} \quad (\text{C.6})$$

where the subscript, Sq , indicates the squared system. Using the direct inversion of the plant model, \mathbf{P}_{Sq} , the following ILC update law for the squared system is obtained;

$$\mathbf{L}_{U,Sq} = \mathbf{I}; \mathbf{L}_{E,Sq} = \mathbf{P}_{Sq}^{-1} \quad (\text{C.7})$$

For the Opt-In ILC of the non-square system given in (C.5), the solutions provided in Eqs. (5.14) and (5.15) are used with the input weighting matrix, \mathbf{S} , given as

$$\mathbf{S} = \begin{bmatrix} \mathbf{I} & \mathbf{0} \\ \mathbf{0} & \alpha \mathbf{I} \end{bmatrix} \quad (\text{C.8})$$

where α is provided as

$$\alpha = \left(\frac{K_{M,RM}}{K_{M,VCA}} \right)^2 \quad (\text{C.9})$$

using the motor constants of VCA and RM for calculating the Joule heating from each actuator (Duan and Okwudire, 2018). The input ratio, $\alpha = 1,770$, is used for the remainder of this section, meaning that a unit control effort of FS costs 1,770 times more than a unit control effort of the CS. In other words, the CS actuator (i.e., RM) is much more efficient than the FS counterpart (i.e., VCA) when generating the traction force. The Joule heating generated by each actuator, P_h , in W, is computed with

$$P_h = \left(\frac{F_{RMS}}{K_M} \right)^2 \quad (\text{C.10})$$

where F_{RMS} is the RMS force generated by the actuator.

In this section, $\mathbf{B} = \mathbf{I}$ for the fastest error convergence is adopted. The control efforts using the two ILC approaches and the reference trajectory shown in Figure C.3 are compared in Table C.2, highlighting the optimal use of control inputs with the optimal inversion-based ILC approach; the control efforts in RMS are reduced by up to 72% when the optimal inversion-based ILC is used for optimal (i.e., efficient) control allocation. The reduced RMS forces provide over 94% reduction in Joule heating generated by the actuators. However, the steady-state tracking performance is better with the squared system's inversion-based ILC, but the difference (which is practically insignificant given the 4.88 nm resolution of the output measurement of the coarse-fine stage testbed) is attributed to the numerical precision/accuracy. The condition number of the matrix inversion (i.e., \mathbf{P}_{Sq}^{-1} and $(\mathbf{P}\mathbf{S}^{-1}\mathbf{P}^T)^{-1}$ for the squared and over-actuated systems, respectively) is larger with the optimal inversion-based ILC case due to the large input ratio, α . Therefore, it is more likely to have numerical errors during the computation with the matrix inverse. The simulated

ILC results (i.e., tracking error and control efforts) are shown in Figure C.4; the steady-state tracking errors are virtually zero for the considered two cases.

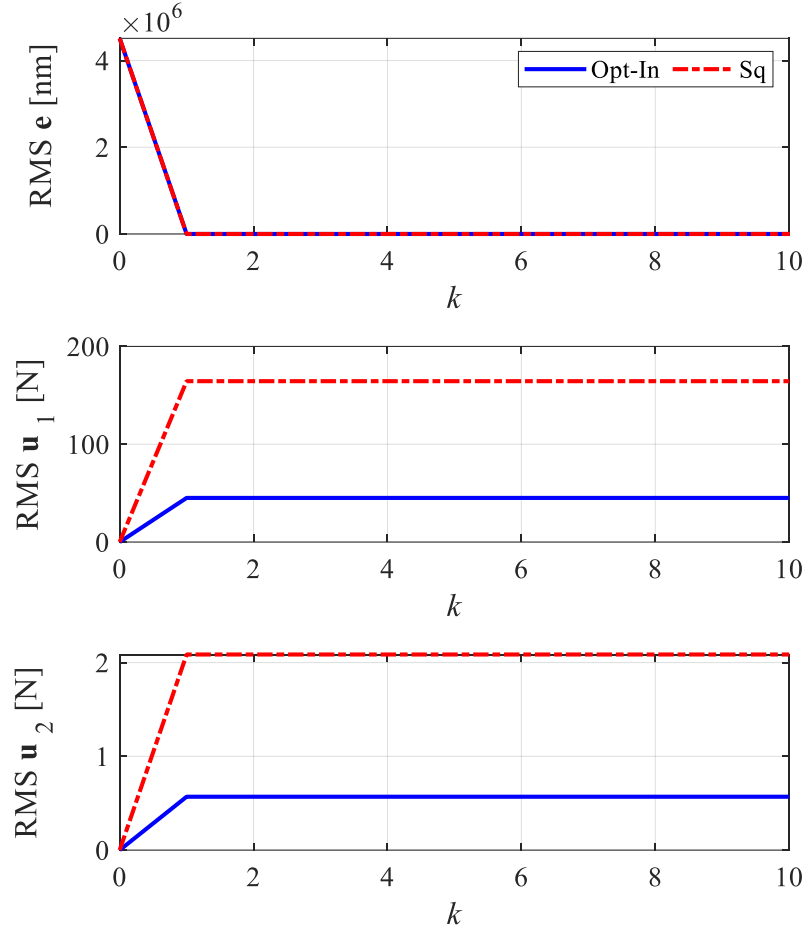


Figure C.4 Simulated ILC performance over iteration.

Table C.2 Control efforts comparison between the inversion-based squared ILC and the optimal inversion-based ILC approaches.

Steady-state Performance	Squared ILC	Optimal inversion-based ILC
RMS \mathbf{u}_1 [N]	164	45.1
RMS \mathbf{u}_2 [N]	2.09	0.570
$P_{h,1}$ [W]	6.82	0.516
$P_{h,2}$ [W]	1.94	0.144
RMS \mathbf{e} [nm]	8.51×10^{-8}	2.37×10^{-1}
Condition number	5.78×10^8	1.74×10^{13}

C.2.2 Tunable error convergence rate and effect of output measurement noise

As a simple way to select the error convergence rate, $\mathbf{B} = b\mathbf{I}$ is introduced in Section 5.1.2. In this section, the effect of b on the convergence rate of optimal inversion-based ILC and the influence of noise on the steady-state error are demonstrated. The noise is assumed to be Gaussian with 100 nm RMS and a total of 300 ILC iterations are carried out for each b case. As shown in Figure C.5, the fastest error convergence is realized with $b = 1$ as expected (i.e., the error convergence is realized with only one iteration). Notice that the identical convergence rate is achieved for the same $|b - 1|$ (see Section 5.1.2). For instance, $b = 0.3$ and $b = 1.7$ share the same convergence rate. However, due to the output measurement noise, their steady-state tracking errors differ (i.e., 108 nm RMS vs. 258 nm RMS, respectively, as predicted by Eq. (5.24)). The theoretical prediction given in Eq. (5.24) is supported by the steady-state tracking performance shown in Figure C.6, in which the RMS errors of the last 100 iterations (i.e., from the 201st to the 300th iterations) are plotted with and without the noise.

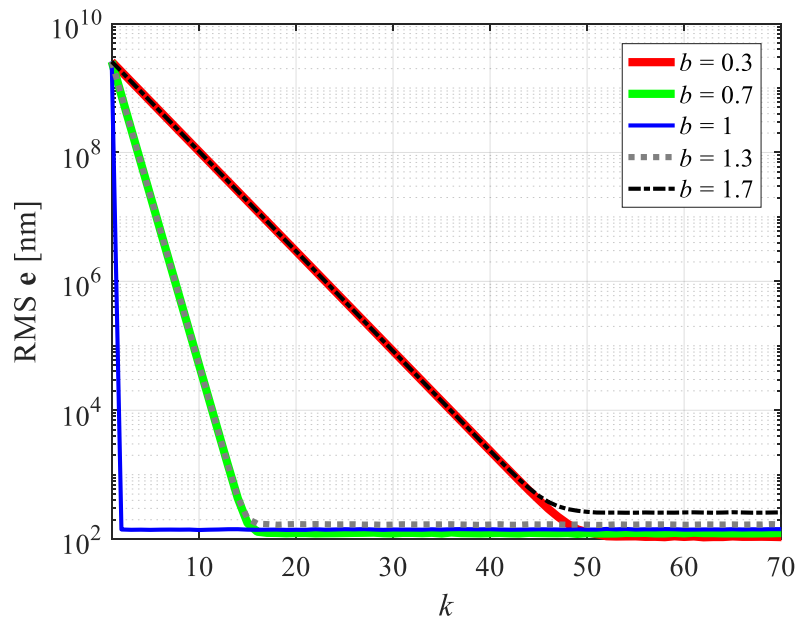


Figure C.5 Tunable convergence rate of the optimal inversion-based ILC by adjusting b . Gaussian output measurement noise (100 nm RMS) is added. Notice that even though the convergence rate is identical for $|1 - b|$, the steady-state error is different due to the noise as predicted by Eq. (5.24).

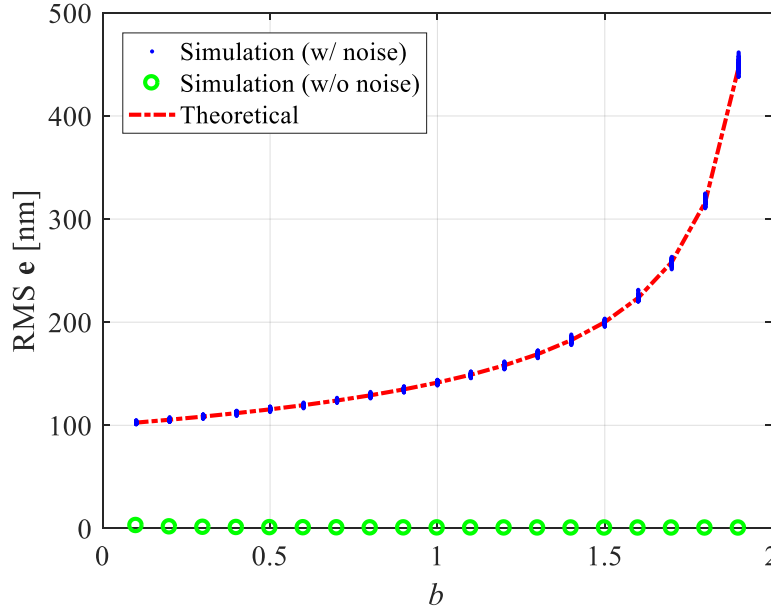
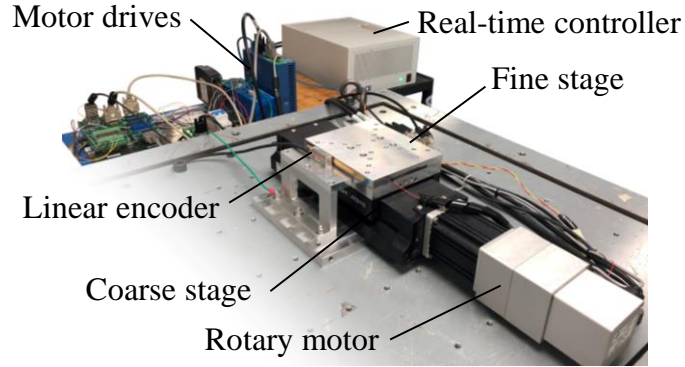


Figure C.6 Comparison of tracking errors with and without output measurement noise (100 nm RMS). The RMS values of tracking errors from 201st to 300th iterations are plotted. The theoretical RMS tracking error as a function of b given in Eq. (5.24) is provided for reference.

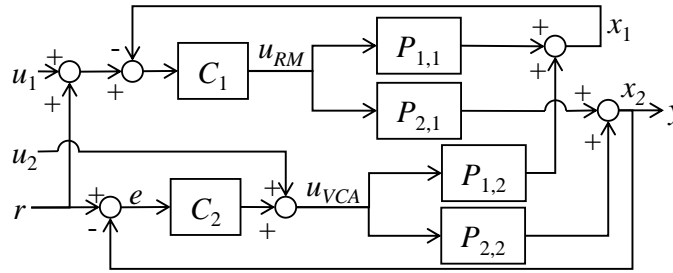
C.3 Experimental example

C.3.1 Coarse-fine stage with feedback controller

While the simulations carried out in preceding section ignored model uncertainty, model uncertainty is bound to be present in reality; hence, the need for introducing robustness into optimal inversion-based ILC using an optimized model as discussed in Chapter 5.2. This section demonstrates the experimental implementation of the optimal inversion-based ILC with optimized model on the coarse-fine stage testbed whose CAD model is shown in Figure C.1. The implementation of the control system is performed at 0.1 ms sampling interval on a real-time controller (dSPACE, DS1007). The experimental set-up is shown in Figure C.7 (a). The stage dynamics including the feedback controllers is described with the block diagram shown in Figure C.7 (b). When $u_1 = 0$ and $u_2 = 0$ are used for the nominal system without the optimal control allocation, the feedback controller of the FS, C_2 , corrects the output tracking errors incurred by the CS. As the input-output relationship between u_{VCA} and x_1 is negligible, $P_{1,2} = 0$ is used for the remainder of this paper (Kim *et al.*, 2004)



(a)



(b)

Figure C.7 (a) Coarse-fine stage experimental set-up, (b) Block diagram for feedback controlled coarse-fine stage.

C.3.2 System identification and optimal inversion-based ILC update law of coarse-fine stage with feedback controller

In this section, the dynamics of coarse-fine stage with PID-type feedback controller shown in Figure C.7 (b) is identified using swept sine input signals and the optimal inversion-based ILC update law is generated. To establish the system model uncertainty bounds, multiple swept sine system identification trials are carried out with varying input amplitudes. The CS's FRFs are obtained with the variable reference acceleration amplitudes from 0.25 m/s^2 to 2 m/s^2 sent to u_1 , while the FS is not powered (i.e., C_2 , u_2 and r are set to 0 during the CS system identification, which is done in closed loop, i.e., $C_1 \neq 0$). Likewise, the CS is not powered (i.e., $C_1 = 0$) during the FS system identification. The reference acceleration amplitudes for the FS identification are from 0.05 m/s^2 to 0.3 m/s^2 sent to r . After several trials for each input port, the FRFs shown in Figure C.8 (a), (b), and (c) are obtained. The experimentally obtained uncertainty areas for the

magnitude and phase are marked with the gray shaded regions, respectively. The following input-output relationships are used for system identification:

$$Sen_1 = \frac{u_{RM}}{u_1} = \frac{C_1}{1 + C_1 P_{1,1}} \quad (C.11)$$

$$G_{2,1} = \frac{x_2}{u_1} = \frac{C_1 P_{2,1}}{1 + C_1 P_{1,1}} \quad (C.12)$$

$$P_{2,2} = \frac{x_2}{u_{VCA}} \quad (C.13)$$

where Sen_1 is the output sensitivity function of the coarse stage to estimate the control effort generated by the CS input, u_1 .

For Opt-In ILC of the coarse-fine stage, r is the iteration-invariant reference, while the coarse actuator's control input, u_{RM} , is indirectly updated with u_1 using the knowledge of Sen_1 . Because of the large amount of friction within the bearings and the ball screw assembly, the CS is less repeatable than the FS and large uncertainties exist (See Figure C.8). Additionally, the RM control input signal (u_{RM}) for the next iteration cannot precisely predict whether the travel limit of the FS will be reached. Therefore, the reference trajectory of CS is updated iteratively using u_1 . However, the FS shows linear and repeatable behavior over the tested range of input amplitudes as shown in Figure C.8 (c), hence, u_{VCA} is directly updated with u_2 . The Opt-In ILC update law for the coarse-fine stage is derived by minimizing the objective function given as

$$J = \begin{bmatrix} \mathbf{u}_{RM} \\ \mathbf{u}_{VCA} \end{bmatrix}^T \begin{bmatrix} \mathbf{I} & 0 \\ 0 & \alpha \mathbf{I} \end{bmatrix} \begin{bmatrix} \mathbf{u}_{RM} \\ \mathbf{u}_{VCA} \end{bmatrix} \quad (C.14)$$

in the lifted time domain, as in Eq. (5.4). Because \mathbf{u}_{RM} is updated indirectly via \mathbf{u}_1 , the following substitution is made using Eq. (C.11) and $u_2 = u_{VCA}$;

$$J = \begin{bmatrix} \mathbf{u}_1 \\ \mathbf{u}_2 \end{bmatrix}^T \begin{bmatrix} (\mathbf{Sen}_1)^T \mathbf{Sen}_1 & 0 \\ 0 & \alpha \mathbf{I} \end{bmatrix} \begin{bmatrix} \mathbf{u}_1 \\ \mathbf{u}_2 \end{bmatrix} \quad (C.15)$$

The tracking error of the $k+1^{\text{st}}$ iteration is given as

$$\mathbf{e}_{k+1} = \mathbf{r} - \underbrace{\begin{bmatrix} \mathbf{G}_{2,1} & \mathbf{P}_{2,2} \end{bmatrix}}_{\mathbf{P}} \underbrace{\begin{bmatrix} \mathbf{u}_1 \\ \mathbf{u}_2 \\ \mathbf{u}_{k+1} \end{bmatrix}}_{\mathbf{u}_{k+1}} \quad (\text{C.16})$$

With the plant model, the optimal inversion-based ILC update law is derived following the steps laid out in Chapter 5.1 and is provided as

$$L_U = \begin{bmatrix} \frac{G_{2,1}^* G_{2,1}}{Sen_1^* Sen_1} & \frac{G_{2,1}^* P_{2,2}}{Sen_1^* Sen_1} \\ \frac{P_{2,2}^* G_{2,1}}{\alpha} & \frac{P_{2,2}^* P_{2,2}}{\alpha} \end{bmatrix} \frac{1}{Dn} \quad (\text{C.17})$$

$$L_E = \begin{bmatrix} \frac{G_{2,1}^*}{Sen_1^* Sen_1} \\ \frac{P_{2,2}^*}{\alpha} \end{bmatrix} \frac{1}{Dn} \quad (\text{C.18})$$

where * is used to indicate the complex conjugate and Dn is given as

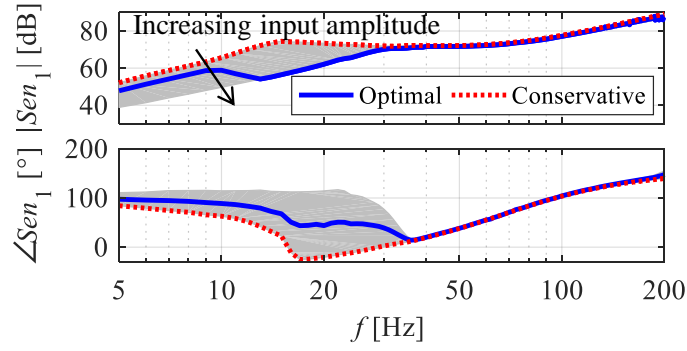
$$Dn = \frac{G_{2,1}^* G_{2,1}}{Sen_1^* Sen_1} + \frac{P_{2,2}^* P_{2,2}}{\alpha} \quad (\text{C.19})$$

Note that $b = 1$ is used to achieve the fastest error convergence.

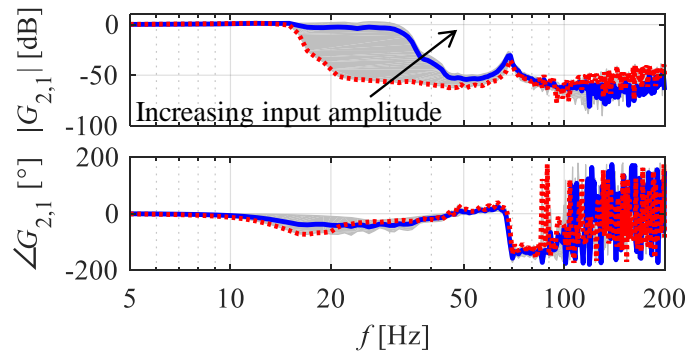
C.3.3 Conservative selection of model to ensure robustness

A common approach to ensure robustness given an uncertain system is to focus on the worst case with regard to stability (*Zhou et al., 1996*). For Opt-In ILC, this means selecting the nominal plant model, P , and a Q -filter for generating the ILC update laws of Eqs. (C.17) and (C.18) to ensure that stability is guaranteed in the worst case. Observing the FRFs of Figure C.8, the

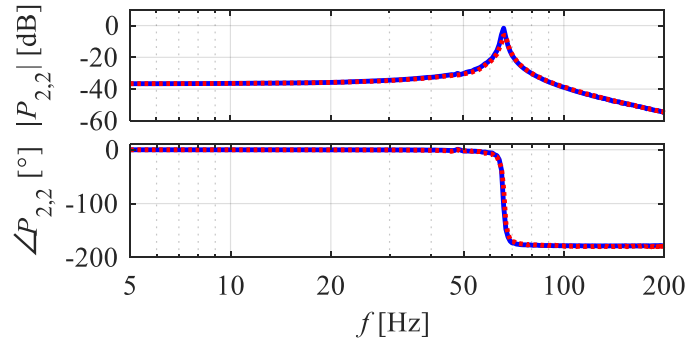
nominal plant is selected as shown in dashed red lines. For the CS, the FRFs generated using the smallest input amplitudes are selected for Sen_1 and $G_{2,1}$, because the selection would generate the ILC update law with the least use of the uncertain CS dynamics for error correction. Since $P_{2,2}$ has little uncertainty, any of the available plant models could be selected without much impact on the results; therefore, the average of all the swept sine trials is selected. Using the just-described worst-case nominal plant selections, the Q -filter is selected to satisfy the RMC constraint of (5.31); the resulting Q -filter is plotted in red dashed lines in Figure C.9. Notice that it is very conservative (i.e., has very low magnitudes) in the frequency ranges where a lot of uncertainty exists in the plant FRFs shown in Figure C.8.



(a)



(b)



(c)

Figure C.8 Frequency response functions (FRFs) used to construct the ILC update law – (a) Sen_1 [N/mm], (b) $G_{2,1}$ [mm/mm], and (c) $P_{2,2}$ [mm/N]; shaded regions represent the experimentally obtained system uncertainties. The dashed red lines represent conservatively selected nominal models, while the solid blue lines represent optimally selected nominal models for the uncertain system.

C.3.4 Optimal selection of model to ensure robustness and maximize tracking performance

Instead of following the conservative approach discussed in Section C.3.3 above, the model optimization approach discussed in Section 5.2 is employed to select the nominal plant, P , and Q -filter for use in generating the ILC update laws of (C.17) and (C.18) for the uncertain system. This entails using the objective function introduced in (5.31) to solve for optimal P and Q that result in the minimum tracking errors in the presence of the worst-case uncertainty at each frequency, θ_i :

$$\begin{aligned} \underset{v}{\text{minimize}} \quad & J_s(v(e^{j\theta_i})) = \max \left(\left[I - H(v) \right]^T \left[I - H(v) \right] \right) \\ \text{s.t.} \quad & \left\| Q(v) \left[L_U(v) - L_E(v) P_C \right] \right\|_2 < \frac{1}{\gamma} \end{aligned} \quad (\text{C.20})$$

The safety factor of $\gamma = 2$, accounting for the approximations involved with the DFT, is used. Note that there are seven optimization variables within v ;

$$\begin{aligned} v(e^{j\theta_i}) &= [v_1 \quad v_2 \quad v_3 \quad v_4 \quad v_5 \quad v_6 \quad v_7]; \\ v_1 &= |Sen_1|; \quad v_2 = \angle Sen_1; \quad v_3 = |G_{2,1}|; \\ v_4 &= \angle G_{2,1}; \quad v_5 = |P_{2,2}|; \quad v_6 = \angle P_{2,2}; \quad v_7 = |Q| \end{aligned} \quad (\text{C.21})$$

where the frequency argument, $e^{j\theta_i}$, is omitted for the sake of conciseness. The optimization is carried out with the *fmincon* function of MATLAB R2018a, treating each frequency in FRFs obtained from the system identification independently. The solved optimal nominal plant models and Q -filter gain are shown in Figure C.8 (a), (b), (c) and Figure C.9, respectively, with blue solid lines. Notice from Figure C.9 that the optimal Q -filter selection is much more aggressive than that found using the conservative approach (i.e., its magnitude is larger than the conservatively designed filter). The Opt-In ILC update law with the optimal selection of P as found using Eqs. (C.17), (C.18) and (C.19) is shown in Figure C.10 (a) and (b).

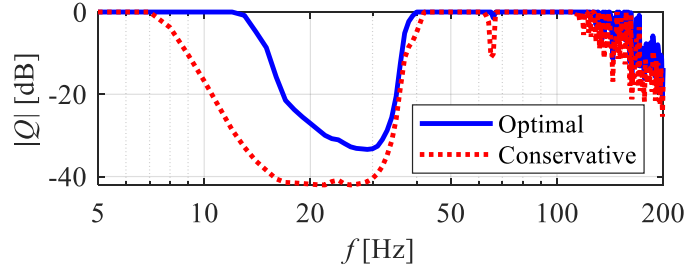


Figure C.9 Comparison of zero-phase robustness filter, Q , selected based on optimal and conservative selection of plant model.

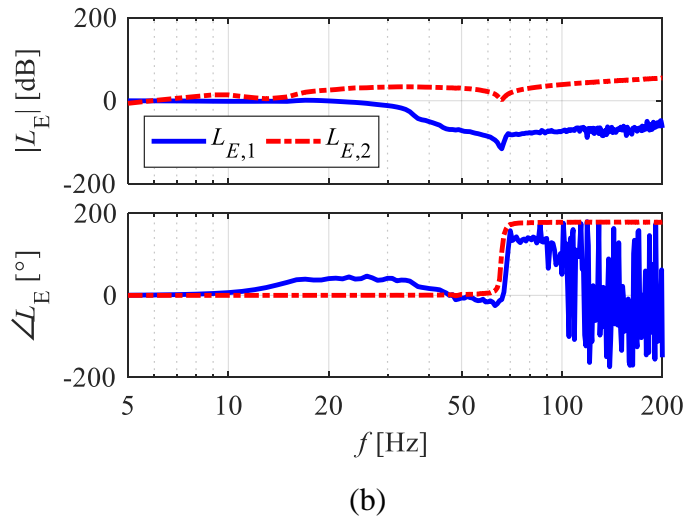
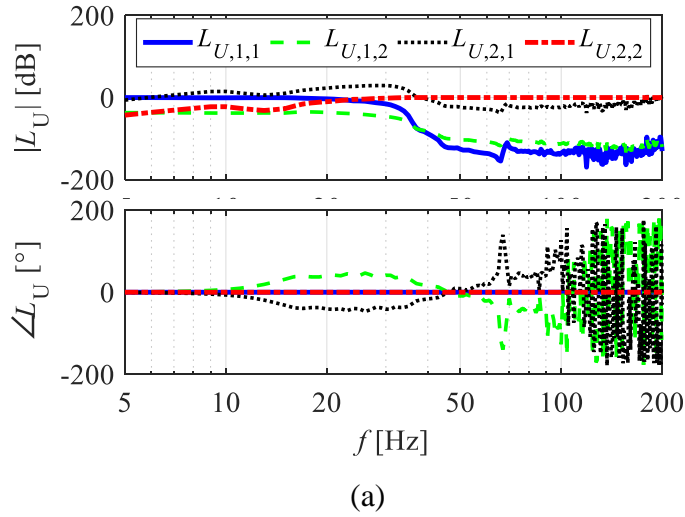


Figure C.10 Optimal inversion-based ILC update law for the coarse-fine stage using optimized model; (a) L_U and (b) L_E gains are applied to the previous iteration's input and error signals, respectively.

Because the RM is more efficient in the low frequency region ($f < \sim 25$ Hz), larger magnitude is obtained for $L_{U,1,1}$ than $L_{U,2,2}$. As frequency increases, the VCA becomes more

efficient; thus, the magnitude of $L_{U,2,2}$ becomes larger. The off-diagonal terms, $L_{U,1,2}$ and $L_{U,2,1}$, transfer control inputs from one input to the other. As shown in Figure C.10 (b), the low frequency errors are corrected by the RM, while the high frequency errors are delegated to the VCA, again due to their corresponding efficiencies at the respective frequencies.

For the initial iteration, the control inputs $\mathbf{u}_1 = \mathbf{0}$ and $\mathbf{u}_2 = \mathbf{0}$ are applied to the stage. Then, the recorded tracking error and control input signals in discrete time domain are converted into the frequency domain using DFT (*Kim and Zou, 2013*). The next iteration's control input signals in the frequency domain are generated using the ILC update law with the frequency-by-frequency addition/multiplication process. The obtained control input signals are converted back to the discrete time domain using the IDFT (*Kim and Zou, 2013*).

C.3.5 Case study: Sinusoidal sweep

In this section, the swept sinusoidal signal reference shown in Figure C.3 is used to highlight the importance of the optimal selection of P and Q -filter in Opt-In ILC. Figure C.11 compares the tracking errors and control efforts of Opt-In ILC using the conservatively and optimally selected P and Q -filter. Notice that when the conservative plant models and Q -filter are used for the Opt-In ILC update law generation, the control effort allocation and error correction abilities of the Opt-In ILC are reduced. As a result, the reference tracking task relies more on the feedback controller, meaning that the VCA participates in the tracking task for the low frequency ranges, where the use of RM can be more efficient.

The steady-state performance, obtained using the last 15 iterations are presented in Table C.3. Compared to the case with the optimal selection of plant models and Q -filter, 2% and 12% increases in the steady-state tracking error and VCA control efforts (i.e., 25% increase in VCA Joule heating), respectively, are obtained with the conservative selection. However, the conservative selection uses 4% less RM control effort (i.e., 8% reduction in RM Joule heating). From a practical standpoint, due to the distance between the RM and the position output of interest (i.e., the table's position), the RM heating is much less detrimental to the stage's positioning accuracy.

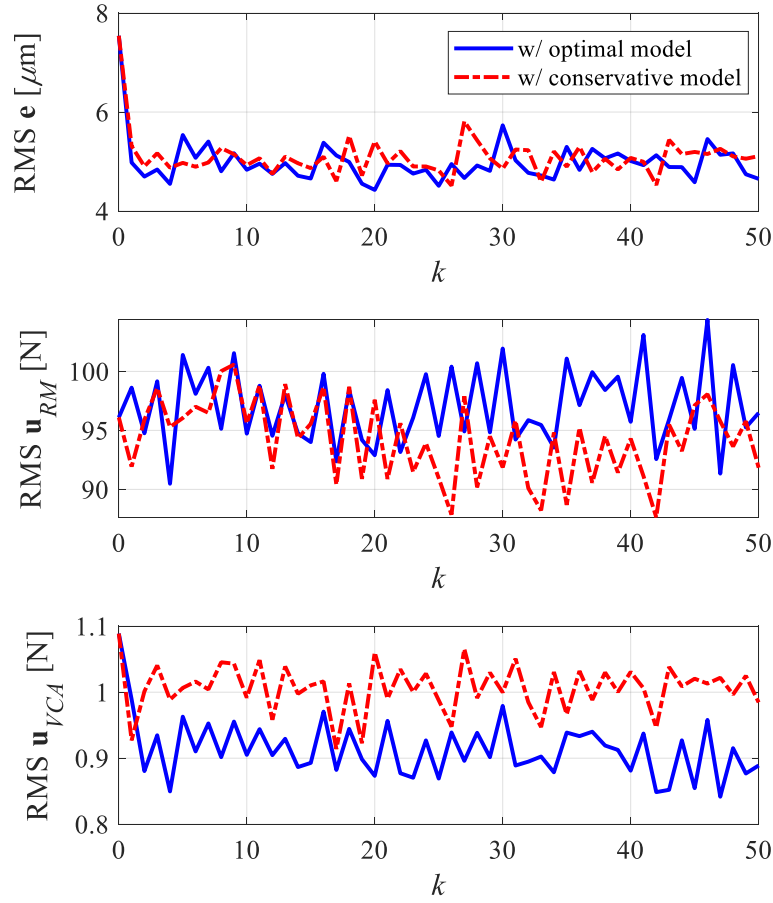


Figure C.11 Optimal inversion-based (Opt-In) ILC update for sinusoidal sweep case study; RMS tracking error, RMS control input for coarse actuator (i.e., rotary motor), \mathbf{u}_{RM} , and RMS control input for fine actuator (i.e., voice coil actuator), \mathbf{u}_{VCA} , are shown.

Table C.3 Steady-state performance of experiments without ILC and using optimal inversion-based ILC (with optimal and conservative models) based on the last 15 iterations.

	Opt-In ILC (w/ optimal model)	Opt-In ILC (w/ conservative model)
$\text{RMS } \mathbf{e}$ [μm]	4.99 ± 0.02	5.07 ± 0.02
$\text{RMS } \mathbf{u}_{RM}$ [N]	97.6 ± 3.6	93.7 ± 2.8
$\text{RMS } \mathbf{u}_{VCA}$ [N]	0.90 ± 0.04	1.01 ± 0.02
$P_{h, RM}$ [W]	2.41	2.23
$P_{h, VCA}$ [W]	0.36	0.45

C.4 Summary

The Opt-In ILC approach for over-actuated systems, proposed in Sections 5.1 and 5.2, is validated using a coarse-fine stage testbed. The proposed ILC approach achieves the optimal allocation of control efforts using a model of the plant, while the ILC convergence rate can be specified by user with an error dynamics matrix. Simulation studies are carried out using a model of the coarse-fine stage testbed to demonstrate the benefit of proposed Opt-In ILC compared to a squaring based ILC approach. Up to 72% reduction of control effort is demonstrated. Further simulation results validate the effect of noise on the steady-state error of the ILC, as predicted by theoretical formulations derived in Chapter 5; they confirm the importance of choosing the convergence rate in such a way as not to amplify the effect of noise on the steady-state error. Experiments are conducted to demonstrate the effectiveness of the proposed ILC in the presence of modeling errors, which are bound to occur in practice. To minimize the steady-state tracking errors and guarantee robustness against plant model uncertainties, a frequency domain method for selecting the best MIMO plant model and Q -filter for Opt-In ILC, given the model uncertainty bounds, is presented. Compared to a case using conservative selection of the plant model, the optimized model achieves 2% improvement in the steady-state tracking performance, while using 12% less control effort (i.e., 25% less Joule heating) of the fine actuator which is more critical to thermal induced errors of the stage.

BIBLIOGRAPHY

- 3D Micromac. *microDICE – Laser Micromachining*. (<https://3d-micromac.com/laser-micromachining/products/microdice>; accessed on Sep. 28th, 2018)
- Aerotech Inc. *PlanarHDX Air-Bearing XY Silicon-Carbide Stage*. (<https://www.aerotech.com/product-catalog/stages/linear-x-y-stages/planarhdx.aspx?p=%2fproduct-catalog%2fstages%2flinear-x-y-stages.aspx>; accessed on Sep. 21st, 2018). (a)
- Aerotech Inc. *Integrated Granite Motion Systems*. (<https://www.aerotech.com/product-catalog/integrated-granite-motion-systems.aspx>; accessed on Oct. 15th, 2018). (b)
- Altintas Y, Verl A, Brecher C, Uriarte L, Pritschow G. *Machine tool feed drives*. CIRP Annals-Manufacturing Technology. 2011; 60 (2);779-796.
- Amann N, Owens D, Rogers E. *Iterative learning control for discrete-time systems with exponential rate of convergence*. IEE Proceedings-Control Theory and Applications. 1996; 143 (2); 217-224.
- Arimoto S, Kawamura S, Miyazaki F. *Bettering operation of robots by learning*. Journal of Robotic systems. 1984; 1 (2); 123-40.
- Åström K, Hägglund T. *The future of PID control*. Control engineering practice. 2001; 9 (11); 1163-1175.
- Barton K, Alleyne A. *A norm optimal approach to time-varying ILC with application to a multi-axis robotic testbed*. IEEE Transactions on Control Systems Technology. 2011; 19 (1); 166-180.
- Boeren F, Bareja A, Kok T, Oomen T. *Frequency-domain ILC approach for repeating and varying tasks: With application to semiconductor bonding equipment*. IEEE/ASME Transactions on Mechatronics. 2016; 21 (6); 2716-2727.
- Brown W, Ulsoy A. *A Maneuver Based Design of a Passive-Assist Device for Augmenting Active Joints*. Journal of Mechanisms and Robotics. 2013; 5 (3); 031003.
- Brown W, Ulsoy A. *Robust design of Passive Assist Devices for multi-DOF robotic manipulator arms*. Robotica. 2017; 35 (11); 2238-2255.
- Bristow D, Tharayil M, Alleyne A. *A survey of iterative learning control*. IEEE Control Systems. 2006; 26 (3); 96-114.

- Bruijnen D, Van Dijk N. *Combined input shaping and feedforward control for flexible motion systems*. American Control Conference, 2012; 2473-2478.
- Butler H. *Position Control in Lithographic Equipment*. IEEE Control Systems Magazine. 2011; 31 (5); 28-47.
- Butler H. *Acceleration feedback in a lithographic tool*. Control Engineering Practice. 2012; 20 (4); 453-64.
- Butler H. *Adaptive feedforward for a wafer stage in a lithographic tool*. IEEE Transactions on Control Systems Technology. 2013; 21 (3); 875-881.
- Butterworth J, Pao L, Abramovitch D. *Analysis and comparison of three discrete-time feedforward model-inverse control techniques for nonminimum-phase systems*. Mechatronics. 2012; 22 (5); 577-587.
- Çengel Y, Boles M. *Thermodynamics: An engineering approach*. McGraw-Hill Higher Education; 2007.
- Chen H, Zhang M, Mu H, Zhu Y, Hu C, Cai T. *Conceptual design and trajectory planning of a precision repetitive-scanning stage with separated drive unit for energy saving*. IEEE/ASME Transactions on Mechatronics. 2016; 21 (4); 2142-2153.
- Choi K, Lee J. *Passive compliant wafer stage for single-step nano-imprint lithography*. Review of scientific instruments. 2005; 76 (7); 075106.
- Chou P, Rao A, Sturzenbecker M, Wu F, Brecher V. *Automatic defect classification for semiconductor manufacturing*. Machine Vision and Applications. 1997; 9 (4); 201-214.
- Clayton G, Tien S, Leang K, Zou Q, Devasia S. *A review of feedforward control approaches in nanopositioning for high-speed SPM*. Journal of dynamic systems, measurement, and control. 2009; 131 (6); 061101.
- Cusimano G. *Generalization of a method for the selection of drive systems and transmissions under dynamic loads*. Mechanism and machine theory. 2005; 40 (5); 530-558.
- De Roover D, Bosgra O. *Synthesis of robust multivariable iterative learning controllers with application to a wafer stage motion system*. international Journal of Control. 2000; 73 (10); 968-79.
- DeBra D. *Vibration isolation of precision machine tools and instruments*. CIRP Annals-Manufacturing Technology. 1992; 41 (2); 711-718.
- Denkena B, Hesse P, Gümmer O. *Energy optimized jerk-decoupling technology for translatory feed axes*. CIRP annals. 2009; 58 (1); 339-342.
- Desktop Metal. *Production*. (<https://www.desktopmetal.com/products/production/>; accessed on Sep. 28th, 2018)

Devore J. *Probability and statistics for engineering and the sciences*. Cengage Learning; 2011.

Duan M, Okwudire C. *Minimum-time cornering for CNC machines using an optimal control method with NURBS parameterization*. The International Journal of Advanced Manufacturing Technology. 2016a; 85 (5-8); 1405-1418.

Duan M, Okwudire C. *Energy-Efficient Controller Design for a Redundantly Actuated Hybrid Feed Drive With Application to Machining*. IEEE/ASME Transactions on Mechatronics. 2016b; 21 (4); 1822-1834.

Duan M, Okwudire C. *Proxy-Based Optimal Control Allocation for Dual-Input Over-Actuated Systems*. IEEE/ASME Transactions on Mechatronics. 2018; 23 (2); 895-905.

Duan M, Yoon D, Okwudire C. *A limited-preview filtered B-spline approach to tracking control—With application to vibration-induced error compensation of a 3D printer*. Mechatronics. 2018; 56; 287-296.

Elfizy A, Bone G, Elbestawi M. *Design and control of a dual-stage feed drive*. International Journal of Machine Tools and Manufacture. 2005; 45 (2); 153-165.

Erkorkmaz K, Gorniak J, Gordon D. *Precision machine tool X–Y stage utilizing a planar air bearing arrangement*. CIRP Annals-Manufacturing Technology 2010; 59 (1); 425-428.

Fan K, Fei Y, Yu X, Wang W, Chen Y. *Study of a noncontact type micro-CMM with arch-bridge and nanopositioning stages*. Robotics and computer-integrated manufacturing. 2007; 23 (3); 276-84.

Fesperman R, Ozturk O, Hocken R, Ruben S, Tsao TC, Phipps J, Lemmons T, Brien J, Caskey G. *Multi-scale alignment and positioning system—MAPS*. Precision Engineering. 2012; 36 (4); 517-37.

Finders J, Dusa M, Vleeming B, Hepp B, Maenhoudt M, Cheng S, Vandeweyer T. *Double patterning lithography for 32 nm: critical dimensions uniformity and overlay control considerations*. Journal of Micro/Nanolithography, MEMS, and MOEMS. 2009; 8 (1); 011002.

Gao W, Arai Y, Shibuya A, Kiyono S, Park C. *Measurement of multi-degree-of-freedom error motions of a precision linear air-bearing stage*. Precision engineering. 2006; 30 (1); 96-103.

Galburt D. *Method, system, and apparatus for management of reaction loads in a lithography system*. US Patent; 2004; 6784978.

Gale M, Rossi M, Pedersen J, Schuetz H. *Fabrication of continuous-relief micro-optical elements by direct laser writing in photoresists*. Optical Engineering. 1994; 33 (11); 3556-3567.

- Ge X, Stein J, Ersal T. *A Frequency-Dependent Filter Design Approach for Norm-Optimal Iterative Learning Control and Its Fundamental Trade-Off Between Robustness, Convergence Speed, and Steady-State Error*. Journal of Dynamic Systems, Measurement, and Control. 2018; 140 (2); 021004.
- Ghosh J, Paden B. *A pseudoinverse-based iterative learning control*. IEEE Transactions on Automatic Control. 2002; 47 (5); 831-837.
- Gorinevsky D. *Loop shaping for iterative control of batch processes*. IEEE control systems. 2002; 22 (6); 55-65.
- Gunnarsson S, Norrlöf M. *On the disturbance properties of high order iterative learning control algorithms*. Automatica, 2006; 42 (11); 2041-2034.
- Halevi Y, Carpanzano E, Montalbano G. *Minimum energy control of redundant linear manipulators*. Journal of Dynamic Systems, Measurement, and Control. 2014; 136 (5); 051016.
- Halbach K. *Design of permanent multipole magnets with oriented rare earth cobalt material*. Nuclear instruments and methods. 1980; 169 (1); 1-10.
- Härkegård O, Glad S. *Resolving actuator redundancy—optimal control vs. control allocation*. Automatica. 2005; 41 (1); 137-144.
- Harte T, Hätönen J, Owens D. *Discrete-time inverse model-based iterative learning control: stability, monotonicity and robustness*. International Journal of Control. 2005; 78 (8); 577-586.
- Heertjes M, Hennekens D, Steinbuch M. *MIMO feed-forward design in wafer scanners using a gradient approximation-based algorithm*. Control Engineering Practice. 2010; 18 (5); 495-506.
- Holmes M, Hocken R, Trumper D. *The long-range scanning stage: a novel platform for scanned-probe microscopy*. Precision engineering. 2000; 24 (3); 191-209.
- Horn R, Johnson C. *Matrix Analysis*. Cambridge University Press; 1985
- Intel Corporation. “*Making of a Chip*” Illustrations. (http://download.intel.com/newsroom/kits/ml50/pdfs/Sand-to-Silicon_22nm-April2015.pdf; accessed on Sep. 21st, 2018)
- Iwasaki M, Seki K, Maeda Y. *High-precision motion control techniques: A promising approach to improving motion performance*. IEEE Industrial Electronics Magazine. 2012; 6 (1); 32-40.
- Jin J. *Modified pseudoinverse redistribution methods for redundant controls allocation*. Journal of Guidance, Control, and Dynamics. 2005; 28 (5); 1076-1079.
- Johansen T, Fossen T. *Control allocation—a survey*. Automatica. 2013; 49 (5); 1087-1103.

K&J Magnetics, Inc. B666-N52. (<https://www.kjmagnetics.com/proddetail.asp?prod=B666-N52>; accessed on Oct. 17th, 2018)

Karnopp D. *Active and semi-active vibration isolation*. Journal of Vibration and Acoustics. 1995; 117 (B); 177-185.

Kempf C, Kobayashi S. *Disturbance observer and feedforward design for a high-speed direct-drive positioning table*. IEEE Transactions on control systems Technology. 1999; 7 (5); 513-526.

Kim B, Li J, Tsao T. *Two-parameter robust repetitive control with application to a novel dual-stage actuator for noncircular machining*. IEEE/ASME Transactions on mechatronics. 2004; 9 (4); 644-652.

Kim D, Kim S. *An iterative learning control method with application for CNC machine tools*. IEEE Transactions on Industry Applications. 1996; 32 (1); 66-72.

Kim J, Jeong Y, Cho D. *Thermal behavior of a machine tool equipped with linear motors*. International Journal of Machine Tools and Manufacture. 2004; 44 (7-8); 749-758.

Kim K, Zou Q. *A modeling-free inversion-based iterative feedforward control for precision output tracking of linear time-invariant systems*. IEEE/ASME Transactions on Mechatronics. 2013; 18 (6); 1767-1777.

Kim S, Park J. *Computer aided optimum motor selection for dc servo drive systems*. International Journal of Machine Tools and Manufacture. 1990; 30 (2); 227-236.

Kim W, Trumper D. *High-precision magnetic levitation stage for photolithography*. Precision Engineering. 1998; 22 (2); 66-77.

Komada S, Ishida M, Ohnishi K, Hori T. *Disturbance observer-based motion control of direct drive motors*. IEEE Transactions on Energy Conversion. 1991; 6 (3); 553-539.

Koren Y, Heisel U, Jovane F, Moriwaki T, Pritschow G, Ulsoy G, Van Brussel H. *Reconfigurable manufacturing systems*. CIRP annals. 1999; 48 (2); 527-540.

Laub A. *Matrix analysis for scientists and engineers*. Siam. 2005

Lee J, Lee K, Kim W. *Model-based iterative learning control with a quadratic criterion for time-varying linear systems*. Automatica. 2000; 36 (5); 641-657.

Leu M, Wong H, Ji Z. *Planning of component placement/insertion sequence and feeder setup in PCB assembly using genetic algorithm*. Journal of electronic packaging. 1993; 115 (4); 424-432.

Li H, Le M, Gong Z, Lin W. *Motion profile design to reduce residual vibration of high-speed positioning stages*. IEEE/ASME Transactions On Mechatronics. 2009; 14 (2); 264-269.

- Lu X. *6D direct-drive technology for planar motion stages*. CIRP Annals-Manufacturing Technology. 2012; 61 (1); 359-362.
- Luo Y, Serrani A, Yurkovich S, Oppenheimer M, Doman D. *Model-predictive dynamic control allocation scheme for reentry vehicles*. Journal of Guidance, Control, and Dynamics. 2007; 30 (1); 100-113.
- Ma B, Herchenroeder J, Smith B, Suda M, Brown D, Chen Z. *Recent development in bonded NdFeB magnets*. Journal of magnetism and magnetic materials. 2002; 239 (1-3); 418-423.
- Mack C. *Fifty years of Moore's law*. IEEE Transactions on semiconductor manufacturing. 2011; 24 (2); 202-207.
- Mayr J, Jedrzejewski J, Uhlmann E, Donmez M, Knapp W, Härtig F, Wendt K, Moriwaki T, Shore P, Schmitt R, Brecher C. *Thermal issues in machine tools*. CIRP Annals-Manufacturing Technology. 2012; 61 (2); 771-791.
- McLaren M. *DUV*. ASML Investor Day. 2014; (http://staticwww.asml.com/doclib/investor/asml_4_Investor_Day-DUV_MM McLaren.pdf; accessed on Sep. 21st, 2018).
- Moore G. *Cramming More Components Onto Integrated Circuits*, Electronics Magazine. 1965; 38 (8); 114-117.
- Morimoto S, Tong Y, Takeda Y, Hirasa T. *Loss minimization control of permanent magnet synchronous motor drives*. IEEE Transactions on industrial electronics. 1994; 41 (5); 511-517.
- Moser R, Barrot F, Sandtner J, Bleuler H. *Optimization of two-dimensional permanent magnet arrays for diamagnetic levitation*. 17th International Conference on Magnetically Levitated Systems and Linear Drives (Maglev). 2002.
- Newport Corporation. *High Performance Air Bearing Stage Capabilities & Solutions*. (https://www.newport.com/medias/sys_master/images/images/h0d/h6b/8797212835870/Motion-PL30-Brochure.pdf; accessed on Oct. 24th, 2018)
- Nomura T, Suzuki R. *Six-axis controlled nanometer-order positioning stage for microfabrication*. Nanotechnology. 1992; 3 (1); 21-28.
- Novak W, Premji Z, Nayak U, Ebihara A. *Precision motion stage with single guide beam and follower stage*. US Patent. 1997; 5623853.
- Okazaki S. *High resolution optical lithography or high throughput electron beam lithography: The technical struggle from the micro to the nano-fabrication evolution*. Microelectronic Engineering. 2015; 133; 23-35.
- Okwudire C, Rodgers J. *Design and control of a novel hybrid feed drive for high performance and energy efficient machining*. CIRP Annals-Manufacturing Technology. 2013; 62 (1); 391-394.

- Oomen T, Rojas C. *Sparse iterative learning control with application to a wafer stage: Achieving performance, resource efficiency, and task flexibility*. Mechatronics. 2017; 46; 134-147.
- Owens D. *Multivariable norm optimal and parameter optimal iterative learning control: a unified formulation*. International Journal of Control. 2012; 85 (8); 1010-1025.
- Park Systems. *Park NX20 300 mm*. (<https://www.parksystems.com/index.php/products/large-sample-afm/park-nx20-300-mm>; accessed on Sep. 28th, 2018)
- Pellicciari M, Berselli G, Balugani F. *On designing optimal trajectories for servo-actuated mechanisms: detailed virtual prototyping and experimental evaluation*. IEEE/ASME Transactions on Mechatronics. 2015; 20 (5); 2039-2052.
- Piegl L, Tiller W. *The NURBS book*. Springer Science & Business Media; 2012.
- Physik Instrumente. *PIglide HS Planar Scanner with Air Bearing*. (<https://www.physikinstrumente.com/en/products/xy-stages/a-322-piglides-hs-planar-scanner-with-air-bearing-900713/#specification>; accessed on Oct. 24th, 2018) Inc.,
- Poon A, Novak W, *Reticle stage with reaction force cancellation*. US Patent, 2003; 6597435.
- Ramani K, Duan M, Okwudire C, Ulsoy A. *Tracking Control of Linear Time-Invariant Nonminimum Phase Systems Using Filtered Basis Functions*. Journal of Dynamic Systems, Measurement, and Control. 2017; 139 (1); 011001.
- Ravaud R, Lemarquand G, Lemarquand V, Depollier C. *Analytical calculation of the magnetic field created by permanent-magnet rings*. IEEE Transactions on Magnetics. 2008; 44 (8);1982-1989.
- Rivin E. *Vibration isolation of precision equipment*. Precision Engineering. 1995; 17 (1); 41-56.
- Rivin E. *Dynamic Properties of Vibration Isolation Systems*. ASME Press; 2003.
- Ryaboy V. *Static and dynamic stability of pneumatic vibration isolators and systems of isolators*. Journal of sound and vibration. 2014; 333 (1); 31-51.
- Sandstrom T, Wahlsten M, Sundelin E, Hansson G, Svensson A. *Mask and lithography techniques for FPD*. 31st European Mask and Lithography Conference, 2015; 9661; 966103.
- Schmidt R. *Lithographic positioning device and device manufacturing method*. US Patent; 2006; 7006199.
- Schmidt R. *Ultra-precision Engineering in Lithographic Exposure Equipment for the Semiconductor Industry*. Philosophical Transactions of the Royal Society A: Mathematical, Physical and Engineering Sciences. 2012; 370 (1973); 3950-3972.

- Schmidt R, Schitter G, Rankers A, van Eijk J. *The Design of High Performance Mechatronics: High-Tech Functionality by Multidisciplinary System Integration*. IOS Press; 2014.
- Semba T, Hirano T, Hong J, Fan L. *Dual-stage servo controller for HDD using MEMS microactuator*. IEEE Transactions on Magnetics. 1999; 35 (6); 2271-2273.
- Sencer B, Tajima S. *Frequency Optimal Feed Motion Planning in Computer Numerical Controlled Machine Tools for Vibration Avoidance*. Journal of Manufacturing Science and Engineering. 2017; 139 (1); 011006.
- Smith S, Chetwynd D, Bowen D. *Design and assessment of monolithic high precision translation mechanisms*. Journal of physics E: Scientific instruments. 1987; 20 (8); 977-983.
- Sodano H, Bae J, Inman D, Belvin W. *Improved concept and model of eddy current damper*. Journal of Vibration and Acoustics. 2006; 128 (3); 294-302.
- Soong T, Spencer B. *Supplemental energy dissipation: state-of-the-art and state-of-the-practice*. Engineering structures. 2002; 24 (3); 243-259.
- Stokowski S, Vaez-Iravani M. *Wafer inspection technology challenges for ULSI manufacturing*. AIP Conference Proceedings 1998; 449 (1); 405-415.
- Sun J, Jolly M, Norris M. *Passive, adaptive and active tuned vibration absorbers*. Journal of mechanical design. 1995; 117; 234-242.
- Tan K, Huang S, Lee T. *Robust adaptive numerical compensation for friction and force ripple in permanent-magnet linear motors*. IEEE Transactions on Magnetics. 2002; 38 (1); 221-228.
- Tomizuka M. *Zero phase error tracking algorithm for digital control*. Journal of Dynamic Systems, Measurement, and Control. 1987; 109 (1); 65-68.
- Van Den Braembussche P, Swevers J, Van Brussel H, Vanherck P. *Accurate tracking control of linear synchronous motor machine tool axes*. Mechatronics. 1996; 6 (5); 507-521.
- Van de Straete H, Degezelle P, De Schutter J, Belmans R. *Servo motor selection criterion for mechatronic applications*. IEEE/ASME Transactions on mechatronics. 1998; 3 (1); 43-50.
- Van de Wijdeven J, Donkers T, Bosgra O. *Iterative learning control for uncertain systems: Robust monotonic convergence analysis*. Automatica. 2009; 45 (10); 2383-2391.
- Van Herpen R, Oomen T, Kikken E, van de Wal M, Aangenent W, Steinbuch M. *Exploiting additional actuators and sensors for nano-positioning robust motion control*. Mechatronics. 2014; 24 (6); 619-631.
- Van Schothorst G, Van Eijk J, Loopstra E, Schmidt R, Peeters F. *Lithographic apparatus and device manufacturing method*. US Patent. 2007; 7248339.

- Van Zundert J, Oomen T. *On inversion-based approaches for feedforward and ILC*. Mechatronics. 2018; 50; 282-291.
- Wang C, Horng J. *Constrained minimum-time path planning for robot manipulators via virtual knots of the cubic B-spline functions*. IEEE transactions on automatic control. 1990; 35 (5); 573-577.
- Wang Z, Cheng X, Nakamoto K, Kobayashi S, Yamazaki K. *Design and Development of a Precision Machine Tool Using Counter Motion Mechanisms*. International Journal of Machine Tools and Manufacture. 2010; 50 (4); 357-365.
- Weck M, McKeown P, Bonse R, Herbst U. *Reduction and compensation of thermal errors in machine tools*. CIRP Annals-Manufacturing Technology. 1995; 44 (2); 589-598.
- Wei Y. *Electronic device and assistance structure thereof*. US Patent Application. 2007; US2007/0059076A1.
- Xu L, Yao B. *Output feedback adaptive robust precision motion control of linear motors*. Automatica. 2001; 37 (7); 1029-1039.
- Yan Y, Wang H, Zou Q. *A decoupled inversion-based iterative control approach to multi-axis precision positioning: 3D nanopositioning example*. Automatica. 2012; 48 (1); 167-176.
- Ye Y, Wang D. *Clean system inversion learning control law*. Automatica. 2005; 41 (9); 1549-1556.
- You Y, Ahn H. *A passive reaction force compensation (RFC) mechanism for a linear motor motion stage*. International journal of precision engineering and manufacturing. 2014; 15 (5); 797-801.
- Yoon D, Zeng B, Okwudire C. *Decouplable Coarse-Fine Stage for Improved Precision and Efficiency in Point-to-point Positioning*. Annual meeting of American Society for Precision Engineering. 2017.
- Yoon D, Okwudire C. *Reference Trajectory Generation of Decouplable Coarse-fine Stage for Point-to-point Positioning Applications*. Annual meeting of American Society for Precision Engineering. 2018.
- Zhou K, Doyle J, Glover K. *Robust and optimal control*. Prentice Hall. 1996.
- Zsiga N, van Dooren S, Elbert P, Onder C. *A new method for analysis and design of iterative learning control algorithms in the time-domain*. Control Engineering Practice. 2016; 57; 39-49.